

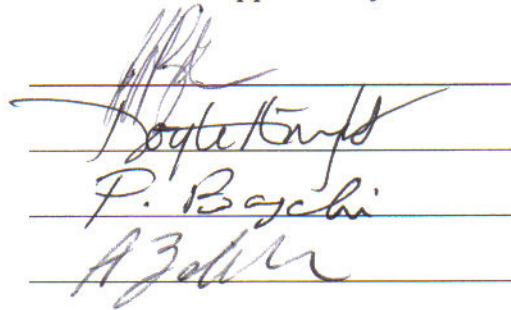
THREE-DIMENSIONAL COMPUTATIONAL MODELING
AND SIMULATION OF BIOLOGICAL CELLS AND
CAPSULES

BY SAI DODDI

A dissertation submitted to the
Graduate School—New Brunswick
Rutgers, The State University of New Jersey
in partial fulfillment of the requirements
for the degree of
Doctor of Philosophy
Graduate Program in Mechanical and Aerospace Engineering

Written under the direction of
Professor Prosenjit Bagchi

and approved by



The image shows three horizontal lines of paper with handwritten signatures. The first signature is in blue ink and appears to be 'P. Bagchi'. The second signature is in black ink and appears to be 'A. Zoller'. The third signature is in black ink and appears to be 'A. Zoller'.

New Brunswick, New Jersey

October, 2008

ABSTRACT OF THE DISSERTATION

Three-dimensional computational modeling and simulation of biological cells and capsules

by Sai Doddi

Dissertation Director: Professor Prosenjit Bagchi

Three-dimensional computational modeling and simulation are presented on the flow-induced motion of highly deformable particles which are representative of biological cells, such as red blood cells. We focus on the dynamics of capsules, that is, liquid drops surrounded by hyperelastic membranes. Unlike liquid drops where the fluid-fluid interface is characterized by isotropic surface tension, that for a capsule is governed by more complex constitutive laws. The numerical method is based on a front-tracking/immersed boundary method for capsule deformation, and a finite-difference/fourier-transform method for the flow solver. The methodology is able to consider large deformation of capsules, capsule-capsule interaction, semi-dense suspension, and inertial effect. Using the simulation tool, we address a sequence of problems:

(a) Capsule motion in wall-bounded pressure-driven flows: The motion of a capsule in a channel flow is investigated in absence of inertia and under large deformation. It is shown that a deformable capsule slowly drifts lateral to the flow and away from the wall while moving axially with the flow. Based on the theory of small deformation, and the present numerical results, an approximate expression for migration velocity under large deformation

is developed.

(b) Binary interaction in wall-bounded pressure-driven flows: Hydrodynamic interaction between two capsules in a channel flow is investigated in absence of inertia. Effect of wall-proximity on the shear-induced diffusion process, in which one capsule rolls over the other, is studied for spherical and ellipsoidal resting shapes.

(c) Effect of inertia on binary collision: Hydrodynamic interaction between two capsules in a linear shear flow is investigated in presence of inertia. The shear-induced diffusion process is shown to be absent. Instead, a new interaction mode is found in which the capsules engage in spiraling motion.

(d) Simulation of semi-dense suspension: We then consider direct numerical simulations (DNS) of suspension of multiple capsules of spherical and biconcave resting shapes. Detailed analysis of the numerical results and their relevance to in vitro blood flow are presented. It is shown that the two-phase model of blood in microvessels underpredicts the DNS flow rate. We proceed to develop a three-layer model based on the microrheology extracted from the DNS, and show that it accurately predicts the DNS velocity.

Acknowledgements

First and foremost, I would like to thank my advisor, Prof. Prosenjit Bagchi for the guidance and support provided throughout my doctoral study. He has been more than an advisor and a guide to me. He has been readily available to help me whenever I stumbled, for which I am fortunate. He is an excellent advisor, with enormous patience to help out his students. His enthusiasm and passion have taught me how to truly appreciate science. He is very knowledgeable with a good vision in problems related to fluid mechanics. I thank him wholeheartedly for his careful mentoring.

I would also like to thank the committee members for taking the time to read the thesis and providing valuable suggestions. I also extend my thanks to many faculty members at Rutgers, who have provided me with good advice during my Ph.D. I cannot also forget the MAE BBQ lunches, and I thank the mechanical and aerospace engineering department.

I would also like to thank my friends Chia, Chen and Sun, the technical discussions with whom helped me enormously. I enjoyed our closely knit fluid mechanics group under Prof. Bagchi, specially our group lunches. My interactions with Kirit, Vijay and Murthy are memorable. I appreciate them for their support. I thank my colleagues Pallab and Tushar for keeping me sane with their conversations, and my roommates Prabeer and Pradeep for encouraging and disciplining me while sharing their experience.

Partial funding from NSF grants (BES-0603035 and CTS-0625936), computational support from the National Center for Supercomputing Applications at Illinois, San Diego Supercomputing Center, and NERSC resources at Lawrence Berkeley National Laboratory is acknowledged.

Last but not the least, I thank my family, especially my Dad for guiding and motivating me at every stage of my life. I cannot thank him enough for his gratitude and love.

Dedication

To my family, whose encouragement and sacrifices lie behind my accomplishments.

Table of Contents

Abstract	ii
Acknowledgements	iv
Dedication	v
List of Tables	x
List of Figures	xi
1. Introduction	1
1.1. Circulatory System	1
1.2. Blood	1
1.2.1. Red Blood Cell	2
1.3. Rheological Models for Blood Cells as Capsules	3
1.3.1. Dynamics of Single Capsule	5
1.4. Blood in Microcirculation	6
1.4.1. Fahraeus and Fahraeus-Lindqvist effect	7
1.4.2. Cell-free layer	7
1.4.3. Lateral Migration	10
1.4.4. Challenges	10
1.5. Scope of the thesis	11
2. Numerical Methodology	14
2.1. Flow Configuration and Simulation Technique	14
2.1.1. Problem setup	14

2.1.2.	Fluid-structure interaction	15
2.1.3.	Numerical treatment of membrane deformation	17
2.1.4.	Surface discretization	20
2.1.5.	Interface tracking	21
2.1.6.	Flow solver	21
2.1.7.	Numerical resolution	24
2.2.	Validation	24
2.2.1.	Capsule deformation in linear shear flow	24
2.2.2.	Resolution test	34
3.	Lateral Migration of a Capsule in a Plane Poiseuille Flow in a Channel	37
3.1.	Introduction	37
3.2.	Flow Configuration and Simulation Technique	41
3.2.1.	Problem setup	41
3.2.2.	Dimensionless parameters	41
3.3.	Results and Discussion	42
3.3.1.	Migration at $\lambda = 1$	42
3.3.2.	Larger capsules	57
3.3.3.	Effect of λ	62
3.3.4.	Effect of capsule separation	66
3.4.	Conclusion	67
4.	Lateral Migration and Pairwise Interaction of Liquid Capsules in a Plane Poiseuille Flow in a Channel	69
4.1.	Introduction	69
4.2.	Problem Setup	70
4.3.	Results and Discussion	72
4.3.1.	Capsule-Capsule interaction	72

4.3.2. Ellipsoidal capsules	87
4.4. Conclusion	93
5. Effect of Inertia on the Hydrodynamic Interaction between Two Liquid Capsules in Simple Shear Flow	95
5.1. Introduction	95
5.2. Problem Setup	97
5.3. Results and Discussion	98
5.3.1. Capsule Deformation at Finite Re	98
5.3.2. Capsule–Capsule Interaction at $Re \ll 1$	102
5.3.3. Capsule–Capsule Interaction at Finite Re : Short Time Behavior	104
5.3.4. Capsule–Capsule Interaction at Finite Re : Long-Time Behavior	113
5.3.5. Regimes of Capsule–Capsule Interaction at Finite Re	115
5.4. Summary and Conclusion	118
6. Three-dimensional Computational Modeling and Simulation of Multiple Cells Flowing in Microvessels	121
6.1. Introduction	121
6.2. Results	123
6.2.1. Tumbling of biconcave cells	123
6.2.2. Single-file motion	124
6.2.3. Multi-file motion	128
6.2.4. Comparison of DNS results with two-phase model	147
6.2.5. A three-layer model of blood flow in microvessels	153
6.3. Conclusion	156
7. Conclusions of Thesis and Directions for Future Work	157
7.1. Summary and conclusions	157
7.2. Future directions	161

Bibliography	163
Vita	175

List of Tables

2.1. Validation: Comparison of steady state deformation D with Ramanujan & Pozrikidis (1998) (RP), Lac <i>et al.</i> (2004) (L1), Li and Sarkar (2008) (LS) and small deformation theory (S.D) of Barthès-Biesel & Rallison (1981).	29
2.2. Validation: Comparison of capsule orientation θ/π at steady state with Ramanujan & Pozrikidis (1998) (RP), and Lac <i>et al.</i> (2004) (L1). RP's data at $Ca = 0.025$ is not included since θ did not reach a steady value in their simulation.	31
2.3. Validation: Comparison of tank-treading period $\dot{\gamma}T$, with Ramanujan & Pozrikidis (1998) (RP), and Lac <i>et al.</i> (2004) (L1). * TTP is computed following a revolution of a marker point. † TTP is computed by integrating $dl/ v $ over the membrane circumference in the (x, y) -plane, as done in L1, where dl is a line segment of the capsule profile, and v is the membrane velocity.	31
6.1. Size ratio (H/d) , vessel hematocrit (H_t) , number of cells per computational box (N_c) , and Eulerian resolution used in the present simulations.	129
6.2. Viscosity of the core (μ_c) and cell-free layer (μ_f) , and the thickness $\beta - \delta$ of the transition layer obtained from the simulations	152

List of Figures

1.1. A Scanning Electron Microscope image of red blood cells (RBC), white blood cells (WBC), and disc shaped platelets. Image source: National Cancer Institute.	2
1.2. (a) Section of a red blood cell. Part of the RBC is magnified to show the composition of the RBC membrane. (b) The lipid bilayer of the RBC membrane is shown.	3
1.3. Top panel: Effect of diameter of the tube on the relative apparent viscosity for 45% volume fraction of red blood cells. Solid curve is the empirical fit to data (Pries <i>et al.</i> 1990). Bottom panel: Effect of diameter of the tube on the hematocrit ratio H_T/H_D	8
1.4. Flow of human red blood cells moving through glass tubes with approximate diameters $4.5 \mu m$ (top), $7 \mu m$ (middle), and $15 \mu m$ (bottom), in the experiments by Alex R. Pries (Pozrikidis 2003); the flow direction is from left to right.	9
2.1. Three dimensional computational domain for simulation of capsule suspension.	15
2.2. The Eulerian and Lagrangian grids.	16
2.3. (a) Lagrangian elements on the capsule surface. (b) Deformation of a planar triangular element in space, and comparison of the deformed and undeformed element in a common plane.	18
2.4. (a) Capsule deformation in linear shear flow. 2D shapes in the shear plane are shown after steady state is reached. $-\circ-$ Initial shape, $\cdots \cdots Ca = 0.05$, $-\text{---} Ca = 0.1$, $-\text{---} Ca = 0.2$. (b) Flow field at $Ca = 0.1$ after steady state is reached.	26

2.5. Comparison of deformation of capsule for present results with experiment (Rehage <i>et al.</i> 2002) and linear theory of Barthès-Biesel & Rallison (1981).	27
2.6. Validation of the numerical methodology: Deformation parameter D versus time. Present results. (a) — Ramanujan & Pozrikidis (1998). (b) — Lac <i>et al.</i> (2004). Values next to the curves indicate capillary numbers. In order to obtain the curves from RP and L1, the figures in their papers were scanned and then uploaded in Tecplot.	28
2.7. Resolution tests at $Ca = 0.2$ showing the steady values of D . (a) Effects of varying Eulerian resolution $((N_E)^3 \square$, and Lagrangian resolution $(N_L) \diamond$. N_L is the number of triangular elements on the capsule surface. (b) Effects of varying timestep size $(\Delta t) \nabla$, and computational domain size $(H_x) \triangleright$. . .	30
2.8. Principal stress distribution for $Ca = 0.025$. Compressive (negative) stress (indicated by white shade) in the equatorial region can be seen.	32
2.9. Validation of the numerical methodology: Steady-state values of D for $\lambda \neq 1$. $-\square-$ Ramanujan & Pozrikidis (1998); $\cdots \diamond \cdots$ present results.	33
2.10. Validation: Trajectory of a material point on the capsule membrane at $Ca = 0.2$. Solid line (x -coordinate); dashed line (y -coordinate). Lines without symbols are results from Lac <i>et al.</i> (2004). Lines with symbols are present results.	34
2.11. Resolution test: (a) Deformation history, and (b) final steady shape in linear shear flow $Ca = 0.1$: —, 80^3 Eulerian points and 1280 Lagrangian elements; — — 120^3 Eulerian points and 1280 Lagrangian elements; 120^3 Eulerian points and 5120 Lagrangian elements. In (a), inset shows details.	35
3.1. Schematic of the flow configuration. The computational domain is indicated by dashed lines.	40

3.2.	Migration of a capsule in a pressure-driven flow in a channel. Sequence of capsule shapes during initial transience is shown for $Ca = 0.2$ (top row) and $Ca = 0.8$ (bottom three rows). Here $t^* = tU_{cl}/H$. X,Y,Z coordinates are scaled by channel height H . $Y/H = 0$ is bottom wall of the channel, and $Y/H = 0.5$ is channel center. Here $\lambda = 1$, and $a/H = 0.16$	43
3.3.	Same as in figure 3.2, but over an extended period of time. $Ca = 0.2$ (top), and $Ca = 0.8$ (bottom).	44
3.4.	History of (a) lateral distance, (b) lateral velocity, (c) slip velocity, (d) deformation, and (e) orientation (w.r.t. X-axis) of a capsule as a function of Ca $Ca = 0.1$; — $Ca = 0.2$; - - - $Ca = 0.4$, and - - - $Ca = 0.8$. Here $a/H=0.16$, and $\lambda = 1$	46
3.5.	Comparison of a free capsule with quasi-steady results for $Ca = 0.2$, $\lambda = 1$, and $a/H = 0.16$. In (a) and (b) lines are for the free capsule, and dots are for the quasi-steady results. Capsules shapes at two different locations are shown in the bottom. Solid line is the free capsule, and dash line is the quasi-steady result.	48
3.6.	Same as in figure 3.5, but for $Ca = 0.8$	49
3.7.	Dependence of migration velocity, slip velocity, deformation, and orientation on Ca while keeping a/H and Y_c/H constants at 0.16, and 0.18, respectively. The dashed line corresponds to the linear theory.	51
3.8.	(a) Variation of V_y , (b) V_{slip} , and (c) D w.r.t. Y_c while keeping Ca and $a/H = 0.16$ fixed.	54
3.9.	Variation of V_y w.r.t. a/H at constant Ca and Y_c/H . Ca is fixed at 0.2. . .	55
3.10.	(a) Comparison of the scaled shape function C_s (solid line), and the numerical migration velocity (filled circles) for $a/H = 0.16$. (b) Replotting figure 3.9 by scaling V_y by $(F_1 F_2)$	56

3.11. Migration of a capsule at $a/H = 0.5$, and $Ca = 0.2$. Top: deformed shapes for free capsule (solid line), and quasi-steady simulations (dash line). Bottom: lateral velocity for free capsule (solid line) and quasi-steady results (filled circles). Also shown is the effect of increasing separation distance between consecutive capsules: filled circles, open circles and boxes correspond to $L_{x0}/a = 2, 6$ and 8 , respectively.	59
3.12. Velocity vectors drawn in the XY plane passing through, and in a frame of reference moving with, the capsule center of mass. (a)–(c) are for $a/H = 0.5$, $Ca = 0.2$ at $Y_c/H = 0.35, 0.44$, and 0.46 , respectively. (d) for $a/H = 0.16$. .	60
3.13. Effect of separation distance on flow pattern: velocity vectors (in a frame of reference moving with the velocity of the capsule center of mass) corresponding to the case shown in figure 3.12a–c but for $L_{x0}/a = 8$	61
3.14. Membrane stress distribution for the migrating capsule shown in figure 3.11. Dark regions correspond to compressive stress.	62
3.15. Free capsule versus quasi-steady results for $\lambda \neq 1$. Lines represent free capsule and symbols represent quasi-steady simulations. Solid lines and filled circles represent $\lambda = 5$, dash lines and open circles represent $\lambda = 0.2$. $a/H = 0.16$, $Ca = 0.2$	63
3.16. Deformed shapes for $a/H = 0.5$, $Ca = 0.2$ at $\lambda = 0.2$ (top) and $\lambda = 5$ (bottom). Solid line is the free capsule, and dotted line is the quasi-steady result.	64
3.17. Migration velocity, deformation, and orientation as functions of Y_c . $a/H = 0.16$, $Ca = 0.2$. $\square \lambda = 1$, $\Delta \lambda = 0.2$, $\nabla \lambda = 5$	65
3.18. Effect of separation distance L_{x0} . $\square Ca = 0.2, a/H = 0.16$; $\circ Ca = 0.4, a/H = 0.16$; $\diamond Ca = 0.2, a/H = 0.5$. Migration velocities shown here correspond to the quasi-steady simulations.	66
4.1. Schematic of the computational domain with capsules. The undisturbed flow is parabolic.	70

4.2. Schematic of the initial configuration of capsules in the domain for various cases (discussed in sections 4.3 and 4.3.1). The boundaries of the periodic domain are indicated by dashed lines. (a) Migration of an isolated capsule, (b) Interaction of two capsules separated axially and (c) Interaction of capsules separated both axially and laterally.	71
4.3. Migration of an array of equispaced capsules. Effect of capsule-to-capsule separation distance on (a) the lateral position and (b) migration velocity. Thin lines without symbols correspond to the array of capsules of size $a/H = 0.16$ spaced along the x -direction for which the following cases are shown: — $L_{x0}/H = 2$; - - - - $L_{x0}/H = 1$; - - - $L_{x0}/H = 1/3$; and $\cdot \cdot \cdot \cdot \cdot L_{x0}/H = 1/5$. The thin lines with symbols correspond to the array of capsules of size $a/H = 0.16$ spaced along the z -direction for which the following cases are shown: — Δ — $L_{z0}/H = 1/3$; and — \square — $L_{z0}/H = 1/5$. The thick lines correspond to the array of capsules of size $a/H=0.32$ spaced along the x -direction for which the following cases are shown: — $L_{x0}/H = 1$; and - - - $L_{x0}/H = 1/2$. For all cases $\lambda = 1$ is considered. For $a/H = 0.16$, we considered $Ca = 0.4$, whereas for $a/H = 0.32$, we considered $Ca = 0.2$	73
4.4. Migration of a pair of closely-spaced capsules with the same initial lateral locations of the centroids as discussed in Section A.2. Evolution of the capsule shape is shown. The parameters considered are $Ca = 0.2$ and $\lambda = 1$. Here $y_{c0}/H = 0.18$ for both capsules, and $L_{x0}/H = 0.29$	76

- 4.5. Migration of a pair of closely-spaced capsules having same initial lateral locations. Shown here are (a) lateral location, (b) lateral velocity, (c) axial velocity, and (d) lateral and absolute separation distances between the capsules. The line patterns used in (a) to (c) are as follows: ——— $Ca = 0.2$, $L_{x0}/H = 0.29$, $y_{c0}/H = 0.18$; - - - $Ca = 0.1$, $L_{x0}/H = 0.29$, $y_{c0}/H = 0.18$; ····· $Ca = 0.2$, $L_{x0}/H = 0.29$, $y_{c0}/H = 0.29$; and · · · · - $Ca = 0.1$, $L_{x0}/H = 0.24$, $y_{c0}/H = 0.18$. (d) Lateral separation distance (— · · · —, right axis), and absolute separation distance (———, left axis) between the capsules for a representative case of $y_{c0} = 0.18$, $Ca = 0.2$ and $L_{x0}/H = 0.29$. For all cases in (a) to (d), $\lambda = 1$ 78
- 4.6. Migration of a pair of closely-spaced capsules with different initial lateral locations of the centroids as in Section A.3. The flow is from left to right. Here $y_{c0}/H = 0.21$ for the upstream ('1') capsule, and $y_{c0}/H = 0.18$ for the downstream ('2') capsule. Other parameters are: $L_{x0}/H = 0.29$, $Ca = 0.2$, and $\lambda = 1$. Shapes at $t^* = 0$ and at later times are shown. 79
- 4.7. Migration of a pair of closely-spaced capsules with different initial lateral locations of the centroids as shown in figure 9. Lateral position and lateral velocity are shown in (a) and (b). The lateral separation distance between the capsules, and the relative velocity between them are shown in (c) and (d), respectively. For all figures following line patterns are used: ····· $\lambda = 1$, $Ca = 0.2$; - - - - $\lambda = 1$, $Ca = 0.8$; and ——— $\lambda = 5$, $Ca = 0.2$. In (a) thin lines correspond to the results of an isolated capsule, and the thick lines for the capsule-pairs. In (b) to (d) only the results for the capsule-pairs are shown. In (a) and (b), results for both upstream and downstream capsules marked by '1' and '2' are shown. 81

- 4.8. Effect of increasing the number of capsule-pairs. Top Panel: Initial configuration and shapes at $t^*=8$. Here $Ca = 0.2$ and $\lambda = 1$ are considered. The lateral positions and velocities are shown in (a) and (b), respectively. The results of a single capsule-pair (from figure 4.7) and of an isolated capsule are also shown for comparison. Line patterns used for (a) and (b) are as follows: — four capsules; - - - a capsule-pair; and \cdots an isolated capsule. For the case of four capsules, lateral location and velocity of ‘1’ and ‘2’ coincide with those of ‘3’ and ‘4’, respectively. 83
- 4.9. Migration of a pair of non-identical capsules (Section A.4). Effect of different Ca is considered. Lateral position versus time is shown for the capsule-pair (solid line), and for an ‘isolated’ capsule (dash line) released from the same initial location and with the same parameters. (a) (case i) The upstream capsule has $Ca = 0.2$, and the downstream capsule has $Ca = 0.8$. (b) (case ii) The upstream capsule has $Ca = 0.8$, and downstream capsule has $Ca = 0.2$. Here $\lambda = 1$ and $a/H = 0.16$ for all cases shown. 84
- 4.10. Migration of a pair of non-identical capsules (Section A.4). Effect of dissimilar a/H is considered. For the larger capsule $a/H = 0.32$, and for the smaller one $a/H = 0.16$. The figures on the left show the capsule shapes at various times. The figures on the right show the lateral positions versus time. Solid lines are for the case of the capsule pair. Dashed lines correspond to the result of an ‘isolated’ capsule released from the same location with similar parameters. Here $\lambda = 1$ and $Ca = 0.2$ for all cases. 86
- 4.11. Migration of an isolated ellipsoidal capsule. Here $y/H = 0$ is the bottom wall of the channel, and $y/H = 0.5$ is the center. Initial shape and deformed shapes at later times are shown. The flow is from left to right. The figure corresponds to $\lambda = 5$, and $Ca = 0.2$ 88

4.12. Migration of ellipsoidal capsules. (a) Lateral position, (b) lateral velocity, and (c) instantaneous orientation of the major axis of the capsule versus time are shown. For all cases $Ca = 0.2$. Line patterns used here are as follows: — isolated ellipsoid with $\lambda = 1$; - - - - - isolated sphere having the same volume and $\lambda = 1$; - - - - - isolated ellipsoid with $\lambda = 5$; and $\cdots\cdots$, an array of ellipsoids arranged along the x-direction with center-to-center distance $L_{x0} = H/3$ and $\lambda = 1$	90
4.13. Migration of a pair of closely-spaced ellipsoids with their centroids located initially at the same lateral position $y_{c0}/H = 0.21$. Line patterns used are as follows: - - - $\lambda = 1$; — $\lambda = 5$. Also shown is the result for an isolated ellipsoid ($\cdots\cdots$) at $\lambda = 1$. For all cases $Ca = 0.2$	91
4.14. Lateral migration of a pair of closely-spaced ellipsoids with their centroids located initially at different lateral positions. Shown here are (a) lateral location, (b) lateral velocity, and (c) instantaneous angular orientation. The line patterns used in (a) and (b) are as follows: - - - $\lambda = 1$; — $\lambda = 5$. Also shown is the result of an isolated capsule ($\cdots\cdots$) for $\lambda = 1$. In plot (c), angular orientation for only $\lambda = 1$ case is shown, where - - - represents the upstream capsule, - - - - the downstream capsule, and $\cdots\cdots$ represents an isolated capsule. For all cases, $Ca = 0.2$	92
5.1. Schematic of interaction of a pair of rigid and deformable bodies in shear flow: (a) rigid, and (b) deformable. Here Δy_1 and Δy_2 are the initial and final lateral distances of the bodies.	96
5.2. Schematic of the initial configuration showing the computational domain and initial location of the capsules in shear flow.	98
5.3. Deformation of single capsule at finite Re . (a) steady shapes (b) deformation parameter D , and (c) angular orientation θ . Line patterns are: - - - - - $Re = 10$; — $Re=25$; $\cdots\cdots$ $Re=50$ ($We = 2, 5, 10$, respectively). In (a), the initial capsule shape is shown by $\text{---}\circ\text{---}$	100

5.4.	Flow field around single capsule at (a) $Re \ll 1$, (b) $Re = 10$, and (d) $Re = 50$. The stagnation points on one side of the flow are marked with long arrows.	101
5.5.	Sequence of capsule-capsule interaction at $Re \ll 1$. Capsule shapes for $Ca=0.2$ are shown.	103
5.6.	Lateral separation Δy versus Δx for $Re \ll 1$. Shown here are $Ca=0.05$, $Ca=0.2$, $Ca=0.4$. t^* increases from left to right. At $t^* = 0$, $\Delta y_0 = 0.2$.	104
5.7.	Sequence of capsule-capsule interaction at finite Re . Shown here is $Re=10$ ($We = 2$), $\Delta x_0/a = 4$, $\Delta y_0/a = 0.2$.	106
5.8.	(a) Capsule trajectories (x_c versus y_c) at finite Re . (b)–(c) lateral coordinates of capsule centroids (y_c) versus t^* . For (a)–(c), line patterns are: $Re \ll 1$; $Re=0.5$; $Re=1.5$; $Re=2.3$; $Re=3$; $Re=10$; thick line $Re=50$. Symbol ‘o’ in (a) is the initial location of capsule center.	107
5.9.	Capsule trajectories at finite Re . (a) Effect of Δy_0 for $Re = 50$. $\Delta y_0/a = 0.57$; $\Delta y_0/a = 0.4$; $\Delta y_0/a = 0.2$. (b)–(c) Effect of Δx_0 . (b) $\Delta x_0 = 8$, and (c) $\Delta x_0 = 1.5$. For (b) and (c) line patterns are: $Re = 3$; $Re = 10$; $Re = 50$. Diamond symbols indicate the initial location of the capsule centroids.	110
5.10.	Minimum horizontal distance between the capsule-pair at finite Re . $\square \Delta x_0/a = 8$, $\Delta y_0/a = 0.2$; $\triangleright \Delta x_0/a = 4$, $\Delta y_0/a = 0.3$; $\nabla \Delta x_0/a = 4$, $\Delta y_0/a = 0.2$; $\triangle \Delta x_0/a = 4$, $\Delta y_0/a = 0.1$; $\circ \Delta x_0/a = 4$, $\Delta y_0/a = 0.05$; $\diamond \Delta x_0/a = 1.5$, $\Delta y_0/a = 0.2$.	112
5.11.	Long-time trajectories of capsules at finite Re . Line patterns are: $Re=10$, $Re = 25$, $Re=50$. Diamond symbols indicate the initial capsule locations.	114
5.12.	Time sequence of fluid velocity vectors for capsule-capsule interaction at $Re=10$. (a)–(e) are at $t^*=5, 9, 12, 20$, and 28 .	116

5.13. Same as in previous figure but for $Re=50$. (a)–(d) are at $t^*=18, 23, 28$, and 33.	117
5.14. Regimes of capsule-capsule interaction at finite Re and We . ●, Self-diffusion type motion; ▲, outward spiraling motion; × inward spiraling motion; and ◇, fixed-orbit motion.	119
6.1. (a) Tumbling motion of a biconcave cell. (b) and (c) show cell trajectory (x_c and y_c), velocity (u/U_{cl} and v/U_{cl}), and angular orientation (θ/π) with the x -axis.	125
6.2. Transient shapes of the initially spherical capsule with $Ca = 0.6$ and $H/d = 1.25$ shown in (a). Also shown are 2D slices on the x - y and x - z planes for three values of Ca with $Ca = 0.6, 0.1$ and 0.02 corresponding to (b), (c) and (d) respectively, at $t^* = 1.6$	126
6.3. Transient shapes of the initially biconcave capsule with $Ca = 0.6$ and $H/d = 1.37$ shown in (a). Also shown are 2D slices on the x - y and x - z planes for three values of Ca with $Ca = 0.05, 0.2$ and 0.6 corresponding to (b), (c) and (d) respectively, at $t^* = 4.8$	127
6.4. Instantaneous snapshots for suspension of spherical cells after the flow has reached a stationary state for $H/d = 1.6$ (top), $H/d = 3.1$ (middle), and $H/d = 6.3$ (bottom).	130
6.5. Time history of apparent viscosity. a: $Ca = 0.05, H_t = 0.26, d/H = 0.16$; b: $Ca = 0.6, H_t = 0.26, d/H = 0.16$; c: $Ca = 0.05, H_t = 0.18, d/H = 0.16$; d: $Ca = 0.05, H_t = 0.18, d/H = 0.22$; e: $Ca = 0.6, H_t = 0.18, d/H = 0.22$; f: $Ca = 0.6, H_t = 0.12, d/H = 0.22$; g: $Ca = 0.05, H_t = 0.05, d/H = 0.22$; . . .	132
6.6. Instantaneous snapshots for suspension of biconcave cells. (a) Initial distribution and cell shape for $H/d = 3.1$. (b) and (c) show distribution and cell shape for $H/d = 3.1$ and 4.9 , respectively, after the flow has reached a stationary state.	134

6.7.	Sample cell trajectory (left panel) and velocity traces (right panel) for $H/d =$ 4.5. (a) $Ca = 0.6$, $H_t = 0.05$; (b) $Ca = 0.005$, $H_t = 0.05$; (c) $Ca = 0.6$, $H_t = 0.18$; (d) $Ca = 0.005$, $H_t = 0.18$	136
6.8.	RMS fluctuation y' over channel cross-section. Effect of (a) hematocrit, (b) Ca , and (c) H/d . Fluctuations in two cross-stream directions are compared in (d).	138
6.9.	RMS velocity fluctuation over channel cross-section. (a) Effect of hematocrit is shown for $H/d = 6.3$ and $Ca = 0.05$. Also shown is the in vivo data of Bishop <i>et al.</i> (2002) (dotted line). (b) RMS of three velocity components.	139
6.10.	Cross-sectional variation of hematocrit. Results are shown for half channel width; $y/H = 0$ is the wall and $y/H = 0.5$ is the center.	141
6.11.	Dimensionless cell-free layer width $\delta/(H/2)$ as a function of (a) H_t for two values of Ca and H/d for spherical cells, and (b) as a function of H/d for biconcave and spherical cells. Also shown in (b) is the in vivo data of Kim <i>et al.</i> (2007).	142
6.12.	Mean velocity profile. Dotted line is the parabolic flow. In (b) symbols are the Lagrangian cell velocity.	144
6.13.	Fahraeus-Lindqvist and Fahraeus effects. Variation of (a) relative apparent viscosity μ_{rel} and (b) hematocrit ratio H_t/H_d as a function of vessel size for different Ca at $H_t = 26\%$. Results for spherical cells are shown for $Ca = 0.005$ —□—, $Ca = 0.05$ —○—, and $Ca = 0.6$ —▽—. Results for biconcave capsules are shown for $Ca = 0.05$ —●— and $Ca = 0.2$ —△—. In (a), dash line is the correlation of Pries <i>et al.</i> (1992) based on in vivo data. The insets in (a) and (b) shows the results for lower range of H/d	146
6.14.	Cross-section variation of viscosity obtained from the simulations for some sample cases for $H/d = 6.3$. Results are shown for half channel width; $y/H = 0$ is the wall and $y/H = 0.5$ is the center.	149

6.15. Schematic of two-phase (a) versus three-layer (b) models. In (c), cross-section variation of viscosity is shown. Only the lower half of the channel is shown.	150
6.16. Comparison of mean velocity obtained from simulations (symbols), and predicted by two-phase model (eq 6.2.10, dash lines) and three-layer model (eq 6.2.19, solid lines). Results are shown for $H/d = 6.3$. In (a) H_t is varied while Ca is held fixed. In (b) Ca is varied and H_t is held fixed.	155

Chapter 1

Introduction

1.1 Circulatory System

The human circulatory system is composed of the heart, blood, and blood vessels facilitating the delivery of oxygen and nutrients to every cell in the body. Blood is pumped by the heart through the arterial and venular systems. The large arteries supply blood to smaller vessels, known as arterioles, which then supply blood to even smaller vessels known as capillaries. The nutrients and oxygen diffuse through the thin walls of the capillaries to the adjacent tissue. The oxygen depleted blood is then collected in venules, and then in veins, and finally it returns to the heart. The circulatory system can be divided into macro and micro-circulation. The macro-circulation refers to the flow of blood in large blood vessels, such as aorta, large arteries and veins, having internal diameter greater than about $500\text{ }\mu\text{m}$. The micro-circulation refers to the flow of blood in vessels in the diameter range of $5\text{--}500\text{ }\mu\text{m}$, and it consists of arterioles, venules and capillaries.

1.2 Blood

Blood is a multiphase suspension that is primarily composed of plasma, red blood cells, white blood cells and platelets (figure 1.1). Plasma is a liquid that constitutes about 55% of total blood volume. Blood cells are suspended in plasma. It also contains many sub-micron and nano-scale particulates, such as proteins and lipids, apart from minerals, glucose and enzymes. Nearly 90% of plasma is made of water; hence the density and viscosity of plasma ($\sim 1.2\text{ cP}$) are nearly equal to the viscosity of water (1 cP).

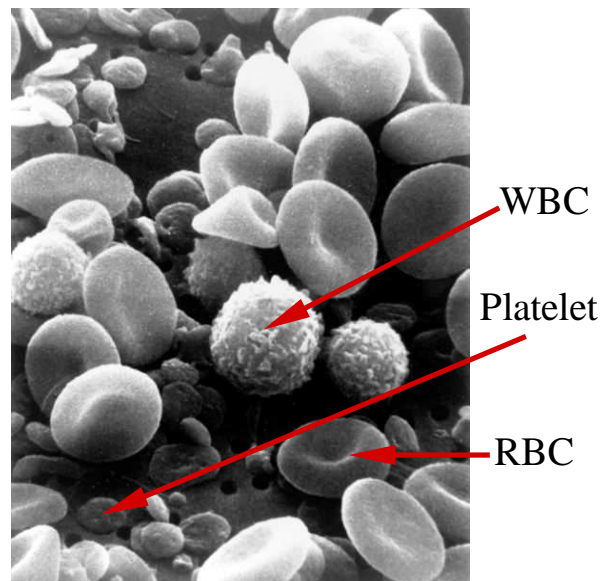


Figure 1.1: A Scanning Electron Microscope image of red blood cells (RBC), white blood cells (WBC), and disc shaped platelets. Image source: National Cancer Institute.

1.2.1 Red Blood Cell

Red blood cells (RBC) or erythrocytes are sacs of liquid protein called hemoglobin, that are enclosed by deformable membranes. They constitute 40–45% of the total blood volume. The volume fraction of the red blood cells in blood is termed **hematocrit**. An undeformed RBC is biconcave discoid in shape. The diameter of a typical RBC is about $8\ \mu\text{m}$ with a thickness of $2\ \mu\text{m}$. RBCs normally do not have a nucleus. The membrane of an RBC is composed of a lipid bi-layer with an underlying two-dimensional actin network called cytoskeleton (figure 1.2). This structure gives the RBC its membrane stiffness and helps retain the undeformed shape under resting condition. Under external force, RBCs easily deform. However, during deformation, the surface area of an RBC remains constant. The deformability of RBCs is essential for them to flow through even the smallest blood vessels. The viscosity of the liquid inside the cell (hemoglobin) is five times the viscosity of plasma (Skalak *et al.* 1989).

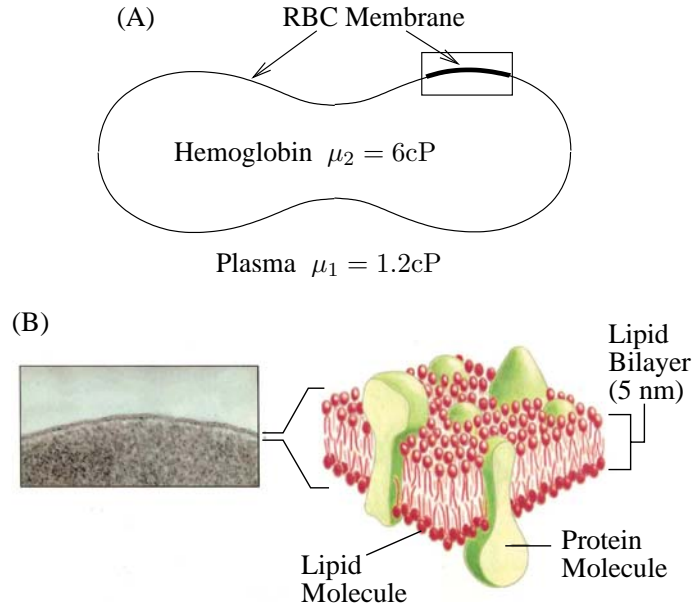


Figure 1.2: (a) Section of a red blood cell. Part of the RBC is magnified to show the composition of the RBC membrane. (b) The lipid bilayer of the RBC membrane is shown.

1.3 Rheological Models for Blood Cells as Capsules

The deformability of the cell membrane, and the liquid-like nature of the cytoplasm make the entire cell deform when subject to an external fluid flow. The ability of a cell to deform primarily arises from the properties of its membrane and cytoplasm. The membrane of a red blood cell is composed of a lipid bi-layer of about 5 nm thickness, and a 2D skeletal structure which lies beneath the bi-layer. The skeletal structure is made of actin filaments, and is known as cytoskeleton. The bi-layer has a unique mechanical property that it can be deformed, but not stretched. The 2D cytoskeleton is believed to be responsible for the bending resistance of the red blood cell membrane, which causes a deformed cell to regain its biconcave shape when the external force is withdrawn.

On a mesoscopic scale, the detailed molecular structure of the lipid bi-layer and the underlying cytoskeleton can be neglected. Then, the entire cell can be modeled as a **capsule**, that is a liquid drop surrounded by an infinitesimally thin elastic membrane (Figure 1.2).

Similar to a liquid drop, a capsule deforms when placed in a shear flow. However, there are important differences between a capsule and a liquid drop. For the latter, deformation is determined by the surface tension, and the viscosity of the liquid. For a capsule, typically, four quantities determine its mechanical behavior: the viscosity of the interior liquid (or, cytoplasm), the extensional elastic modulus of the membrane, the shear modulus, and the bending resistance of the membrane. The elastic response of the capsule membrane is then expressed in terms of a **strain energy function**. Some of the models often used to describe the strain energy of the membrane of a blood cell are described below.

Mooney-Rivlin model

Mooney-Rivlin model (see e.g., Pozrikidis 2003) is a rubber elastic model to describe the property of the membrane. The membrane in this model is regarded as a thin layer of homogeneous, isotropic, three-dimensional incompressible material. The strain energy function, W for such a membrane is given by

$$W = \frac{E_s}{6}(1 - \psi)[2\Lambda_2 + e^{-2\Lambda_1} - 1] + \frac{E_s}{6}\psi[2\Lambda_2 e^{-2\Lambda_1} + 2e^{-2\Lambda_1} + e^{2\Lambda_1} - 3]. \quad (1.3.1)$$

In the above equation, ψ is a non-dimensional parameter varying from 0 to 1, which introduces non-linear behavior in the model. Λ_1 and Λ_2 are the strain invariants (Barthès-Biesel and Rallison 1981) given by

$$\Lambda_1 = \log \epsilon_1 \epsilon_2, \quad \text{and}$$

$$\Lambda_2 = (1/2)(\epsilon_1^2 + \epsilon_2^2) - 1,$$

where ϵ_1 and ϵ_2 are the principal extension ratios, and E_s is the surface elastic modulus of the membrane.

Neo-Hookean model

Neo-hookean model is a special case of the Mooney-Rivlin law when $\psi \rightarrow 0$. Then, the strain energy function is given by

$$W = \frac{E_s}{6}(\epsilon_1^2 + \epsilon_2^2 + \epsilon_1^{-2}\epsilon_2^{-2} - 3). \quad (1.3.2)$$

Skalak *et al* model

The above models do not strictly represent a RBC membrane which undergoes deformation without stretching. Skalak *et al.* (1973) proposed a strain energy W to describe the properties of red blood cell membrane given by,

$$W = \frac{B}{2}(\Lambda_2^2 + \Lambda_2 - \frac{e^{2\Lambda_1} - 1}{2}) + \frac{C}{8}(e^{2\Lambda_1} - 1)^2. \quad (1.3.3)$$

where Λ_1 and Λ_2 are the same as defined earlier. For an RBC, the values of the constants, B and C , are $B = 0.5 \times 10^{-2}$ dyn/cm and $C = 5$ dyn/cm, respectively.

Evans-Skalak model

From the measurement of deformation of a human RBC membrane, Evans and Skalak (1980) developed a strain energy function given by

$$W_{RBC} = E_a(\epsilon_1\epsilon_2 - 1)^2 + E_s(\frac{\epsilon_1^2 + \epsilon_2^2}{2\epsilon_1^2\epsilon_2^2} - 1). \quad (1.3.4)$$

Here $E_a = 500$ dyn/cm is an area dilatation modulus, and $E_s = 6 \times 10^{-3}$ dyn/cm is the shear modulus. The high value of E_a and the low value of E_s allow large deformation of an RBC without a significant change in its surface area.

1.3.1 Dynamics of Single Capsule

Dynamics of single capsule has been a subject of investigation for several decades. Deformation of a capsule suspended in a shear flow was measured by Chang & Olbright (1993). Recently, Risso *et al.* (2006) experimentally investigated single-file motion of artificial capsules flowing through narrow tubes. Barthès-Biesel and co-workers (Barthès-Biesel 1980; Barthès-Biesel & Rallison 1981; Barthès-Biesel & Sgaier 1985; Barthès-Biesel 1991) developed the theory of small deformation for a capsule suspended in a shear (or, a general linear) flow. Li *et al.* (1988) computed axisymmetric large deformation of capsules in a pure straining flow, and Leyrat-Maurin & Barthès-Biesel (1994) studied axisymmetric large deformation of a capsule during its passage through a hyperbolic constriction. Queguiner

& Barthès-Biesel (1997) studied the axisymmetric motion of capsules through cylindrical tubes. Pozrikidis (1995) and Ramanujan & Pozrikidis (1998) used boundary integral simulation to consider large deformation of capsules in shear flow. Pozrikidis (2001) and Kwak & Pozrikidis (2001) have also studied the effect of membrane bending resistance on the deformation of a capsule suspended in shear flow and in axisymmetric straining flow. Effect of membrane viscosity on the dynamic response of a capsule was studied by Diaz *et al.* (2000, 2001). Capsule deformation under various constitutive laws for the membrane material was studied by Barthès-Biesel *et al.* (2002) and Lac *et al.* (2004). Effect of membrane pre-stress was studied by Lac & Barthès-Biesel (2005). Eggleton & Popel (1998) studied the large deformation of red blood cell ghosts using immersed boundary method. They have used both the neo-Hookean and Evans-Skalak model to study the deformation of initially spherical and biconcave capsules in shear flow.

1.4 Blood in Microcirculation

Due to its particulate nature, the study of blood, both experimental and theoretical, has been very challenging. Fortunately, for large vessels in macrocirculation, the characteristic size of a blood cell is much smaller than the diameter of the vessel. The flow rate (and hence, the average shear rate) is also very high in these vessels, so that the red blood cells are maximally deformed. In such a case, the presence of individual cells can be neglected and the whole blood can be modeled as a single-phase liquid using an appropriate constitutive relation.

In microcirculation, however, the size of a blood cell is comparable to the diameter of a blood vessel. The shear rate is also low, but strongly varying, in these vessels. The multiphase nature of blood becomes important in these vessels. Blood in such vessels behaves as a non-Newtonian fluid; that is, the viscosity of blood is not constant, rather it depends on the vessel diameter.

The viscosity of blood is an important fluid dynamic and physiological quantity. It determines the pumping power required by the heart. Under many disease conditions, the

viscosity of blood increases. Since the viscosity of blood in microcirculation is not known *a priori*, an **apparent viscosity** of blood is introduced by invoking the Poiseuille law as

$$\mu_{app} = \frac{\pi D^4}{128L} \frac{\Delta P}{Q} \quad (1.4.1)$$

where ΔP is the pressure drop, Q is the volume flow rate, D is the diameter and L is the length of the tube. The relative apparent viscosity, $\mu_{rel} = \mu_{app}/\mu_p$ is the ratio of the apparent viscosity μ_{app} and the viscosity of plasma μ_p . The relative apparent viscosity is sometimes also referred to as **relative viscosity** or **effective viscosity**.

1.4.1 Fahraeus and Fahraeus-Lindqvist effect

The non-Newtonian nature of blood flowing through a small tube was first described by Fahraeus and Lindqvist (Fahraeus & Lindqvist 1931). The Fahraeus-Lindqvist effect refers to a decrease in the viscosity with decreasing vessel diameter (figure 1.3). The figure shows that as the tube diameter decreases below 500 μm , the relative viscosity decreases, until it reaches a minimum when the vessel diameter is about 8 μm . Upon further decrease in vessel diameter, the relative viscosity increases sharply showing a reverse Fahraeus-Lindqvist effect. A somewhat related phenomenon, known as Fahraeus effect, refers to the decrease in hematocrit ratio (H_T/H_D , where H_T is the tube hematocrit and H_D is discharge hematocrit) as the vessel diameter decreases from 500 to 8 μm (figure 1.3). Upon further decrease in vessel diameter, the hematocrit ratio increases sharply.

1.4.2 Cell-free layer

Deformability of the red blood cell is the key to the Fahraeus and Fahraeus-Lindqvist effects. In narrow capillaries with diameters less than 8 μm , the red blood cells need to squeeze themselves in order to move through these vessels. The motion of RBCs in such narrow vessels is often referred to as the **single file** motion (figure 1.4). Cell deformability plays a critical role here. Experiments have shown that RBCs can flow through capillaries as small as 3 μm in diameter. An individual RBC fills the entire cross-section of the vessel, and

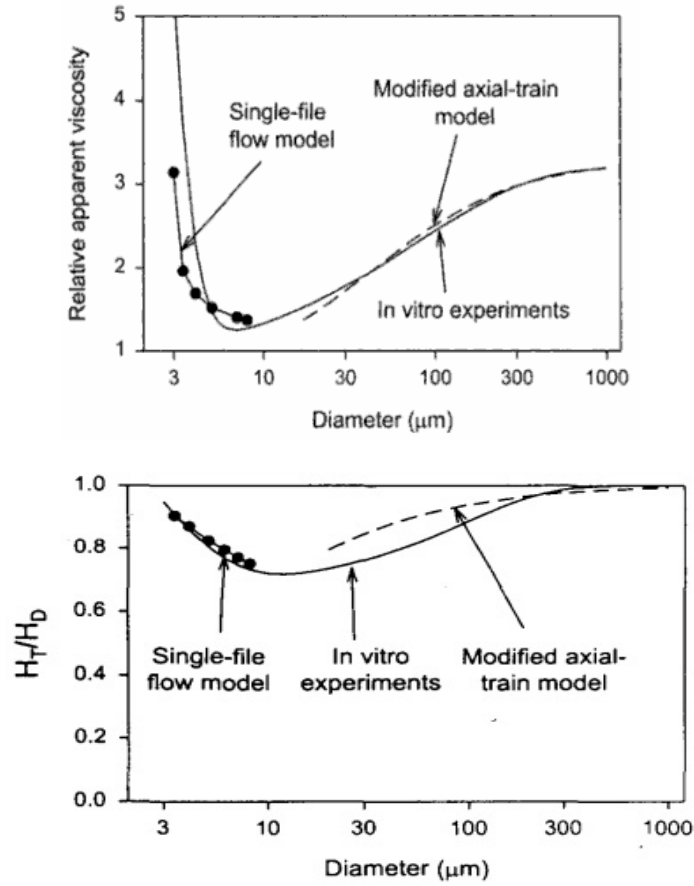


Figure 1.3: Top panel: Effect of diameter of the tube on the relative apparent viscosity for 45% volume fraction of red blood cells. Solid curve is the empirical fit to data (Pries *et al.* 1990). Bottom panel: Effect of diameter of the tube on the hematocrit ratio H_T/H_D .

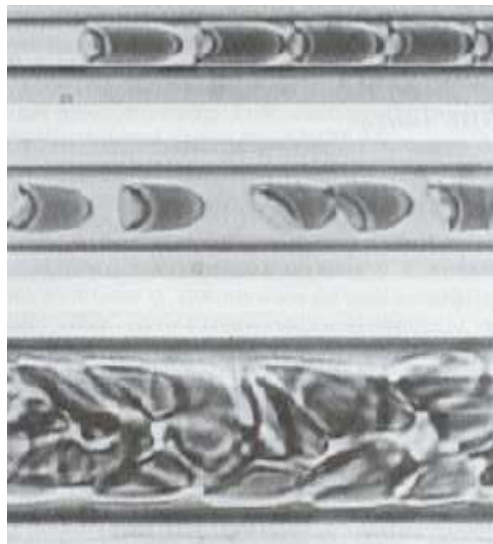


Figure 1.4: Flow of human red blood cells moving through glass tubes with approximate diameters $4.5 \mu\text{m}$ (top), $7 \mu\text{m}$ (middle), and $15 \mu\text{m}$ (bottom), in the experiments by Alex R. Pries (Pozrikidis 2003); the flow direction is from left to right.

the friction between the vessel wall and the cell results in a large pressure drop across the cell, and hence an increased relative viscosity (figure 1.3). As the vessel diameter increases, a cell-free layer forms between the cell and the wall which facilitates the cell to move with less friction. Also, the cells move at higher velocity relative to the average flow velocity since the cells are closer to the tube centerline where the velocity is a maximum. As a result, the relative viscosity decreases. For vessels having $8\text{--}10 \mu\text{m}$ diameter, the RBCs still move in single file, but the gap between the cells and the vessel wall increases significantly. This gap, which contains plasma, refers to as the **cell-free** or **cell-depleted layer**. On the contrary, the core of the vessel is called **cell-rich core**. The cell-free layer has a locally reduced viscosity than the cell-rich core. On the average, the increased thickness of the cell-free layer results in a reduction in the relative viscosity (figure 1.3).

As the vessel diameter increases beyond $\sim 10 \mu\text{m}$, RBCs no longer flow in single file. Rather, they flow in **multi-files** (figure 1.4). The ratio of the cell-free layer thickness to the vessel diameter starts decreasing, and hence the relative viscosity increases. For vessels larger than $\sim 500 \mu\text{m}$ in diameter, the role of the cell-free layer becomes insignificant, and

the relative viscosity becomes nearly constant.

1.4.3 Lateral Migration

The formation of the cell free-layer is due to a migration of the red blood cells lateral to the mainstream flow and away from the wall of the vessel. The lateral migration arises due to the deformation of the red blood cells (Goldsmith 1971). As per the theory of viscous fluid mechanics (Stokes flow), a perfectly rigid particle does not migrate away from the wall, but a deformable particle does (Happel & Brenner 1983). Deformation results in an asymmetry in the flow, and a non-zero lift force directing away from the wall. The lateral migration has been well studied in case of a liquid drop. Extensive studies exist on the lateral migration of an isolated liquid drop in absence of inertia: e.g. Karnis *et al.* (1963), Goldsmith & Mason (1962), Chan & Leal (1979), Hiller & Kowalewski (1987), Coulliette & Pozrikidis (1998), and many others. These studies suggest that the equilibrium position of a liquid drop in a pressure-driven flow depends on λ , the ratio of the viscosity of the liquid drop to that of the surrounding liquid. At a low viscosity ratio of less than unity, the drop settles at the tube axis. But for $\lambda \sim O(1)$, it settles at a position between the wall and the axis. The cross-stream migration also depends on the ratio of the capsule (or drop) diameter to the size of the channel or conduit.

In a dilute suspension, individual RBCs continuously migrate toward the center of the vessel. In a dense suspension, hydrodynamic interaction between adjacent cells also affects their motion. The cell-free layer is formed under a balance of the deformation-induced lateral migration and the dispersion due to the cell-cell interaction (Goldsmith 1971).

1.4.4 Challenges

The motion of RBC in narrow capillaries is often axisymmetric (figure 1.4), and hence amenable to theoretical analysis (Secomb 1987, Queguiner & Barthès-Biesel 1997). Hsu & Secomb (1989), and Coulliette & Pozrikidis (1998) have also extended the work to non-axisymmetric single file motion (figure 1.4). The main difficulty in the theoretical analysis

of the blood flow at small scales arises when the vessel diameter is in the range $\sim 10\text{--}500\ \mu\text{m}$. In such vessels, the cells move in a **multi-file** fashion (figure 1.4). The cell-to-cell interaction also becomes important. Simulation of multiple, deformable blood cells is a major computational challenge. Three-dimensional simulations of bubbles, drops, and rigid particles have been pursued by various groups for both Stokes flow and inertial flows, such as Nott & Brady (1994), Loewenberg & Hinch (1996), Zinchenko & Davis (2002), Mortazavi & Tryggvason (2000), Pozrikidis (2002), Patankar *et al.* (2001), Zhang & Prosperetti (2005), to name a few. Similar investigations with a large number of blood cells or capsules have not been reported.

1.5 Scope of the thesis

The objective of this thesis is to develop computational models and simulations to study the dynamics of capsules, as models for blood cells. The framework is able to consider a wide variety of problems, such as, dynamics of single capsule, capsule-to-capsule binary interaction, and motion of multiple capsules under a variety of flow conditions, such as steady linear shear (Couette flow), parabolic shear (pressure-driven flows), and oscillatory shear flows. The methodology should be able to consider various models for hyperelastic membrane, such as neo-Hookean law, Evans-Skalak law, etc., as introduced in the previous chapter. It should also be able to consider the difference in the viscosity of the liquids interior and exterior to the capsule. Further, it should be readily extensible to consider the effect of inertia, which may play a role during the manufacturing of giant artificial capsules. The specific topics that are addressed in the thesis are described below.

1. **Computational modeling and simulation of capsule deformation (Chapter 2):** We develop a computational methodology for unsteady capsule dynamics in three-dimensions using a front-tracking/immersed boundary method for deformable interface and a finite-difference/Fourier transform method for flow solver. The methodology can address problems ranging from dynamics of a single capsule, interaction between a pair of capsules, motion of multiple capsules under a variety of flows such

a simple or parabolic shear, and oscillatory flows. The computational framework is quite general, and it is currently being applied to address more specific biological problems, such as adhesive rolling motion of a white blood cell (Pappu *et al.* 2008), and interaction between a red blood cell and a white blood cell (Pappu & Bagchi 2007).

2. **Lateral migration of capsule in wall-bounded flow (Chapter 3):** Using the above numerical tool, the first problem that is addressed is the motion of a capsule in a pressure-driven (parabolic) flow through a channel. As mentioned in Chapter 1, a deformable capsule in a wall-bounded flow migrates away from the wall. To date, the migration of a capsule has been addressed only in the limit of small deformation. The focus of this study is the migration of a capsule under large deformation,
3. **Capsule-capsule interaction in wall-bounded flow (Chapter 4):** We consider the hydrodynamic interaction between two capsules as they migrate simultaneously. The objective is to study the effect of a neighboring capsule on migration velocity. This study also illustrates the role of wall effects on shear-induced self-diffusion process which is a key process for mixing in suspensions at low inertia.
4. **Effect of inertia on hydrodynamic interaction between two capsules (Chapter 5):** Next, we consider the effect of inertia on the hydrodynamic interaction between two capsules suspended in a simple shear flow. In absence of inertia, binary collision between two capsules (or, any deformable particles, in general) tends to the ‘shear-induced diffusion’, in which one capsule rolls over the other resulting in an irreversible shift in their trajectory. The objective of this chapter is to study the effect of inertia on the shear-induced diffusion process, as finite-inertia suspension is often encountered during manufacturing of synthetic capsules.

By focusing on the motion of an isolated capsule, and two interacting capsules, the above studies form the basis for addressing the more complex problem of the motion of multiple, interacting capsules in non-dilute suspension, as in the case of blood flow

in a microvessel.

5. **Simulation of capsule suspension (Chapter 6):** As mentioned before, one of the challenges in the computational study of a suspension of capsules, in particular, and of any deformable objects, in general, is to be able to consider a large ensemble of capsules. This is a formidable problem when large deformation of multiple interacting capsules is considered, especially for a geometry which is not triply periodic. The computational methodology developed here is extended to consider the motion of $O(100)$ three-dimensional capsules in a channel flow. Rheology of a suspension of deformable capsules is extracted. These simulations facilitate the development of an improved low-order model for blood flow in microvessels.

Chapter 2

Numerical Methodology

2.1 Flow Configuration and Simulation Technique

2.1.1 Problem setup

We consider three-dimensional simulation of a suspension of deformable capsules (figure 2.1) in a channel. The channel is bounded by two infinite flat plates placed parallel to the X -axis in the XYZ coordinate system as shown. The height of the channel is H . In absence of the capsules, the undisturbed flow \mathbf{u}_0 is either parabolic, driven by a constant pressure gradient dP/dX as

$$\mathbf{u}_0 = \left[\frac{1}{2\mu_0} \left(-\frac{dP}{dX} \right) (HY - Y^2), \quad 0, \quad 0 \right], \quad (2.1.1)$$

or, a linear shear flow at zero pressure-gradient driven by the two walls of the channel as

$$\mathbf{u}_0 = [\dot{\gamma}(Y - H/2), 0, 0], \quad (2.1.2)$$

where $\dot{\gamma}$ is the shear rate. Here Z is the direction of vorticity of the undisturbed flow. The no-slip conditions are imposed at the top and bottom walls as

$$\mathbf{u} = \mathbf{u}_0(Y = 0, H). \quad (2.1.3)$$

The channel is assumed to be infinitely long in the X and Z directions. We use periodicity conditions in these directions to reduce the size of the computational domain. The stream-wise length of the domain is H_x and the length in the Z direction is H_z . As discussed later, the condition of periodicity not only reduces the size of the domain, but also allows us to use Fourier transform for fast computation. The capsules are released in the flow at

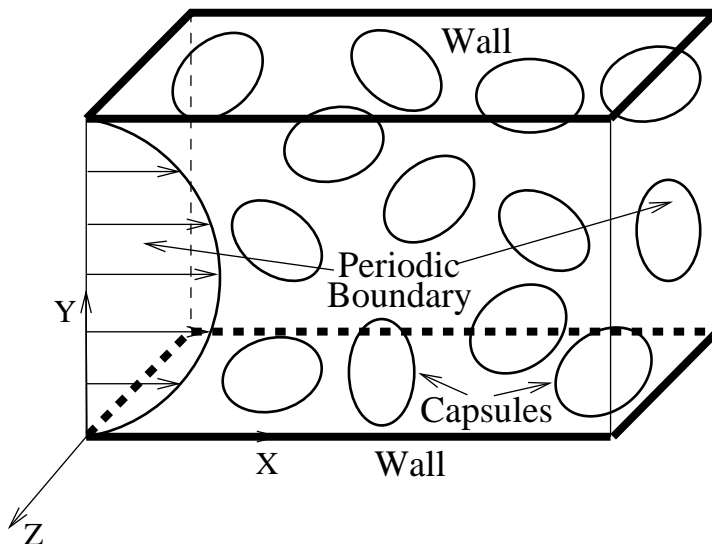


Figure 2.1: Three dimensional computational domain for simulation of capsule suspension.

time $t = 0$. The initial undeformed shape of the capsules can be spherical, ellipsoidal or biconcave.

2.1.2 Fluid-structure interaction

The simulation technique considered here is the front-tracking/immersed boundary method (Peskin 1977, Unverdi & Tryggvason 1992, Tryggvason *et al.* 2001) for multiple fluids with different properties. The main idea of the front-tracking method is to use a single set of equations for both the fluids, inside and outside of the capsule. The fluid equations are solved on a fixed Eulerian grid, and the interface is tracked in a Lagrangian manner by a set of marker points (figure 2.2). The interface is accounted for by introducing a body force $\mathbf{F}(\mathbf{x}, t)$ in the governing equations such that it is zero everywhere in the flow except at the interface:

$$\mathbf{F}(\mathbf{x}, t) = \int_{\partial S} \mathbf{f}(\mathbf{x}', t) \delta(\mathbf{x} - \mathbf{x}') d\mathbf{x}' \quad (2.1.4)$$

where \mathbf{x} is the location of an arbitrary point in the flow domain, \mathbf{x}' is any point on the interface, ∂S is the entire interface, and δ is the three-dimensional Delta function which

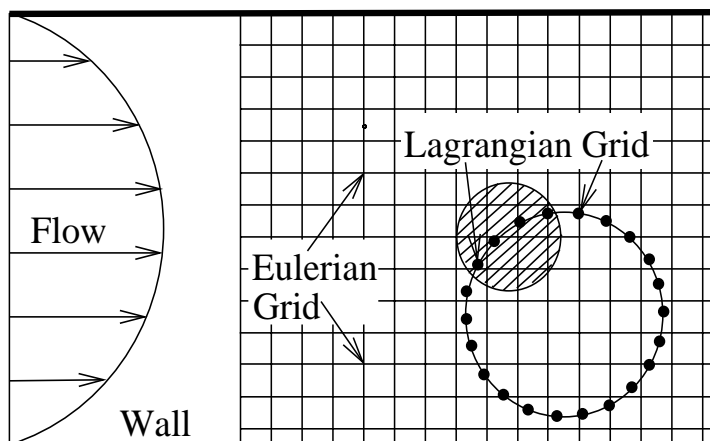


Figure 2.2: The Eulerian and Lagrangian grids.

vanishes everywhere except at the interface. Here \mathbf{f} is the elastic force generated in the membrane due to deformation of the capsule. For incompressible fluids of different viscosity, the governing equations are:

$$\nabla \cdot \mathbf{u} = 0, \quad \text{and} \quad \rho \left[\frac{\partial \mathbf{u}}{\partial t} + \mathbf{u} \cdot \nabla \mathbf{u} \right] = -\nabla p + \nabla \cdot \boldsymbol{\tau} + \mathbf{F} \quad (2.1.5)$$

Here $\mathbf{u}(\mathbf{x}, t)$ is the fluid velocity, ρ is the density, p pressure, and

$$\boldsymbol{\tau} = \mu(\nabla \mathbf{u} + (\nabla \mathbf{u})^T) \quad (2.1.6)$$

is the viscous stress tensor. Here $\mu(\mathbf{x}, t)$ is the viscosity in the entire fluid: within a capsule, $\mu = \mu_c$, and for any point outside, $\mu = \mu_0$. As the capsules move and deform, $\mu(\mathbf{x}, t)$ needs to be updated. Following Tryggvason *et al.* (2001), this is done by solving a Poisson equation for an indicator function $I(\mathbf{x})$ such that

$$\mu(\mathbf{x}) = \mu_0 + (\mu_c - \mu_0)I(\mathbf{x}). \quad (2.1.7)$$

The δ function used in (2.1.4) is constructed by multiplying three 1D δ functions as

$$\delta(\mathbf{x} - \mathbf{x}') = \delta(x - x')\delta(y - y')\delta(z - z'). \quad (2.1.8)$$

For numerical implementation, a smooth representation of the δ -function is used as

$$\begin{aligned} D(\mathbf{x} - \mathbf{x}') &= \frac{1}{64\Delta^3} \prod_{i=1}^3 \left(1 + \cos \frac{\pi}{2\Delta} (x_i - x'_i) \right) \quad \text{for } |x_i - x'_i| \leq 2\Delta, \quad i = 1, 2, 3, \\ D(\mathbf{x} - \mathbf{x}') &= 0 \quad \text{otherwise,} \end{aligned} \quad (2.1.9)$$

where Δ is the Eulerian grid size (Unverdi & Tryggvason 1992). As a result, the membrane force and viscosity vary smoothly over four Eulerian grid points surrounding the interface. In discrete form, the integral in (2.1.4) can be written as

$$\mathbf{F}(\mathbf{x}_j) = \Sigma_i D(\mathbf{x}_j - \mathbf{x}'_i) \mathbf{f}(\mathbf{x}'_i) \quad (2.1.10)$$

where i and j represent Lagrangian and Eulerian points, respectively.

2.1.3 Numerical treatment of membrane deformation

The capsule membrane follows the neo-Hookean law for which the strain energy function is given by

$$W = \frac{E_s}{6} (\epsilon_1^2 + \epsilon_2^2 + \epsilon_1^{-2} \epsilon_2^{-2} - 3) \quad (2.1.11)$$

where ϵ_1 and ϵ_2 are the principal stretch ratios and E_s is the surface elastic modulus. We assume that the bending resistance of the membrane is negligible.

The deformation of the membrane is treated using a finite element model developed by Charrier *et al.* (1989) and Shrivastava & Tang (1993), and later implemented by Eggleton & Popel (1998) within the framework of immersed boundary method to consider large deformation of capsules. First, the membrane is discretized using flat triangular elements (figure 2.3a). A Lagrangian node on the surface is surrounded by five or six triangular elements. It is assumed that the elements remain flat even after large deformation of the capsule. In the model, the forces acting on the three vertices of a triangular element are obtained by computing the displacements of the vertices of the deformed element with respect to the undeformed element. For this purpose, the undeformed and deformed surface elements are transformed to a common plane P using rigid-body rotations (figure 2.3b). By

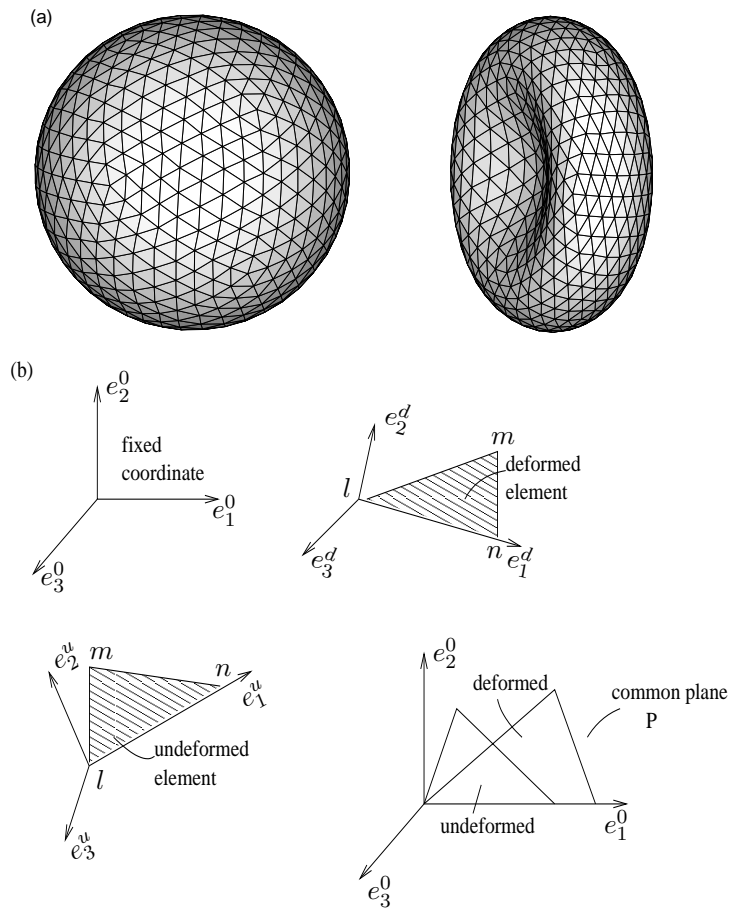


Figure 2.3: (a) Lagrangian elements on the capsule surface. (b) Deformation of a planar triangular element in space, and comparison of the deformed and undeformed element in a common plane.

denoting the three vertices of a triangular element as l, m , and n (see figure 2.3b), and the undeformed and deformed coordinates of the element as \mathbf{x} and \mathbf{X} , respectively, the transformation rules used for coordinate rotation are

$$\mathbf{x}_l^P = \mathbf{0}, \quad \mathbf{x}_m^P = \mathbf{M}(\mathbf{x}_m - \mathbf{x}_l), \quad \mathbf{x}_n^P = \mathbf{M}(\mathbf{x}_n - \mathbf{x}_l), \quad \text{and}, \quad (2.1.12)$$

$$\mathbf{X}_l^P = \mathbf{0}, \quad \mathbf{X}_m^P = \mathbf{R}(\mathbf{X}_m - \mathbf{X}_l), \quad \mathbf{X}_n^P = \mathbf{R}(\mathbf{X}_n - \mathbf{X}_l), \quad (2.1.13)$$

where \mathbf{x}_l^P and \mathbf{X}_l^P etc. are the coordinates of the vertices of the undeformed and deformed elements on the common plane P ; \mathbf{M} and \mathbf{R} are the transformation matrices defined as $M_{ij} = e_i^u e_j^0$ and $R_{ij} = e_i^d e_j^0$, where \mathbf{e}^0 , \mathbf{e}^u , and \mathbf{e}^d are the unit vectors attached to a fixed reference frame, to the undeformed element, and to the deformed element, respectively (figure 2.3b). Once the deformed and undeformed elements are transformed to the common plane P , the problem is reduced to a 2D (planar) deformation on $\{x^P, y^P\}$, where x^P, y^P denote a *local* coordinate system attached to the plane P . The displacements of the three vertices can be obtained which do not include the contribution from a rigid-body rotation. Using the principle of virtual work, the forces in the common plane P are then obtained as

$$\mathbf{f}_l^P = \frac{\partial W}{\partial \epsilon_1} \frac{\partial \epsilon_1}{\partial \mathbf{v}_l} + \frac{\partial W}{\partial \epsilon_2} \frac{\partial \epsilon_2}{\partial \mathbf{v}_l} \quad (2.1.14)$$

for the vertex l , and similarly for vertices m and n . Here \mathbf{v} is the displacement of a vertex, and ϵ_1 and ϵ_2 are the principal values of the in-plane stretch ratios. The force \mathbf{f}^P lies in plane P .

We now assume that the displacement \mathbf{v} varies linearly *inside* the element so that

$$\mathbf{v} = N_l \mathbf{v}_l + N_m \mathbf{v}_m + N_n \mathbf{v}_n. \quad (2.1.15)$$

and the shape functions N_l , N_m and N_n are expressed as

$$N_l = a_l x^P + b_l y^P + c_l \quad (2.1.16)$$

for the vertex l , and similarly for vertices m and n . The coefficients a_l etc. are found by letting $N_l = 1$ at vertex l , and $N_l = 0$ at vertices m and n , and so on. Once the shape

functions are known, the displacement gradients within the element, such as $\partial \mathbf{v}/\partial x^P$, and $\partial \mathbf{v}/\partial y^P$, can be found by differentiating (2.1.15).

At this point we need to express the in-plane stretch ratios ϵ_1 and ϵ_2 in terms of the gradients $\partial \mathbf{v}/\partial x^P$ etc, in order to evaluate the derivatives in (2.1.14). For a planar deformation, ϵ_1 and ϵ_2 can be related to the deformation gradient tensor \mathbf{D} as

$$\epsilon_1^2 = \frac{1}{2} \left[G_{11} + G_{22} + \sqrt{\{(G_{11} - G_{22})^2 + 4G_{12}^2\}} \right], \quad (2.1.17)$$

$$\epsilon_2^2 = \frac{1}{2} \left[G_{11} + G_{22} - \sqrt{\{(G_{11} - G_{22})^2 + 4G_{12}^2\}} \right], \quad (2.1.18)$$

where $\mathbf{G} = \mathbf{D}^T \mathbf{D}$ is a symmetric positive definite matrix. Using the expressions for $\partial \mathbf{v}/\partial x^P$, and $\partial \mathbf{v}/\partial y^P$, the components of \mathbf{G} can be written explicitly in terms of the shape functions N and the nodal displacement \mathbf{v} . The derivatives in (2.1.14), such as $\partial \epsilon_1/\partial \mathbf{v}$, can then be written explicitly, and hence \mathbf{f}^P can be evaluated at each of the vertices of an element. Once the in-plane forces for individual element are found, they need to be transformed to the global coordinates. This is done by using the transformation rule $\mathbf{f} = \mathbf{R}^T \mathbf{f}^P$, where \mathbf{R} is the transformation matrix as explained above. The resultant force $\mathbf{f}(\mathbf{x}', t)$ at any node is obtained by vector resultant of the forces contributed by all the elements which share that node.

2.1.4 Surface discretization

The surface of the capsule is discretized using flat triangular elements. The triangulated surface mesh needed for the simulations is obtained from the GNU Triangulated Surface (GTS) Library. GTS is an Open Source Free Software Library intended to provide a set of useful functions for scientists dealing with 3D computational surface meshes. GTS provides a set of useful functions to deal with 3D surfaces meshed with interconnected triangles including collision detection, multiresolution models, constrained Delaunay triangulations and robust set operations (union, intersection, differences). The discretized surface for a sphere and a RBC is shown in figure 2.3.

2.1.5 Interface tracking

The capsule membrane is tracked in a Lagrangian manner. The velocity of the interface is computed at each time step, after solving the Navier-Stokes equations, as

$$\mathbf{u}(\mathbf{x}') = \int_S \mathbf{u}(\mathbf{x}) \delta(\mathbf{x} - \mathbf{x}') d\mathbf{x}, \quad (2.1.19)$$

where S indicates the entire flow domain. Though the summation is over all Eulerian nodes, only the ‘local’ nodes contribute to the membrane velocity. The discrete form of the delta function used here is the same given by (2.1.8). In this way, a weighted interpolation of the Eulerian fluid velocity is performed which ensures that the continuity of velocity across the membrane is satisfied. The Lagrangian points on the membrane are then advected as

$$\frac{d\mathbf{x}'}{dt} = \mathbf{u}(\mathbf{x}'). \quad (2.1.20)$$

Numerically, the above equation is treated explicitly using the second-order Adams-Bashforth scheme as

$$\mathbf{x}'_{n+1} = \mathbf{x}'_n + \Delta t \left[\frac{3}{2} \mathbf{u}(\mathbf{x}'_n) - \frac{1}{2} \mathbf{u}(\mathbf{x}'_{n-1}) \right], \quad (2.1.21)$$

where n , $n + 1$, etc. are the time instances.

2.1.6 Flow solver

The time-marching of the flow solver is done using a two-step time-split scheme. In the first step, known as the predictor step, an advection-diffusion equation is solved

$$\rho \left[\frac{\partial \mathbf{u}}{\partial t} + \mathbf{u} \cdot \nabla \mathbf{u} \right] = \nabla \cdot \boldsymbol{\tau} + \mathbf{F}. \quad (2.1.22)$$

The interfacial force is retained in the advection-diffusion equation. For constant density but variable viscosity, as in case of capsule and cell suspension, the above equation can be written, for the three velocity components, as

$$\rho \left[\frac{\partial u}{\partial t} + (\mathbf{NL})_x \right] = \mu \nabla^2 u + 2 \frac{\partial \mu}{\partial x} \frac{\partial u}{\partial x} + \frac{\partial \mu}{\partial y} \left(\frac{\partial u}{\partial y} + \frac{\partial v}{\partial x} \right) + \frac{\partial \mu}{\partial z} \left(\frac{\partial u}{\partial z} + \frac{\partial w}{\partial x} \right) + F_x \quad (2.1.23a)$$

$$\rho \left[\frac{\partial v}{\partial t} + (\mathbf{NL})_y \right] = \mu \nabla^2 v + \frac{\partial \mu}{\partial x} \left(\frac{\partial v}{\partial x} + \frac{\partial u}{\partial y} \right) + 2 \frac{\partial \mu}{\partial y} \frac{\partial v}{\partial y} + \frac{\partial \mu}{\partial z} \left(\frac{\partial v}{\partial z} + \frac{\partial w}{\partial y} \right) + F_y \quad (2.1.23b)$$

$$\rho \left[\frac{\partial w}{\partial t} + (\mathbf{NL})_z \right] = \mu \nabla^2 w + \frac{\partial \mu}{\partial x} \left(\frac{\partial w}{\partial x} + \frac{\partial u}{\partial z} \right) + \frac{\partial \mu}{\partial y} \left(\frac{\partial w}{\partial y} + \frac{\partial v}{\partial z} \right) + 2 \frac{\partial \mu}{\partial z} \frac{\partial w}{\partial z} + F_z \quad (2.1.23c)$$

where $\mathbf{NL} = \mathbf{u} \cdot \nabla \mathbf{u}$. In the time-integration, the nonlinear terms are treated explicitly using a second-order Adams-Bashforth scheme and the viscous terms are treated semi-implicitly using the Crank-Nicolson scheme,

$$\rho \frac{\mathbf{u}^* - \mathbf{u}^n}{\Delta t} = \frac{1}{2} [\mathbf{D}(\mathbf{u}^*) + \mathbf{D}(\mathbf{u}^n)] - \frac{3}{2} (\mathbf{NL}) \mathbf{u}^n + \frac{1}{2} (\mathbf{NL}) \mathbf{u}^{n-1}, \quad (2.1.24)$$

where \mathbf{u}^* is the predicted velocity at an intermediate time level between ‘n’ and ‘n+1’ which is not divergence-free, Δt is the time step size, \mathbf{D} denotes the diffusion terms, and \mathbf{NL} denotes the nonlinear terms in the Navier-Stokes equations. Spatial derivatives are computed using 2nd order finite-difference scheme.

Since the diffusion terms are treated semi-implicitly, the advection-diffusion equation has to be solved either iteratively, or by direct inversion. Here we adopt the latter approach. Also note that the advection-diffusion equation contains evolving viscosity $\mu(\mathbf{x}, t)$, and its spatial derivatives. In order to be invertible, the diffusion operators must be separable. This is done by using an Alternate Direction Implicit (ADI) scheme in which the equation is solved in four steps as follows

$$\begin{aligned} \text{Step 1. } \rho \frac{u^{****} - u^n}{\Delta t} = & - \left[\frac{3}{2} (\mathbf{NL})_x^n - \frac{1}{2} (\mathbf{NL})_x^{n-1} \right] + \left[\frac{3}{2} F_x^n - \frac{1}{2} F_x^{n-1} \right] \\ & + \left[\frac{3}{2} \left(\frac{\partial \mu}{\partial y} \frac{\partial v}{\partial x} + \frac{\partial \mu}{\partial z} \frac{\partial w}{\partial x} \right)^n - \frac{1}{2} \left(\frac{\partial \mu}{\partial y} \frac{\partial v}{\partial x} + \frac{\partial \mu}{\partial z} \frac{\partial w}{\partial x} \right)^{n-1} \right] \\ & + \left[\frac{1}{2} \left(\mu \nabla^2 u + 2 \frac{\partial \mu}{\partial x} \frac{\partial u}{\partial x} + \frac{\partial \mu}{\partial z} \frac{\partial u}{\partial z} + \frac{\partial \mu}{\partial y} \frac{\partial u}{\partial y} \right)^n \right] \end{aligned} \quad (2.1.25a)$$

$$\text{Step 2. } \rho \frac{u^{***} - u^{****}}{\Delta t} = \frac{1}{2} \left(\mu \frac{\partial^2 u^{****}}{\partial x^2} + 2 \frac{\partial \mu}{\partial x} \frac{\partial u^{****}}{\partial x} \right) \quad (2.1.25b)$$

$$\text{Step 3. } \rho \frac{u^{**} - u^{***}}{\Delta t} = \frac{1}{2} \left(\mu \frac{\partial^2 u^{**}}{\partial z^2} + \frac{\partial \mu}{\partial z} \frac{\partial u^{**}}{\partial z} \right) \quad (2.1.25c)$$

$$\text{Step 4. } \rho \frac{u^* - u^{**}}{\Delta t} = \frac{1}{2} \left(\mu \frac{\partial^2 u^*}{\partial y^2} + \frac{\partial \mu}{\partial y} \frac{\partial u^*}{\partial y} \right) \quad (2.1.25d)$$

for u , and similarly for v , and w . The viscosity μ and its derivatives are assumed to be known from level ‘n’. The step 1 is explicit, and can be readily obtained. For steps (2) to (4), we use tri-diagonal matrix solver. Since x and z directions are periodic, cyclic-tri-diagonal solver is used for steps (2) and (3).

The second step involves solving a Poisson equation for the pressure as

$$\nabla^2 P^{n+1} = \frac{1}{\Delta t} \nabla \cdot \mathbf{u}^*. \quad (2.1.26)$$

The Poisson equation must be solved fully implicitly to force the final velocity field to be divergence-free. Due to periodicity in the z direction, we use the Fourier transform. The resultant equation is given by

$$[\mathbf{D}_Y] \hat{P}^{n+1} + \hat{P}^{n+1} [\mathbf{D}_1] = \widehat{\text{RHS}}_p, \quad (2.1.27)$$

$$\text{where } [\mathbf{D}_1] = [\mathbf{D}_X] - [\mathbf{I}] k_Z^2 \quad (2.1.28)$$

where $\widehat{\text{RHS}}_p$ is the right hand side of (2.1.26). This equation is solved for \hat{P}^{n+1} by making use of a matrix diagonalization procedure. The operator matrices are diagonalized as,

$$[\mathbf{D}_Y] = [\mathbf{R}] \lambda_{\mathbf{R}} [\mathbf{R}^{-1}], \quad (2.1.29)$$

$$[\mathbf{D}_1] = [\mathbf{T}] \lambda_{\mathbf{T}} [\mathbf{T}^{-1}] \quad (2.1.30)$$

where \mathbf{R} , \mathbf{T} are the matrices formed by the eigenvectors of matrix \mathbf{D}_Y and \mathbf{D}_1 , and $\lambda_{\mathbf{R}}$ and $\lambda_{\mathbf{T}}$ are the eigenvalues of \mathbf{D}_Y and \mathbf{D}_1 respectively. Then the pressure at the interior points is obtained as

$$\hat{P}^{n+1} = [\mathbf{R}] \left[\frac{\mathbf{R}^{-1} (\widehat{\text{RHS}}_p) \mathbf{T}}{\lambda_{\mathbf{R}} + \lambda_{\mathbf{T}}} \right] [\mathbf{T}^{-1}], \quad (2.1.31)$$

The velocity field obtained from the predictor step is then projected onto a divergence-free space to obtain the velocity field at time level ‘n+1’ as

$$\frac{\mathbf{u}^{n+1} - \mathbf{u}^*}{\Delta t} = -\nabla P^{n+1} \quad (2.1.32)$$

Once the velocity field is known, the position of the capsules is updated as described before using (2.1.19) and (2.1.20). Then $\mu(\mathbf{x}, t)$ is updated by solving a Poisson equation for the indicator function $I(\mathbf{x})$ as

$$\nabla^2 I = \nabla \cdot \mathbf{G}, \quad (2.1.33)$$

where

$$\mathbf{G} = \sum_i D(\mathbf{x}_j - \mathbf{x}'_i) \mathbf{n} \Delta s, \quad (2.1.34)$$

and D is the discrete δ function as given in (2.1.8), \mathbf{n} is the unit normal to the cell surface, and Δs is the triangular surface element. Solution procedure for the above equation is similar to that for the pressure.

2.1.7 Numerical resolution

Typical Eulerian resolution used in this study is $120 \times 120 \times 120$ to $160 \times 160 \times 160$, and Lagrangian resolution used is 1280–5120 triangular elements. Dimensionless timestep used in the simulation is 10^{-3} .

2.2 Validation

2.2.1 Capsule deformation in linear shear flow

We now present a series of validation of our present code. For this purpose, we consider deformation of an initially spherical capsule subject to a linear shear flow as

$$\mathbf{u}_0 = [\dot{\gamma}(Y - H/2), 0, 0], \quad (2.2.1)$$

where $\dot{\gamma}$ is the shear rate. The flow is bounded in the Y direction by two parallel walls which are placed H distance apart. The Z direction is the direction of vorticity. The no-slip condition is imposed at the top and bottom walls as

$$\mathbf{u} = \mathbf{u}_0(Y = 0, H). \quad (2.2.2)$$

Periodic conditions are imposed at the other boundaries of the domain as discussed in previous section. The computational domain for this problem is a cube with each side having length H . The capsule is placed at the middle ($X_{c0} = H/2, Y_{c0} = H/2, Z_{c0} = H/2$) of the computational domain. The capillary number for the shear flow problem is defined as $Ca = \dot{\gamma}a\mu_0/2Eh$. The other important parameter is the viscosity ratio of the interior to exterior fluid $\lambda = \mu_c/\mu_0$.

Consider first $\lambda = 1$ case. The initially spherical capsule deforms in a shear flow and attains an ellipsoidal shape. The steady-state shape of the deformed capsule is shown in figure 2.4a as a function of Ca . Capsule deformation increases, and it aligns more towards the X -axis with increasing Ca . This qualitative trend agrees with previous numerical results of Ramanujan & Pozrikidis (1998) (henceforth called RP) and Lac *et al.* (2004) (henceforth called L1).

The flow field inside and around a deformed capsule is shown in figure 2.4b. The rotational motion of the fluid can be seen in the figure.

Rehage *et al.* (2002) have experimentally studied the deformation of a capsule enclosed by a polyamide membrane subject to simple shear flow. We have compared our results with theirs along with the linear theory of Barthès-Biesel & Rallison (1981) in figure 2.5. The comparison is agreeable. At higher shear rates or Ca , the linear theory deviates from the actual deformation obtained through both experiment and present simulation as expected.

Quantitative comparisons with the results of RP and L1 are considered next. We consider time history of the deformation parameter, $D = (L - B)/(L + B)$ where L and B are the major and minor axis of the ellipsoid in the plane of the shear. Our results are compared with those of RP in figure 2.6a and of L1 in figure 2.6b. In Table 2.1, we list the numerical values of the steady-state deformation D obtained from our simulations, from RP, from L1, and also from small deformation analysis of Barthès-Biesel & Rallison (1981). We also compare our results with those of Li and Sarkar (2008) for $Ca = 0.1$ and 0.2 , who used a similar but independently-developed front-tracking code to simulate capsule deformation.

At low Ca , our results agree well with those predicted by the small deformation analysis.

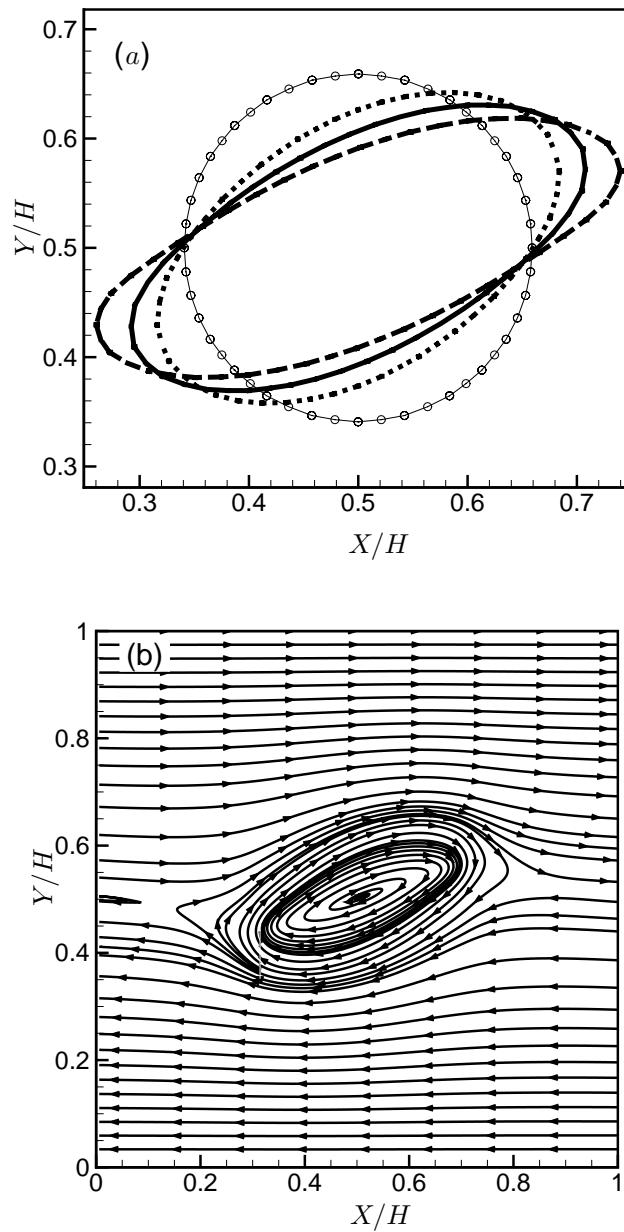


Figure 2.4: (a) Capsule deformation in linear shear flow. 2D shapes in the shear plane are shown after steady state is reached. $-\circ-$ Initial shape, $\cdots \cdots$ $Ca = 0.05$, $—$ $Ca = 0.1$, $- - -$ $Ca = 0.2$. (b) Flow field at $Ca = 0.1$ after steady state is reached.

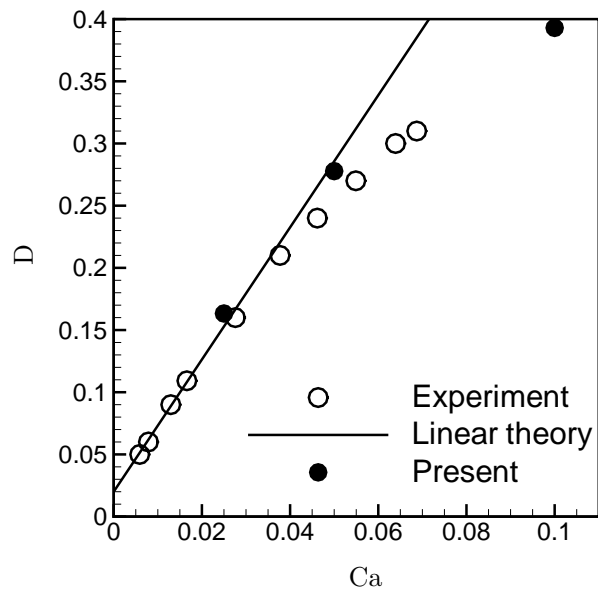


Figure 2.5: Comparison of deformation of capsule for present results with experiment (Rehage *et al.* 2002) and linear theory of Barthès-Biesel & Rallison (1981).

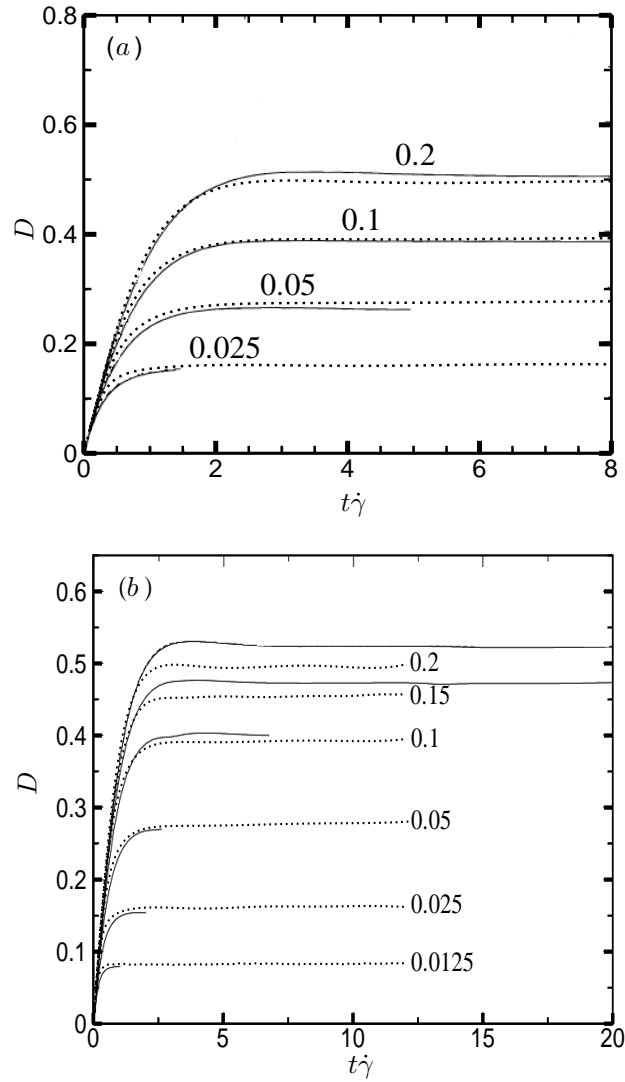


Figure 2.6: Validation of the numerical methodology: Deformation parameter D versus time. \cdots Present results. (a) — Ramanujan & Pozrikidis (1998). (b) — Lac *et al.* (2004). Values next to the curves indicate capillary numbers. In order to obtain the curves from RP and L1, the figures in their papers were scanned and then uploaded in Tecplot.

Table 2.1: Validation: Comparison of steady state deformation D with Ramanujan & Pozrikidis (1998) (RP), Lac *et al.* (2004) (L1), Li and Sarkar (2008) (LS) and small deformation theory (S.D) of Barthès-Biesel & Rallison (1981).

Ca	Present	RP	L1	SD	LS
0.0125	0.083			0.08	
0.025	0.162	0.16	0.15	0.16	
0.05	0.278	0.27	0.27	0.32	
0.1	0.392	0.39	0.40	0.63	0.37
0.15	0.460		0.47		
0.2	0.496	0.5	0.52		0.49

It should be noted that RP’s results correspond to a zero-thickness shell, rather than a neo-Hookean membrane. RP mentioned that the resulting deformation is 4% less than the one that would be obtained with a neo-Hookean membrane. For $Ca \leq 0.1$, our front-tracking method predicts slightly higher values of deformation D compared to those obtained by RP. For $Ca = 0.025, 0.05$, and 0.1 , we predict 1.25%, 2.96%, and 0.5% higher values of D , respectively. For $Ca = 0.2$, we predict slightly lower (0.8%) value of D as compared to that of RP. In comparison to Lac *et al.* (2004), we predict higher values of D for $Ca < 0.1$; our prediction is 8%, and 2.96% higher for $Ca = 0.025$, and 0.05 , respectively. In contrast, for $Ca \geq 0.1$, we predict lower values of D compared to those of Lac *et al.* (2004); our predicted values are 2%, 2.12%, and 4.6% less for $Ca = 0.1, 0.15$, and 0.2 , respectively.

It is somewhat surprising that at higher Ca , we predicted less (though very small) D compared to that of RP. Before discussing the origin of these differences, we compare our results with those of Li and Sarkar (2008). Interestingly (and surprisingly), Li and Sarkar, similar to us, predicted lower deformation than those predicted by RP and Lac *et al.* (2004). Compared to the results obtained by Li and Sarkar, our results are closer to those of Lac *et al.* (2004). Li and Sarkar predicted 7.5%, and 5.8% less values of D compared to those predicted by Lac *et al.* (2004) for $Ca = 0.1$ and 0.2 , respectively.

Extensive tests at $Ca = 0.2$ are done by varying Eulerian resolution (N_E), Lagrangian resolution (N_L), timestep size (Δt), and the size of the computational domain (H_x). The

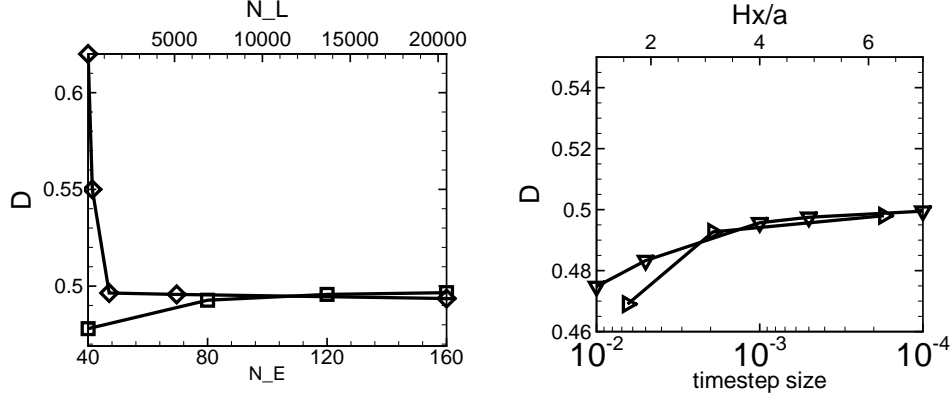


Figure 2.7: Resolution tests at $Ca = 0.2$ showing the steady values of D . (a) Effects of varying Eulerian resolution $((N_E)^3)$ \square , and Lagrangian resolution (N_L) \diamond . N_L is the number of triangular elements on the capsule surface. (b) Effects of varying timestep size (Δt) ∇ , and computational domain size (H_x) \triangleright .

steady-state value of D with respect to these variables are shown in figure 2.7. In figure 2.7a, the effect of varying Eulerian resolution is shown. Capsule deformation increases with increasing Eulerian resolution, but reaches a converged solution for Eulerian resolution above 120^3 . When the Eulerian resolution is changed from 40^3 to 80^3 , D increases by 3.1%, but when the resolution is increased from 120^3 to 160^3 , D increases by only 0.2%. Most of our simulations are done at 120^3 and some at 160^3 . The effect of Lagrangian resolution (in terms of the number of triangular elements on the capsule surface denoted by N_L) is also shown in figure 2.7a by keeping the Eulerian resolution fixed at 120^3 . Deformation decreases with increasing N_L . We note that D is significantly over-predicted for $N_L < 1280$. Above this N_L , D is nearly constant; as N_L is increased from 5120 to 20480, D changes by only 0.4%.

The effects of varying timestep size (Δt) and computation box size (H_x) are shown in figure 2.7b for $Ca = 0.2$. The deformation parameter D increases with decreasing Δt and increasing H_x , but reaches asymptotic values for $\Delta t \leq 10^{-3}$ and $H_x/a > 3$. As Δt is decreased from 0.01 to 0.001, D increases by 4.2%, but as Δt is decreased from 0.001 to

Table 2.2: Validation: Comparison of capsule orientation θ/π at steady state with Ramanujan & Pozrikidis (1998) (RP), and Lac *et al.* (2004) (L1). RP's data at $Ca = 0.025$ is not included since θ did not reach a steady value in their simulation.

Ca	Present	RP	L1
0.0125	0.215		
0.025	0.201		0.2
0.05	0.168	0.17	0.17
0.1	0.136	0.14	0.14
0.15	0.121		0.12
0.2	0.107	0.11	0.10

Table 2.3: Validation: Comparison of tank-treading period $\dot{\gamma}T$, with Ramanujan & Pozrikidis (1998) (RP), and Lac *et al.* (2004) (L1). * TTP is computed following a revolution of a marker point. † TTP is computed by integrating $dl/|v|$ over the membrane circumference in the (x, y) -plane, as done in L1, where dl is a line segment of the capsule profile, and v is the membrane velocity.

Ca	Present *	Present †	RP	L1
0.025	14.1	13.4	13.4	13.0
0.05	16.2	15.0	14.6	14.9
0.1	19.0	17.8	16.6	17.8
0.15	20.9	20.0		19.6
0.2	22.2	21.3	19.7	22.1

0.0001, D increases by only 0.8%. As H_x/a is increased from 0.5π to π , D increases by 5.1%, but as H_x/a is increased from π to 2π , D increases by only 1%. Results presented in figures 2.4–2.11, and in Tables 2.1–2.3 are for $H_x/a = \pi$.

Figure 2.7 shows that at the best resolution ($N_E = 160^3$), our prediction for D ($= 0.5$) is the closest to, but still 4% less than, that obtained by Lac *et al.* (2004) ($= 0.52$). This prediction is, however, better than that obtained by Li & Sarkar (2008) ($= 0.49$).

In Table 2.2, we present the values of the inclination angle θ that the major axis of the capsule makes with the X axis after it has reached a steady-state. The orientation angles obtained from our simulations also agree very well with those of RP and L1.

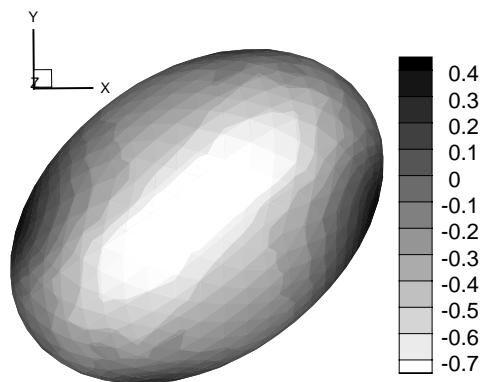


Figure 2.8: Principal stress distribution for $Ca = 0.025$. Compressive (negative) stress (indicated by white shade) in the equatorial region can be seen.

In Table 2.3, we present the period of the tank-treading motion (TTP) of the capsule, and compared that with the results of RP and L1. TTP is computed in two different ways: by following a full revolution of a marker point, and by integrating $dl/|v|$ where dl is a line segment over the capsule profile in (x, y) -plane, and v is marker point velocity. As shown in Table 2.3, the former approach gives higher values of TTP. For $Ca \leq 0.15$, TTP computed using the second approach agrees well with those of L1 with maximum difference of 3% at $Ca = 0.025$. For $Ca = 0.2$, Lac *et al.* used the first approach, and their result agrees within 0.45% of ours.

At low Ca , neo-Hookean membrane tends to exhibit buckling (L1; Li & Sarkar). As shown by these authors, buckling onsets due to membrane zones undergoing compression in the equatorial region. In figure 2.8 we show the distribution of the elastic tension in the membrane for $Ca = 0.025$. Compressive (negative) stress in the equatorial region of the capsule is evident in the figure.

In figure 2.9, we show the effect of the viscosity ratio $\lambda = \mu_c/\mu_0$ on the steady state values of D , and compare our results with those of RP. This figure again shows that for

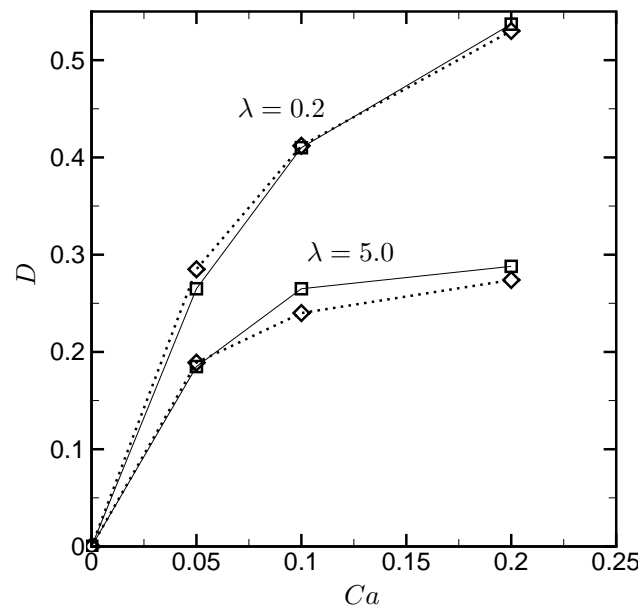


Figure 2.9: Validation of the numerical methodology: Steady-state values of D for $\lambda \neq 1$.
 \square — Ramanujan & Pozrikidis (1998); $\cdots \diamond \cdots$ present results.

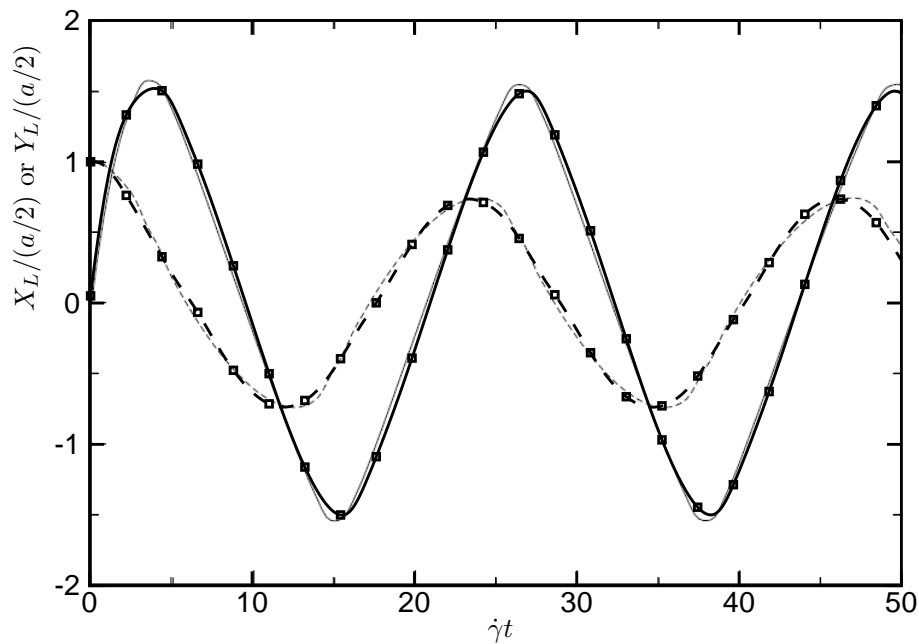


Figure 2.10: Validation: Trajectory of a material point on the capsule membrane at $Ca = 0.2$. Solid line (x -coordinate); dashed line (y -coordinate). Lines without symbols are results from Lac *et al.* (2004). Lines with symbols are present results.

$\lambda \neq 1$, as well, our results are in good agreement with those of RP.

The trajectory of a marker point on the capsule surface is shown in figure 2.10 and compared with the results of Lac *et al.* (2004). This result also shows excellent agreement between the two simulations.

2.2.2 Resolution test

Sensitivity of our results to the Eulerian and Lagrangian resolutions was shown earlier in figure 2.7 for $Ca = 0.2$. Further results for $Ca = 0.1$ are shown in figure 2.11 by considering three test simulations at different resolutions: (i) 80^3 Eulerian grids and 1280 Lagrangian elements, (ii) 120^3 Eulerian grids and 1280 Lagrangian elements, and (iii) 120^3 Eulerian grids

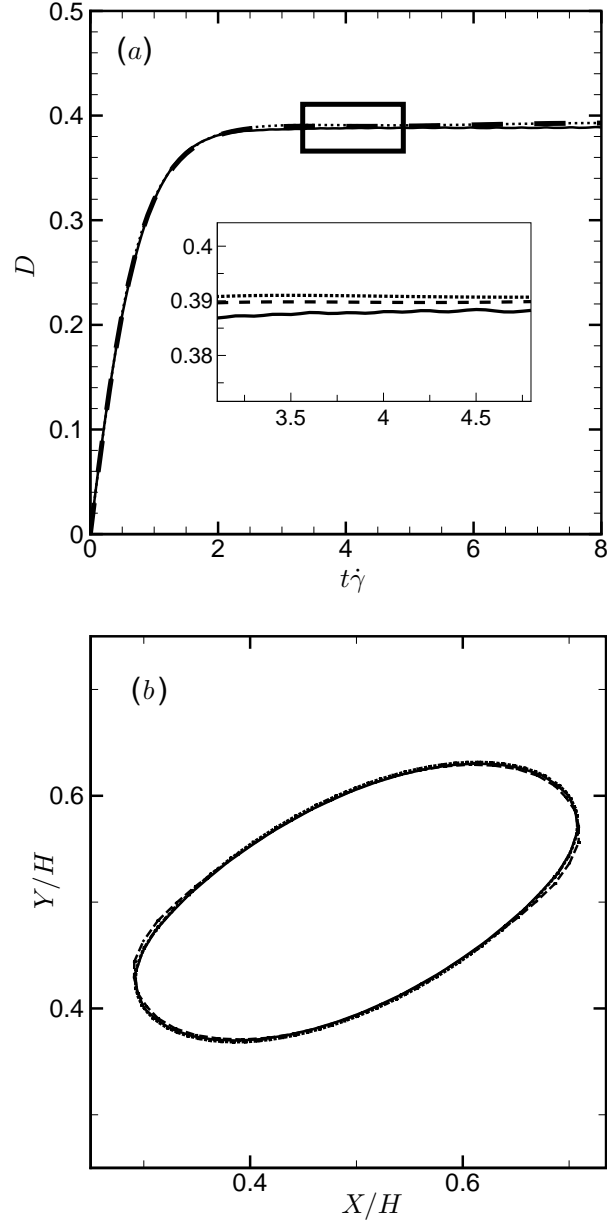


Figure 2.11: Resolution test: (a) Deformation history, and (b) final steady shape in linear shear flow $Ca = 0.1$: —, 80^3 Eulerian points and 1280 Lagrangian elements; - - - 120^3 Eulerian points and 1280 Lagrangian elements; 120^3 Eulerian points and 5120 Lagrangian elements. In (a), inset shows details.

and 5120 Lagrangian elements. In figure 2.11a, we show the time history of deformation parameter D and in figure 2.11b, we show the final steady shape in the shear plane. No significant difference is observed between the three test cases.

We also keep track of the capsule volume during the simulations. The change in the cell volume is less than $\pm 0.1\%$ from its initial volume. The projection method used here for the flow solver satisfies the mass conservation up to $\approx 10^{-14}$ at every grid point in the computational domain.

Chapter 3

Lateral Migration of a Capsule in a Plane Poiseuille Flow in a Channel

3.1 Introduction

Capsules suspended in a liquid flowing through conduits are often encountered in many biological processes, and in biomedical devices. Examples are the motion of blood cells through blood vessels, flow chambers, and cell separation devices. In a wall-bounded shear flow, the motion of a capsule (and, liquid drop) is characterized by its migration lateral to the wall. Lateral migration of liquid drops or capsules plays an important role during the flow of a suspension of particles in which case a particle-free region is developed near the wall. Reduced local viscosity in the particle-free region helps reducing the resistance to flow in small vessels, and is critical for blood flow in microcirculation.

Lateral migration of liquid drops has been a subject of investigation for many years. Here we briefly discuss a few studies on the migration of liquid drops. In the limit of zero inertia, a liquid drop moves laterally in a wall-bounded shear flow due to the asymmetry introduced by the deformation of the particle by the imposed shear. A liquid drop in a linear shear flow bounded by a single wall continues to migrate away from the wall, whereas in a wall-bounded parabolic flow, it settles at the centerline or in between the centerline and a wall. Experimental studies on drop motion in wall-bounded shear flow have been carried out by Karnis *et al.* (1963), Goldsmith & Mason (1962), Karnis & Mason (1967), Chan & Leal (1981), Hiller & Kowalewski (1987), and Smart & Leighton (1991), among others. Early theoretical works on drop migration in presence of wall in the limit of small deformation have been considered by Cox (1969), Chaffey *et al.* (1967), Ho & Leal (1975),

and others (see, e.g. Leal 1980, for a review). Chaffey *et al.* (1967) predicted that the lateral velocity of a droplet in a wall-bounded linear shear flow decreases inversely with the square of the distance from the wall. Chan & Leal (1979) extended the small deformation analysis to drop migration in wall-bounded Couette and plane parabolic flows. For a Newtonian drop suspended in a parabolic flow of another Newtonian fluid, their results showed that the drop migrates away from the wall and settles at the centerline for drop-to-medium viscosity ratio (λ) of less than unity. But for $\lambda \sim O(1)$, it settles at a position between the wall and the axis. Using the method of reflections, Shapira & Haber (1988) obtained an approximate expression of the deformation and drag force on a drop moving parallel to a wall in a quiescent fluid bounded by two walls. The wall effects on the drop deformation was shown to be greater for drops located close to the walls, and to vanish for drops moving along the centerline. Shapira & Haber (1990) extended the analysis to Couette flow in presence of a wall. Uijttewaal *et al.* (1993) used boundary integral method to study drop deformation and migration in linear shear flow in presence of a wall, and observed large deviations from the theory of Chan & Leal (1979) and Shapira & Haber (1988, 1990) at small wall distances and large drop deformation. Uijttewaal & Nijhof (1995) extended the boundary integral method to consider viscosity ratios other than unity. Coulliette & Pozrikidis (1998) studied transient motion of three-dimensional liquid drops in cylindrical tubes at $\lambda = 1.0$ using boundary integral simulation, and observed migration towards the tube center. Li & Pozrikidis (2000) also considered wall-bounded shear flow and plane Poiseuille channel flow of two-dimensional suspensions of liquid drops. Recently, Griggs *et al.* (2007) formulated an efficient three-dimensional boundary-integral method for motion of deformable drops between two parallel walls that can consider a wide range of capillary number, drop-to-channel size ratio, and drop-to-medium viscosity ratio.

In the case of a finite Reynolds number liquid drop, the effect of inertia and drop deformation both contribute to lateral migration. Mortazavi & Tryggvason (2000) showed that in presence of high inertia, an isolated liquid drop undergoes a transient oscillatory motion about its equilibrium position, and a steady-state may not be achieved at sufficiently

high Reynolds number.

In the limit of a rigid spherical particle, lateral migration is possible only in presence of inertia, and an extensive literature exists on this subject. Here we avoid the discussion on the subject, and refer to a recent article by Magnaudet *et al.* (2003) which provides an excellent review of the topic.

Unlike liquid drops, capsule migration in wall-bounded shear flow is relatively less studied. Experiments performed by Goldsmith (1971) using dilute suspensions of red blood cells showed center-ward migration, similar to the case of liquid drops. Extending the theory of small deformation, Helmy & Barthès-Biesel (1982) studied the migration of a capsule in an unbounded parabolic flow, and showed that similar to a liquid drop, an isolated capsule migrates laterally toward the centerline due to its deformation under external shear. Pozrikidis (2005) presented boundary-element simulation of spherical, oblate ellipsoidal and biconcave capsules in tube flow, and observed that spherical capsules slowly migrate towards the tube centerline, and oblate and biconcave capsules developed parachute and slipper-like shapes, respectively.

Three-dimensional numerical simulation is presented on the motion of a deformable capsule undergoing large deformation in a plane Poiseuille flow in a channel at small inertia. Lateral migration of the capsule towards the centerline of the channel is observed. Results are presented over a range of capillary number, viscosity ratio, capsule-to-channel size ratio, and lateral location. After an initial transient phase during which the capsule deforms very quickly, the flow of the capsule is observed to be a quasi-steady process irrespective of capillary number (Ca), capsule-to-channel size ratio (a/H), and viscosity ratio (λ). Migration velocity and capsule deformation are observed to increase with increasing Ca and a/H , but decrease with increasing λ , and increasing distance from the wall. Numerical results on the capsule migration are compared with the analytical results for liquid drops (Chan & Leal 1979), and capsules with Hookean membrane (Helmy & Barthès-Biesel 1980) which are valid in the limit of small deformation. Unlike the prediction for liquid drops (Chan & Leal

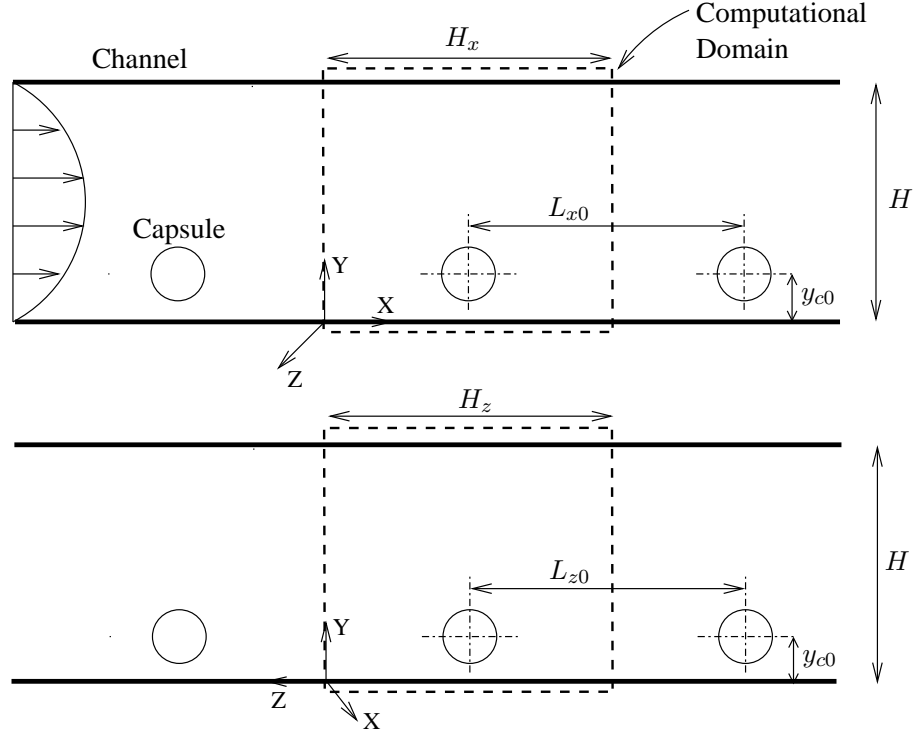


Figure 3.1: Schematic of the flow configuration. The computational domain is indicated by dashed lines.

1979), capsules are observed to migrate toward the centerline for $0.2 \leq \lambda \leq 5$ range considered here. The migration velocity is observed to depend linearly on $(a/H)^3$, in agreement with the small-deformation theory, but non-linearly on Ca and the distance from the wall, in violation of the theory. Using the present numerical results and the analytical results of Shapira & Haber (1988), we present a correlation that can reasonably predict migration velocity of a capsule for moderate values of a/H and Ca .

3.2 Flow Configuration and Simulation Technique

3.2.1 Problem setup

The flow configuration is described in figure 3.1. We consider the motion of an array of capsules in a channel bounded by two infinite flat plates placed parallel to the X -axis in the XYZ coordinate system as shown. The height of the channel is H . The separation between adjacent capsules in the X direction is denoted by L_{x0} and in the Z direction by L_{z0} . The fluids, inside and outside of the capsules, are incompressible and Newtonian. The fluids have same density but may differ in viscosity. Viscosity of the liquid interior of the capsule is denoted by μ_c , while that of the external liquid is μ_0 . In absence of the capsules, the undisturbed flow \mathbf{u}_0 is a fully-developed parabolic (Poiseuille) flow, and is directed from $X = -\infty$ to $X = +\infty$, and is driven by a constant pressure gradient dP/dX as

$$\mathbf{u}_0 = \left[\frac{1}{2\mu_0} \left(-\frac{dP}{dX} \right) (HY - Y^2), \quad 0, \quad 0 \right]. \quad (3.2.1)$$

Here Z is the direction of vorticity of the undisturbed flow. The capsules are released in this flow at time $t = 0$ off the center of the channel. The initial location of the capsule centroid is denoted by X_{c0} , Y_{c0} , Z_{c0} , which are varied in the simulations as described later.

3.2.2 Dimensionless parameters

The centerline velocity of the undisturbed parabolic flow is U_{cl} . The undeformed shape of the capsule is spherical. The diameter of the capsule is denoted by a . The governing equations are made dimensionless using H as the characteristic length scale, U_{cl} as the velocity scale, and H/U_{cl} as the time scale. The dimensionless time is denoted by t^* . The major dimensionless parameters are: the capillary number $Ca = \mu_0 U_{cl}/Eh$ which is the ratio of the viscous force to the elastic force of the capsule membrane, the ratio of the viscosity of the interior fluid to that of the exterior fluid $\lambda = \mu_c/\mu_0$, and the size ratio a/H . The Reynolds number of the capsules, defined as $Re = \rho U_{cl} a/\mu_0$, is 0.01, and hence the effect of inertia is negligible. Other geometric parameters are the initial separation distance between the capsules, L_{x0}/H , and L_{z0}/H , in the x and z directions, respectively.

3.3 Results and Discussion

3.3.1 Migration at $\lambda = 1$

We now consider the motion of a capsule in a fully-developed Poiseuille flow in a channel. As mentioned before, the imposed periodicity of the computational domain along the X and Z directions implies that we consider the motion of an array of capsules (figure 3.1), rather than a perfectly ‘isolated’ capsule. The inter-capsule distance is taken to be $L_{x0} = L_{z0} = H$. The effect of inter-capsule spacing will be considered in a later section.

The initial transience immediately after the capsule is released in the flow is shown in figure 3.2 for $Ca=0.2$ and 0.8 . For this case, we consider $a/H=0.16$. We use 1280 and 5120 Lagrangian elements for $Ca = 0.2$ and 0.8 , respectively. The capsule is released close to the wall at $Y_c/H = 0.175$ at $t^* = 0$. It deforms very quickly (within $t^* < 1$, as shown) under the action of the imposed shear, and aligns itself at an angle with the direction of the flow. For $Ca = 0.2$, the capsule attains an ellipsoidal shape, but for $Ca = 0.8$, the capsule shape at $t^* > 1$ is asymmetrical with high-curvature corner in the near-wall side. As expected, deformation and alignment w.r.t. the X -axis are higher for $Ca = 0.8$.

Migration of the capsule over an extended time ($tU_{cl}/a > 400$) until the capsule comes close to the center of the channel is shown in figure 3.3. For both Ca , the capsules migrate continually towards the centerline. Deformation decreases as the capsule moves closer towards the center in the low shear region. For $Ca = 0.8$, the shape is asymmetric when the capsule is located near the bottom wall, and near the channel center. Figures 3.2 and 3.3 suggest that the rate of deformation is significant during the initial transience. Once this initial transience is passed, capsule shape remains nearly steady as it migrates away from the wall.

In figure 3.4 we show the history of lateral location, migration velocity V_y , slip velocity V_{slip} , deformation, and angular orientation w.r.t. X -axis for $Ca = 0.1, 0.2, 0.4$, and 0.8 . For all cases, $a/H = 0.16$ and capsules are released at $Y_c/H = 0.175$. At high Ca , capsule shape is not ellipsoidal. In this case, deformation D is calculated as $(L_{\max} - L_{\perp}) / (L_{\max} + L_{\perp})$ where

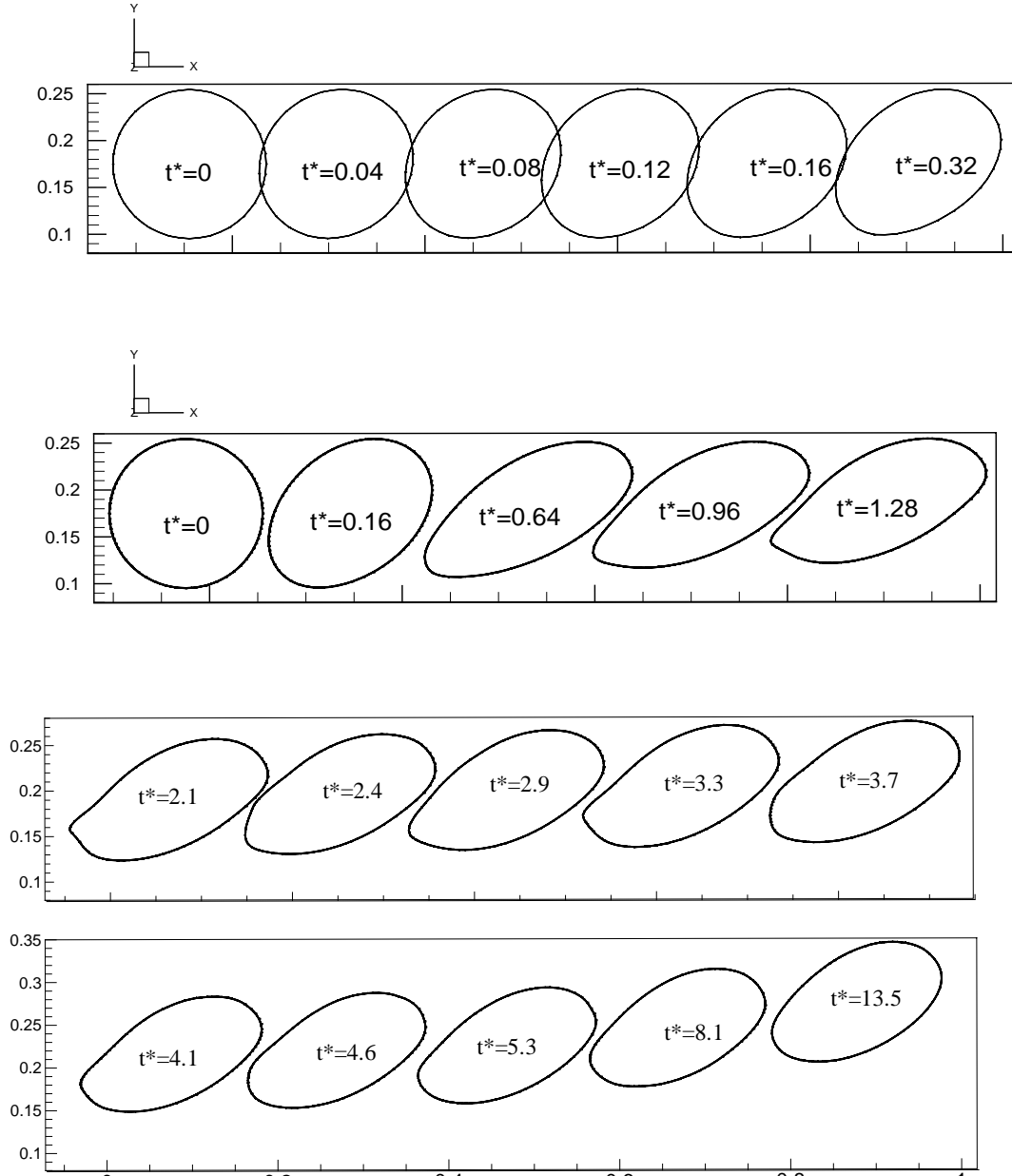


Figure 3.2: Migration of a capsule in a pressure-driven flow in a channel. Sequence of capsule shapes during initial transience is shown for $Ca = 0.2$ (top row) and $Ca = 0.8$ (bottom three rows). Here $t^* = tU_{cl}/H$. X, Y, Z coordinates are scaled by channel height H . $Y/H = 0$ is bottom wall of the channel, and $Y/H = 0.5$ is channel center. Here $\lambda = 1$, and $a/H = 0.16$.

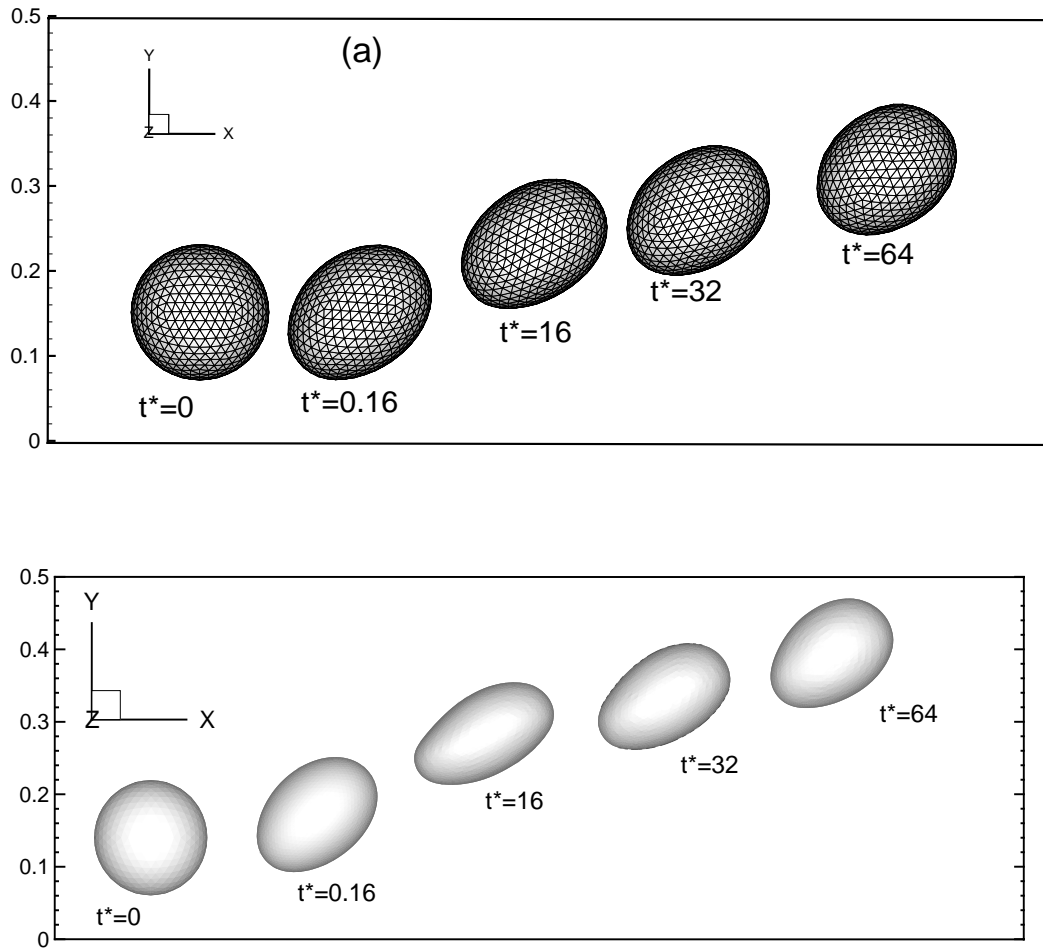


Figure 3.3: Same as in figure 3.2, but over an extended period of time. $Ca = 0.2$ (top), and $Ca = 0.8$ (bottom).

L_{\max} is the maximum distance between two points on the capsule profile on (x, y) -plane, and L_{\perp} is the distance between capsule membrane in the direction normal to L_{\max} in the same plane. For an ellipsoidal capsule, L_{\max} is the major axis, and L_{\perp} is the minor axis. The orientation angle θ reported for non-ellipsoidal shape is the angle between L_{\max} and x -axis. As the flow starts, D attains its peak value within a short time ($t^* < 1$) implying that the capsule deforms quickly before it moves significantly in the lateral direction. The migration velocity and slip velocity also reach their maximum, and the orientation angle reaches its minimum, during the rapid initial transience. The migration velocity and deformation are observed to be higher with increasing Ca implying that the lateral migration is essentially due to the departure from the initially undeformed spherical shape as in case of a liquid drop. The angular orientation w.r.t. the X -axis decreases with increasing Ca , which is also consistent with the results in linear shear flow, and seem to remain the same even in presence of the wall-bounded parabolic flow. The slip velocity V_{slip} , defined as the Poiseuille velocity at the instantaneous center of the capsule minus the X -component of the capsule velocity, is shown in figure 3.4c. The slip velocity is always positive meaning that the capsule lags behind the fluid. The slip velocity becomes higher with decreasing Ca . The slip velocity is order of magnitude less than the capsule translational velocity. In the limit $Ca \rightarrow \infty$, the slip velocity would vanish, whereas in the limit that the capsule is perfectly rigid, it would be maximum for a given lateral location. This qualitative trend is reflected in the simulation results. Once the initial transience is passed, the capsules start migrating toward the channel center. During subsequent motion, the deformation, migration and slip velocity decrease, and the orientation increases with time as the capsule drifts toward low shear region. The decrease in slip velocity over time (i.e. with lateral location) is also in qualitative agreement with the asymptotic theory of small rigid spheres as well as neutrally buoyant drops at small deformation. The capsule migrates toward the center of the channel for all values of Ca considered here. The migration in general is slow. For $Ca = 0.8$ the capsule travels only about half of its diameter in the lateral direction, while translating nearly 50 diameters along the axial direction.

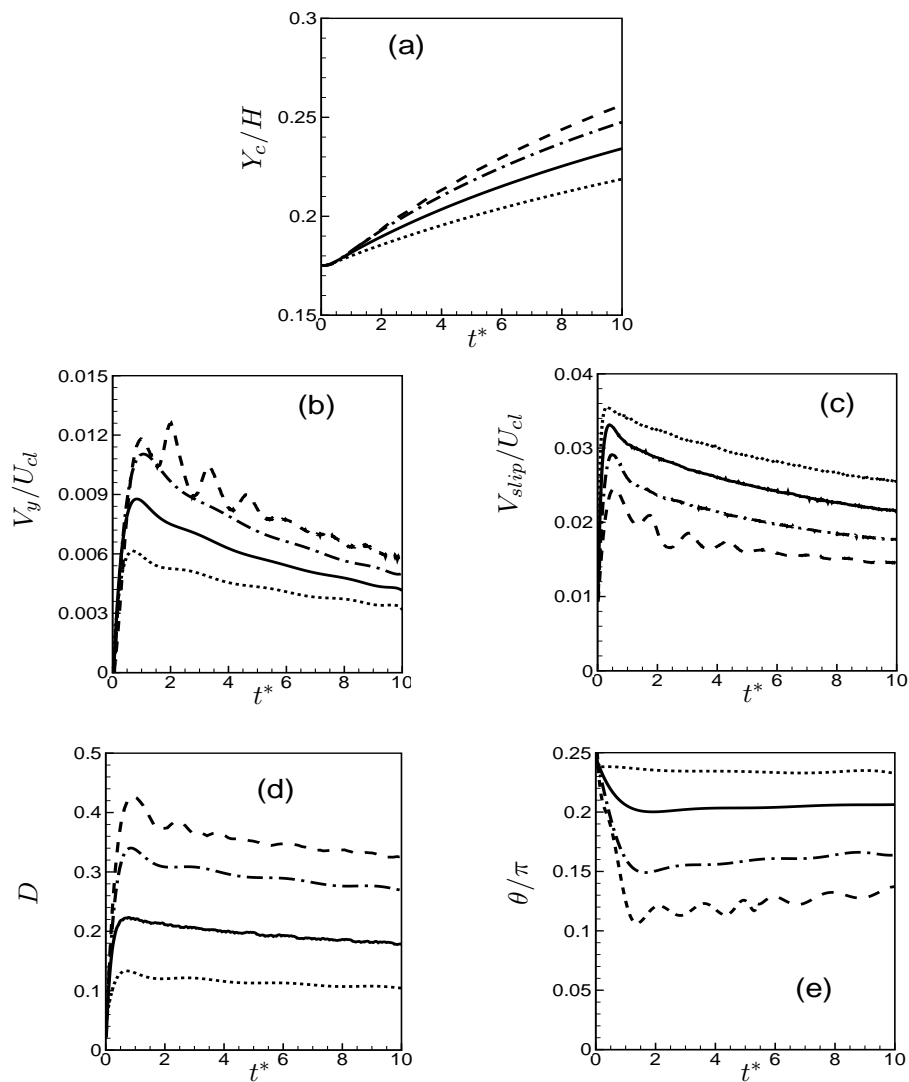


Figure 3.4: History of (a) lateral distance, (b) lateral velocity, (c) slip velocity, (d) deformation, and (e) orientation (w.r.t. X-axis) of a capsule as a function of Ca . $\cdots \cdots$ $Ca = 0.1$; — $Ca = 0.2$; $-\cdot-\cdot-$ $Ca = 0.4$, and $---$ $Ca = 0.8$. Here $a/H=0.16$, and $\lambda = 1$.

Figure 3.4 shows oscillations in V_y , V_{slip} , D , and θ for $Ca = 0.8$. The oscillations arise from the shape oscillation of the capsule which can be seen from capsule profiles given in figure 3.2. This figure shows that immediately after the release ($t^* = 0.16$ and 0.64), capsule shape is ellipsoidal. But for $t^* \geq 0.96$, sharp edge is developed near the wall-ward side due to the higher local shear stress acting on this region of the capsule arising from the no-slip condition imposed on the wall. Because of the tank-treading, the sharp curvature travels along the membrane, and it dissipates as it moves away from the wall ($t^* = 2.4$). Subsequently, another sharp curvature develops near the wallward region ($t^* = 3.3$ and 4.1), which also travels along the membrane away from the wall. As the capsule migrates away from the wall, the sharp curvature weakens. Due to repeated emergence and smoothing of the sharp curvature, magnitude and direction of L_{\max} and L_{\perp} oscillate, causing an oscillation in D and θ . Oscillations in V_y and V_{slip} also arise due to shape oscillation. V_y is locally minimum when the curvature is high, and maximum when it is smoothened. The oscillations are not evident beyond $t^* = 5$ over which the capsule travels only 0.28 of its diameter. Thus, these oscillations are during initial transience. Since migration is a slow process, and as shown in figure 3.3, the capsule does not reach the center even at $t^* = 64$, these oscillations do not have any effect on the long-term migration.

It is of interest to see if the motion of the capsule, after the initial transience is passed, is quasi-steady. We compare the motion of a ‘free’ capsule with the results of a ‘quasi-steady’ simulation in figures 3.5 and 3.6 for $Ca = 0.2$ and 0.8 , respectively. For the simulation of a free capsule, the capsule is released near the bottom wall and the simulation is continued until it reaches close to the center. For the quasi-steady simulations, an undeformed spherical capsule is released at various lateral locations along the trajectory of the free capsule, and the simulations are stopped just after the initial transience is passed. Since the capsule has not moved significantly in the lateral direction during this short simulation, the results, such as migration velocity, deformation etc., can be taken as the ‘quasi-steady’ results corresponding to that lateral location.

In figures 3.5 and 3.6, we compare four quantities: migration velocity, slip velocity,

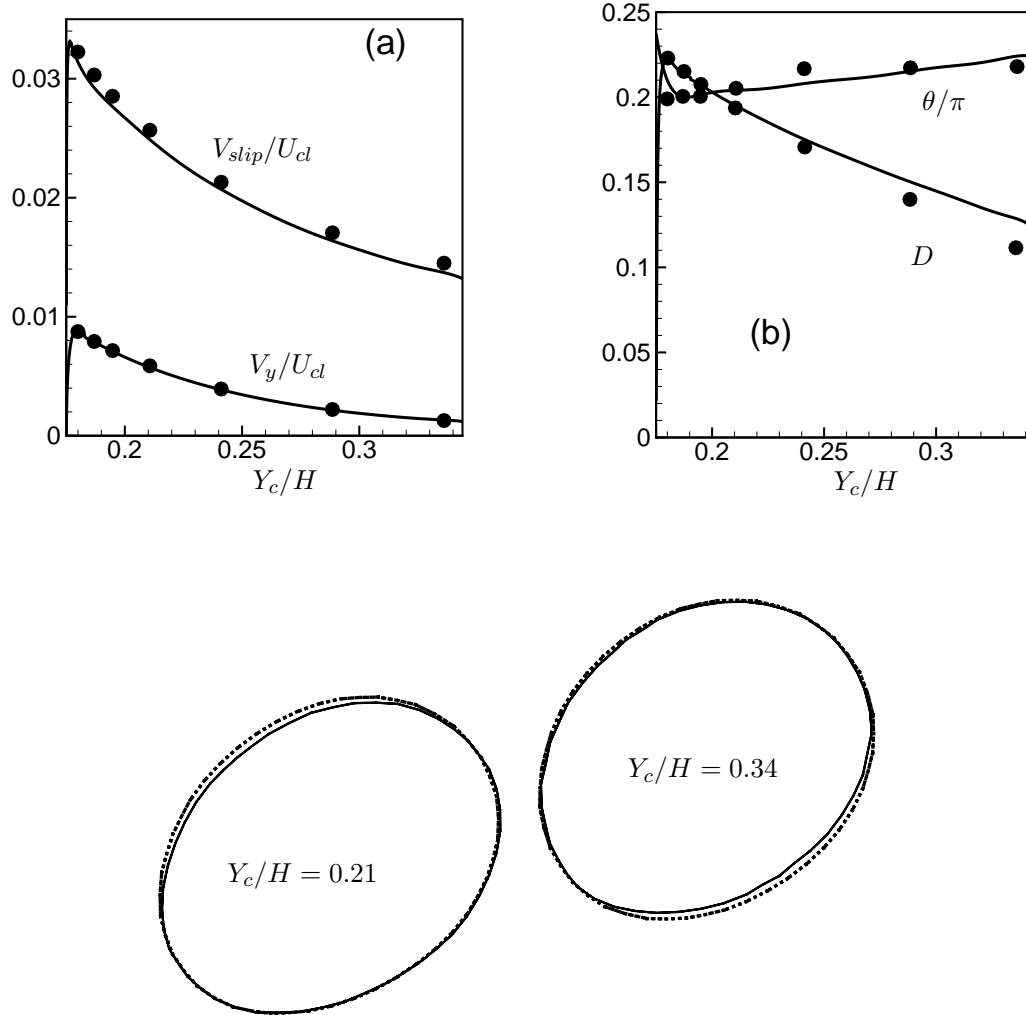


Figure 3.5: Comparison of a free capsule with quasi-steady results for $Ca = 0.2$, $\lambda = 1$, and $a/H = 0.16$. In (a) and (b) lines are for the free capsule, and dots are for the quasi-steady results. Capsules shapes at two different locations are shown in the bottom. Solid line is the free capsule, and dash line is the quasi-steady result.

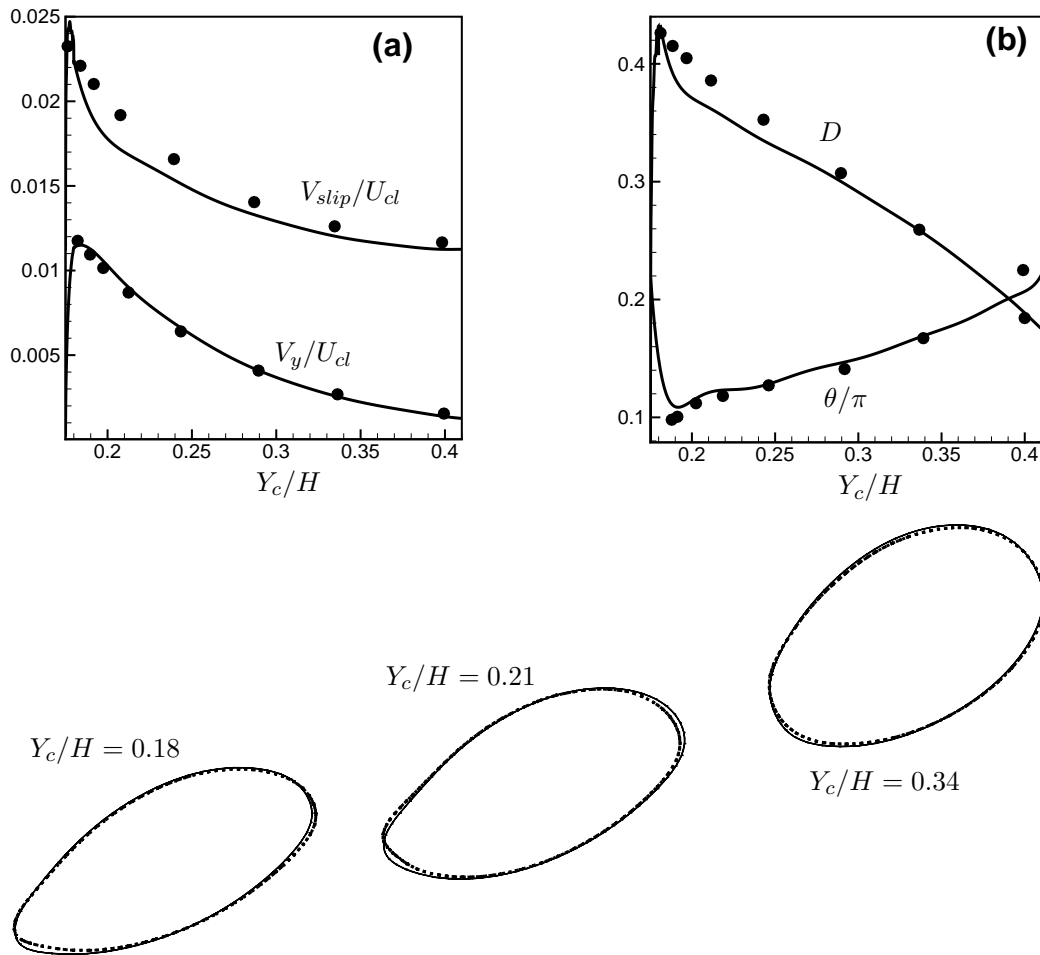


Figure 3.6: Same as in figure 3.5, but for $Ca = 0.8$

deformation, and angular orientation, of the free capsule and quasi-steady result. In the figure the lines represent the free capsule, and the points represent quasi-steady results. As can be seen for both $Ca = 0.2$ and 0.8 , all four quantities show excellent agreement between the free capsule and the quasi-steady results. Note that in the limit the capsule is located at the center of the channel, the slip velocity is still non-zero and proportional to $(a/H)^2$ according to the linear theory. The asymptotic behavior of computed V_{slip} in figure 3.4c yields the same order of magnitude value as $(a/H)^2$.

In figures 3.5 and 3.6, we also overlap the shapes of the freely moving capsule and the quasi-steady results for various lateral locations. The capsule shapes match very well which further confirms that the migration is a quasi-steady process.

The quasi-steady nature of the capsule migration can be understood by comparing the migration time $T_y = a/V_y$, to the response time of the capsule shape $T_c = \mu a/Eh$. The capillary number $Ca = \mu U_{cl}/Eh$ can be expressed as the ratio of T_c and the axial convection time $T_x = a/V_x$, where $V_x \approx U_{cl}$. Since $V_y \ll V_x$ (that is, $T_x/T_y \ll 1$), and $Ca < 1$, we see that $T_c \ll T_y$.

It is also of interest to compare the present results with previous analytical predictions. Migration of a capsule with Hookean membrane was considered by Helmy & Barthès-Biesel (1982) in an unbounded cylindrical Poiseuille flow in the limit of $Ca(a/D_0) \ll 1$, where D_0 is a length scale of the undisturbed flow, which is the tube diameter for the Poiseuille flow. They predicted

$$\frac{V_y}{U_{cl}} = -\frac{29}{6} Ca \left(\frac{b}{a}\right) \left(\frac{a}{D_0}\right)^3 \quad (3.3.1)$$

for Poisson ratio equal to $1/2$ for the membrane. Here b is the distance of the capsule center from the flow centerline.

Chan & Leal (1979) considered migration of a deformable liquid drop of surface tension σ in an unbounded plane Poiseuille flow in the limit of small deformation, and obtained

$$\frac{V_y}{U_{cl}} = -\frac{8}{5} \frac{\mu_0 U_{cl}}{\sigma} \left[1 - 2 \left(\frac{Y_c}{H}\right)\right] \left(\frac{a}{H}\right)^3 \quad (3.3.2)$$

for $\lambda = 1$. Despite the differences in the background flow, and the nature of the particle,

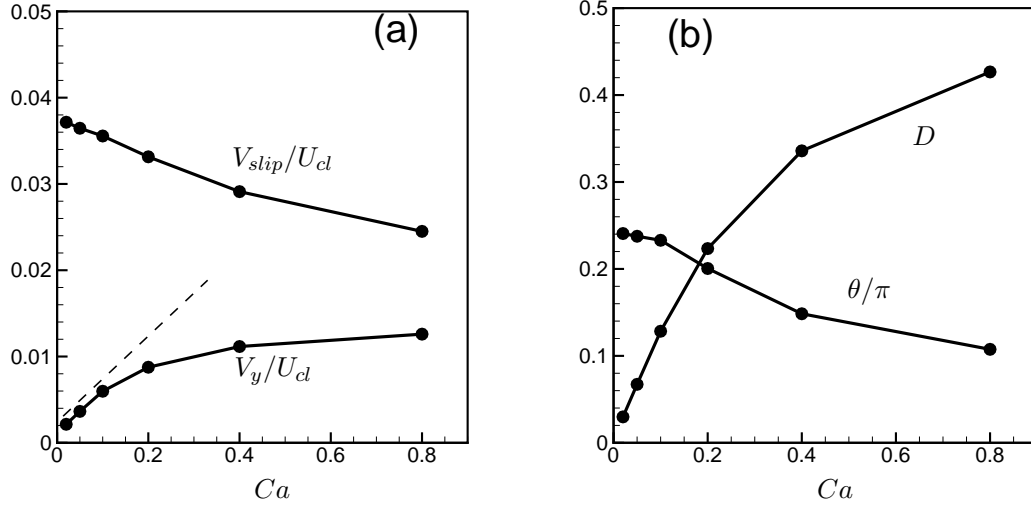


Figure 3.7: Dependence of migration velocity, slip velocity, deformation, and orientation on Ca while keeping a/H and Y_c/H constants at 0.16, and 0.18, respectively. The dashed line corresponds to the linear theory.

(3.3.1) and (3.3.2) predict the similar qualitative dependence of V_y/U_{cl} on Ca , Y_c/H and a/H , and differ only in the numerical prefactors. Though exact comparison is not possible due to the differences in the background flow and the nature of the particle, it is of interest to see if the qualitative dependence of V_y/U_{cl} w.r.t. Ca , Y_c/H and a/H predicted by (3.3.1) or (3.3.2) agree with our simulation.

In figure 3.7a we show the migration velocity as a function of Ca while keeping a/H and Y_c/H constants at 0.16 and 0.18, respectively. The capsules were released at $Y_c/H = 0.175$, and hence the wall effect is strong. While (3.3.1) and (3.3.2) predict a linear dependence of V_y on Ca , the simulations predict a non-linear dependence. The results in figure 3.7 are shown for $0.025 \leq Ca \leq 0.8$. Assuming that the linear dependence of V_y on Ca is valid at low Ca (which is likely to be the case), and extrapolating the result to higher Ca (dash line in figure 3.7a), we see that the linear theory over-predicts the migration velocity at higher Ca . This is because the linear theory also over-predicts also the capsule deformation at higher Ca (Chapter 2, Table 2.1).

We also show slip velocity, deformation, and orientation as functions of Ca in figure 3.7. Figure 3.7a shows that the slip velocity decreases with increasing Ca . For a small, rigid sphere in a circular Poiseuille flow, the ratio $V_{slip}/U_{cl} = b^2/(D_0/2)^2 - (2/3)(a/D_0)^2$, to the leading order (Brenner 1970, Goldman *et al.* 1967) where b and D_0 are defined above. In the linear theory of Helmy & Barthès-Biesel (1980), the axial velocity of the capsule does not depend on Ca , and the ratio V_{slip}/U_{cl} is the same as that of a small rigid sphere. Our simulations show that V_{slip}/U_{cl} depends on Ca . Further, the order of magnitude of V_{slip}/U_{cl} obtained from the simulation and shown in figure 3.7a is significantly lower than the prediction by the linear theory even when $Ca = 0.025$ is considered. On the contrary, the simulation and the linear theory would predict nearly similar order of V_{slip} as $b \rightarrow 0$, that is when the capsule is located far from the wall as observed in figure 3.6a. Shapira & Haber (1990), on the contrary, obtained that V_{slip}/U_{cl} is proportional to $Ca (a/Y_c)^2$, for a wall-bounded linear shear flow in the limit of small deformation. Assuming that the linear dependence of V_{slip} on Ca is valid at low Ca even for parabolic flow, and extrapolating the result to higher Ca , one can say from figure 3.7a that the linear theory, when taken into consideration the effect of Ca , would underpredict the slip velocity at higher Ca .

In figure 3.7b, deformation D and orientation angles are shown. D appears to approach a plateau as Ca increases which explains the plateau in migration velocity. This plateau in D can arise from two effects. In an unbounded linear shear flow, D does not increase linearly at large Ca , and shows reduced rate of change at higher Ca . In addition, the presence of the wall and parabolic nature of the flow can further prevent the capsule from deforming at higher Ca . In an wall-bounded flow, migration arises from two effects. A particle moving near a wall would experience a lift force even in absence of the flow due to the asymmetry introduced by the wall. In addition the presence of a shear flow would introduce additional asymmetry in the governing equations at low inertia leading to the deformation-induced lift force. Thus the migration velocity is proportional to the product of slip velocity and amount of deformation. This explains, as seen in figure 3.7, that D increases but V_{slip} decreases with increasing Ca resulting a plateau in V_y at higher Ca .

In figure 3.7b, the orientation angle at very low Ca is close to its theoretical value of $\pi/4$ for low deformation. It decreases with increasing Ca departing from the linear theory, but appears to plateau at higher Ca due in part, possibly, to the wall effect.

In figure 3.8 we plot V_y , V_{slip} , and D as functions of Y_c/H while keeping Ca and a/H fixed. Unlike the linear dependence in (3.3.1) and (3.3.2), the simulations predict non-linear dependence of V_y w.r.t. Y_c/H .

In figure 3.8b, variation of V_{slip} w.r.t Y_c/H shows also a non-linear decrease. The slip velocity is higher near the wall and decreases away from the wall. The higher slip velocity near the wall arises from the no-slip condition imposed on the wall which causes a higher local shear rate in the gap between the capsule and the wall. When wall-effect is included (Chan & Leal 1979; Chaffey *et al.* 1967; Magnaudet 2003), V_{slip} should decrease as $(1 - Y_c/(H/2))^2$, in the leading order for small rigid spheres as well as neutrally buoyant drops under small deformation. Our numerical results indicate that V_{slip} decreases faster than this rate near the wall, and slower near the centerline. D shown in figure 3.8c also suggests a faster decrease near the wall than that near the centerline.

In figure 3.9 we plot V_y as a function of $(a/H)^3$ while keeping Ca and Y_c/H constants. Interestingly, the linear dependence of V_y w.r.t. $(a/H)^3$ as predicted by (3.3.1) and (3.3.2) happens to be the case in the numerical results as well.

Shapira & Haber (1988) studied the wall effect on the shape of a drop moving in a quiescent fluid confined between two parallel plates in the limit $a/H \ll 1$, and predicted

$$D = \frac{175}{384} \frac{\mu V_x}{\sigma} \left(\frac{a}{H} \right)^2 C_s \quad (3.3.3)$$

where C_s is a function of Y_c/H which is maximum at the channel wall, and zero at the center, implying that drop deformation decreases as it is located closer to the center, and that deformation is zero at the center as is the case for small a/H . Though Shapira & Haber (1988) considered a non-migrating drop with a constant orientation at $\pi/4$, we find that the expression of C_s can be used to predict the dependence of V_y on Y_c . This is shown in figure 3.10a where data points are numerical V_y at various Y_c locations, and solid lines are the shape function C_s scaled by a factor for each Ca .

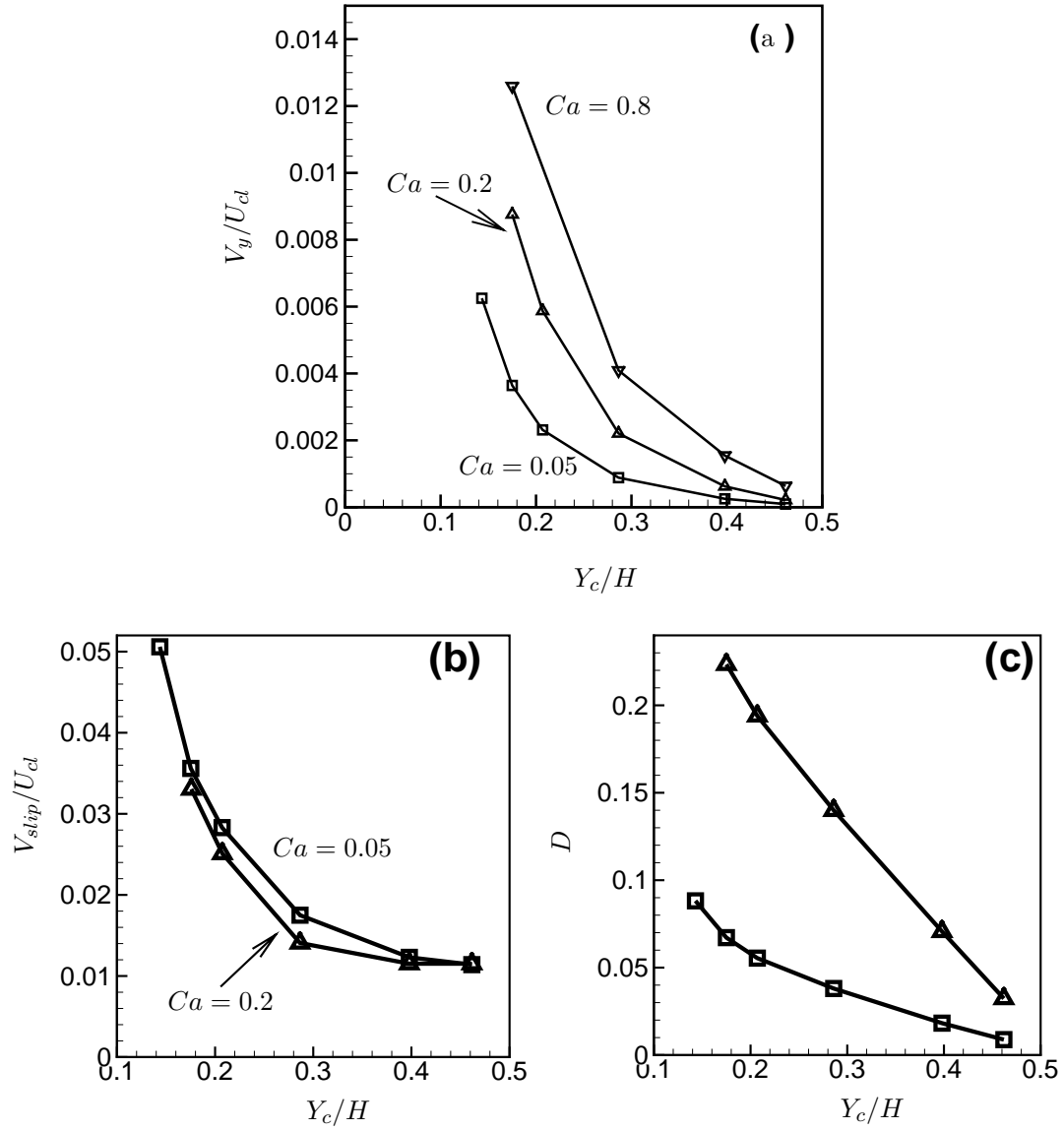


Figure 3.8: (a) Variation of V_y , (b) V_{slip} , and (c) D w.r.t. Y_c while keeping Ca and $a/H = 0.16$ fixed.

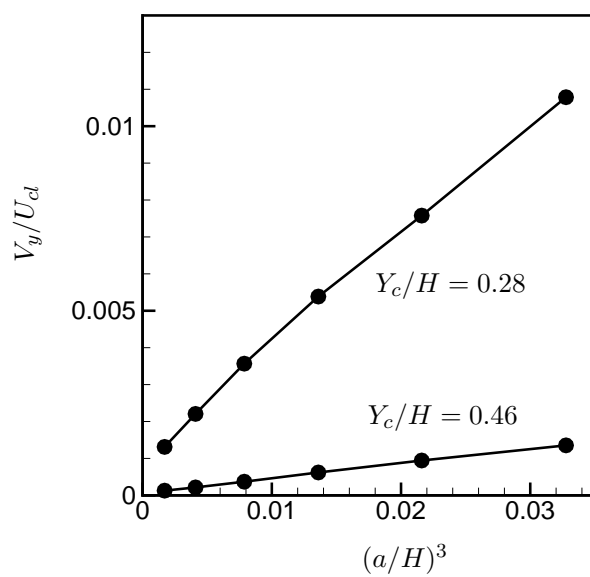


Figure 3.9: Variation of V_y w.r.t. a/H at constant Ca and Y_c/H . Ca is fixed at 0.2.

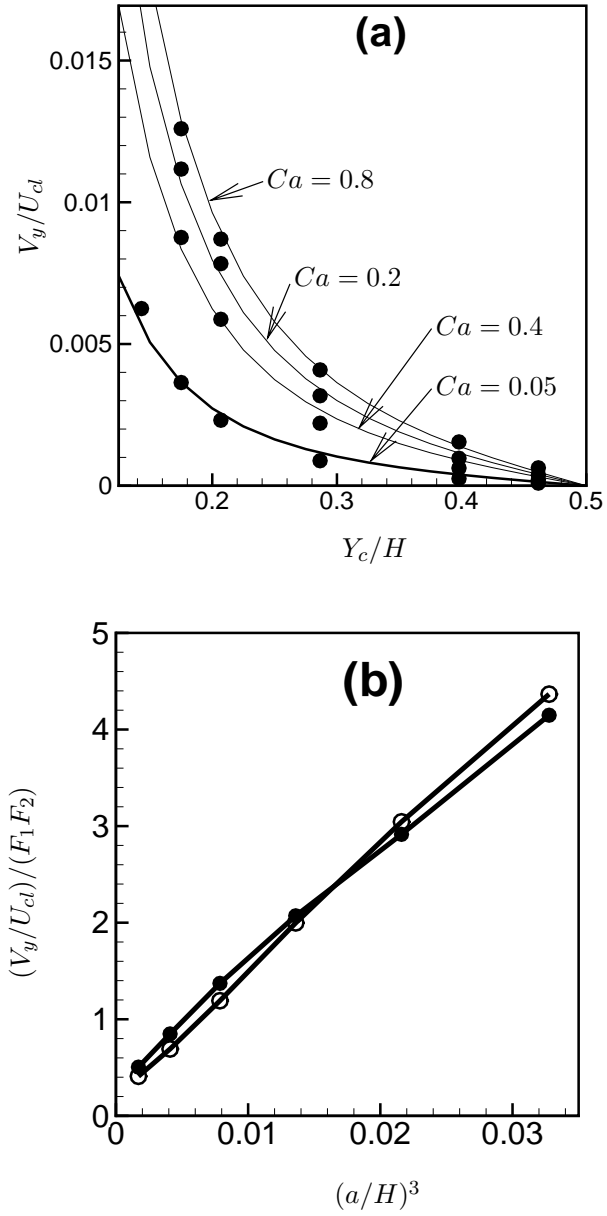


Figure 3.10: (a) Comparison of the scaled shape function C_s (solid line), and the numerical migration velocity (filled circles) for $a/H = 0.16$. (b) Replotting figure 3.9 by scaling V_y by $(F_1 F_2)$.

The results shown in figure 3.10a are for a fixed $a/H = 0.16$, the lowest size ratio considered. Since the numerical results agree with the theoretical prediction (3.3.1,3.3.2) on the linear dependence of V_y on a/H , the scaling factor used for C_s should depend only on Ca . Based on the numerical results in figures 3.9 and 3.10a, and following the theoretical results of Shapira & Haber (1988), an approximate expression for the migration velocity can be proposed as

$$\frac{V_y}{U_{cl}} = F_1(Ca) F_2(Y_c/H) \left(\frac{a}{H}\right)^3 \quad (3.3.4)$$

where the functions F_1 and F_2 are functions of Ca and Y_c/H , respectively, and are given as

$$F_1 = \exp[-0.3458 \ln(Ca) + 7.3878] \quad (3.3.5)$$

and,

$$F_2 = \exp \left[-11.1758 \left(\frac{Y_c}{H} \right) - 2.7429 \right]. \quad (3.3.6)$$

F_2 is a simplified form of the original shape function C_s given by Shapira & Haber. In figure 3.10b, we replot the migration velocity shown in figure 3.9 (which was for a constant $Ca = 0.2$ but different Y_c/H) by scaling V_y/U_{cl} by $(F_1 F_2)$. We find that curves for different Y_c/H collapse, and vary linearly with $(a/H)^3$. Equations (3.3.4)–(3.3.6) can thus be used to reasonably predict migration rate of a capsule in a parabolic flow in a channel for moderate values of (a/H) and Ca .

3.3.2 Larger capsules

We consider $a/H = 0.5$ for which we use 5120 Lagrangian elements on the capsule surface. The computational domain is cubic, and the distance between the adjacent capsule centers in the array is $L_{x0} = L_{z0} = H$. The capsule is released at $Y_c/H = 0.334$. Figure 3.11 shows the deformed shapes at various lateral locations for $Ca = 0.2$. Unlike the smaller capsules which attain ellipsoidal shape after the initial transience is passed, the initial shape (at $Y_c/H = 0.34$ in figure 3.11) for $a/H = 0.5$ resembles a tear-drop and is asymmetric with the high-curvature end facing the bottom wall. Center-ward migration is evident in the

figure. As the capsule approaches the center, it changes from a tear-drop to a slipper shape. In the figure, we also overlap the quasi-steady shapes with those of the free capsules, and see that even for the larger capsule, the two simulations predict similar shapes. The migration velocity for the free capsule and the quasi-steady values are presented in figure 3.11 which also shows that the quasi-steady values match well with the the results of the free capsules once the initial transience is passed.

Figure 3.12 shows the fluid velocity vectors at three time instances during the migration of the larger capsule. The figures here are drawn in a reference frame moving with the velocity of the center of mass of the capsule. Also shown is the vector plot for $a/H = 0.16$ at one time instance. During the initial phase of migration of the larger capsule, a clockwise rotating vortex is generated inside the capsule. The center of this vortex is located close to the capsule centroid. Due to the proximity of the larger capsules in the array, ($a/L_{x0} = 0.5$), the fluid in between the adjacent capsules also develops a counter rotating vortex (marked by dash arrow in the figure). In case of smaller capsules, such vortex exterior of the capsule is absent.

As the larger capsule approaches the center of the channel, the interior vortex moves upward, while a new smaller counter rotating vortex is generated near the bottom. In the exterior fluid as well, two counter rotating vortices can be seen, which are not present for the smaller capsule. The presence of exterior vortices for large a/H , and the transition from one vortex to two counter-rotating vortices as shown by our extended simulations, can have implications in case of tracer diffusion in capillary blood vessels in presence of erythrocytes. It should be mentioned that the strength of the internal vortex is actually very weak.

For larger capsules of $a/H = 0.5$, the effect of separation distance between consecutive capsules is shown in figure 3.11. We consider $L_{x0}/a = 2, 6$ and 8 . The separation distance does have a significant effect on migration velocity when the capsule is located closer to the wall. As L_{x0}/a is changed from 2 to 6 , V_y increases by a factor of 1.5 ; when L_{x0}/a is changed from 6 to 8 , V_y increases by a factor of 1.05 . Thus V_y is expected to converge with increasing L_{x0}/a . For this case, we have not performed a simulation with even higher

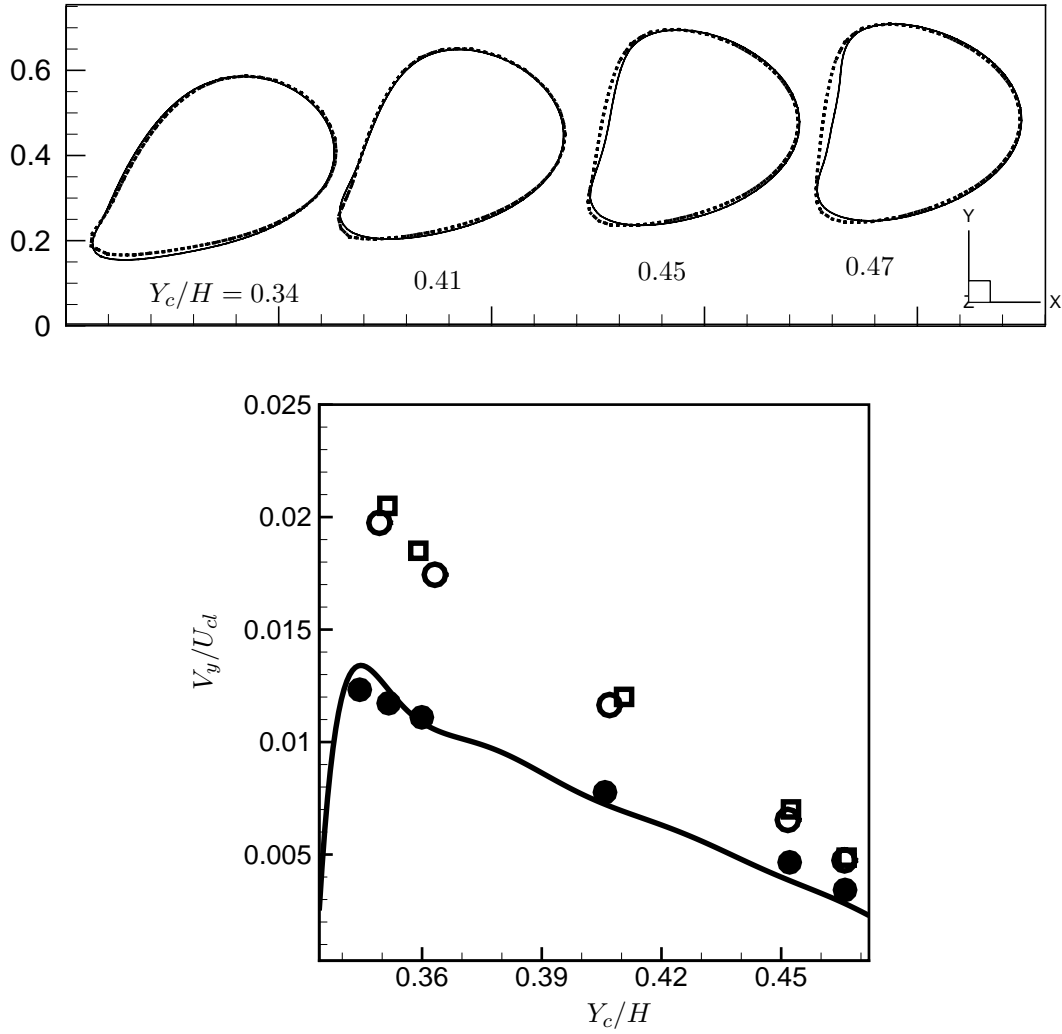


Figure 3.11: Migration of a capsule at $a/H = 0.5$, and $Ca = 0.2$. Top: deformed shapes for free capsule (solid line), and quasi-steady simulations (dash line). Bottom: lateral velocity for free capsule (solid line) and quasi-steady results (filled circles). Also shown is the effect of increasing separation distance between consecutive capsules: filled circles, open circles and boxes correspond to $L_{x0}/a = 2, 6$ and 8 , respectively.

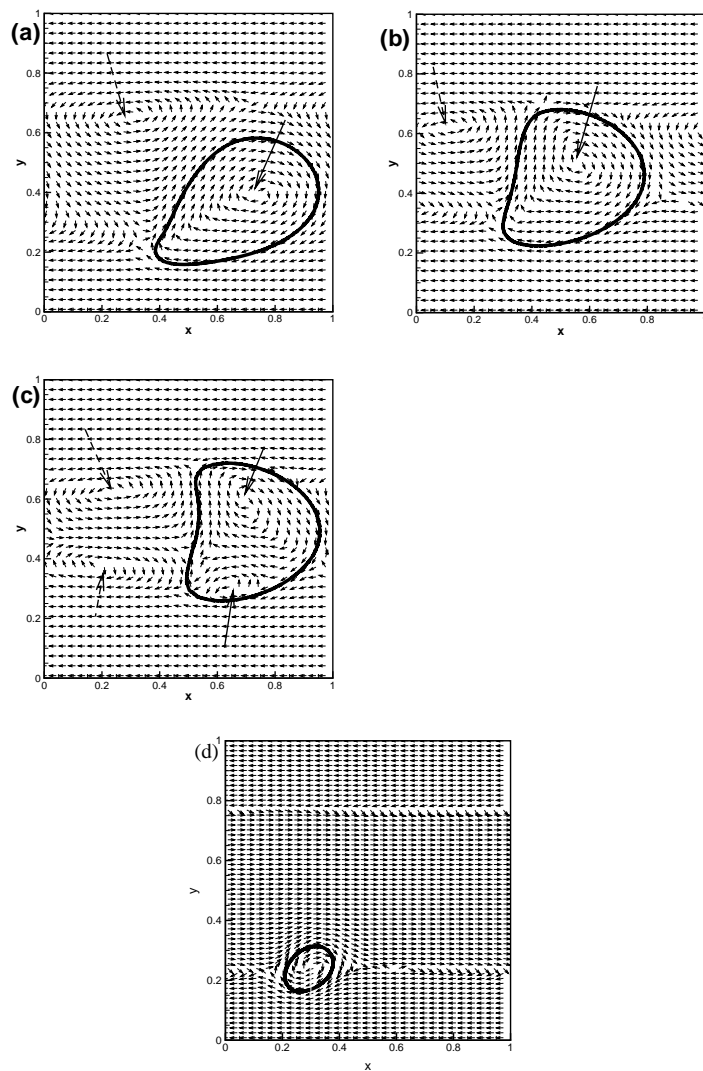


Figure 3.12: Velocity vectors drawn in the XY plane passing through, and in a frame of reference moving with, the capsule center of mass. (a)–(c) are for $a/H = 0.5$, $Ca = 0.2$ at $Y_c/H = 0.35$, 0.44 , and 0.46 , respectively. (d) for $a/H = 0.16$.

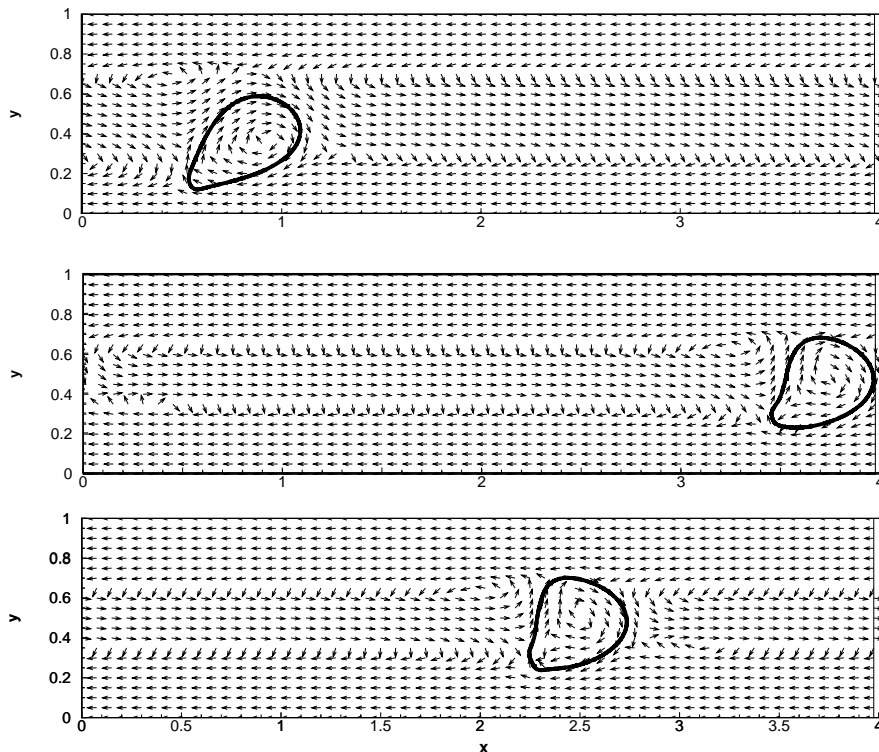


Figure 3.13: Effect of separation distance on flow pattern: velocity vectors (in a frame of reference moving with the velocity of the capsule center of mass) corresponding to the case shown in figure 3.12a–c but for $L_{x0}/a = 8$.

L_{x0}/a due to computational cost, as $L_{x0}/a = 8$ itself was simulated using $320 \times 80 \times 80$ resolution. The effect of L_{x0} appears to decrease as the capsule moves away from the wall. Further result on the effect of L_{x0}/a on V_y for $a/H = 0.16$ is given later in figure 3.18 where convergence of V_y with increasing L_{x0}/a is evident.

The flow pattern for $L_{x0}/a = 8$ is shown in figure 3.13 which can be compared with the results for $L_{x0}/a = 2$ shown in figure 3.12. Evolution of the internal and external vortices as the capsule migrates away from the wall is qualitatively similar for $L_{x0}/a = 8$ and 2.

For larger capsules shown in figure 3.11, the back of the membrane undergoes compression. This is shown in figure 3.14 where we plot the principal stress. Regions having

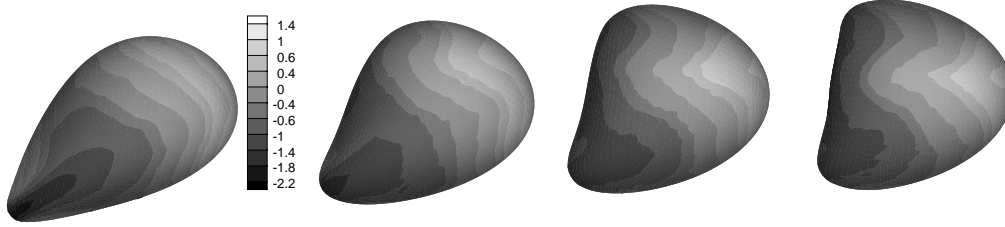


Figure 3.14: Membrane stress distribution for the migrating capsule shown in figure 3.11. Dark regions correspond to compressive stress.

negative stress are seen in this figure.

3.3.3 Effect of λ

Effect of λ is considered next by two simulations at $\lambda = 5$ and 0.2 (both for $a/H = 0.16$) shown in figure 3.15. Deformation, orientation, migration and slip velocity of a free capsule released at $Y_c/H = 0.175$ at $t^* = 0$ are shown. Also shown are the results from quasi-steady simulations of undeformed spherical capsules released at various lateral locations. The results from the free-capsule simulation and those of quasi-steady simulations agree well implying that the quasi-steady nature of migration is valid over the range of viscosity ratio considered here.

The capsule shapes for free capsule and for quasi-steady results are compared in figure 3.16 for $a/H = 0.5$, and $\lambda = 5$ and 0.2 at various lateral locations. The two simulations predict nearly overlapping shapes implying the quasi-steady nature of migration even for larger capsules at a viscosity ratio other than unity.

The migration velocity, deformation and orientation of the capsules for $\lambda = 5$, 0.2 and 1 over a wider range of lateral locations are shown in figure 3.17 for $a/H = 0.16$, $Ca = 0.2$. As expected, the migration rate, deformation and orientation angle decrease with increasing λ . The migration velocity and deformation decrease as the capsule approach channel center. We also note that results for $\lambda = 1$ and 0.2 nearly overlap with each other, which is consistent

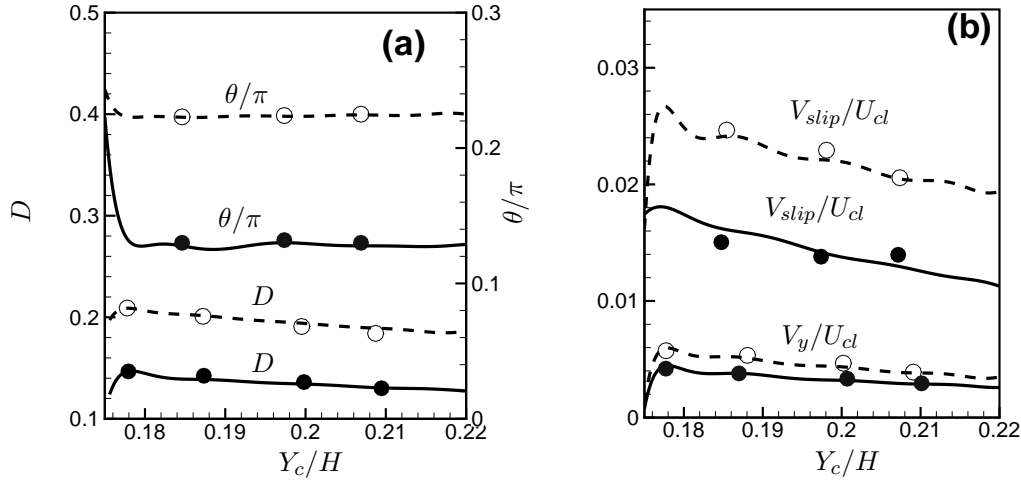


Figure 3.15: Free capsule versus quasi-steady results for $\lambda \neq 1$. Lines represent free capsule and symbols represent quasi-steady simulations. Solid lines and filled circles represent $\lambda = 5$, dash lines and open circles represent $\lambda = 0.2$. $a/H = 0.16$, $Ca = 0.2$.

with the linear shear results presented earlier in figure 2.9 which showed that deformation did not change much from that of $\lambda = 1$ when λ is reduced below unity, but it changed significantly when $\lambda > 1$. Also note in figure 3.17c that near the center of the channel, the deformation curves for $\lambda = 1$ and $\lambda = 5$ cross each other. This is likely because a capsule with higher λ is slower to respond to the changing shear rate than the one with lower λ . The characteristic time for deformation is proportional to $1 + \lambda$. This also explains why migration velocities are nearly the same for $\lambda = 1$ and $\lambda < 1$, but much lower for $\lambda > 1$.

It may be noted that the expression of drop migration by Chan & Leal suggests that for $\lambda < 0.5$ and $\lambda > 10$, the drop migrates toward the center of a channel, while for $0.5 < \lambda < 10$, it migrates toward the wall. The simulations performed here over a range of Ca and λ suggested that the capsule migrates always toward the center of the channel.

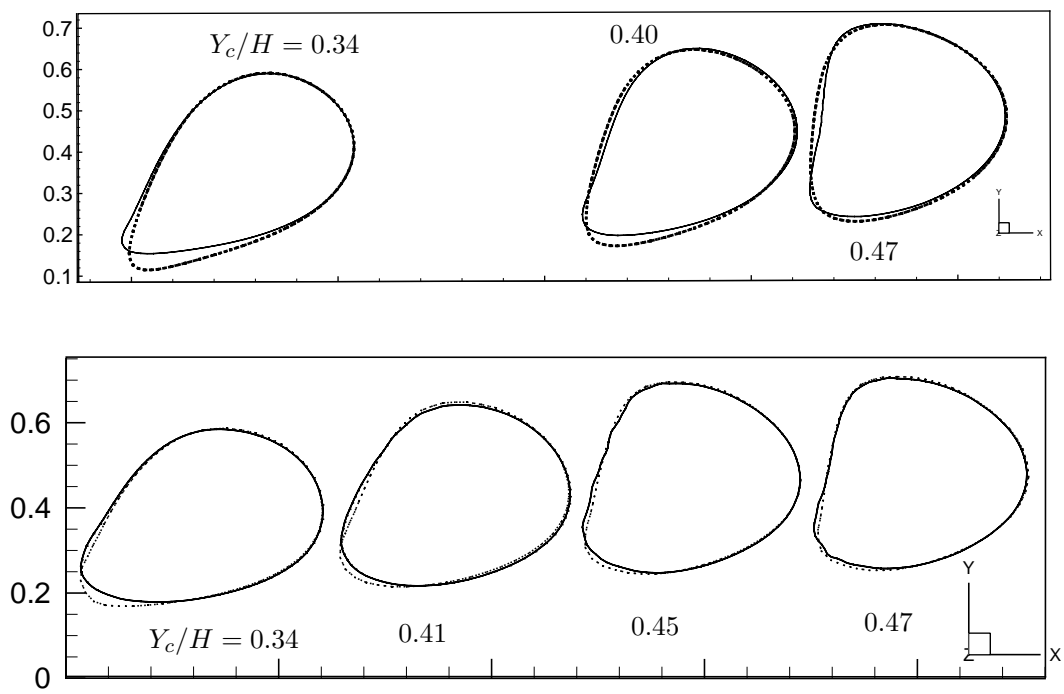


Figure 3.16: Deformed shapes for $a/H = 0.5$, $Ca = 0.2$ at $\lambda = 0.2$ (top) and $\lambda = 5$ (bottom). Solid line is the free capsule, and dotted line is the quasi-steady result.

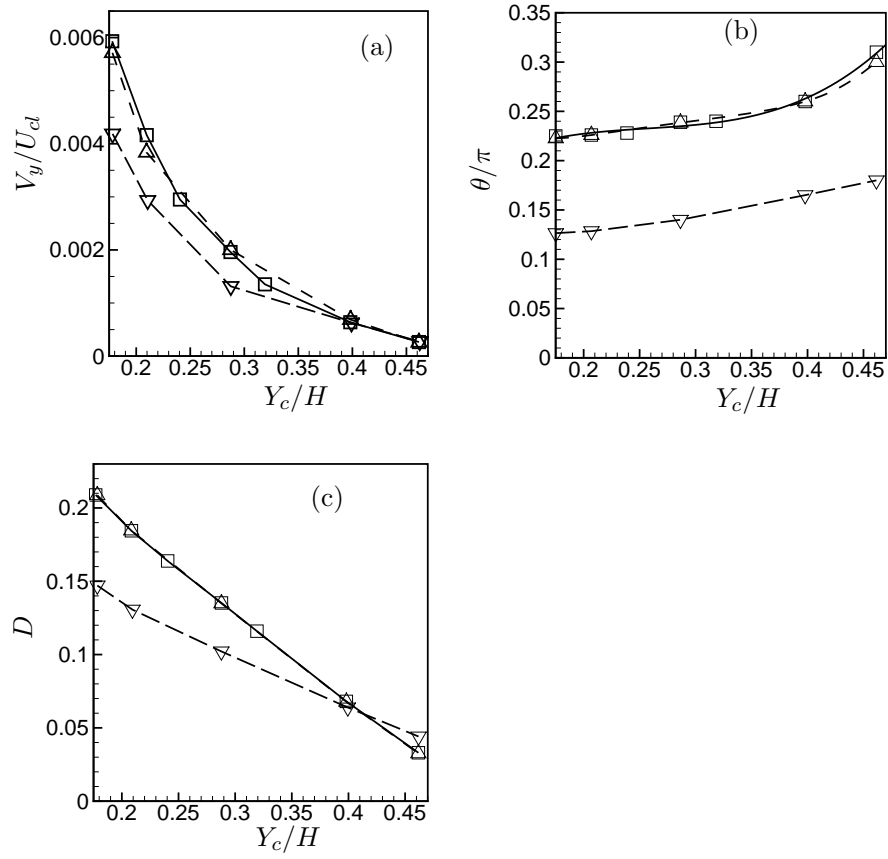


Figure 3.17: Migration velocity, deformation, and orientation as functions of Y_c . $a/H = 0.16$, $Ca = 0.2$. $\square \lambda = 1$, $\triangle \lambda = 0.2$, $\nabla \lambda = 5$.

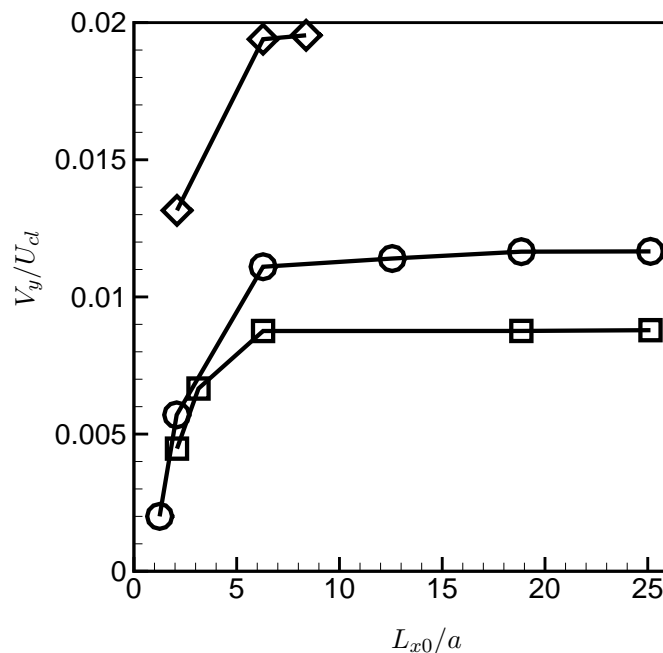


Figure 3.18: Effect of separation distance L_{x0} . □ $Ca = 0.2, a/H = 0.16$; ○ $Ca = 0.4, a/H = 0.16$; ◇ $Ca = 0.2, a/H = 0.5$. Migration velocities shown here correspond to the quasi-steady simulations.

3.3.4 Effect of capsule separation

The effect of separation distance on the migration velocity and flow pattern for $a/H = 0.5$ was shown earlier in figures 3.11 and 3.13. Further results for $a/H = 0.16$ at $Ca = 0.2$ and 0.4 , and $a/H = 0.5$ at $Ca = 0.2$ are shown in figure 3.18. Here the dimensionless separation distance L_{x0}/a is varied from 1.25 to 25. As discussed earlier, migration velocity changes significantly for small separation distance, but converges beyond $L_{x0}/a \approx 6$. The migration velocity decreases as $-1/r$ where r is the separation distance. Comparison of V_y at four L_{x0}/H suggests that the results presented in the previous sections would change very little by increasing the separation distance, but they would change significantly with decreasing separation distance.

3.4 Conclusion

We present results on the lateral migration of a capsule in a plane Poiseuille flow simulated over extended period of time. The migration is observed to be a quasi-steady process, except an initial transient phase during which the capsule deforms very quickly, over a wide range of Ca , size ratio (a/H), and viscosity ratio (λ).

Dependence of the migration velocity with respect to Ca , size ratio and capsule location is studied and compared with the small-deformation theory for liquid drops, and capsules with Hookean membrane. Unlike the linear theory, migration velocity shows a non-linear dependence on Ca and capsule location. The linear theory is seen to overpredict the migration velocity, and underpredict the slip velocity at higher Ca . This departure could be due to both large deformation and small wall distance. Interestingly, however, the linear dependence on $(a/H)^3$ as predicted by the theory appears to be valid even in the limit of large deformation, as shown by the simulation results. Using the present numerical results, and the analytical results of Shapira & Haber (1988), we then present a correlation that can reasonably predict migration velocity of a capsule for moderate values of a/H and Ca . Unlike the prediction for liquid drops (Chan & Leal 1979), capsules are observed to migrate toward the center for $0.2 \leq \lambda \leq 5$ range considered here.

Results presented here depict the effect of curvature in the velocity profile, as well as the wall effects. For the undisturbed Poiseuille flow considered here, it is difficult to isolate the wall effect and the curved velocity profile due to the way the computational problem is set up. In order to isolate the wall effect using the present computational setup, one can consider a linear shear flow where the capsule can be placed away from the wall without any change in the shear rate. Identifying such wall effects in the case of large deformation of a capsule is left for future investigation.

While experimental data on lateral migration of single liquid drop are available in the literature (e.g. Smart & Leighton 1991), we are not aware of similar data on capsule migration. Indeed there are experimental results available on capsule deformation in linear shear flow, and on single-file motion (see Chapter 1). Results on lateral migration of

erythrocytes in tube or channel flow are not abundant. Experiments by Goldsmith and co-workers (e.g. Goldsmith 1971) was mentioned earlier. Recently, Secomb *et al.* (2007) presented two-dimensional simulation on erythrocyte migration in 8- μm capillary. The simulation result was verified qualitatively by experimental data on cell trajectories observed in microvessels of the rat mesentery. The results presented in this article are, however, for three-dimensional capsules in a planar flow, and hence cannot be directly compared with their numerical or experimental data. It appears that migration experiments using spherical capsules are necessary.

Chapter 4

Lateral Migration and Pairwise Interaction of Liquid Capsules in a Plane Poiseuille Flow in a Channel

4.1 Introduction

In the last chapter, we studied motion of a liquid capsule in wall-bounded flows in a dilute suspension. In a non-dilute suspension of liquid drops or capsules, both deformation-induced migration, and particle-particle hydrodynamic interaction are present. The particle-particle interaction may affect the migration process. Goldsmith (1971), in experiments with non-dilute suspension of red blood cells, observed that the center-ward migration of the cells was hindered, and cell-free region near the wall was reduced as the cell volume fraction increased. To the best of our knowledge, the only study that addressed both particle-particle interaction and deformation-induced migration is the one by Li & Pozrikidis (2000) who considered a suspension of liquid drops in a pressure-driven flow. Although an ensemble of 25 drops was considered, their study was limited to two dimensions. Similar studies in three dimensions, and using liquid capsules are non-existent. In the present study we address the lateral migration of a capsule-pair in Poiseuille flow through a channel bounded by two infinite parallel plates.

In the first part of the chapter, we consider spherical undeformed shape. It is shown that the migration velocity is significantly affected due to the presence of a neighboring capsule. We also find a new dynamic behavior in which the capsules engage in a leap-frog motion. We then consider shear-induced diffusion of capsules in wall-bounded parabolic flows and show that this mechanism dominates over deformation-induced lateral migration.

In the second part of the chapter, we first consider the motion of an ellipsoidal capsule. It

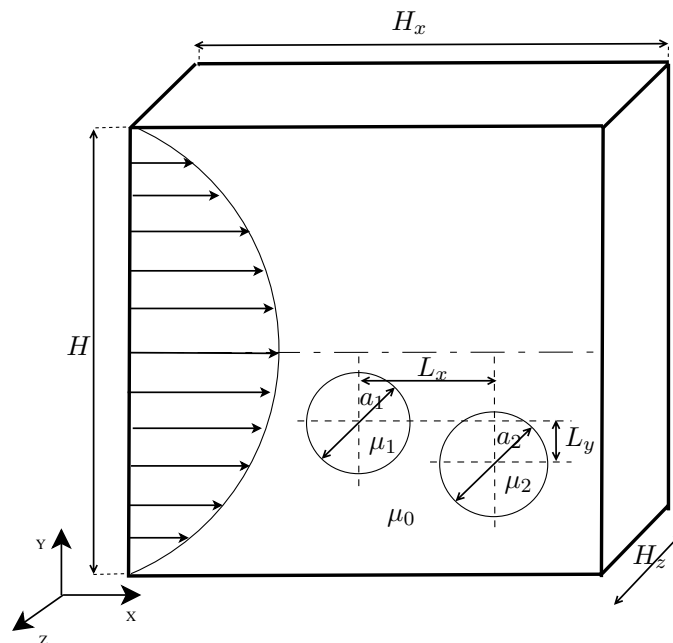


Figure 4.1: Schematic of the computational domain with capsules. The undisturbed flow is parabolic.

is shown that the ellipsoidal capsule undergoes tumbling motion while migrating away from the wall, as observed in experiments using erythrocytes in shear flow. The hydrodynamic interaction between a migrating capsule-pair is considered next. The leap-frog behavior and shear-induced diffusion, as observed for spherical capsule, are also present for ellipsoidal capsule, and hence, possibly, for erythrocytes.

4.2 Problem Setup

The flow configuration is described in figure 4.1 for a pair of closely spaced capsules in a channel. The fluid, both inside and outside of the capsules, is incompressible and Newtonian. The channel is periodic in the streamwise (x) direction, and in the z -direction. In the y -direction, the flow is bounded by two no-slip walls. In absence of the capsules, the flow is parabolic (Poiseuille flow), and is driven by a constant pressure gradient ∇P . The

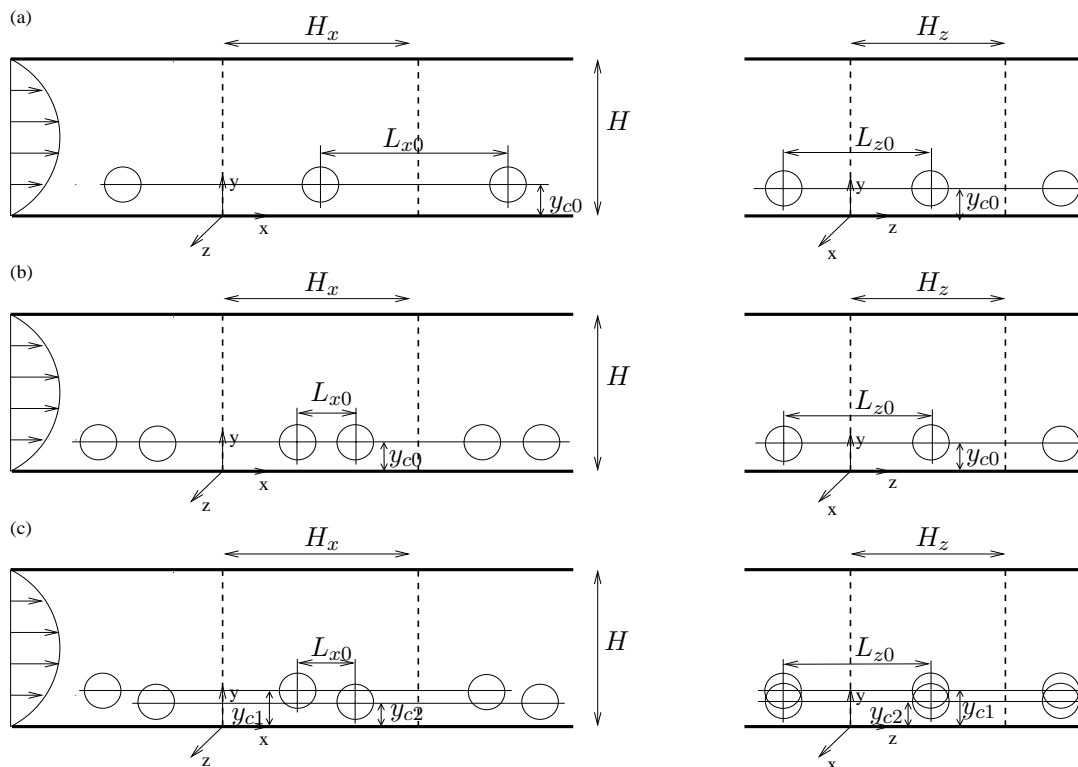


Figure 4.2: Schematic of the initial configuration of capsules in the domain for various cases (discussed in sections 4.3 and 4.3.1). The boundaries of the periodic domain are indicated by dashed lines. (a) Migration of an isolated capsule, (b) Interaction of two capsules separated axially and (c) Interaction of capsules separated both axially and laterally.

undeformed diameter of the capsule is denoted by a , and the height of the channel by H . The streamwise length of the channel is H_x and the length in the z direction is H_z . Note that the channel is periodic in x and z directions. In some of our computations $H_x = H_z = H$ for which the computation domain is a cube. The centerline velocity of the undisturbed parabolic flow is U_{cl} . The governing equations are made dimensionless using H as the characteristic length scale, U_{cl} as the velocity scale, and H/U_{cl} as the time scale. The dimensionless time is denoted by t^* . The major dimensionless parameters are: the capillary number $Ca = \mu_0 U_{cl} / Eh$ which is the ratio of the viscous force to the elastic force of the capsule membrane, ratio of the viscosity of the interior fluid to that of the exterior

fluid $\lambda = \mu_c/\mu_0$, and the size ratio a/H . Other geometric parameters are the initial lateral location of the centroid of a capsule y_{c0} , and the initial separation distance L_{x0} , L_{y0} , in the x and y directions respectively, between the centers of the two adjacent capsules. The instantaneous separation between the capsules is denoted by L_x and L_y . The Reynolds number of the capsules, $Re = \rho U_{cl} a / \mu_0$, is much less than unity.

Typical Eulerian resolution used in this study is $120 \times 120 \times 120$, and typical Lagrangian resolution used is 1280 triangular elements. In some cases, e.g. for capsules with high Ca and for an array of closely-spaced capsules, we use 5120 triangular elements, and $160 \times 160 \times 160$ Eulerian points. It should be mentioned that there should be sufficient resolution between the inter-capsule spacing in order to resolve the close range interaction between adjacent capsules. For the simulations presented here, we verify that there are at least six mesh points between the inter-capsule spacing. Dimensionless timestep used in the simulation is $\sim 10^{-3}$.

4.3 Results and Discussion

4.3.1 Capsule-Capsule interaction

A.1. Array of equispaced capsules with same y_{c0}

The results presented so far correspond to a single capsule in a cubic computation domain of dimensionless sides of unit length. The domain is periodic in the x and z directions. The configuration is equivalent to a series of capsules placed in a long channel at the same initial lateral location y_{c0} but with a separation distance of $L_{x0}/H = L_{z0}/H = 1$ between adjacent capsules in x and z directions (Figure 4.2). In this section we address the effect of changing the separation distance. Note that the x direction is the mean flow direction, and z direction is the direction of vorticity.

First, consider the effect of increasing the separation distance along the axial (x) direction. The z direction is still periodic over unit length. Figure 4.3 shows the time dependent

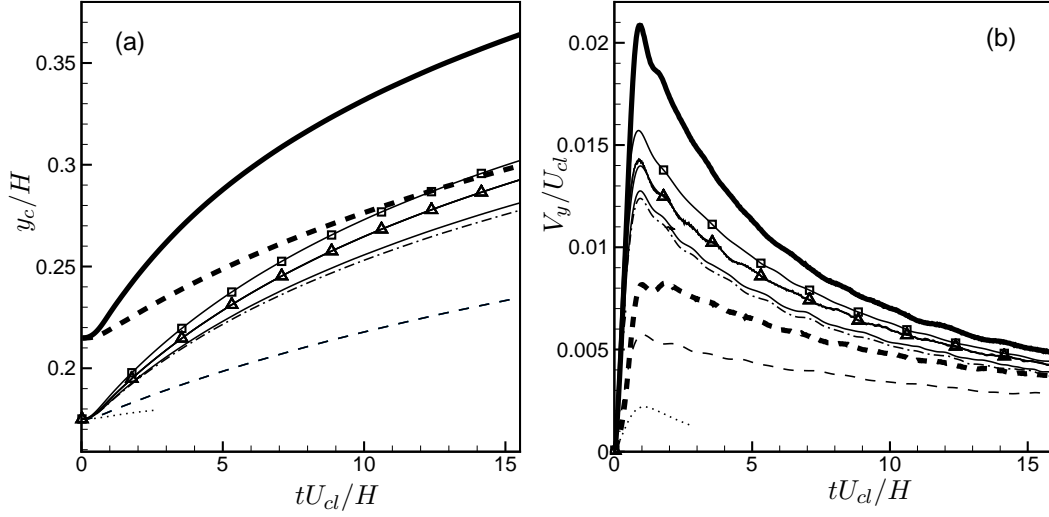


Figure 4.3: Migration of an array of equispaced capsules. Effect of capsule-to-capsule separation distance on (a) the lateral position and (b) migration velocity. Thin lines without symbols correspond to the array of capsules of size $a/H = 0.16$ spaced along the x -direction for which the following cases are shown: — $L_{x0}/H = 2$; - - - - $L_{x0}/H = 1$; - - - $L_{x0}/H = 1/3$; and $\cdots\cdots$ $L_{x0}/H = 1/5$. The thin lines with symbols correspond to the array of capsules of size $a/H = 0.16$ spaced along the z -direction for which the following cases are shown: — Δ — $L_{z0}/H = 1/3$; and — \square — $L_{z0}/H = 1/5$. The thick lines correspond to the array of capsules of size $a/H = 0.32$ spaced along the x -direction for which the following cases are shown: — $L_{x0}/H = 1$; and - - - - $L_{x0}/H = 1/2$. For all cases $\lambda = 1$ is considered. For $a/H = 0.16$, we considered $Ca = 0.4$, whereas for $a/H = 0.32$, we considered $Ca = 0.2$.

lateral position and velocity of the capsules as the intercapsule distance along the x direction is increased to $L_{x0}/H = 2$. For comparison, results corresponding to the separation distance $L_{x0}/H = 1$ are also plotted. It can be seen that when the separation distance is increased to $L_{x0}/H = 2$, the capsule velocity and the location of the center are only slightly affected compared to the results for the separation distance of $L_{x0}/H = 1$. Thus, it may be inferred that the results presented in the previous section using the periodic computation box of unit length are very close to those for a long channel.

Next, consider decreasing the capsule-to-capsule separation distance along the x direction. We have simulated two cases: $L_{x0}/H = 1/3$ and $1/5$ (figure 4.3). Again, the flow in

the z -direction remains periodic over unit length. We observe that decreasing the separation distance between the capsules results into a significant reduction in the migration rate. The case with $L_{x0}/H = 1/5$ was simulated with a higher Eulerian resolution of 160^3 to ensure that the region between two adjacent capsules is well resolved. Due to computational cost, this case is not simulated for a long time; however, the trend is sufficient to show that the migration rate is significantly reduced due to the reduction of the intercapsule distance. We also observe that all capsules in the array maintain the relative distance between them, and all of them migrate at the same rate during the course of their motion.

The results described above are for $a/H = 0.16$. We also considered the effect of increasing the capsule size to $a/H = 0.32$ (figure 4.3). Overall, same behavior is observed for both $a/H = 0.32$ and $a/H = 0.16$. Migration in case of $L_{x0}/H = 2$ is only marginally faster than that with $L_{x0}/H = 1$. Indeed the difference between the migration rates at $L_{x0}/H = 1$ and $L_{x0}/H = 2$ increases as a/H changes from 0.16 to 0.32, but the difference is not significant. When the intercapsule distance is decreased to $L_{x0}/H = 1/2$, we see a significant reduction in the migration velocity for $a/H = 0.32$, similar to the case for $a/H = 0.16$. In figure 4.3, we show only the results for $L_{x0}/H = 1/2$ for $a/H = 0.32$.

We note that Coulliette & Pozrikidis (1998) simulated motion of an array of drops placed at the same lateral position in a cylindrical tube, similar to the configuration considered here. Although they did not report the migration rate of the array, their results show that with decreasing separation distance the deformation of the drops is reduced. Similar trend is observed in our case, though the separation distance considered here is much lower than that considered in Coulliette & Pozrikidis (1998). Since the migration rate increases with increasing deformation, our results together with Coulliette & Pozrikidis (1998) suggest that a closely-spaced array along the mean flow direction has a reduced migration rate compared to that of an isolated capsule/drop.

Next we consider the effect of changing the separation distance L_{z0} along the z direction, which is the direction of vorticity. The periodicity in the x direction is now maintained at $L_{x0}/H = 1$. The lateral location and velocity are plotted in figure 4.3. We note that

increasing the separation distance in the z direction by a factor of two does not make any discernible change, and hence this case is not shown in the plot. However, reducing the separation in the z direction increases the migration velocity. This is in contrast to the reduction of migration velocity seen previously for the capsule array arranged along the mean flow direction.

The changes in migration velocity as seen above can be explained by considering the changes in deformation and tank-treading motion. The lateral migration depends on both tank-treading and deformation. For the capsule array along the x -direction, the tank-treading motion weakens as the spacing between the capsules decreases. This, combined with reduced deformation discussed earlier results into a reduction of the migration rate. In the case of the array spaced in z direction, the arrangement seems to approach the geometry of a cylindrical capsule along the z direction. This results into more blockage of the flow in the streamwise direction, and hence, possibly, a higher lift force, and higher migration rate. This observation is in agreement with the results of Mortazavi & Tryggvason (2000) who observed that the migration rate for a two-dimensional liquid drop is slightly higher than that for a three-dimensional drop.

In experiments using non-dilute suspension of red blood cells, Goldsmith (1971) observed that the lateral migration of the cells is reduced, and the formation of the cell-free region near the wall is hindered. Goldsmith attributed this reduction to the interaction with the neighboring particles providing an obstruction to lateral migration. The results from our simulations show that lateral motion could be reduced even for an array of capsules arranged along the mean flow direction and without any obstruction in the lateral direction.

A.2. Non-equispaced capsules

Next we consider an array of capsules arranged along the x direction, which are not separated by equal distance. Specifically, we consider two closely-spaced capsules with separation distance $L_{x0}/H \neq 1/2$. The flow is otherwise periodic over unit length in the x and z directions. The initial lateral locations y_{c0} of the two capsules are kept the same. The

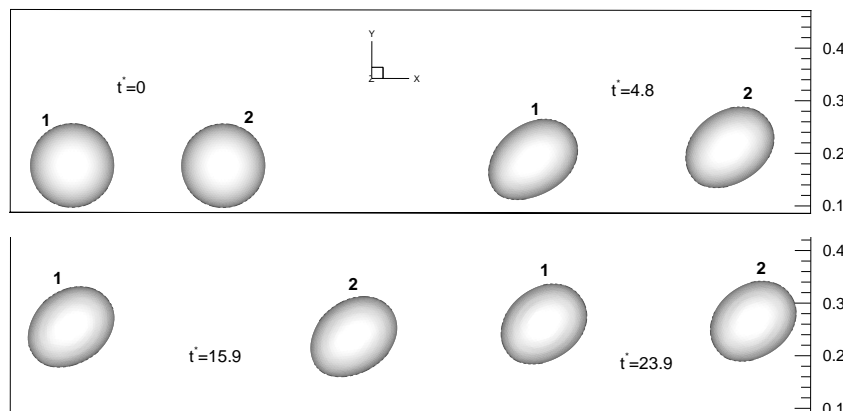


Figure 4.4: Migration of a pair of closely-spaced capsules with the same initial lateral locations of the centroids as discussed in Section A.2. Evolution of the capsule shape is shown. The parameters considered are $Ca = 0.2$ and $\lambda = 1$. Here $y_{c0}/H = 0.18$ for both capsules, and $L_{x0}/H = 0.29$.

arrangement and shapes of the capsules at time $t^* = 0$ and at later times are shown in figure 4.4. In the figure, the mean flow is from left to right. The upstream capsule is marked as ‘1’ and the downstream capsule as ‘2’.

The lateral positions, and migration velocities of the capsules are shown in figure 4.5. The results are markedly different compared to those of an equi-spaced arrangement. The capsules do not migrate simultaneously, and they do not have the same migration velocity. At the beginning, the downstream capsule migrates faster than the upstream capsule. In the process, the former moves closer to the center of the channel and attains a higher axial velocity. The separation distance between the capsules increases. As the downstream capsule 2 migrates toward the center, its migration velocity decreases, but at a rate faster than that of an isolated capsule. Meanwhile, the migration velocity of the upstream capsule 1 increases. Eventually the upstream capsule moves closer to the downstream capsule, and the separation distance between them decreases. The upstream capsule continues migrating and moves faster toward the center than the downstream capsule. Thus, a leap-frog process between the capsules is established. The leap-frog process keeps repeating as the capsules

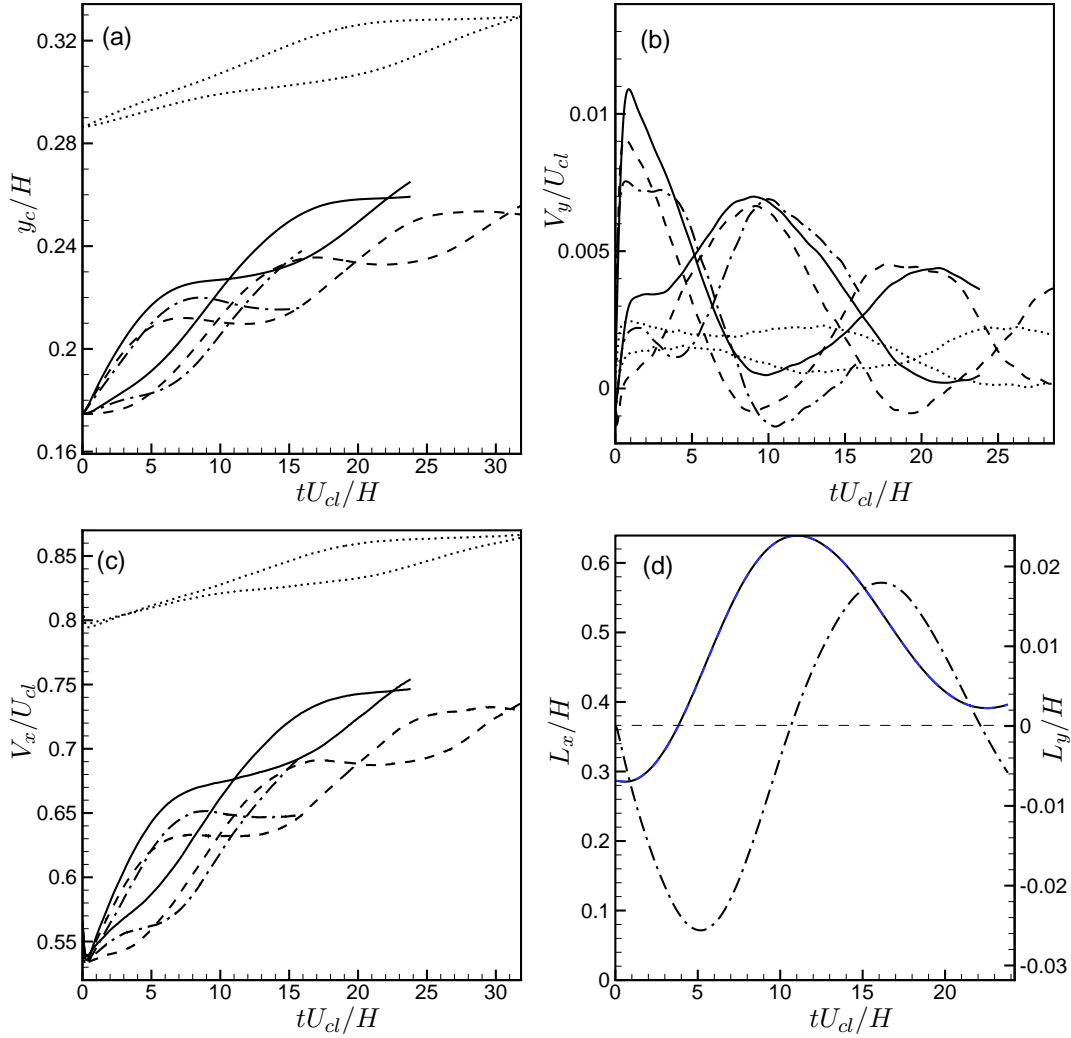
migrate toward the center of the channel. The leap-frog behavior of the capsules seen here has been reported earlier by Li & Pozrikidis (2000) for 2D simulation of liquid drops.

As shown in figure 4.5, the leap-frog behavior and crossover in the lateral positions of the capsules are observed for a wide range of parameters. Some of the simulations shown in the figure are performed over a long time to confirm that the behavior is persistent. The time to reach the first crossover, and the time between two crossovers are seen to depend on Ca and y_{c0} . As shown in figure 4.5a, a smaller Ca results into an early and more frequent crossover. A smaller y_{c0} , and hence close proximity to the wall, also has the same effect. The leap-frog behavior is less prominent as the initial location moves closer to the center. The earliest crossover occurs for the case of $Ca = 0.1$, $L_{x0}/H = 0.29$, and $y_{c0}/H = 0.18$ at time $t^* = 9.5$ when the capsules have traveled about 35 diameter along the axial direction. The slowest crossover occurs for capsules released at $y_{c0}/H = 0.29$, with the first crossover occurring at $t^* = 32$ when the capsules have traveled about 170 diameter in the axial direction.

Figures 4.5b and 4.5c show the lateral and axial velocities, respectively. The axial velocity shows similar leap-frog behavior. The lateral velocities for both capsules oscillate with time, but are opposite in phase. The result is also significantly different from that of an isolated capsule. Most strikingly, the lateral velocity components periodically attain negative values, in a few cases, implying that the capsules migrate toward the wall for some time during their motion. This is in stark contrast to the result for an isolated capsule, and for an array of equi-distant capsules, where the lateral velocity is observed to be always positive. In figure 4.5d, we show the time evolution of the absolute separation distance, and the lateral separation distance $y_{c,1} - y_{c,2}$ between the capsule centers. Clearly, the lateral separation distance, starting from zero at $t = 0$, oscillates about the zero mean. The absolute separation distance also oscillates.

A.3. Non-equispaced capsules with different y_{c0}

Next we consider two capsules with initial separation in the x direction as L_{x0} , same as before (section A.2), but also with an initial separation in the y direction as L_{y0} . The capsule



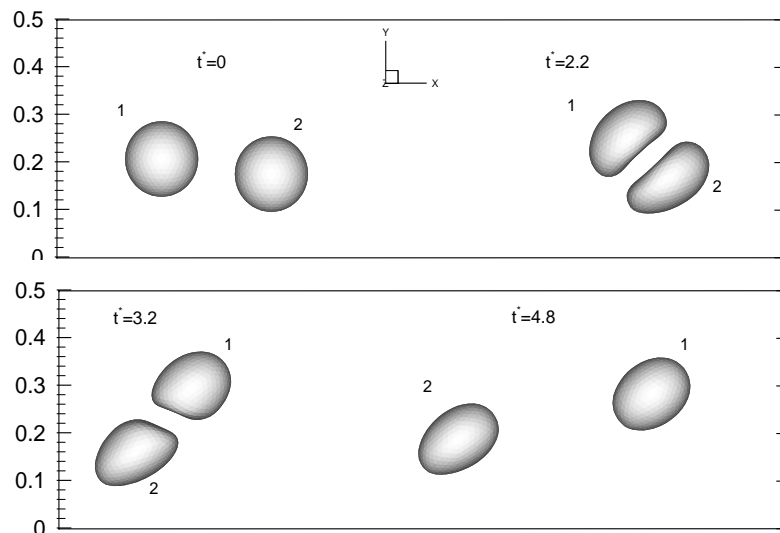


Figure 4.6: Migration of a pair of closely-spaced capsules with different initial lateral locations of the centroids as in Section A.3. The flow is from left to right. Here $y_{c0}/H = 0.21$ for the upstream (‘1’) capsule, and $y_{c0}/H = 0.18$ for the downstream (‘2’) capsule. Other parameters are: $L_{x0}/H = 0.29$, $Ca = 0.2$, and $\lambda = 1$. Shapes at $t^* = 0$ and at later times are shown.

pair is placed in the cubic box of unit length (figure 4.1). The flow is otherwise periodic in x and z directions. The capsule configurations at time $t = 0$ and at later times are shown in figure 4.6 for one case. The upstream capsule (‘1’) is located initially above the downstream (‘2’) capsule. As the flow starts, the upstream capsule moves over the downstream capsule, and the lateral distance between them increases. The interaction is repeated due to the periodicity in x , and the lateral separation between the capsules continues to increase while both capsules undergo a net migration toward the channel center.

The process shown in figure 4.6 is similar to the one observed for liquid drops in linear shear flows in previous studies, e.g. by Loewenberg & Hinch (1997) for three-dimensional liquid drops, and Charles & Pozrikidis (1998) for two-dimensional drops, and is the self-diffusion of deformable particles by pairwise interaction. In a linear shear flow, the pairwise interaction between two liquid drops results in an increased separation distance. The long time separation distance depends on the initial separation distance, viscosity ratio, and

weakly on the capillary number. Loewenberg & Hinch (1997) and Charles & Pozrikidis (1998) showed that the lateral separation distance decreases with increasing Ca , and λ . A recent study by Lac *et al.* (2007) reported that the hydrodynamic interaction between two capsules in simple shear flow also resulted in self-diffusion of the capsules, similar to liquid drops.

The lateral position, velocity, and separation distance between the capsules are shown in figure 4.7. Results suggest that the migration is dominated by self-diffusion. Also shown are the lateral positions of single capsules starting from the same initial position. The pairwise interaction results into an increase in the migration rate for the upstream capsule 1, and a decrease for the downstream capsule 2. Though the pair has a net migration toward the channel center, both capsules periodically attain negative lateral velocity. The peak in the lateral velocity of the initially upstream capsule could be an order of magnitude higher than the migration velocity of an isolated capsule. Also note that for an isolated capsule, deformation-induced lateral migration strongly depends on the capillary number (Chapter 3, figure 3.4a). For the case of the capsule-pair, the additional displacement due to pairwise interaction does not strongly depend on the capillary number (figure 4.7c), which is in agreement with the observation of Loewenberg & Hinch (1997) for liquid drops. As the lateral separation distance increases with time, the pairwise interaction weakens. Similar results have been observed in our simulations for larger capsule size with $a/H = 0.32$.

Previously in figure 4.3, we studied the effect of decreasing the axial spacings L_{x0} between the capsules that are arranged in an array along the flow (x) direction. The initial lateral positions of the centers y_{c0} of all capsules were kept the same. We observed that for equi-spaced arrangement, decreasing the spacing L_{x0} between the capsules results into a reduction of the lateral velocity. We now consider similar arrangement for capsule-pairs as shown in figure 4.8. Instead of one pair of capsules, we now consider two pairs with pair-to-pair separation of $L = H/2$. It is interesting to note that reducing the separation distance between the capsule-pairs does not inhibit migration. On the contrary, an increased dispersion of the capsules due to more frequent interactions is observed. Capsules located

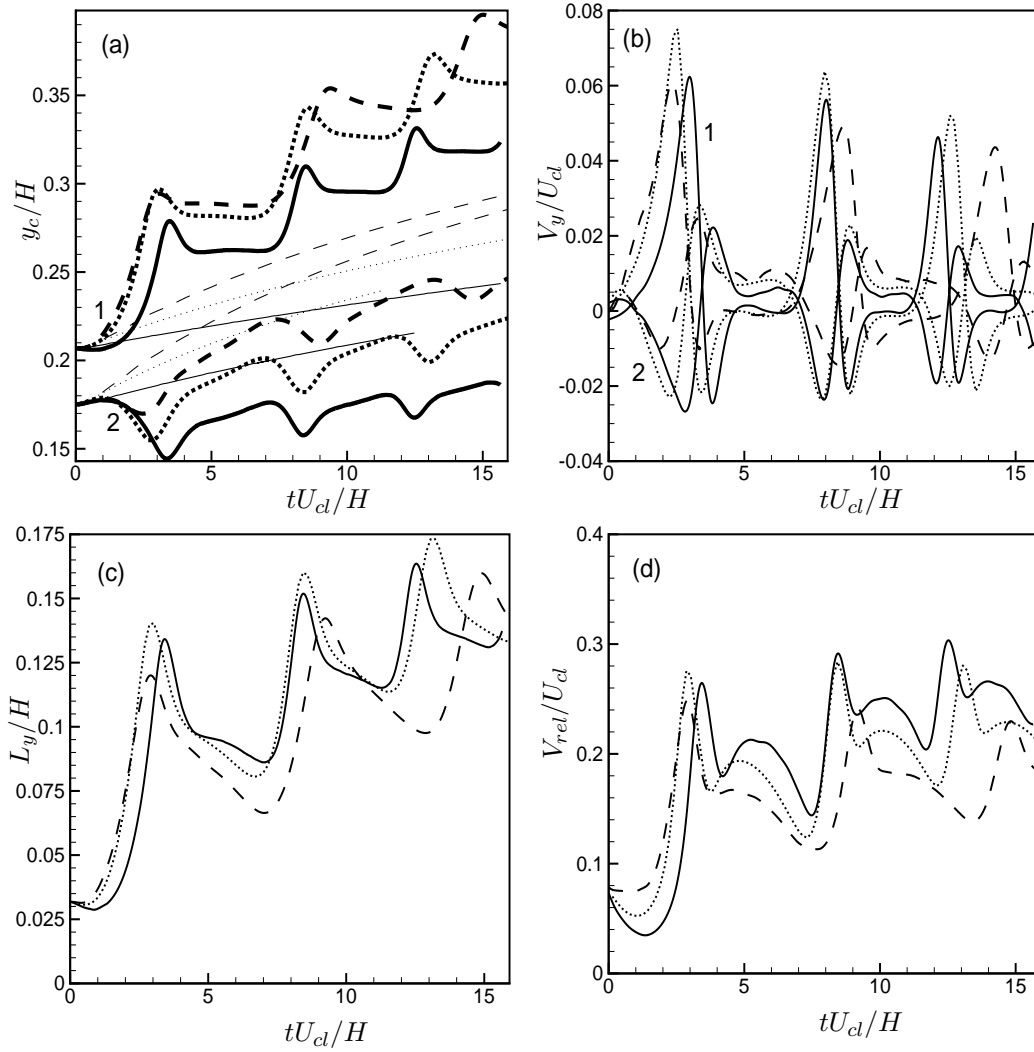


Figure 4.7: Migration of a pair of closely-spaced capsules with different initial lateral locations of the centroids as shown in figure 9. Lateral position and lateral velocity are shown in (a) and (b). The lateral separation distance between the capsules, and the relative velocity between them are shown in (c) and (d), respectively. For all figures following line patterns are used: \cdots $\lambda = 1, Ca = 0.2$; $---$ $\lambda = 1, Ca = 0.8$; and $—$ $\lambda = 5, Ca = 0.2$. In (a) thin lines correspond to the results of an isolated capsule, and the thick lines for the capsule-pairs. In (b) to (d) only the results for the capsule-pairs are shown. In (a) and (b), results for both upstream and downstream capsules marked by '1' and '2' are shown.

closer to the center move faster toward the center, while those located closer to the wall show no significant center-ward motion. Increased interaction also results in more oscillations in the lateral velocity which periodically becomes negative for all capsules.

A.4. Non-identical capsules

So far we have considered capsules of identical Ca and a/H . We now extend our simulation of the foregoing configuration to consider non-identical capsules. In particular, we consider two capsules forming the pair having different Ca and a/H . This case has relevance for the study of bi- and poly-disperse suspensions. The effect of non-identical Ca is shown in figure 4.9. Two cases are considered here: (i) the upstream capsule (‘1’) with $Ca = 0.2$, and the downstream capsule (‘2’) with $Ca = 0.8$, and (ii) vice versa. The upstream capsule is released at a lateral location slightly closer to the channel center. Migration of an isolated capsule for identical parameters is also shown for comparison.

Consider the case (i) first. In absence of the pairwise interaction, the results for isolated capsules suggest that the downstream capsule with $Ca = 0.8$ would have a higher migration rate than the upstream capsule with $Ca = 0.2$. Due to the pairwise interaction, on the contrary, the upstream capsule has a much higher migration rate, and it moves faster toward the channel center. The migration of the downstream capsule, though somewhat reduced, seems to be less affected compared to that of an isolated capsule. Interestingly, the upstream capsule shows negative lateral velocity over a significant fraction of the time during the course of its motion. For the case (ii), capsule 1 has higher migration rate, and capsule 2 has lower migration rate, as expected, based on the results for the isolated capsules.

Several interesting observations can be made in figure 4.9. First, the net migration for the pair is higher in case (i) than in case (ii). Second, the lateral separation between the capsules is higher for case (ii). Further, the frequency of encounter between the capsule is higher in the case (ii) than in the case (i). Also note that for a capsule-pair with similar Ca , the local maxima in the lateral position of the upstream capsule and the local minima

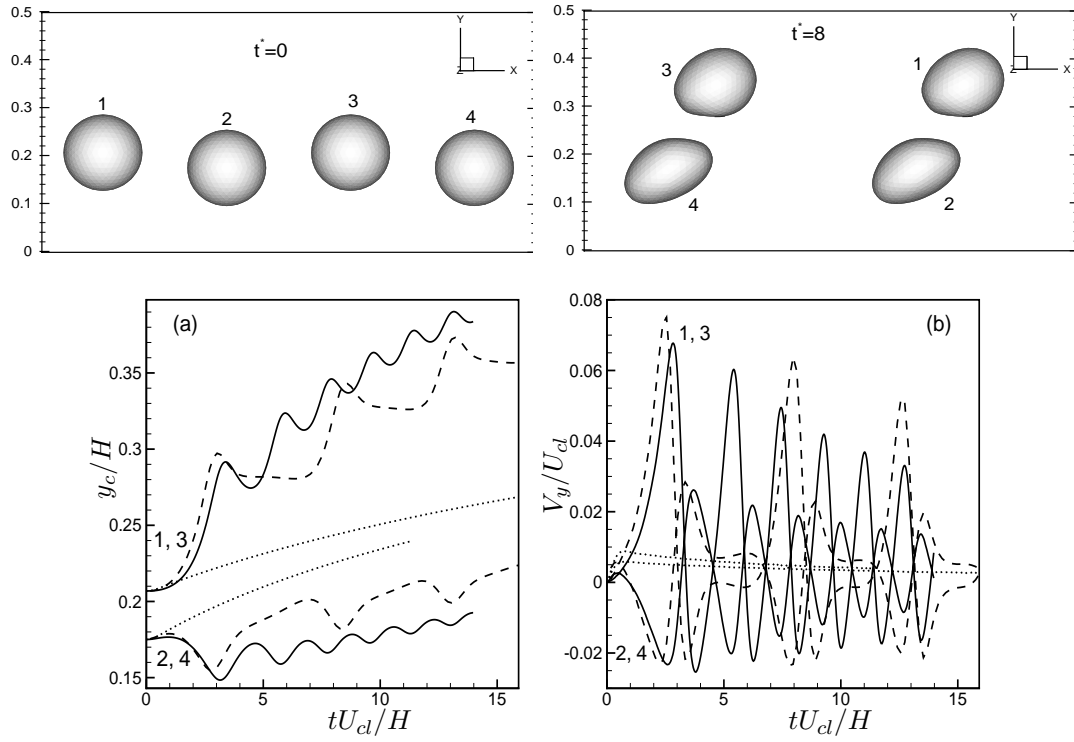


Figure 4.8: Effect of increasing the number of capsule-pairs. Top Panel: Initial configuration and shapes at $t^*=8$. Here $Ca = 0.2$ and $\lambda = 1$ are considered. The lateral positions and velocities are shown in (a) and (b), respectively. The results of a single capsule-pair (from figure 4.7) and of an isolated capsule are also shown for comparison. Line patterns used for (a) and (b) are as follows: — four capsules; - - - a capsule-pair; and ····· an isolated capsule. For the case of four capsules, lateral location and velocity of ‘1’ and ‘2’ coincide with those of ‘3’ and ‘4’, respectively.

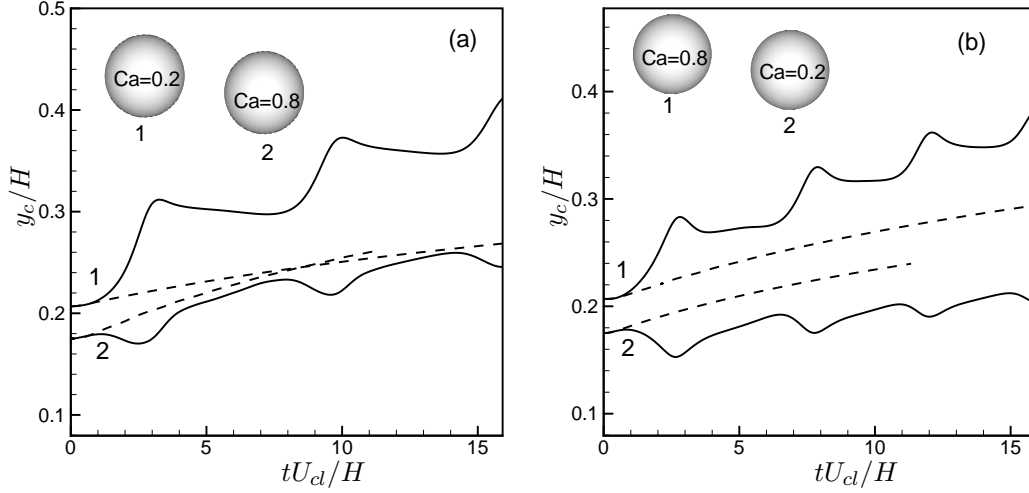


Figure 4.9: Migration of a pair of non-identical capsules (Section A.4). Effect of different Ca is considered. Lateral position versus time is shown for the capsule-pair (solid line), and for an 'isolated' capsule (dash line) released from the same initial location and with the same parameters. (a) (case i) The upstream capsule has $Ca = 0.2$, and the downstream capsule has $Ca = 0.8$. (b) (case ii) The upstream capsule has $Ca = 0.8$, and downstream capsule has $Ca = 0.2$. Here $\lambda = 1$ and $a/H = 0.16$ for all cases shown.

in that of the downstream capsule occur nearly at the same time. For the non-identical pair shown in figure 4.9a for the case (i), the maxima and minima do not occur at the same time. These observations suggest that the pairwise interaction between bi-disperse capsules, even in linear shear flow, may have some features different from mono-disperse capsules.

Effect of dissimilar a/H is presented in figure 4.10. Here we consider two cases: (i) the upstream capsule with $a/H = 0.16$, and the downstream capsule with $a/H = 0.32$, and (ii) vice versa. The Ca for both capsules is fixed at 0.2. For cases (i) and (ii), the centroid of the downstream capsule is initially located closer to the wall than that of the upstream capsule. Consider the case (i) first. As the flow starts, the capsules deform. The smaller capsule assumes an ellipsoid shape, while the larger one assumes a tear-drop shape. As the capsules approach each other, a flat contact area is formed. The ellipsoidal/tear-drop shapes are recovered when the capsules move apart. As the upstream smaller capsule tries to move over the larger downstream capsule, the former is dispersed toward the center by

the latter. Thus the migration of the smaller capsule is strongly affected by the capsule-capsule interaction and is significantly different from that of an isolated capsule. Large oscillations in the lateral position and velocity of the smaller capsule can be seen in the figure. On the contrary, migration of the larger capsule is not significantly affected by the pairwise interaction, and is similar to that of an isolated capsule. We have continued the simulation for a long time until $t^* = 40$. Over a long time the smaller capsule is dispersed toward the opposite wall as the larger capsule approaches the center. In absence of the pairwise interaction, the smaller capsule would have remained closer to the bottom wall for an extended time. The result suggests that for a bi-disperse suspension, significant dispersion and mixing may arise due to pairwise interaction. For the reverse arrangement of the capsule-pair (case ii), the net migration rate of the larger capsule is now higher than that of an isolated capsule. However, the pairwise interaction does make an effect on the larger capsule which is reflected in the increased oscillations in its lateral locations. The migration of the smaller capsule is significantly affected. After time $t^* = 16$, the smaller capsule seems to have made nearly no net lateral migration.

An interesting feature of figures 4.7–4.10 is the number of local maxima/minima in the lateral positions of the upstream/downstream capsules. The maxima/minima represents an encounter between the capsules. In a given time t , the number of encounters depend on the initial location, capillary number, viscosity ratio, and the capsule size. More frequent encounters result into more lateral dispersion. To facilitate discussion, we plot the lateral separation distance L_y between the centroids of the capsules in figure 4.7c. A maximum in L_y is considered as an encounter between the capsules. First we note that the first encounter between the capsules occurs earlier for the case of $\lambda = 1, Ca = 0.8$ than that for the case of $\lambda = 5, Ca = 0.2$. Moreover, the local maxima in the lateral separation decreases with increasing Ca and λ . These results are consistent with those of Loewenberg & Hinch (1997) for pairwise interaction between liquid drops in a linear shear flow. However, as the simulations continue for longer time, somewhat different behavior is observed. First we note that the time interval between two encounters gradually decreases. Also, the number

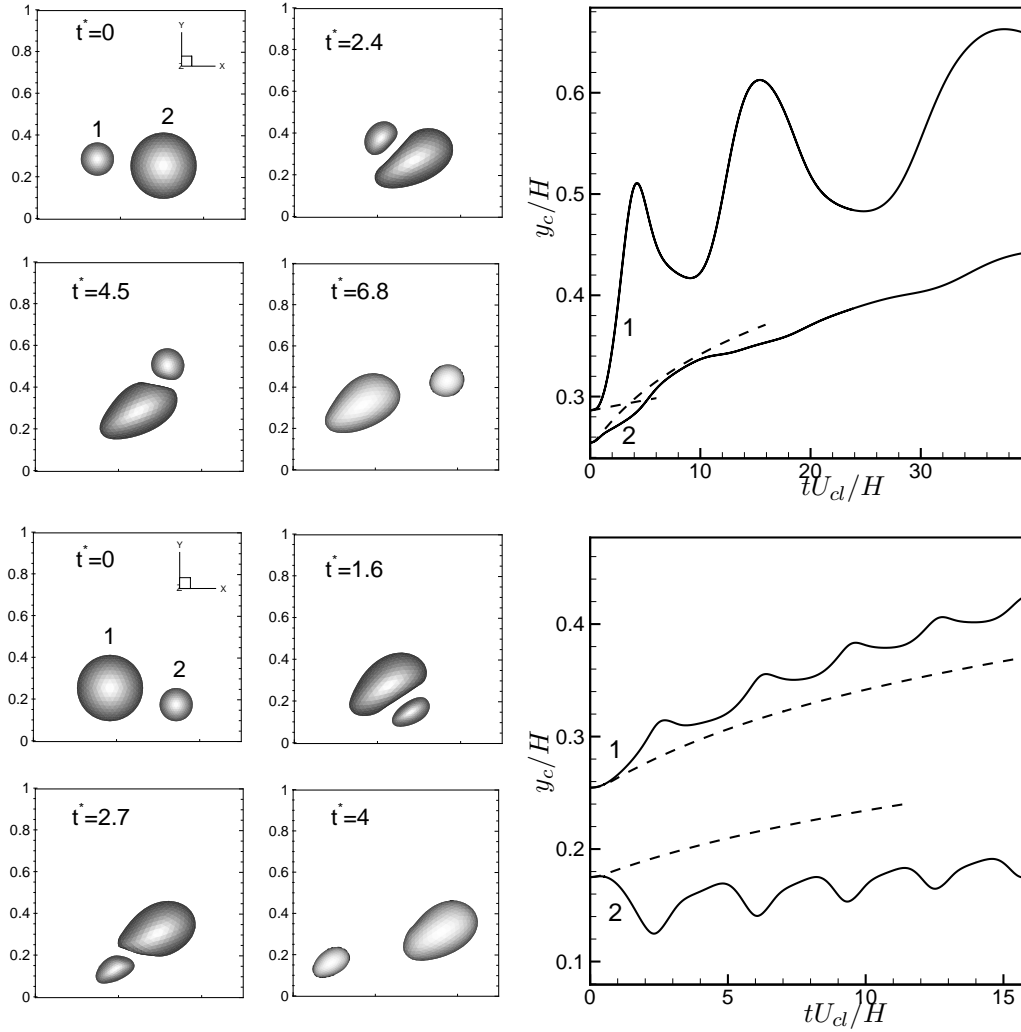


Figure 4.10: Migration of a pair of non-identical capsules (Section A.4). Effect of dissimilar a/H is considered. For the larger capsule $a/H = 0.32$, and for the smaller one $a/H = 0.16$. The figures on the left show the capsule shapes at various times. The figures on the right show the lateral positions versus time. Solid lines are for the case of the capsule pair. Dashed lines correspond to the result of an ‘isolated’ capsule released from the same location with similar parameters. Here $\lambda = 1$ and $Ca = 0.2$ for all cases.

of encounters decreases with increasing Ca and decreasing λ . Thus, although the pair with $\lambda = 5$ has the slowest approach rate for the first encounter, it shows more frequent encounter over a long time.

The number of encounters between the capsules in a time window depends on the relative velocity between them. A higher relative velocity results into more frequent encounters. In figure 4.7d, the relative velocity between the capsule centers is shown for various cases. The relative velocity shows a complex behavior with time. In figure 4.7d, for $t^* > 5$, the relative velocity is lower for a more deformable capsule pair. A capsule-pair with higher Ca and lower λ has a higher net migration rate toward the center. As seen in figure 4.7a, at a given time t^* , a capsule-pair with higher Ca and lower λ is located closer to the center. Because of the parabolic nature of the undisturbed velocity profile, this pair will have a lower relative velocity than a pair located closer to the wall. Hence, the number of encounters between the capsules decreases with increasing Ca and decreasing λ .

The relative velocity between the capsules is strongly affected for the non-identical capsules of varying sizes (not shown in figure). It is higher when the larger capsule is closer to the channel center than the smaller capsule. Thus the highest number of encounters over a given time is observed in figure 4.10 with the larger capsule located initially slightly above the smaller one. The case of non-identical Ca also shows similar trend; higher number of encounters is seen when the more deformable capsule in the pair is placed closer to the center of the channel resulting into a greater relative velocity between the pair (figure 4.9b).

4.3.2 Ellipsoidal capsules

In this section we consider capsules with ellipsoidal undeformed shape. The ellipsoidal shape somewhat resembles the deformed state of a red blood cell in a shear flow (see, e.g., Secomb 2003). In a shear flow, an isolated red blood cell undergoes a tank-treading and/or tumbling motion. The transition between the two modes depends on the aspect ratio of the ellipsoid and the viscosity ratio λ (Keller & Skalak 1982, Ramanujan & Pozrikidis 1998). In the present simulation with ellipsoids, the aspect ratio is taken as 2. The initial inclination

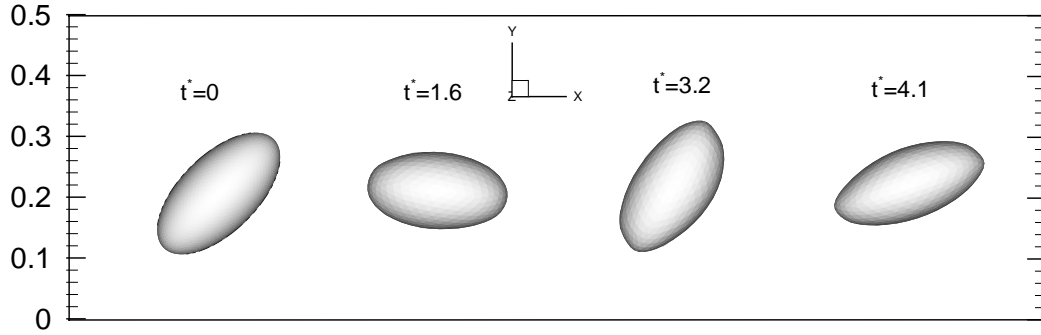


Figure 4.11: Migration of an isolated ellipsoidal capsule. Here $y/H = 0$ is the bottom wall of the channel, and $y/H = 0.5$ is the center. Initial shape and deformed shapes at later times are shown. The flow is from left to right. The figure corresponds to $\lambda = 5$, and $Ca = 0.2$.

angle of the major axis is at 45° with the flow. The volume of the ellipsoid is the same as that of a spherical capsule with $a/H = 0.16$. The simulations are performed with 160^3 Eulerian grids, and 5120 triangular elements on the surface of the ellipsoid. Note that the present model for the capsule membrane using neo-Hookean law does not exactly resemble a red blood cell membrane. The objective here is to see to what extent the lateral motion of an ellipsoid is affected due to its initial shape, as well as due to simultaneous tank-treading and tumbling motions.

An isolated ellipsoidal capsule in a parabolic flow is considered first. The capsule shape at $t^* = 0$ and at later times are shown in figure 4.11 for $Ca = 0.2, \lambda = 5$. The capsule is released at $t^* = 0$ at $y_{c0}/H = 0.21$. As the flow starts, the tumbling motion of the ellipsoid sets in while it migrates toward the center of the channel. The rotation of the ellipsoid coincides with the direction of vorticity of the undisturbed flow. The instantaneous angular orientation θ of the major axis with the mean flow direction is shown in figure 4.12c. It is of interest to compare the present results with the simulations of Pozrikidis (1995) and Ramanujan & Pozrikidis (1998). In these studies, dynamics of ellipsoidal capsules in unbounded linear shear flow are considered. Pozrikidis (1995) observed that for an ellipsoidal capsule at $\lambda = 1$, a steady orientation at $\theta = 0.13\pi$ is attained while the capsule

undergoes tank-treading motion. Tumbling motion is absent for $\lambda = 1$. Ramanujan & Pozrikidis (1998) considered the effect of λ and observed that the tumbling motion is present for an aspect ratio 2 and $\lambda \geq 5$. The results from our simulations as presented in figure 4.12c show that the tumbling motion is possible even for $\lambda = 1$. The difference between the present observation and that of Pozrikidis (1995) and Ramanujan & Pozrikidis (1998) is possibly due to the lateral migration of the capsule, and the presence of the wall.

Lateral position and velocity of the ellipsoidal capsules are shown in figures 4.12a & b. Four different cases are considered: (a) an isolated ellipsoidal capsule with $Ca = 0.2$ and $\lambda = 1$; (b) a spherical capsule with $Ca = 0.2$ and $\lambda = 1$; (c) an isolated ellipsoidal capsule with $Ca = 0.2$ and $\lambda = 5$; and (d) an array of ellipsoidal capsules with $Ca = 0.2$ and $\lambda = 1$ arranged along the streamwise direction with center-to-center separation distance $L_{x0} = H/3$. First, we note that the lateral position of an isolated ellipsoid is higher, though not significantly, than that of the spherical capsule for the same values of Ca and λ , implying that the tumbling motion, and the initial shape do not strongly affect the net migration. The migration velocity (figure 4.12b) shows oscillations due to the tumbling motion. It has a local maxima when the inclination angle $\theta = 90^\circ$, and a minima when $\theta = 0^\circ$. The frequency of oscillations slowly decreases as the capsule migrates away from the wall to regions with lower shear rate. The decrease is consistent with the theory of rotation of a perfectly rigid ellipsoid in Stokes flow, that is, the rotation rate is proportional to the shear rate (Jeffery 1922). Oscillations in the lateral velocity result into small undulations in the lateral position. However, the capsule always migrates toward the center irrespective of the instantaneous orientation angle. The effect of increased viscosity ratio at $\lambda = 5$ is to reduce the migration rate due to the reduced deformation of the capsule. The effect of reduced separation distance between the capsules is also to reduce the migration rate, similar to the earlier observation for the spherical capsules. Interestingly, the reduction of the spacings between the capsules does not prevent the tumbling motion. However, with time, the frequency of rotation of the ellipsoid array decreases faster than that of an isolated ellipsoid, though the array is instantaneously located closer to the wall due to its slower

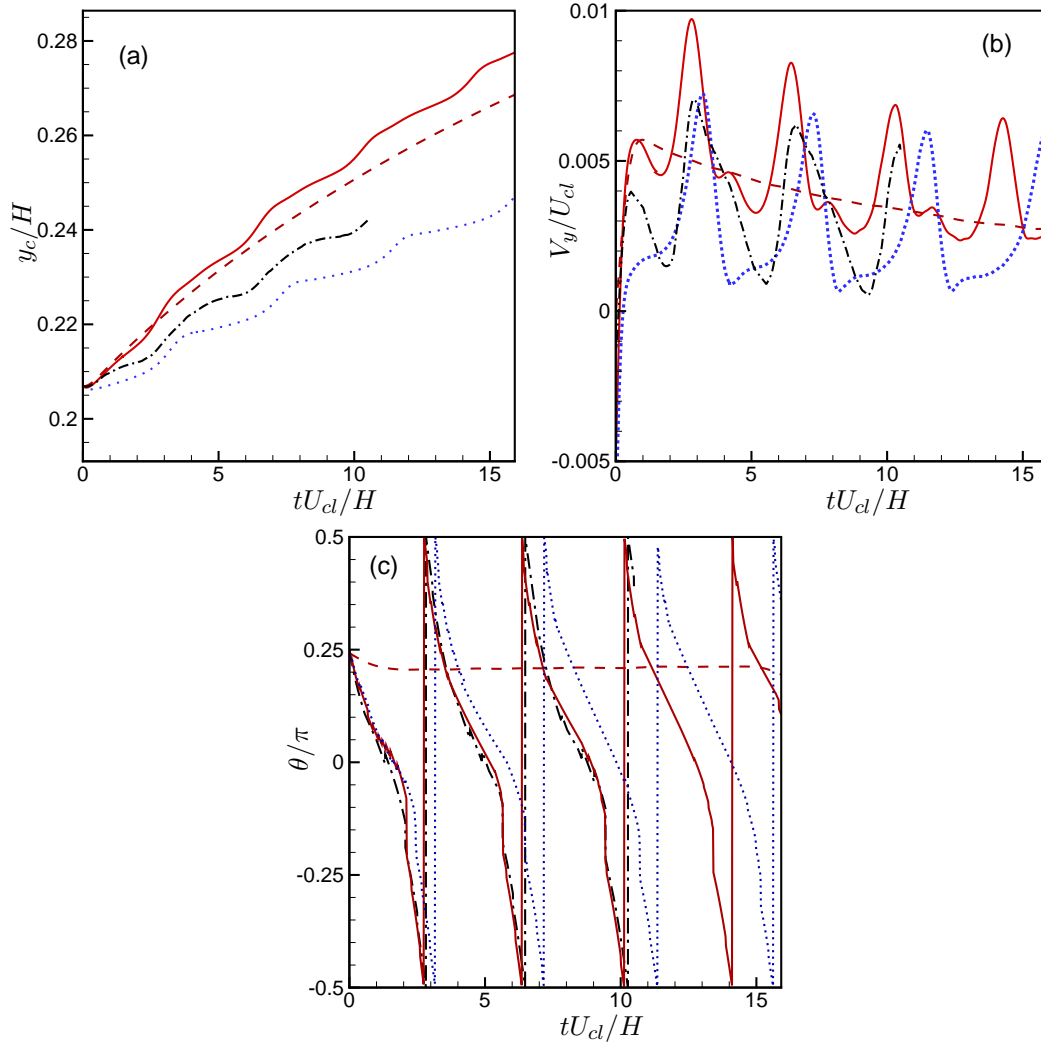


Figure 4.12: Migration of ellipsoidal capsules. (a) Lateral position, (b) lateral velocity, and (c) instantaneous orientation of the major axis of the capsule versus time are shown. For all cases $Ca = 0.2$. Line patterns used here are as follows: — isolated ellipsoid with $\lambda = 1$; - - - - - isolated sphere having the same volume and $\lambda = 1$; ····· isolated ellipsoid with $\lambda = 5$; and ·-·-·, an array of ellipsoids arranged along the x-direction with center-to-center distance $L_{x0} = H/3$ and $\lambda = 1$.

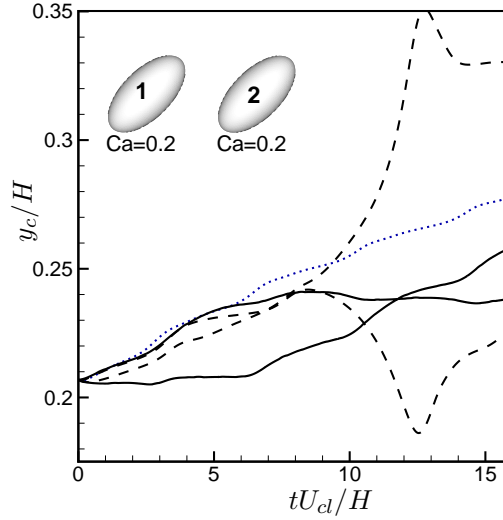


Figure 4.13: Migration of a pair of closely-spaced ellipsoids with their centroids located initially at the same lateral position $y_{c0}/H = 0.21$. Line patterns used are as follows: --- $\lambda = 1$; — $\lambda = 5$. Also shown is the result for an isolated ellipsoid (\cdots) at $\lambda = 1$. For all cases $Ca = 0.2$.

migration.

Pairwise interaction of ellipsoids is considered in figures 4.13 to 4.14. Two initial configurations are considered which are similar to those for the spherical capsules: (a) two ellipsoids placed at the same lateral distance $y_{c0}/H = 0.21$, but separated along the axial direction by $L_{x0}/H = 0.29$, and (b) two ellipsoids with axial separation of $L_{x0}/H = 0.32$, and lateral separation of $L_y/H = 0.03$. For the case (a) as shown in figure 4.13, the leap-frog behavior of the ellipsoids at $\lambda = 5$ is evident. For $\lambda = 1$, the leap-frog motion is absent at the beginning, and the ellipsoids migrate maintaining nearly the same lateral position. At around $t^* = 8$, the pairwise interaction sets in, and self-diffusive type of motion is observed.

For the case (b) as shown in figure 4.14a, results are more closer to the spherical capsule cases for both $\lambda = 1$ and 5. The lateral motion of the ellipsoids is strongly affected by the pairwise interaction. The upstream capsule having its centroid located further away from the wall is strongly displaced toward the center of the channel. The center-ward motion of

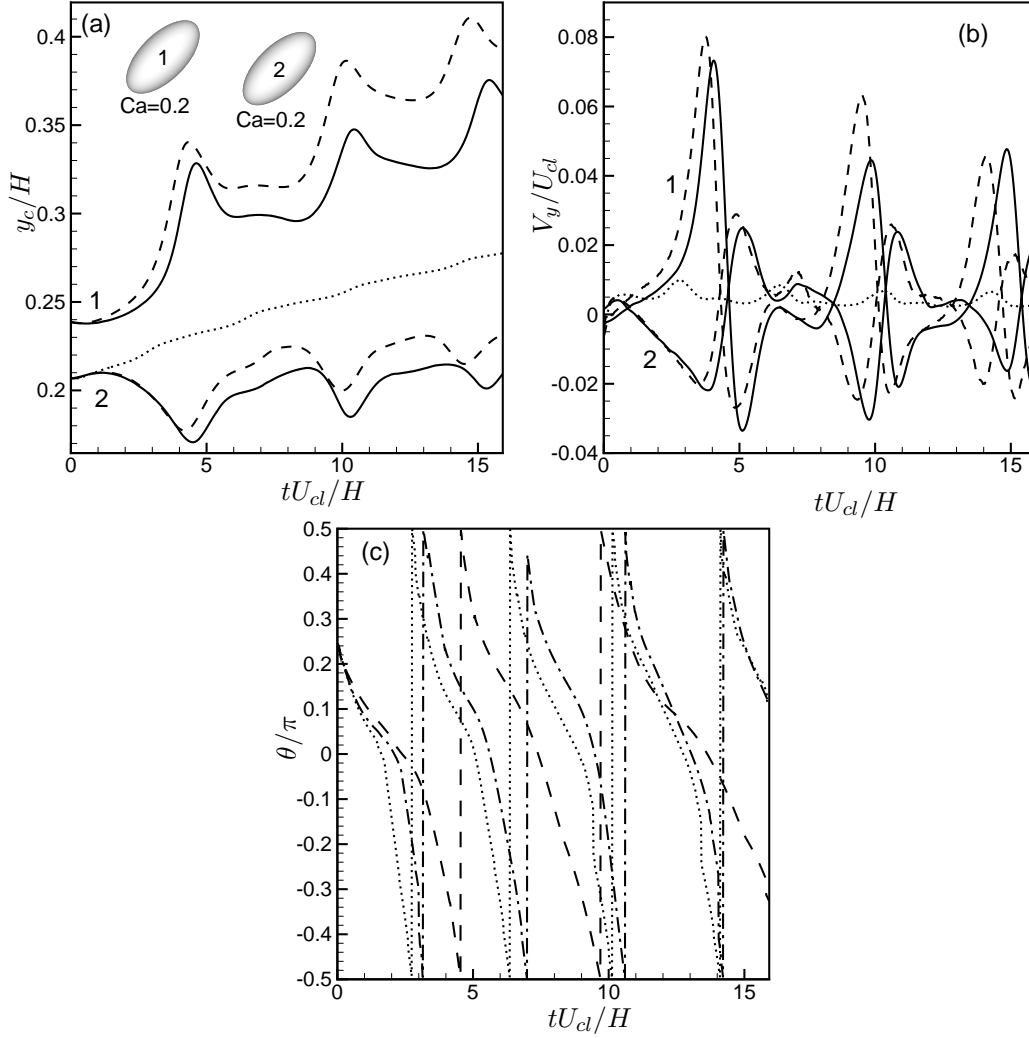


Figure 4.14: Lateral migration of a pair of closely-spaced ellipsoids with their centroids located initially at different lateral positions. Shown here are (a) lateral location, (b) lateral velocity, and (c) instantaneous angular orientation. The line patterns used in (a) and (b) are as follows: $---$ $\lambda = 1$; $—$ $\lambda = 5$. Also shown is the result of an isolated capsule (\cdots) for $\lambda = 1$. In plot (c), angular orientation for only $\lambda = 1$ case is shown, where $---$ represents the upstream capsule, $- - - -$ the downstream capsule, and \cdots represents an isolated capsule. For all cases, $Ca = 0.2$.

the downstream capsule is significantly hindered. For $\lambda = 5$, the downstream capsule shows no significant lateral motion, and it oscillates about a nearly steady mean position. The lateral velocity becomes periodically negative for both ellipsoids, though the net migration of the pair is still toward the center of the channel. The ellipsoid-pair with $\lambda = 5$ migrates slower than the $\lambda = 1$ pair. Tumbling of the capsules is observed here, however it does not seem to have a significant effect on the net migration. The frequency of tumbling of the upstream capsule is lower than that of the downstream capsule. The latter tumbles nearly at the same rate as that of an isolated ellipsoid. The frequency of encounter between the ellipsoids for $\lambda = 1$ case is nearly the same as that for spherical capsules with similar Ca , while it is slightly less for $\lambda = 5$.

4.4 Conclusion

The effect of neighboring capsule on lateral migration is studied by considering a pair of ellipsoidal and spherical capsules in a wall-bounded pressure driven parabolic flow in a channel in absence of inertia. Simulations have been performed for a range of Ca , viscosity ratios and capsule-to-channel size ratio. First, we consider an equispaced array of capsules in the flow direction, and investigate the effect of separation distance on migration velocity. It is found that the rate of migration reduces as the separation distance decreases. However, when the array of capsules is in the vorticity direction, a reversal of trend is obtained, where the rate of migration increases as the separation distance decreases. On the other hand, in both these cases, increasing the separation distance after two periodic domain lengths does not change the migration velocity appreciably. Next, when an array of non-equispaced capsules is considered in the flow direction, an interesting leap-frog behavior is noticed due to the crossover of the capsules, which has no similarity compared to the migration of an isolated capsule. Also, the interaction of non-identical capsules is observed. This is relevant in the case of bi or polydisperse suspensions. In the case of interaction of ellipsoids, the lateral migration is strongly affected by the interaction between them. When the pairwise interaction sets in, a self-diffusive type of motion is observed. By focusing on the motion of

an isolated capsule and interacting capsule pairs, this study forms the basis for the study of interaction between multiple capsules in the case of suspensions.

Chapter 5

Effect of Inertia on the Hydrodynamic Interaction between Two Liquid Capsules in Simple Shear Flow

5.1 Introduction

When two particles are released in a shear flow with different velocities, they first approach, and then roll over each other. If the particles are rigid spheres with zero inertia, then the interaction is reversible, that is, the particles follow the same trajectories when the shear flow is reversed. If the particles are deformable, however, the interaction results into an irreversible trajectory. The separation distance between the particles in the velocity gradient direction is higher after the interaction than before the interaction (Figure 5.1). The phenomenon is termed as shear-induced self-diffusion, and it plays an important role in mixing and microstructural evolution of suspension (Loewenberg & Hinch 1997; Guido & Simeone 1998).

Shear-induced self-diffusion has been mostly studied in the case of suspension of rigid spherical particles. Batchelor & Green (1972) studied the interaction between two rigid spheres in a linear flow, and showed that the trajectories of one sphere relative to the other could be closed (i.e. they do not extend to infinity). The existence of closed trajectories for a pair of spheres was experimentally observed by Darabaner & Mason (1967). If the spheres are perfectly smooth, interaction between a pair of them does not lead to self-diffusion. Self-diffusion of rigid spheres is possible when more than two spheres are present (Acrivos *et al.* 1992; Wang *et al.* 1996), or surface roughness is introduced (Da Cunha & Hinch 1996). Experimental measurements on shear-induced self-diffusion of rigid particles have been obtained by Eckstein *et al.* (1977), Leighton & Acrivos (1987), Chang & Powell

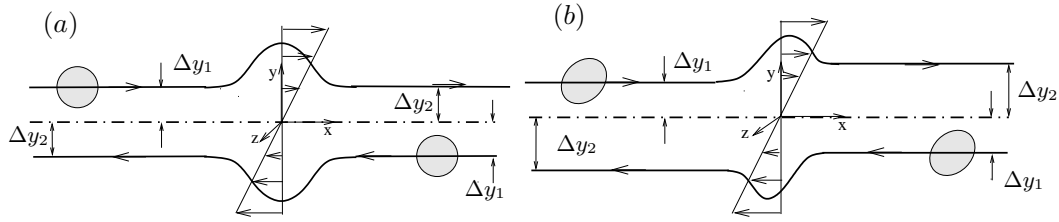


Figure 5.1: Schematic of interaction of a pair of rigid and deformable bodies in shear flow: (a) rigid, and (b) deformable. Here Δy_1 and Δy_2 are the initial and final lateral distances of the bodies.

(1994), and Breedveld *et al.* (1998, 2001). Theoretical and numerical studies on shear-induced diffusion of rigid particles have been considered by Brady & Bossis (1985), Brady & Morris (1997), Foss & Brady (1999), Marchioro & Acrivos (2001), Drazer *et al.* (2002), and Sierou & Brady (2004).

The works mentioned above are all in the limit of Stokes flow. The presence of inertia is expected to affect the interaction between a pair of liquid drops/capsules/rigid spheres, as well as the shear-induced diffusion mechanism. Interaction between a pair of liquid drops in presence of inertia has been extensively studied. These studies are complicated by the fact that the drops often coalesce or break upon interaction at high inertia. Depending on the nature of the coalescence and breakup, various regimes of collision can be identified. Here we avoid the discussion on drop-drop collision, and refer to some recent papers by, for example, Pigeonneau & Feuillebois (2002), Qian & Law (1997), Wang *et al.* (1994), Ashgriz & Poo (1990), Nobari & Tryggvason (1996), Brenn & Kolobaric (2006), Pan & Suga (2005), and Roisman (2004), among others, which give excellent accounts on the subject. We note, however, that the shear-induced diffusion process for non-coalescing and non-breaking liquid drops *in presence of inertia* has not been studied. So is the case for liquid capsules. As for rigid particles, Kromkamp *et al.* (2005) studied pairwise interaction between two circular particles in a shear flow at finite but small inertia. Kromkamp *et al.* (2005) observed that though the shear-induced diffusion mechanism is present, the trajectories of the particles showed markedly different behavior in presence of inertia.

It appears, therefore, that shear-induced diffusion process, and hydrodynamic interaction between three-dimensional deformable particles *in presence of inertia* lack sufficient investigation. In this chapter we address hydrodynamic interaction between two liquid capsules suspended in a linear shear flow in presence of inertia. We choose capsules because unlike liquid drops, they do not coalesce or break upon interaction, and hence provide a ‘cleaner’ system. At the same time, capsules are deformable like liquid drops. Thus, unlike a pair of smooth rigid spheres which does not show shear-induced diffusion, a pair of capsules is expected to show this mechanism. As mentioned above, the only study that addressed shear-induced diffusion of a capsule-pair is the one by Lac *et al.* (2007) in the limit of zero inertia. Here we extend their study to finite inertia. While inertia is not important for biological applications, it is often relevant for artificial capsules in industrial processes related to food and polymer processing (Borhan & Gupta 2003).

In this chapter we present three-dimensional numerical simulation on capsule dynamics using immersed boundary/front-tracking method. The main objective of the chapter is to study the interaction between two capsules in presence of inertia. However, we note that there is virtually no study that addressed the effect of inertia on single capsule dynamics. Therefore, in the first part of the chapter, we briefly consider the dynamics of a single capsule suspended in a shear flow in presence of inertia. This is followed by the results on the effect of inertia on capsule-capsule interaction.

5.2 Problem Setup

The flow configuration is described in figure 5.2. We consider deformation of a capsule, and interaction between two capsules, suspended in a simple (linear) shear flow given by $\mathbf{U} = \{Gy, 0, 0\}$, where G is the shear rate. The initial undeformed shape of a capsule is spherical with diameter a . The fluid, both inside and outside of the capsules, is incompressible and Newtonian. The channel is periodic in the streamwise (x) direction, and in the z -direction. In the y -direction, the flow is bounded by two no-slip walls separated by a distance H . The computational domain is a cube of sides of length H . In the present computation, we take

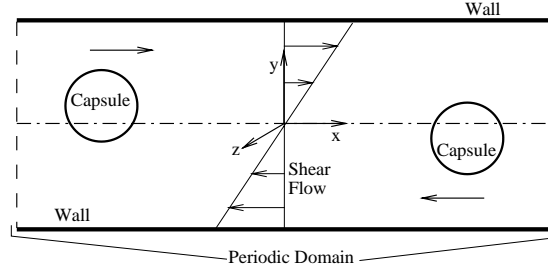


Figure 5.2: Schematic of the initial configuration showing the computational domain and initial location of the capsules in shear flow.

$$a/H = 0.16.$$

The governing equations are made dimensionless using a as the characteristic length scale, and the inverse shear rate G^{-1} as the time scale. The dimensionless time tG^{-1} is denoted by t^* . The major dimensionless parameters are the Capillary number $Ca = \mu Ga/Eh$ which is the ratio of the viscous stress to the elastic force of the capsule membrane, and the Reynolds number $Re = \rho Ga^2/\mu$. In the limit of small inertia, capillary number is the relevant parameter, whereas at finite inertia it is customary to use the Weber number $We = ReCa = \rho G^2 a^3/Eh$ instead of the capillary number. The viscosities of the capsule liquid and the exterior liquid are the same.

5.3 Results and Discussion

5.3.1 Capsule Deformation at Finite Re

As mentioned before, previous works on capsule deformation have been mostly limited to $Re \ll 1$. Using the immersed boundary code, we have simulated capsule deformation in shear flow at finite Re up to 50, and We up to 10. The capsule shapes in this range of Re are shown in figure 5.3a. As in the limit of small inertia, capsules at finite inertia also attain a steady ellipsoidal shape and inclined orientation with the flow. We note that the capsule elongates more as Re (or, We) increases. The deformation parameter D and the

orientation angle θ are shown in figures 5.3b and c, respectively, with respect to time. The asymptotic steady values of D and θ increase with increasing Re (or, We).

Once the capsule attains the steady deformed shape and orientation, the interior liquid and the membrane rotate in a tank-treading manner. The streamlines in and around the capsule at steady state are shown in figure 5.4 for $Re \ll 1$ and for $Re = 10$ and 50 . For all cases, streamlines within the capsule rotate clockwise in accordance with the direction of vorticity of the imposed flow. The streamlines outside the capsule, however, show significant differences at small and high inertia. For $Re \ll 1$ (figure 5.4a) all streamlines around the capsule extend to infinity. Streamlines in $y/a > 0$ half of the domain go from left to right, and those in $y/a < 0$ go from right to left, in agreement with the imposed shear flow. When Re increases to 10 or 50 (figures 5.4b and c), not all streamlines extend to infinity. Rather, the streamlines within $-0.5 < y/a < 0.5$ form a reverse flow. The streamlines coming from left in $0 < y/a < 0.5$ turn around as they approach the capsule, and then they move to the left in $-0.5 < y/a < 0$. The streamlines coming from right in $-0.5 < y/a < 0$, also turn around as they approach the capsule, and move to the right in $0 < y/a < 0.5$. Between the reverse-flow region, and the capsule, a straining flow region with a off-surface stagnation point is generated. As Re increases from 10 to 50, the reverse-flow region expands more in the lateral (y) direction. Note that the flow domain is periodic in x . Thus we actually simulate an array of capsules with centers located H apart. The reverse streamlines in between two adjacent capsules then form a recirculating flow.

The streamline patterns shown here can be compared with those obtained previously for rigid particles suspended in simple shear flow. In the limit of Stokes flow, all streamlines around a rigid spherical or circular particle extends from $-\infty$ to $+\infty$, or vice versa, under a torque-free condition (e.g. Happel & Brenner 1983, Poe & Acrivos 1975, Mikulencak & Morris 2004). At finite inertia, experiments (Poe & Acrivos 1975) and numerical simulations (Kossack & Acrivos 1974, Mikulencak & Morris 2004) have shown the existence of reverse streamlines, and off-surface stagnation points for a torque-free rigid sphere or circular cylinder. The distance between the stagnation points and the center of the particle decreases

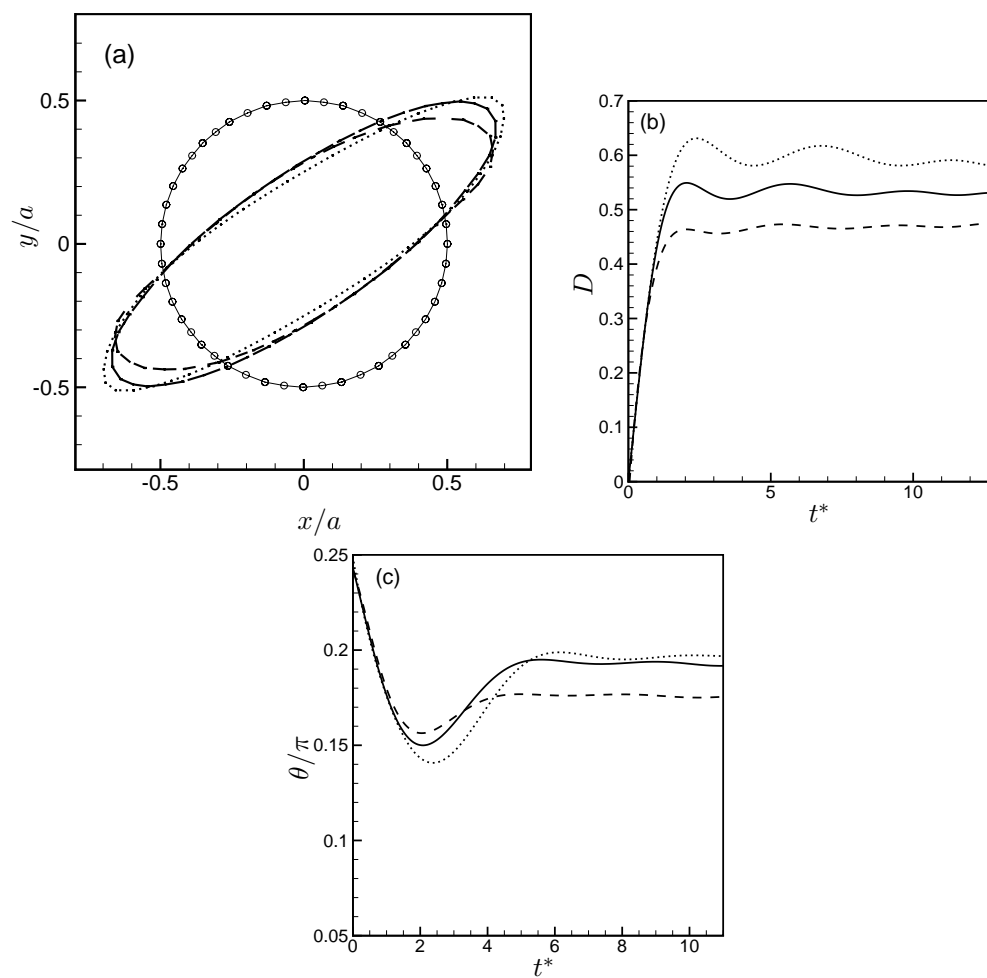


Figure 5.3: Deformation of single capsule at finite Re . (a) steady shapes (b) deformation parameter D , and (c) angular orientation θ . Line patterns are: - - - - - $Re = 10$; ——— $Re=25$; ····· $Re=50$ ($We = 2, 5, 10$, respectively). In (a), the initial capsule shape is shown by \circ .

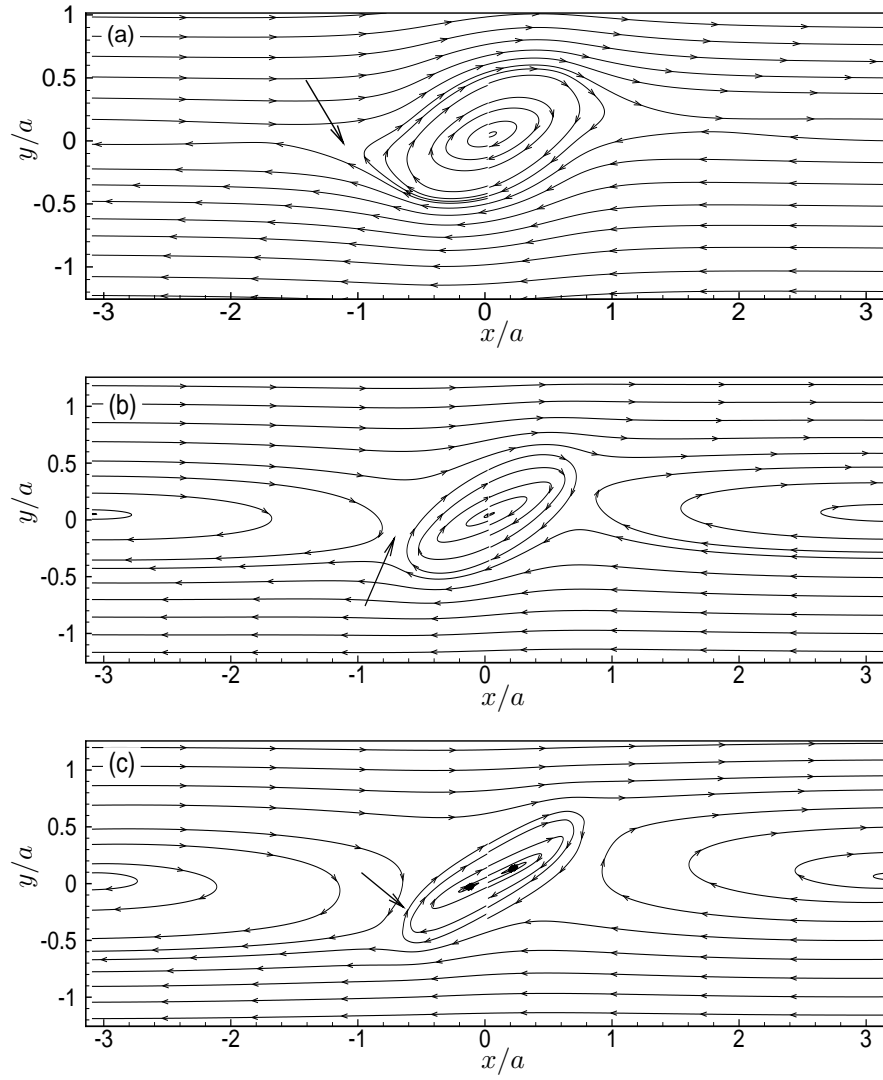


Figure 5.4: Flow field around single capsule at (a) $Re \ll 1$, (b) $Re = 10$, and (c) $Re = 50$. The stagnation points on one side of the flow are marked with long arrows.

as Re increases (Poe & Acrivos 1975). Our results show that the reverse streamlines and off-surface stagnation points also exist for deformable liquid capsules at finite Re .

5.3.2 Capsule–Capsule Interaction at $Re \ll 1$

Next we consider the main results of the chapter, that is, hydrodynamic interaction between two capsules suspended in a shear flow. We first consider the low Re limit, followed by the effect of inertia in the next section. The initial coordinates of the capsule centers are $-x_0, y_0, z_0$, and $x_0, -y_0, z_0$. Thus, the capsules are initially placed off-axis, at small but equal distances above and below the center line at $y = 0$ (figures 5.2). The initial lateral and horizontal separations between the centers of the capsules are denoted by Δy_0 , and Δx_0 . The dimensionless parameter $\Delta y_0/a$ is also called the impact parameter. Due to the non-zero relative velocity between them, the capsules approach each other, and subsequently interact. The sequence of interaction at successive times is shown in figure 5.5 for $Re \ll 1$. Here we consider $Ca = 0.2$, and $\Delta y_0/a = 0.2$, and $\Delta x_0/a = 4$. As the flow starts, the capsules first deform and attain ellipsoidal shapes. As they approach closer, the capsules roll over each other. During the process, both capsules undergo significant deformation, and a flat contact area is formed. Eventually the capsules separate in the x -direction, and the ellipsoidal shapes are recovered. The capsule moving to the right continues to move in that direction, and the one moving to left also continues in that direction.

A close inspection of figure 5.5 reveals that during the interaction, the lateral separation between the capsule first increases and then decreases. The history of the lateral separation Δy between the capsule centroids is shown in figure 5.6. The effect of Ca is also shown here. Δy remains at its initial value of 0.2 until the capsules are close enough. Upon close encounter, Δy increases sharply reaching its maximum when the capsules roll over each other (i.e. $\Delta x \approx 0$). After the interaction, Δy decreases. As the capsules move away from each other, Δy reaches a steady value. The final steady value of Δy (≈ 0.6) is higher than the initial value of 0.2, implying that the hydrodynamic interaction has resulted in a larger permanent lateral separation between the capsules. The process is irreversible,

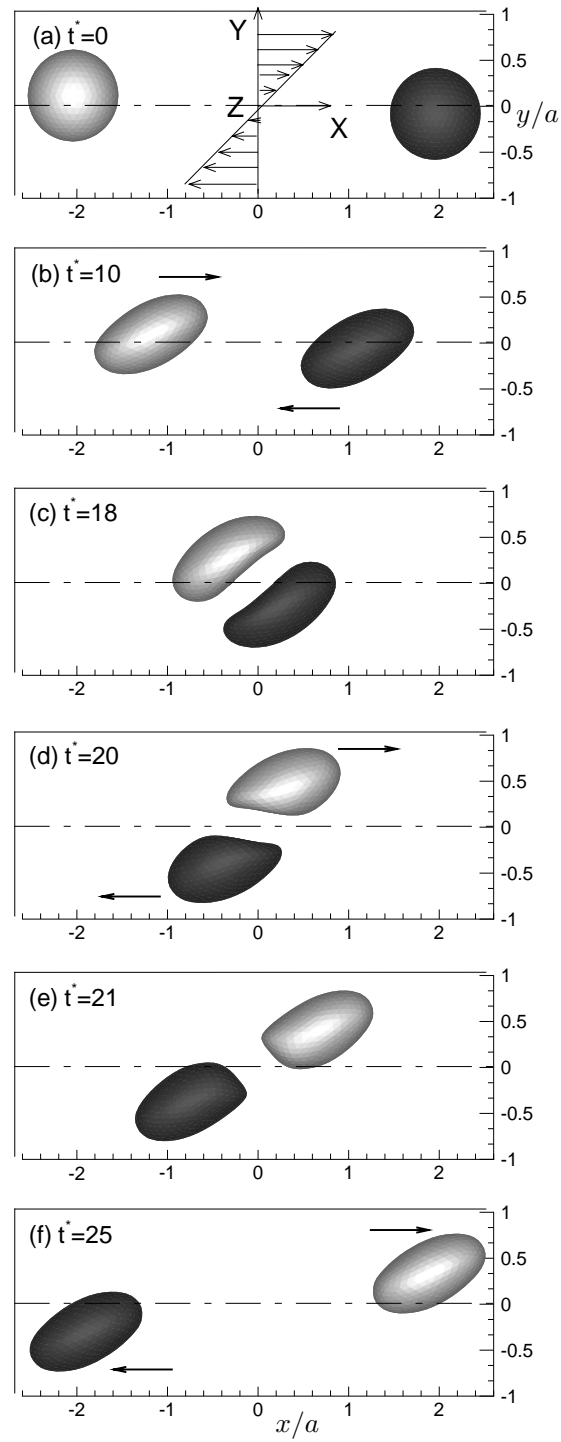


Figure 5.5: Sequence of capsule-capsule interaction at $Re \ll 1$. Capsule shapes for $Ca=0.2$ are shown.

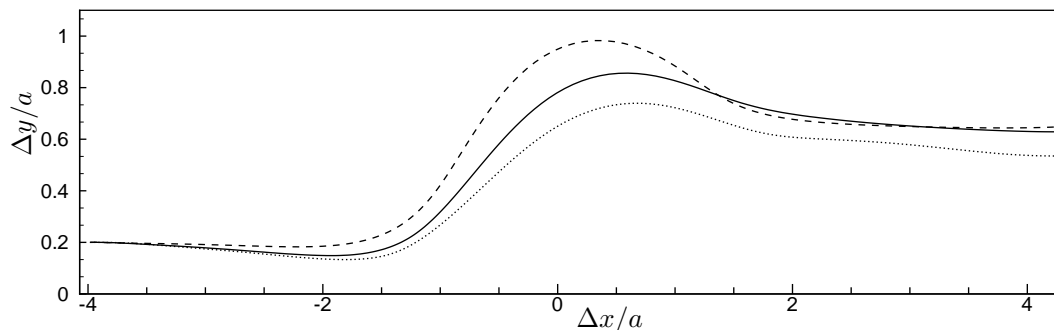


Figure 5.6: Lateral separation Δy versus Δx for $Re \ll 1$. Shown here are - - - - - $Ca=0.05$, ——— $Ca=0.2$, ····· $Ca=0.4$. t^* increases from left to right. At $t^* = 0$, $\Delta y_0 = 0.2$.

and the capsules are said to have undergone shear-induced self-diffusion due to pairwise interaction. The shear-induced diffusion seen here for the liquid capsules is similar to that recently published by Lac *et al.* (2007). It is also similar to the shear-induced diffusion of non-coalescing liquid drops at zero Reynolds numbers (e.g. Loewenberg & Hinch 1997) and at finite Reynolds numbers (e.g. Nobari & Tryggvason 1996), and for rigid particles (e.g. Kromkamp *et al.* 2005) at finite Re .

5.3.3 Capsule–Capsule Interaction at Finite Re : Short Time Behavior

Next we consider the effect of inertia on capsule-capsule interaction. The initial off-sets are $\Delta y_0/a = 0.2$ and $\Delta x_0/a = 4$, same as before. Successive profiles of the capsules are shown in figure 5.7 for $Re = 10$ and $We = 2$. As the flow starts, the capsules deform and attain ellipsoidal shapes. As time progresses, the capsules first approach each other due to the non-zero relative velocity between them (figure 5.7b). As the capsules come closer, however, they do not roll over each other. Rather, they reverse the direction of motion (at $t^* = 12$ in figure 5.7c). The capsule initially moving to the right (shown using light shading) now moves to left, while the one moving to left (shown using dark shading) now moves to right (figure 5.7d). This behavior is remarkably different from that seen earlier at $Re \ll 1$ in figure 5.5, where the capsules rolled over each other, and maintained their

respective directions of motion after the interaction. At around $t^* = 28$ (figure 5.7e), the horizontal separation between the capsules is the maximum. At this point, their directions of motion reverse again, and they again start approaching each other, as evident from figure 5.7f for $t^* = 38$. Subsequently, at around $t^* = 45$, the capsules again reverse their motion, and recede from each other (not shown). The simulation was continued for a long time, and the reversal of the motion was observed to repeat continuously.

A number of numerical experiments at finite Re up to 50 are performed. The trajectories of the capsule centroids for different Re are shown in figure 5.8a. We also show the y -coordinates of the capsule centroids versus time in figures 5.8b and c which may also be helpful to describe the capsule interaction at finite Re . For all Re , the initial horizontal separation is 4, and the vertical separation is $\Delta y_0 = 0.2$. The initial locations of the capsule centroids are marked by circles in figure 5.8a. The capsule located in $x < 0, y > 0$ initially moves to the right, and the one located in $x > 0, y < 0$ moves to the left. Consider first the cases with $Re \ll 1$. The capsules approach each other in nearly horizontal trajectories. As the horizontal separation between them decreases, the capsules roll over each other which results in an increase in the vertical separation between their centers. After the interaction, the capsules move away from each other, and the vertical separation decreases. The capsule initially moving to the right (or left) continues to move in the same direction after the interaction. Next consider $Re = 0.5$. Inertia does not play any significant role at this Re . The trajectories of the capsules at this Re are similar to those obtained for $Re \ll 1$ which show shear-induced diffusion.

Consider next $Re = 1.5$ and 2.3 ($We = 0.075$ and 0.115) in figures 5.8a and b. The effect of inertia is now apparent, as the capsules do not move in horizontal trajectories before the encounter. Rather, they move towards the $y = 0$ axis immediately before the encounter. As a result, the vertical separation between the capsule first decreases. Also note that the capsules move closer to the $y = 0$ axis as Re increases. Upon encounter, the capsules roll over each other. Subsequently, the capsules move away from each other, and continue to maintain their initial direction of motion. Thus the shear-induced diffusion occurs even at

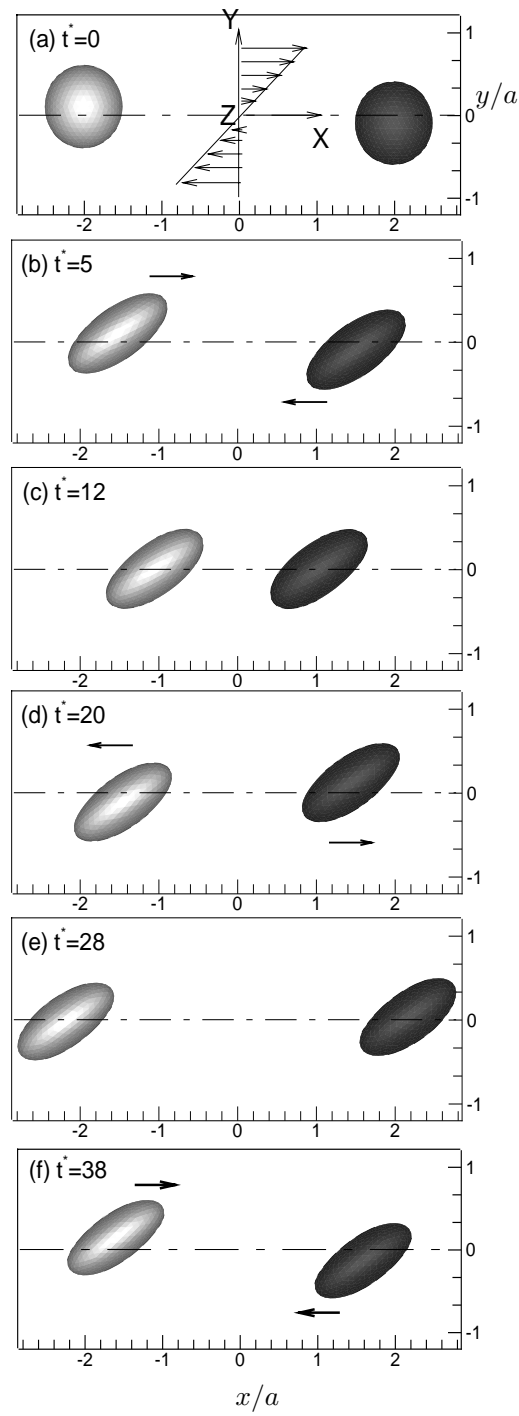


Figure 5.7: Sequence of capsule-capsule interaction at finite Re . Shown here is $Re=10$ ($We = 2$), $\Delta x_0/a = 4$, $\Delta y_0/a = 0.2$.

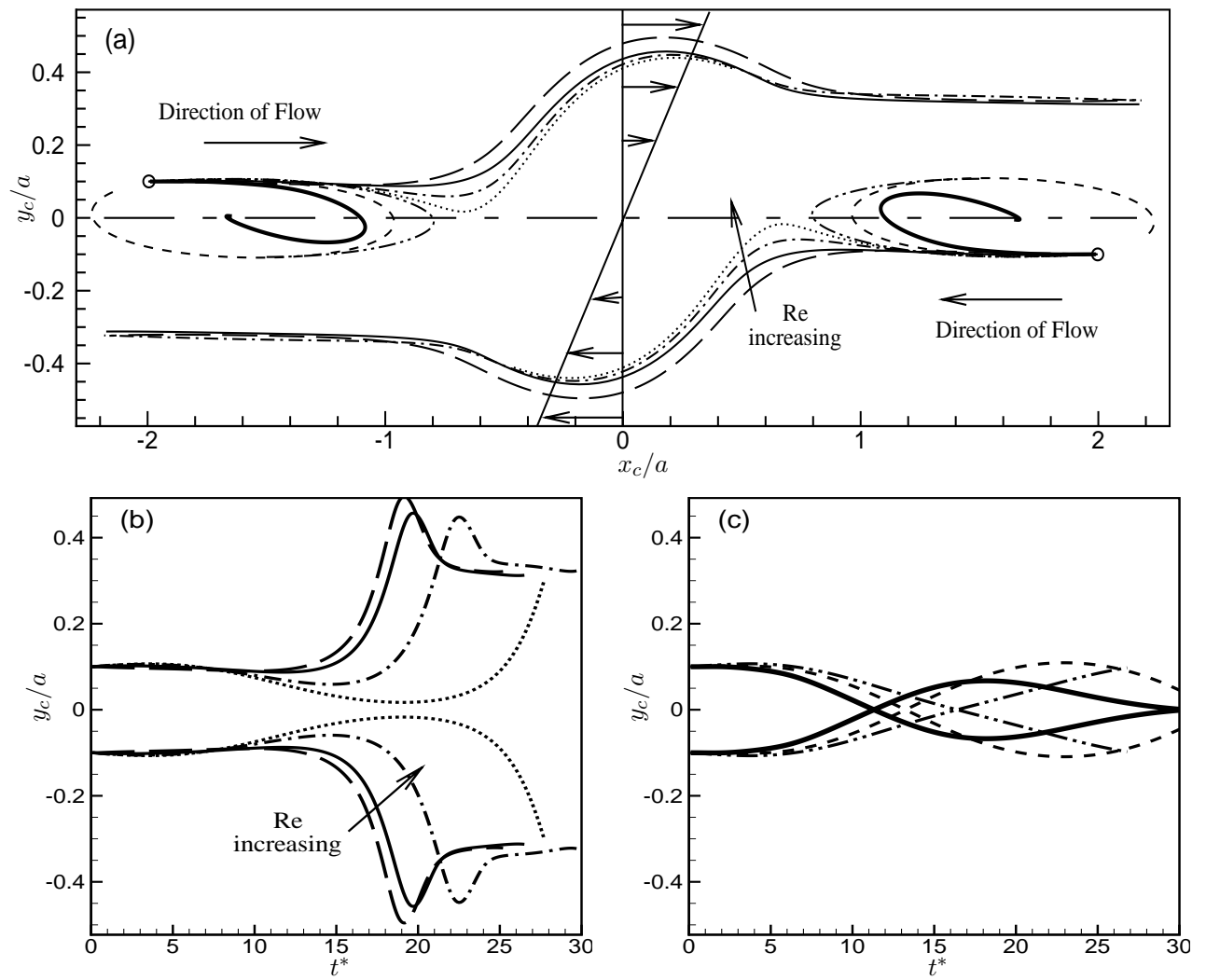


Figure 5.8: (a) Capsule trajectories (x_c versus y_c) at finite Re . (b)–(c) lateral coordinates of capsule centroids (y_c) versus t^* . For (a)–(c), line patterns are: — — — $Re \ll 1$; ——— $Re=0.5$; - - - - $Re=1.5$; $Re=2.3$; - · - · - $Re=3$; - - - - - $Re=10$; thick line $Re=50$. Symbol 'o' in (a) is the initial location of capsule center.

$Re = 1.5$ and 2.3 except that the capsules move laterally towards $y = 0$ axis before the encounter.

When Re increases to 3 (figures 5.8a and c), several remarkable effects of inertia are observed. The capsules first approach each other as before. They also migrate vertically, and move closer towards the $y = 0$ axis. But upon encounter, they do not roll over each other. Rather they reverse their direction of motion upon interaction. The reversal of direction is due to the fact that the capsules cross the $y = 0$ axis. The capsule which is in $y > 0$ before the encounter, moves to $y < 0$ after the encounter, and vice versa. Subsequently, the capsules reverse their direction of motion. The capsule moving to the right (left) before the interaction, moves to the left (right) after the interaction.

When Re increases to 10 and 50, the reversal of motion of the capsules is also observed (figures 5.8a and c). We also note that as Re increases from 3 to 50, the reversal of motion of a capsule happens progressively earlier in time (figure 5.8c).

The interaction between the capsules at finite Re as just described has no similarity in low Re . The shear-induced diffusion phenomenon observed at low Re is completely absent in presence of moderate to high inertia ($Re > 3$). Recently, Kromkamp *et al.* (2005) performed numerical simulations of hydrodynamic interaction between two rigid circular cylinders suspended in a simple shear flow in presence of inertia. The Reynolds number of the particles considered in their study ranges from 0.019 to 0.518. At $Re > 0.058$, they observed that the cylinders move vertically towards the $y = 0$ axis before rolling over each other. This result is similar to that obtained by us for three-dimensional and deformable capsules at $Re = 1.5$ and 2.3 . These two results therefore suggest that inertia alters the trajectories of the particles during the shear-induced diffusion process irrespective of whether the bodies are 2D or 3D, and rigid, or deformable. Kromkamp *et al.* (2005) however, did not consider much higher Reynolds number (e.g. $Re > 1$) as considered in our study. Thus, the reversal of capsule motion for $Re \geq 3$ as described above has not been reported by them.

The effect of the impact parameter $\Delta y_0/a$ is studied next in figure 5.9a. We consider

$Re = 50$ only, but $\Delta y_0/a = 0.2, 0.40$ and 0.57 . Due to the inertia, in all cases, the capsules first approach $y = 0$ axis before encounter. For $\Delta y_0/a = 0.2$ and 0.4 , the capsules cross the $y = 0$ axis, and thus reverse their directions of motion. For $\Delta y_0/a = 0.57$, the capsules do not cross the $y = 0$ axis, and they roll over each other, resulting in shear-induced diffusion. This result implies that the roll-over or reversal of motion depends on the initial vertical separation (impact parameter), not just on Re (or We). We also note that the reversal of motion occurs earlier as the impact parameter decreases. In the limit $\Delta y_0 \rightarrow 0$, there is no interaction between the capsules, and $\Delta x = \Delta x_0$ for all time. In the limit $\Delta y_0 \rightarrow \infty$, also there is no interaction between the capsules, and $\Delta y = \Delta y_0$ for all time.

Figures 5.9b and 5.9c show the effect of Δx_0 . Here $\Delta y_0/a$ is held constant at 0.2 , and $\Delta x_0/a$ is 1.5 and 8 . The Reynolds number considered here is $3, 10$, and 50 ($We = 0.15, 0.5$, and 2.5 , respectively). For all Re at $\Delta x_0/a = 8$ (figure 5.9b), the capsule trajectories are similar to those obtained for $\Delta x_0/a = 4$ (figure 5.8), and they show the reversal of the capsule motion. Thus, the reversal of the motion is expected to occur even at large $\Delta x_0/a$. On the contrary, capsules with $\Delta x_0/a = 1.5$ (figure 5.9c) show remarkably different trend. In this case, reversal of motion occurs only for $Re = 50$, and the diffusion-type motion (roll-over) occurs for $Re = 3$ and 10 .

We now explain the physical reason for the reversal of capsule motion at finite Re . For that, we refer to the streamlines plot presented in figure 5.4. It was noted in figure 5.4 that at $Re \ll 1$, the streamlines outside a capsule smoothly follow the deformed shape of the capsule, and extend to ∞ . If a second capsule is introduced in the flow, it will follow the streamlines, and move around and over the first capsule as seen in figure 5.5 resulting in self-diffusion type motion. At finite Re , on the other hand, the exterior streamlines near the $y = 0$ axis create a recirculating flow. If a second capsule is released within the recirculating flow, it will follow the closed streamlines, and show the reversal of motion. If it is released outside the recirculating flow, it will follow the open streamlines, and roll over the first capsule. The lateral extent of the recirculating flow increases with increasing Re (figure 5.4). At moderate values of Re (e.g. 1.5 and 2.3 in figure 5.8) and Δy_0 (e.g. 0.2), the initial

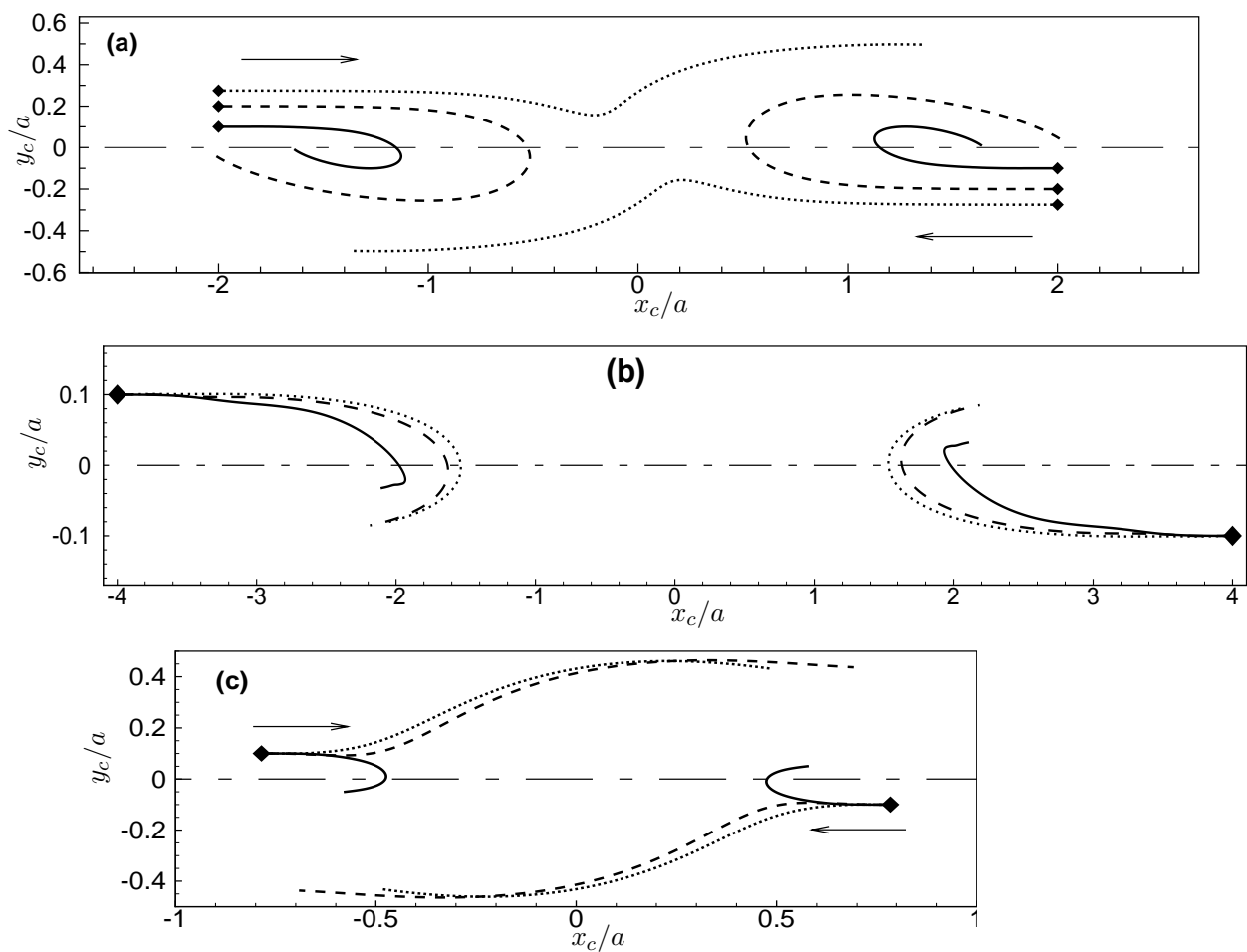


Figure 5.9: Capsule trajectories at finite Re . (a) Effect of Δy_0 for $Re = 50$ $\Delta y_0/a = 0.57$; - - - - - $\Delta y_0/a = 0.4$; — $\Delta y_0/a = 0.2$. (b)–(c) Effect of Δx_0 . (b) $\Delta x_0 = 8$, and (c) $\Delta x_0 = 1.5$. For (b) and (c) line patterns are: $Re = 3$; - - - - - $Re = 10$; — $Re = 50$. Diamond symbols indicate the initial location of the capsule centroids.

locations of the capsules are nearly along the boundary of the recirculating flow. Thus the capsule initially move closer to the $y = 0$ axis before rolling over each other. For higher values of Re (> 3) but moderate values of Δy_0 (e.g. 0.2 in figure 5.8), the initial locations of the capsules are well within the recirculating flow regions, and hence the capsules reverse their motion. For $Re = 50$ and $\Delta y_0 = 0.57$ (figure 5.9a), the initial locations are outside the reverse flow regions, and hence the capsules roll over each other.

Some more interesting observations at finite Re can be made in figures 5.8b and c, which show the y -coordinate of the capsule centroids versus dimensionless time. First, for $Re < 3$, the time t^* taken by the capsules before they tumble increases with increasing Re . This is because as Re increases, the recirculating flow strengthens, and the vertical component of fluid velocity increases in the recirculating region. The capsules move towards the $y = 0$ axis relatively earlier. As a result, the relative velocity between them (based on the undisturbed shear flow) decreases resulting in longer time before they tumble over each other. For $Re \geq 3$, even higher lateral fluid velocity causes the capsules to move quicker towards the $y = 0$ axis, and cross the axis due to inertia. Thus for $Re \geq 3$, the reversal of capsule motion occurs earlier in time with increasing Re . It also implies, as evident from figures 5.8 and 5.9, that with increasing Re (≥ 3) the capsules come less closer to each other.

The reversal of the capsule motion should not be confused with the bouncing collision that is often encountered during head-on collision of liquid drops (see, e.g. Nobari & Tryggvason 1996, Mohamed-Kassim & Longmire 2004). In the latter case, the drops come close to each other before bouncing. In the present case, the capsules at finite inertia do not come close to each other as evident from figures 5.7–5.9. To illustrate this point, we compute the minimum horizontal distance Δx_{min} between the capsules as shown in figure 5.10. We note that Δx_{min} depends on Re , Δx_0 and Δy_0 . For a given Δy_0 , we see that Δx_{min} increases with increasing Re (also see figure 5.9a), due to the increasing strength of the recirculating flow. For a given Re , Δx_{min} increases with decreasing Δy_0 . In the limits $\Delta y_0 \rightarrow 0$ or ∞ , no interaction can take place, and $\Delta x = \Delta x_0$.

One implication of the fact that the capsules do not come close to each other at finite

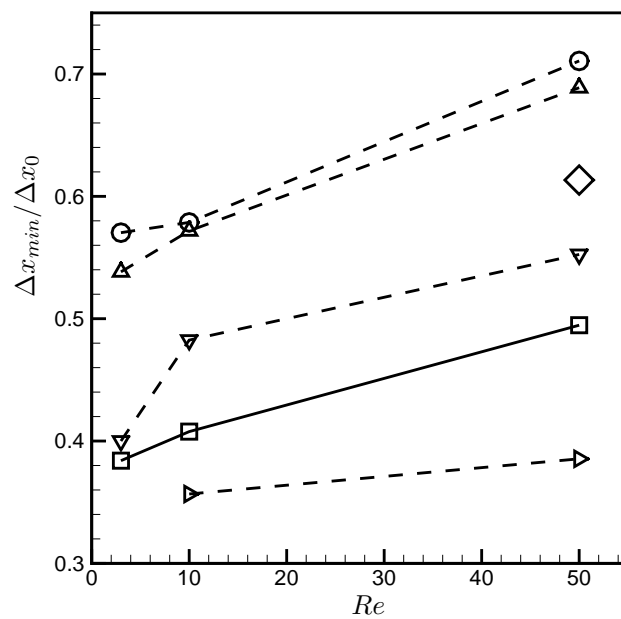


Figure 5.10: Minimum horizontal distance between the capsule-pair at finite Re . $\square \Delta x_0/a = 8, \Delta y_0/a = 0.2$; $\triangleright \Delta x_0/a = 4, \Delta y_0/a = 0.3$; $\nabla \Delta x_0/a = 4, \Delta y_0/a = 0.2$; $\Delta \Delta x_0/a = 4, \Delta y_0/a = 0.1$; $\circ \Delta x_0/a = 4, \Delta y_0/a = 0.05$; $\diamond \Delta x_0/a = 1.5, \Delta y_0/a = 0.2$

Re is that the deformed ellipsoidal shapes of the capsules remain unchanged during the interaction. This is in contrast to the observation at low Re , where capsule shapes deform significantly during the interaction (figure 5.5).

5.3.4 Capsule-Capsule Interaction at Finite Re : Long-Time Behavior

So far we discussed the results on the first encounter between the capsules. Simulations presented above were continued for longer time. We now discuss the long time behavior of the capsules. For this we only consider the cases for which reversal of capsule motion was observed. The long-time behavior can be illustrated by going back to figure 5.7. Here we see that the capsules, after deforming, first approach each other, then recede from each other (at $t^* \approx 12 - 28$), and then again approach each other (at $t^* \approx 28 - 38$). They also periodically move above and below the $y = 0$ axis. The periodic approach and receding motion continued throughout the length of the simulation ($t^* \approx 100$). Simulations at higher Re and We also show similar periodic motion, details of which are described later. Such periodic approach and receding motion over long time at high Re has no similarity at low Re .

Long-time trajectories of the capsules for $Re = 10, 25$ and 50 ($We = 2, 5$ and 10 , respectively) are shown in figure 5.11. The trajectories show that the capsules move in spirals, and thus repeatedly approach and recede. The direction of the spiraling motion coincides with the direction of the vorticity of the imposed shear flow. The trajectories do not show the same behavior for all Re and We . At $Re = 10$, the capsules move spirally outward. At $Re = 25$, the capsules first spiral inward, but eventually continue to spiral in fixed orbits. At $Re = 50$, the capsules spiral inward, and then settle on the $y = 0$ axis after which no significant motion of them is observed. The spiraling motion of the capsules is further illustrated in figure 5.11b showing the capsule centroids (y_c) versus t^* . For both capsules y_c oscillates about $y = 0$. For $Re = 10$, amplitude of oscillations increases with time as is the case for an outward spiral. For $Re = 25$, the amplitude remains constant as is the case for a fixed-orbit motion. For $Re = 50$, oscillations are damped as the capsules

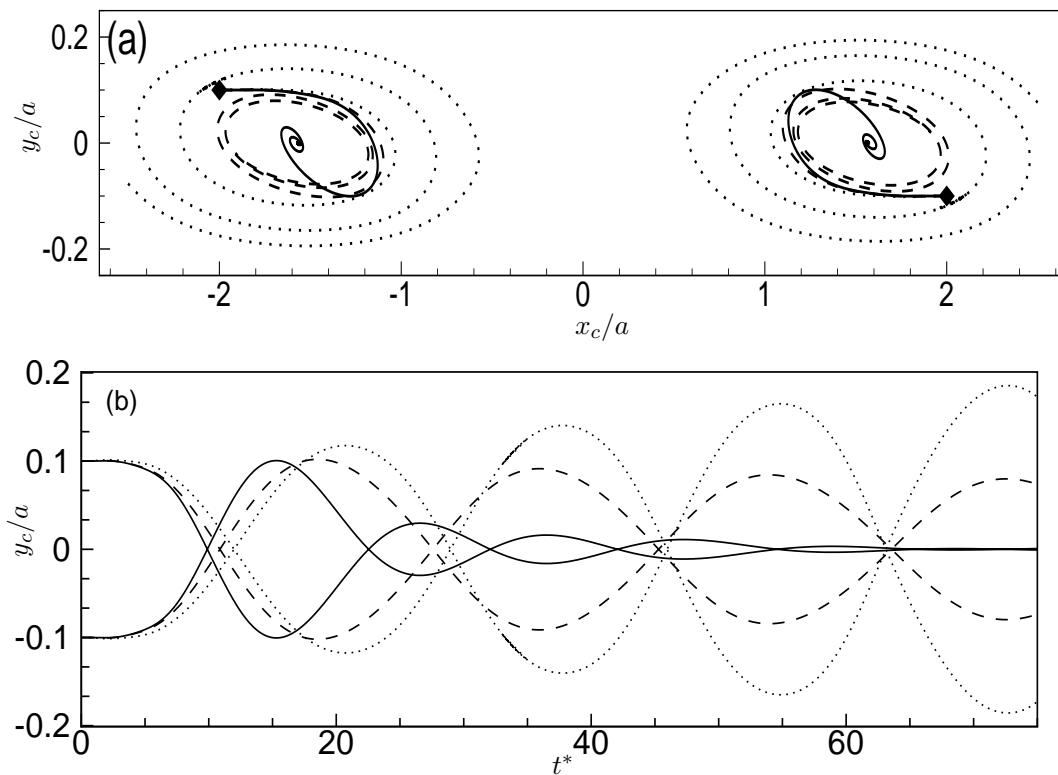


Figure 5.11: Long-time trajectories of capsules at finite Re . Line patterns are: $Re=10$, - - - - - $Re = 25$, ——— $Re=50$. Diamond symbols indicate the initial capsule locations.

spiral inward and eventually settle at $y = 0$ axis.

The explanation for the different spiraling motions (outward, inward or fixed-orbit) can again be based on the existence of the recirculating flow formed in between two adjacent capsules in an array (figure 5.4). The explanation is given using the fluid velocity vectors shown in figures 5.12 and 5.13 where two pairs of capsules are considered since the flow is periodic in x . The capsules are marked by number 1, 2 etc. Consider $Re = 10$ first in figure 5.12. At $t^* = 5$ (figure 5.12a), a recirculating flow exists (marked by ‘R1’ in the figure) between the capsules 1 and 2 where the fluid moves in the clockwise direction. At this moment the centers of capsules 1 and 2 are located above and below $y = 0$, respectively. As

the capsules approach each other, the recirculating flow between them weakens. At $t^* \approx 12$ (figure 5.12c), the capsules are closest to each other, and the recirculating flow between them is absent. Instead, a straining flow region exists (marked by ‘S’ in figure 5.12c). The generation of this straining flow region was also discussed in section III-B. At this point, however, two recirculating regions, marked by ‘R2’ in figure 5.12c, develop between capsules 3 and 1, and between 2 and 4. As a result, capsule 1 now starts moving downward towards $y = 0$, and capsule 2 moves upward towards $y = 0$. Due to inertia, the capsules cross the $y = 0$ axis. Once the capsule 1 is in $y < 0$, and capsule 2 is in $y > 0$, they start receding from each other (figure 5.12d). The intercapsule gap between 1 and 2 starts increasing and a recirculating flow re-emerges there (marked by ‘R1’ in figure 5.12e), whereas straining flow regions re-emerges between 3 and 1, and between 2 and 4. The cycle is then repeated. The vector plots for $Re = 50$ are shown in figure 5.13. As noted earlier in figure 5.4 for single capsule, the off-surface stagnation points are located closer to the capsule as Re increases. As a result, the recirculating flow develops between two capsules even when the inter-capsule gap is relatively small. The effect from two adjacent recirculating regions is nullified by each other, and eventually the capsules attain a stable position at $y = 0$ axis.

5.3.5 Regimes of Capsule-Capsule Interaction at Finite Re

Above results suggest that shear-induced diffusion, which is characteristic of $Re \ll 1$, may or may not be present at finite Re (or, We) depending on the impact parameter $\Delta y_0/a$ and the initial gap $\Delta x_0/a$. In the case where shear-induced diffusion is present, the lateral separation between the capsules first decreases before they roll over each other. In the case when shear-induced diffusion is absent, the capsule-pair engages in a spiraling motion. The spiraling motion could be either outward, inward or fixed-orbit. These regimes of motion are shown in a Re - Δy_0 (or, We - Δy_0) plane in figure 5.14 for a fixed $\Delta x_0/a = 4$. Based on the computational results, four different regimes in capsule-capsule interaction at finite Re can be identified. They are: (i) a self-diffusive type interaction for $Re < 3$ ($We < 1$) and any Δy_0 in which the capsules roll over each other as in case of $Re \ll 1$, (ii) an outwardly

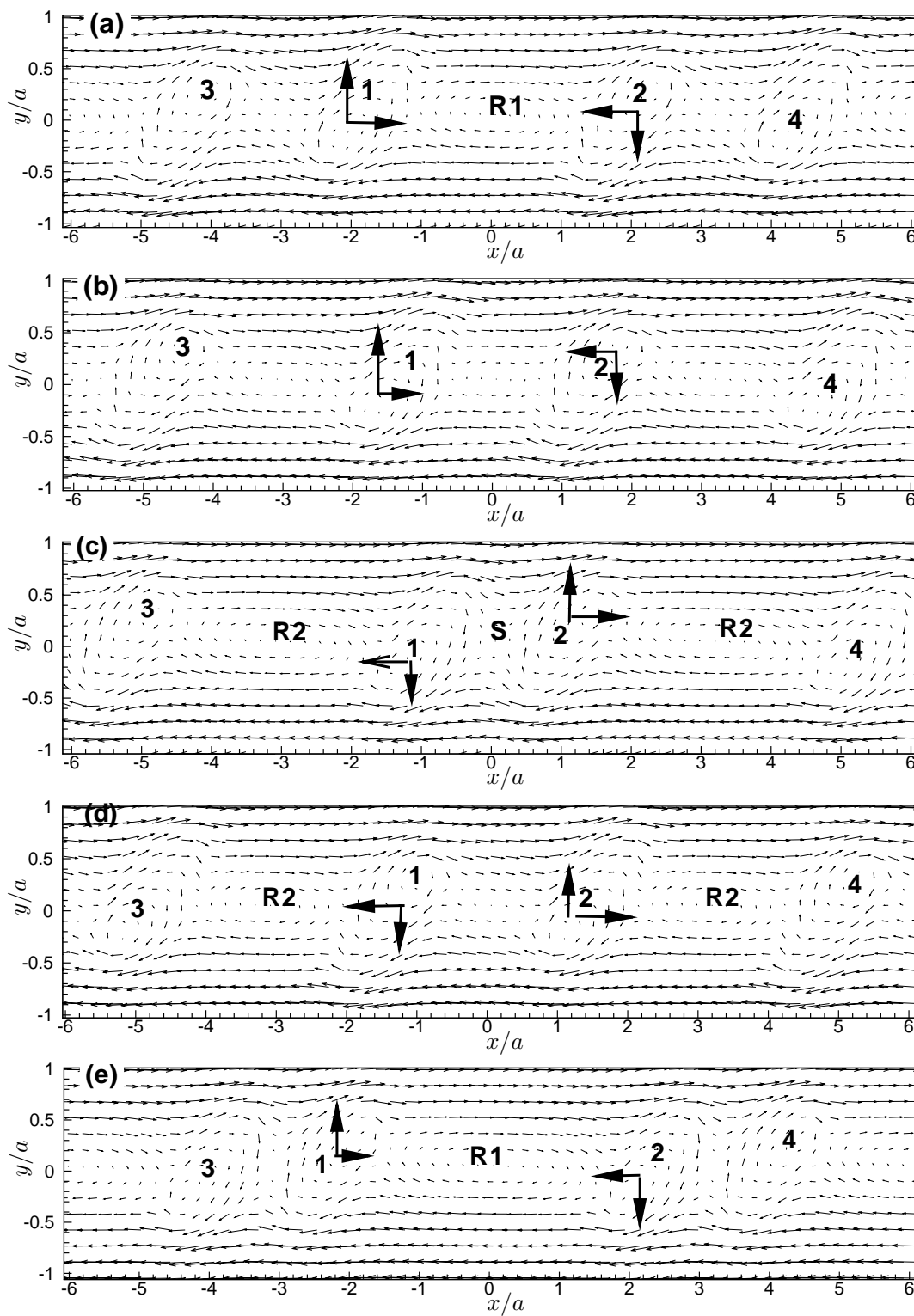


Figure 5.12: Time sequence of fluid velocity vectors for capsule-capsule interaction at $Re=10$. (a)–(e) are at $t^*=5, 9, 12, 20$, and 28 .

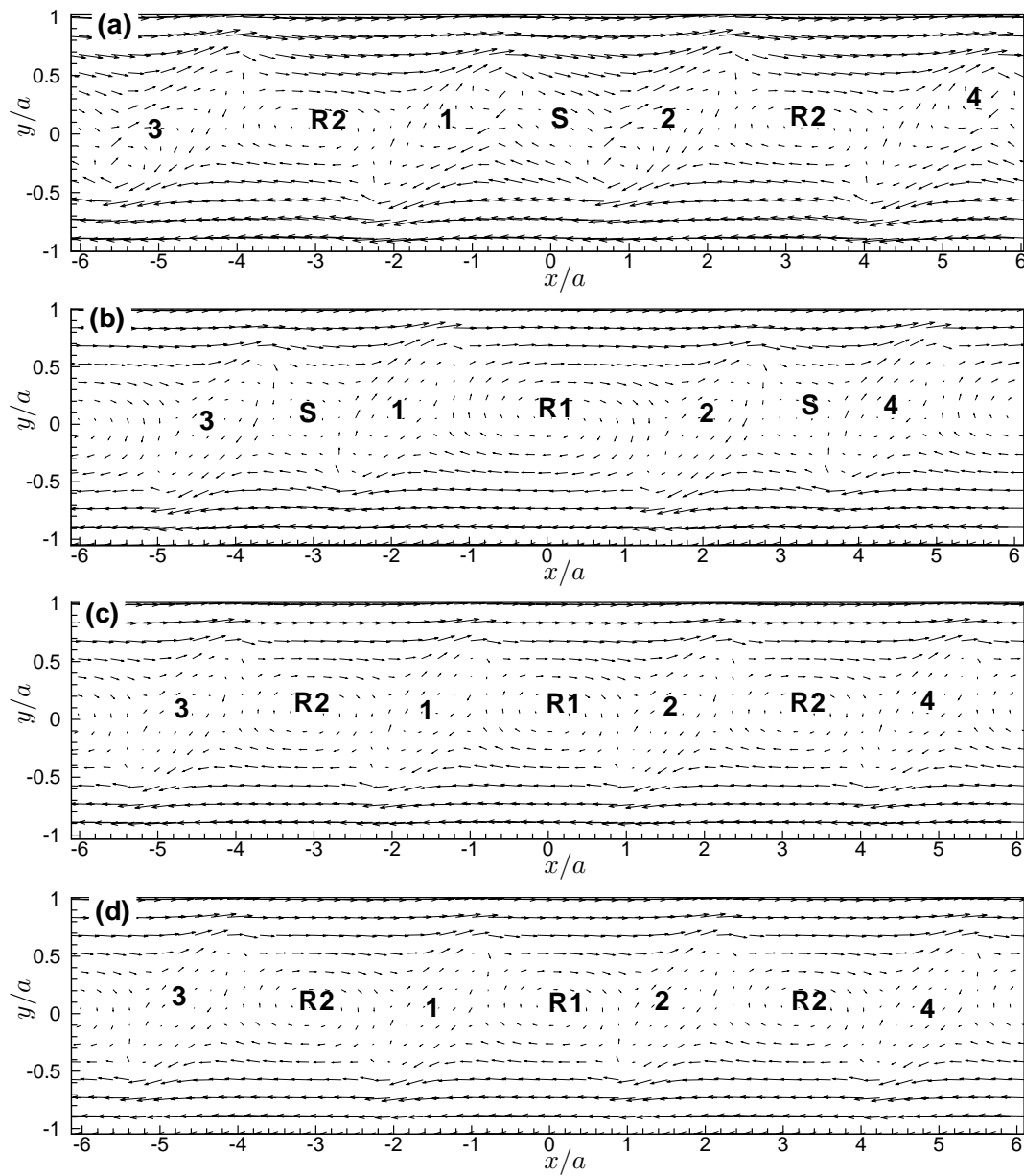


Figure 5.13: Same as in previous figure but for $Re=50$. (a)–(d) are at $t^*=18, 23, 28$, and 33.

spiraling motion for $3 < Re < 20$ ($1 < We < 4$) and for low values of $\Delta y_0/a$ (< 0.4), (iii) a fixed-orbit spiraling motion for $20 < Re < 30$ ($4 < We < 6$) and $\Delta y_0/a < 0.4$, and (iv) an inwardly spiraling motion for $Re > 30$ ($We > 6$) and $\Delta y_0/a < 0.4$ in which the capsules settle at $y = 0$.

5.4 Summary and Conclusion

The main objective of this chapter was to study the effect of inertia on the hydrodynamic interaction between a pair of capsules. In the limit of zero inertia, it has been known from past research that the hydrodynamic interaction between two deformable particles (drops/capsules) suspended in shear flow with a relative velocity results in an irreversible shift in the trajectories of the particles leading to the so-called shear-induced diffusion. In this chapter we investigated the effect of inertia on the deformation of single capsule, on capsule-capsule interaction, and the shear-induced diffusion of them. Throughout the chapter, we draw comparison between the results at finite inertia and at small inertia. The main results from this study are summarized below.

1. At finite inertia, a capsule in a shear flow deforms in to an ellipsoidal shape, and deformation increases with increasing Re . The flow field around a capsule showed reverse flow regions and off-surface stagnation points, similar to those previously reported in case of torque-free spheres and cylinders. The lateral extent of the reverse flow increases with increasing Re .

2. The present methodology has been successful to simulate the shear-induced diffusion resulting from the hydrodynamic interaction between two liquid capsules at $Re \ll 1$. Similar to liquid drops, capsules at $Re \ll 1$ undergo irreversible increase in their lateral separation due to the shear-induced diffusion. During the interaction, the capsules undergo significant deformation. To the best of our knowledge, apart from the present study, there is only one study that addressed the shear-induced diffusion of liquid capsules (Lac *et al.* 2007).

3. Effect of inertia on the interaction between two capsules is quite remarkable. For $1 < Re < 3$, the capsules do undergo the shear-induced diffusion, but their trajectories are

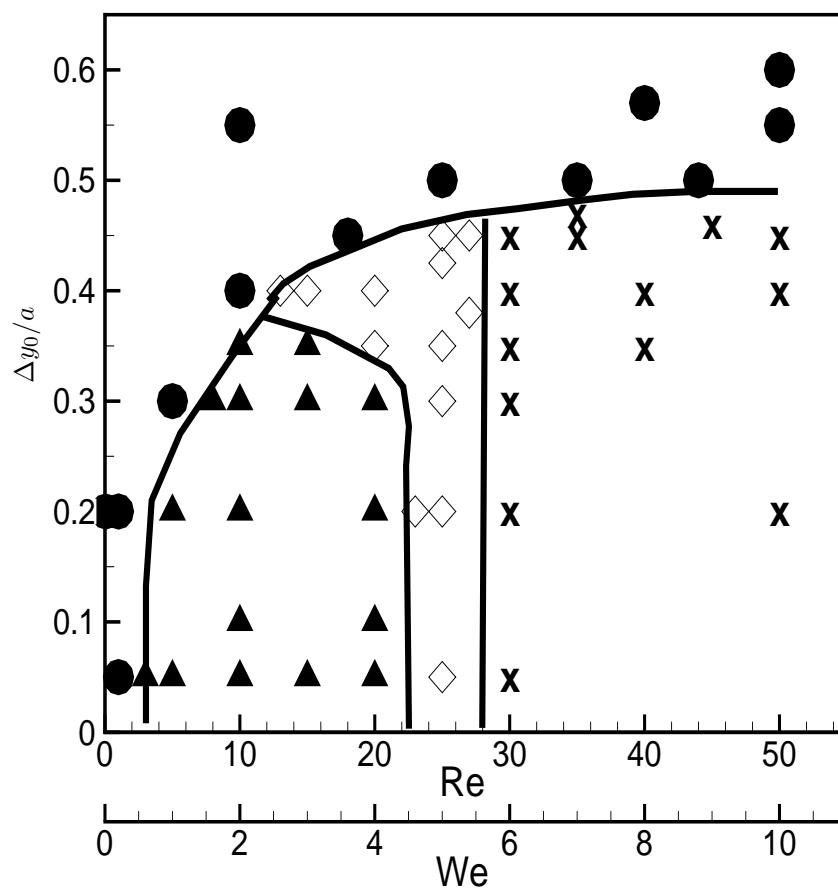


Figure 5.14: Regimes of capsule-capsule interaction at finite Re and We . ●, Self-diffusion type motion; ▲, outward spiraling motion; × inward spiraling motion; and ◇, fixed-orbit motion.

different from those at $Re \ll 1$. Specifically, the lateral separation between the capsules first decreases before they roll over each other. For $Re > 3$, the capsules reverse their directions of motion before coming close to each other. Thus, for $Re > 3$, the shear-induced diffusion can be absent. The reversal of the capsule motion is explained based on the recirculating streamlines formed around the capsule at finite Re . The reversal of motion occurs progressively earlier in time (that is, the capsules come less closer to each other) with increasing Re .

4. The long-time behavior of the capsule-capsule interaction at finite inertia showed that the capsules engage in spiraling motions. The nature of the spiraling motion depends on Re and We , and the initial separation between the capsules. The spiraling motion of the capsules is also explained based on the recirculating streamlines formed around the capsule at finite Re .

5. Based on our simulations, four different regimes of capsule-capsule interaction at finite inertia are identified: (i) a self-diffusive type interaction for $Re < 3$ ($We < 1$), (ii) an outwardly spiraling motion for $3 < Re < 20$ ($1 < We < 4$), (iii) a fixed-orbit spiraling motion for $20 < Re < 30$ ($4 < We < 6$), and (iv) an inwardly spiraling motion for $Re > 30$ ($We > 6$) in which the capsules settle with zero relative velocity. These spiraling motions at finite Re have no analogy at $Re \ll 1$.

One distinct feature of capsule-capsule interaction at finite inertia is that the capsules do not come close enough so that the interaction does not lead to further deformation of them. This is in stark contrast to $Re \ll 1$ limit when the capsules undergo significant deformation during the interaction. These, and other results presented here may have implications in developing a theory of capsule suspension. By considering the binary interaction of capsules, this study forms the basis of addressing the more difficult problem of suspension of deformable capsules or other deformable particles at finite inertia.

Chapter 6

Three-dimensional Computational Modeling and Simulation of Multiple Cells Flowing in Microvessels

6.1 Introduction

In last chapters, we investigated dynamics of single capsule & pair-wise interaction of two capsules as models for motion of deformable cells such as red blood cells. These studies develop the foundation for a more complex problem of motion of multiple, interacting, deformable particles. In this chapter, we consider Direct Numerical Simulation (DNS) of a suspension of a large number of capsules in a channel flow. The objective is to be able to predict physiologically relevant processes, such as the development of the cell-free layer, plug-flow profile, Fahraeus & Fahraeus-Lindqvist effects, as discussed in Chapter 1 (section 1.4.1).

A continuum description of blood flow in microvessels, such as those given by core-annular (or, two-phase) models, is sufficient to qualitatively predict the Fahraeus and Fahraeus-Lindqvist effects. Such models, however, rely on estimates of various physiological parameters, such as the width of the cell-free layer, which can be obtained only by high-resolution experiments (Long *et al.* 2004; Kim *et al.* 2007), or computational simulations in which motion and deformation of individual cell are directly resolved. Significant progress has been made over the past decades in understanding cell motion in unbounded simple shear flow (Eggleton & Popel 1998; Skotheim & Secomb 2007), and axisymmetric and nonaxisymmetric motion of single cell in narrow tubes and channels (Secomb *et al.* 1986; Pozrikidis 2003; Damiano 1998; Hsu & Secomb 1989). Pozrikidis (2005) presented boundary-element simulation of spherical, oblate ellipsoidal and biconcave cells in tube flow.

Secomb *et al.* (2007) developed a 2D finite-element model that included viscoelastic nature of the erythrocytes, and studied cell deformation, tank-treading and radial migration in microvessels. Extension of such models to larger vessels has remained a major computational challenge since multiple cells, often of the order of a few thousands in number, must be considered without sacrificing the detailed mechanics of individual cell.

Recent advances in the development of robust numerical methods and high-performance computational resources have enabled researchers to consider such large-scale simulations. Sun & Munn (2005) used a Lattice-Boltzmann simulation to address blood flow in $20\text{--}40\mu\text{m}$ with cells modeled as 2D rigid disks. Zhang *et al.* (2007) developed a 2D immersed boundary Lattice-Boltzmann technique that can simulate flow of a small number of deformable erythrocytes. Bagchi (2007) used immersed boundary method in 2D to simulate flow of a large number (up to 2500) of deformable erythrocytes in $10\text{--}300\mu\text{m}$ vessels. Ding & Aidun (2006) used a three-dimensional Lattice-Boltzmann technique to consider cluster formation in a large ensemble of deformable erythrocytes in shear flow. Pivkin *et al.* (2006) developed a dissipative-particle-dynamics technique to consider the simultaneous motion of deformable erythrocytes, and their effect on platelet deposition and thrombus formation. Freund (2007) studied margination of leukocytes in presence of deformable erythrocytes in 2D. Recently Zhao *et al.* (2008) developed a fixed-mesh method for the study of deformable fluid-structure interaction in 3D with application to biological systems.

In this chapter, we present three-dimensional computational modeling and simulation of a large number of deformable cells flowing in microchannels. We consider two types of cells, one having initially spherical shape, and the other having biconcave shape representative of erythrocytes in unstressed state. The channel width ranges from about $10\text{--}45\mu\text{m}$, which allows us to consider both single and multi-file motion. The highest number of cells considered in the simulations is 122 within the computational domain. The simulations generated a database with a wealth of information on the dynamics of flowing cell suspension. In this chapter, we present results on radial migration of cells, and their tumbling motion as observed for erythrocytes, analyze the trajectory and velocity of individual cells in the

suspension as functions of cell deformability, hematocrit, and channel width. The Fahraeus and Fahraeus-Lindqvist effects are also predicted by our simulations. The simulations allow us to directly estimate the width of the cell-free layer, and also the cross-section variation of effective viscosity (Chapter 1, section 1.4). We then use these results to show that the two-phase models underpredict the mean velocity of blood obtained in the simulations. We proceed to develop a three-layer model, and show that this gives an accurate prediction of the simulation results. Comparison with in vitro and in vivo data is presented throughout the chapter.

6.2 Results

6.2.1 Tumbling of biconcave cells

We first simulate the tumbling motion of a biconcave capsule. As mentioned in Chapter 1, an erythrocyte has a biconcave shape under resting condition. The shape of the biconcave capsules can be obtained by applying the following transformation on the sphere as (Evans & Fung 1972):

$$X = R_0 x, \tag{6.2.1a}$$

$$Y = \frac{1}{2} R_0 (1 - r^2)^{\frac{1}{2}} (C_0 + C_2 r^2 + C_4 r^4), \tag{6.2.1b}$$

$$Z = R_0 z. \tag{6.2.1c}$$

where X , Y and Z are the coordinates of the erythrocyte and x , y and z are the coordinates of a unit sphere. In the above equation, $r^2 = x^2 + z^2$ and the constants C_0 , C_2 and C_4 are taken to be $C_0 = 0.32$, $C_2 = 2.003$ and $C_4 = -1.123$. R_0 is adjusted to preserve the volume. We consider the motion of a biconcave cell in the channel flow. As shown in figure 6.1a, a biconcave cell undergoes tumbling motion in which it flips like a rigid body while moving axially with the flow. In the figure, a marker point on the cell membrane is also shown. Unlike the spherical capsule cases shown in chapter 3, the marker point does not move significantly with respect to its initial location on the cell membrane implying that the tank-treading motion is nearly absent. We have simulated a number of cases for

varying $Ca = 0.05-0.6$, and for all cases tumbling motion was observed. In experiments using erythrocytes in shear flow, two modes of motion, tank-treading and tumbling, have been observed by previous researchers (Ramanujan & Pozrikidis 1998; Skotheim & Secomb 2007). Results presented here, and elsewhere, suggest that the transition from tank-treading to tumbling motion depends on the the aspect ratio and the internal-to-external viscosity ratio, but not on the membrane elastic modulus. The absence of significant tank-treading for the biconcave discoid as observed in the present simulations is consistent with the analysis of Keller & Skalak (1982) who showed that an ellipsoid with an internal-to-external viscosity ratio of 5 would tumble rather than rotate even at high shear rates. Time history of the axial (x_c) and lateral (y_c) locations of the center-of-mass of the cell, axial and lateral velocity components (u/U_d and v/U_d), and angular orientation (θ/π) of the major axis of the cell with the x -axis are shown in figures 6.1b and 6.1c. The velocity components, as well as the lateral position show fluctuation in time due to the tumbling motion. Negative values of lateral velocity are evident.

6.2.2 Single-file motion

We start with the results of single-file motion of cells in channels under a driving pressure gradient. Single-file motion of erythrocytes is observed in narrow capillaries whose dimension is comparable or smaller than the characteristic cell dimension. In such vessels, cells squeeze to a parachute shape.

Results from our simulations are shown in figure 6.2 for initially spherical capsules of $H/d = 1.25$ and in figure 6.3 for biconcave capsules of $H/d = 1.37$. The capsule volume fraction for both types of cells is 26%. The spherical capsule is placed symmetrically at the channel center at time $t^* = 0$, whereas the biconcave cells are placed slightly off-center. Transient deformation of the spherical cell into a parachute shape at $Ca = 0.6$ is shown in figure 6.2a. In this case, the front and rear of the cells become convex and concave respectively, and sharp cusps develop at the trailing edges. The computed shapes are in qualitative agreement with the observed erythrocyte shapes in narrow capillaries at high

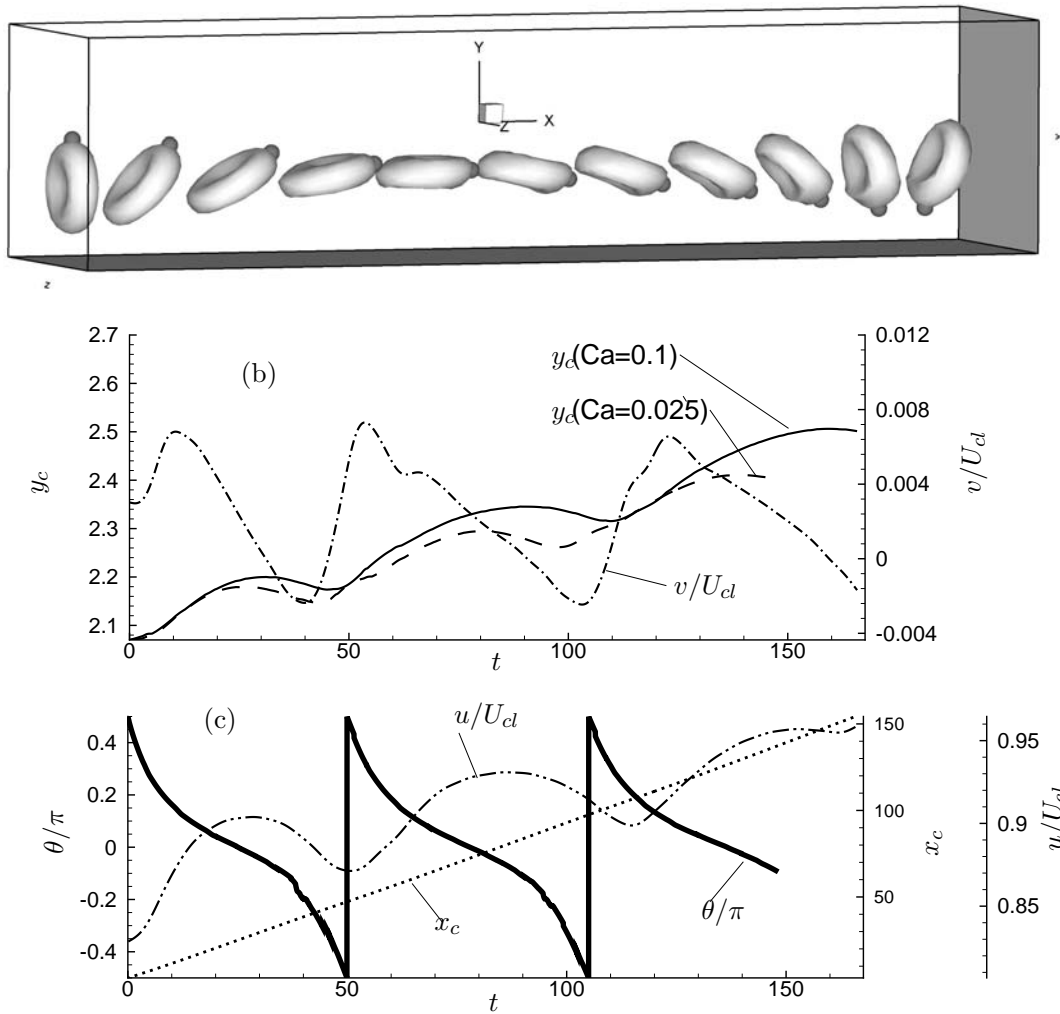


Figure 6.1: (a) Tumbling motion of a biconcave cell. (b) and (c) show cell trajectory (x_c and y_c), velocity (u/U_{cl} and v/U_{cl}), and angular orientation (θ/π) with the x -axis.

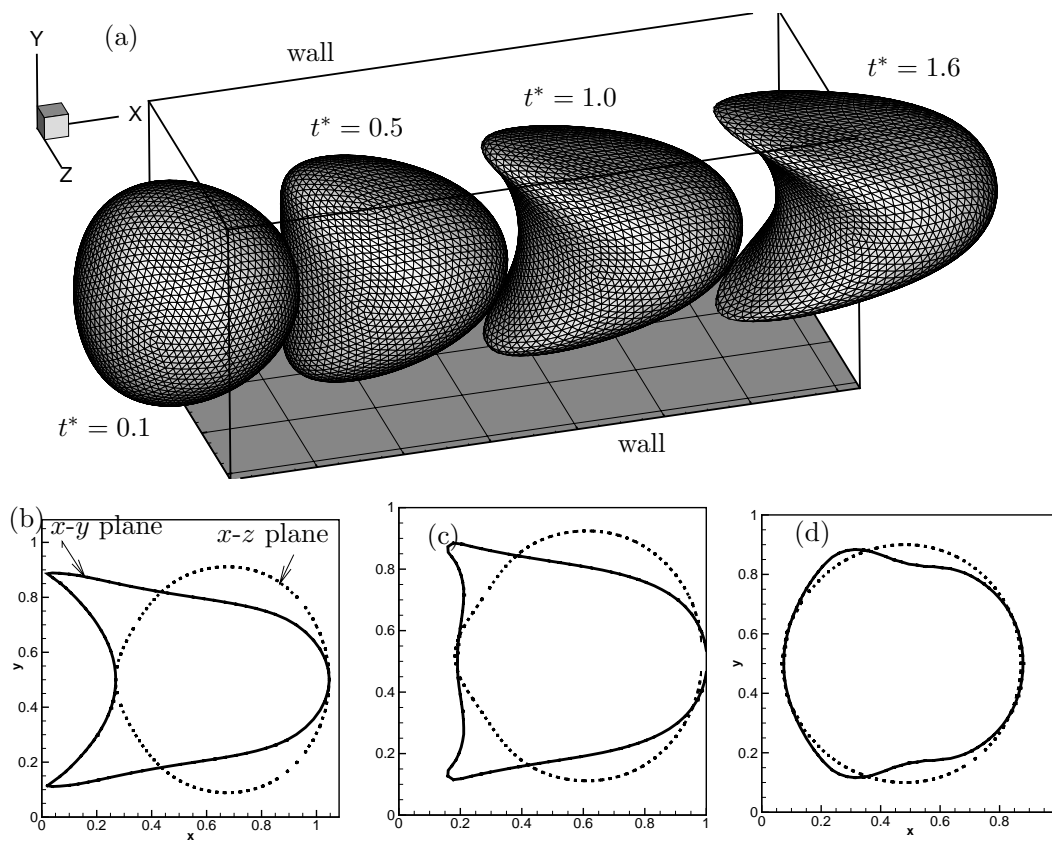


Figure 6.2: Transient shapes of the initially spherical capsule with $Ca = 0.6$ and $H/d = 1.25$ shown in (a). Also shown are 2D slices on the $x-y$ and $x-z$ planes for three values of Ca with $Ca = 0.6$, 0.1 and 0.02 corresponding to (b), (c) and (d) respectively, at $t^* = 1.6$.

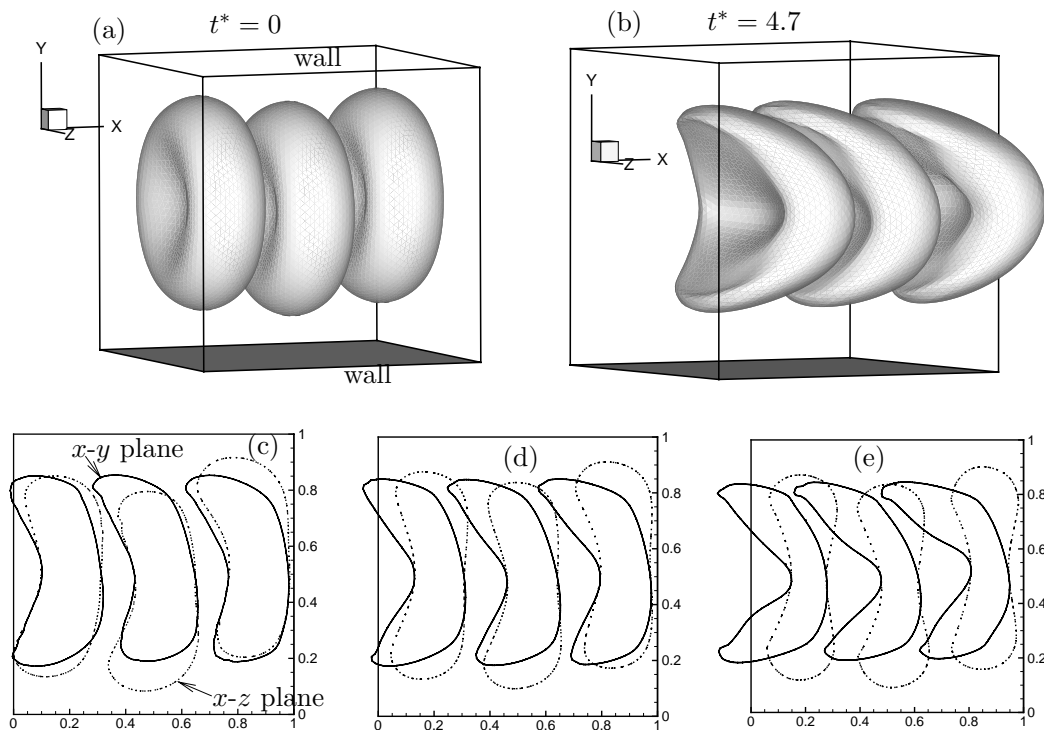


Figure 6.3: Transient shapes of the initially biconcave capsule with $Ca = 0.6$ and $H/d = 1.37$ shown in (a). Also shown are 2D slices on the $x-y$ and $x-z$ planes for three values of Ca with $Ca = 0.05, 0.2$ and 0.6 corresponding to (b), (c) and (d) respectively, at $t^* = 4.8$.

velocities (Secomb 2003). Note that unlike cell motion in a cylindrical tube, the cell shape here is not axisymmetric. 2D slices on the $x-y$ and $x-z$ planes for three values of Ca are shown in figures 6.2b, c and d for spherical capsules at $t^* = 1.6$ and in figures 6.3c, d and e for biconcave cells at $t^* = 4.8$. The maximum deformation occurs in the $x-y$ plane; in the $x-z$ plane the cell shape remains nearly circular or biconcave for all Ca . Amount of deformation decreases and the sharp cusps disappear with decreasing Ca . For $Ca = 0.1$, the spherical cell becomes concave near the trailing edges but changes to convex near the center. At $Ca = 0.02$, only small deviation from the spherical shape is observed. For the biconcave cells at lower Ca , the dimple near the center diminishes, and the cell shapes resemble a cylindrical pellet.

6.2.3 Multi-file motion

Next we present the results on multifile motion of a suspension of deformable cells flowing in a channel under a constant driving pressure. The undeformed channel height to cell size ratio H/d varies from 1.6 to 6.3. The channel (tube) hematocrit, which is the cell volume fraction, $H_t = 5 - 26\%$. The number of cells in the simulations varies from 3 to 131 within the computational domain. Table 6.1 lists the tube hematocrit, size ratio H/d , the number of cells N_c in the computation box, and the Eulerian resolution. For each case, at least three different Ca are simulated. We consider both initially spherical and biconcave capsules. At $t^* = 0$, cells are distributed randomly in the computation domain. For lower H_t , the initial coordinate of the center-of-mass of each capsule can be obtained from a random number generator. This is, however, not an efficient way for higher H_t . For the latter case, we follow the method of Bunner & Tryggvason (2002) in which the cells are first arranged in a regular lattice and then given a small but random displacement. For higher hematocrit, cells span across the entire channel height. For lower H_t , a center-weighted distribution is taken to reduced computation time since the lateral migration would eventually result in to a higher concentration near the center. For the biconcave cells, the cell orientation with respect to the flow is also taken to be random. But the ensemble average orientation at a given lateral location is taken to be close to the local gradient of the flow so that the suspension reaches steady state over a short time. During the course of the simulations, fluid and cell velocity, pressure, cell coordinates are stored at frequent intervals which are post-processed to obtain time-averaged rheology.

Instantaneous cells shapes and distribution from a few representative simulations are shown in figure 6.4 for spherical capsules at $Ca = 0.6$ and $H_t = 26\%$, and in figure 6.6 for biconcave cells at $Ca = 0.6$ and $H_t = 23\%$. The computational domain is also shown for each case. Note that the driving flow is in x direction, and the domain is periodic in x and z directions. Figure 6.4a shows a two-file arrangement for which $H/d = 1.6$, and the computational domain contains two off-centered capsules. This simulation was done using 120^3 Eulerian nodes. Cells deform significantly and attain a slipper shape with a sharp

Table 6.1: Size ratio (H/d), vessel hematocrit (H_t), number of cells per computational box (N_c), and Eulerian resolution used in the present simulations.

	H/d	$H_t\%$	N_c	Resolution
spherical cells	6.3	26	122	$160 \times 161 \times 160$
		18	84	
		12	56	
		5	23	
	4.5	26	44	$120 \times 121 \times 120$
		18	30	
		12	20	
		5	8	
	3.1	26	15	$120 \times 121 \times 120$
	2.4		7	
	1.6		2	
	1.25		1	
biconcave cells	4.9	26	113	$160 \times 161 \times 160$
	3.1	26	31	$120 \times 121 \times 120$
	2.5		16	
	1.4		3	

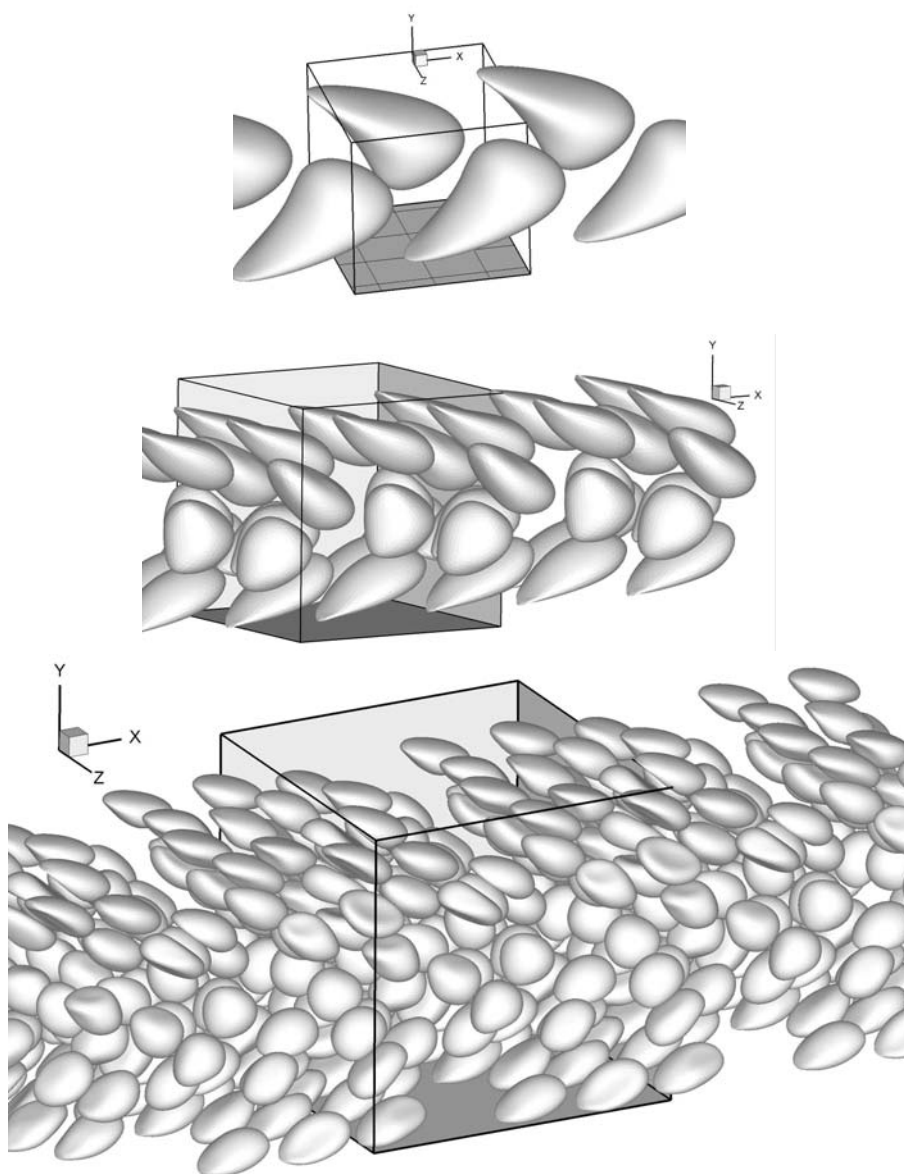


Figure 6.4: Instantaneous snapshots for suspension of spherical cells after the flow has reached a stationary state for $H/d = 1.6$ (top), $H/d = 3.1$ (middle), and $H/d = 6.3$ (bottom).

cusp at the trailing edge. Deformation is non-symmetric due to initial off-centering. The computed shape is in qualitative agreement with the non-axisymmetric single- or two-file motion of erythrocytes at high velocity in glass tubes with internal diameter $\approx 10\text{--}15\ \mu\text{m}$. Figure 6.4b shows a snapshot for a three-file arrangement for $H/d = 3.1$ for which the computational box contains 16 capsules and 120^3 Eulerian nodes. Cells located near the channel walls deform in to a slipper shape with sharp cusps at the trailing edges. Cells flowing near the center deform less due to reduced local shear. Cells moving in a multifile manner are shown in figure 6.4 for $H/d = 6.3$ with 122 capsules in the computational box that is comprised of 160^3 Eulerian points. The slipper shapes are no longer seen; rather, cells near the walls are more ellipsoidal and disk shaped, and those near the center are nearly spherical. Cell deformation in this case is primarily due to interaction with the adjacent cells. For the two-file arrangement in figure 6.4a, there is no ‘slip’ between two cells, and the relative position between them remains constant. For multifile motion as in figures 6.4b and c, cell near the center flow at higher velocity. The relative slip between two cell layers results in increased binary collision as H/d increases. The flattening of the cell surface, and appearance of dimples as seen in figure 6.4c are the consequence of such binary collisions (Loewenberg & Hinch 1997).

Each simulation is run for a long time after the initial transience is passed and the mean quantities are extracted by averaging over a large time window over which the suspension remains statistically stationary. To check if the suspension has reached a statistically steady state, we follow the time history of relative suspension viscosity defined as

$$\mu_{rel}(t^*) = \frac{\mu_{app}(t^*)}{\mu_p} = \frac{Q_p}{Q(t^*)} \quad (6.2.2)$$

where μ_{app} is the instantaneous apparent viscosity of the whole suspension, μ_p is the plasma viscosity, Q_p is the flow rate of Poiseuille’s profile, and

$$Q(t^*) = \left(\iiint_{x,y,z=0}^H u dx dy dz \right) / H \quad (6.2.3)$$

is the time-dependent flow rate averaged over the entire computational box. Figure 6.5 presents $\mu_{rel}(t^*)$ over time for several runs. The relaxation time of the suspension depends

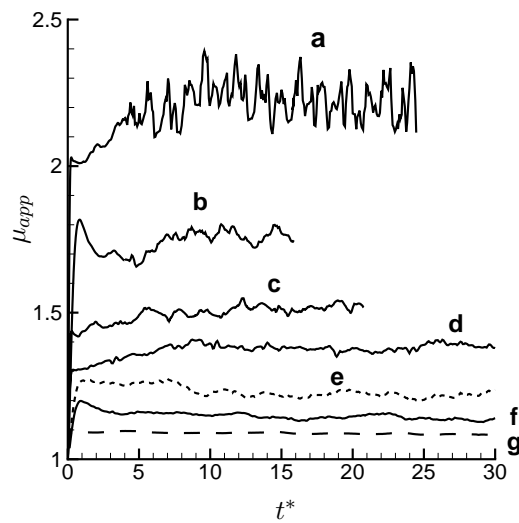


Figure 6.5: Time history of apparent viscosity. a: $Ca = 0.05$, $H_t = 0.26$, $d/H = 0.16$; b: $Ca = 0.6$, $H_t = 0.26$, $d/H = 0.16$; c: $Ca = 0.05$, $H_t = 0.18$, $d/H = 0.16$; d: $Ca = 0.05$, $H_t = 0.18$, $d/H = 0.22$; e: $Ca = 0.6$, $H_t = 0.18$, $d/H = 0.22$; f: $Ca = 0.6$, $H_t = 0.12$, $d/H = 0.22$; g: $Ca = 0.05$, $H_t = 0.05$, $d/H = 0.22$;

on the cell deformability, volume fraction, and H/d ratio. In general, the relaxation time is higher for suspension of more deformable cells at lower hematocrit due to center-ward migration of the cells which is a slower process. For higher hematocrit, cells fill the entire channel cross-section preventing such migration, and the suspension takes shorter time to attain a statistical steady state. The relaxation time is usually less than $t^* = 5$, and the duration of simulations vary from $t^* = 15$ to 60. On average, cells in the simulations travel by a distance of about 15 to 50 computational boxes or 50 to 500 cell diameter.

Visualizations from multiframe motion of biconcave capsules are shown in figure 6.6 Also shown is an initial arrangement. Deformation of cells is evident in the figure. As the flow develops, cells near the upper wall initially rotate in the counterclockwise direction, while those near the lower wall rotate clockwise, in accordance with the direction of vorticity of the flow. However, continuous tumbling motion that is present for a biconcave cell in dilute suspension is no longer observed at higher hematocrit. Interaction with the neighboring cells inhibits continuous tumbling. In some cases, such interaction may cause reversal of the direction of rotation. Eventually cells near the wall align with the flow direction and do not show any further rotation. Alignment decreases with increasing distance from the wall, and most cells near the center flow with nearly vertical alignment. Cells near the wall deform more and lose their biconcave shape, and assume disk-like shape. Cells near the channel center deform less and assume slipper shapes. This behavior is expected since deformation depends on the local shear rate which decreases from the wall toward the center. As the size ratio H/d increases from 3.1 to 4.9, slipper shapes become less evident. Formation of a cell-depleted layer near the wall is evident in the figure. For the biconcave cells, as the figure suggests, cell-free layer develops due to center-ward lateral motion of the cells as well as due to horizontal alignment of the cells close to the wall. For spherical capsules, only the center-ward motion is responsible for the formation of the cell-free layer.

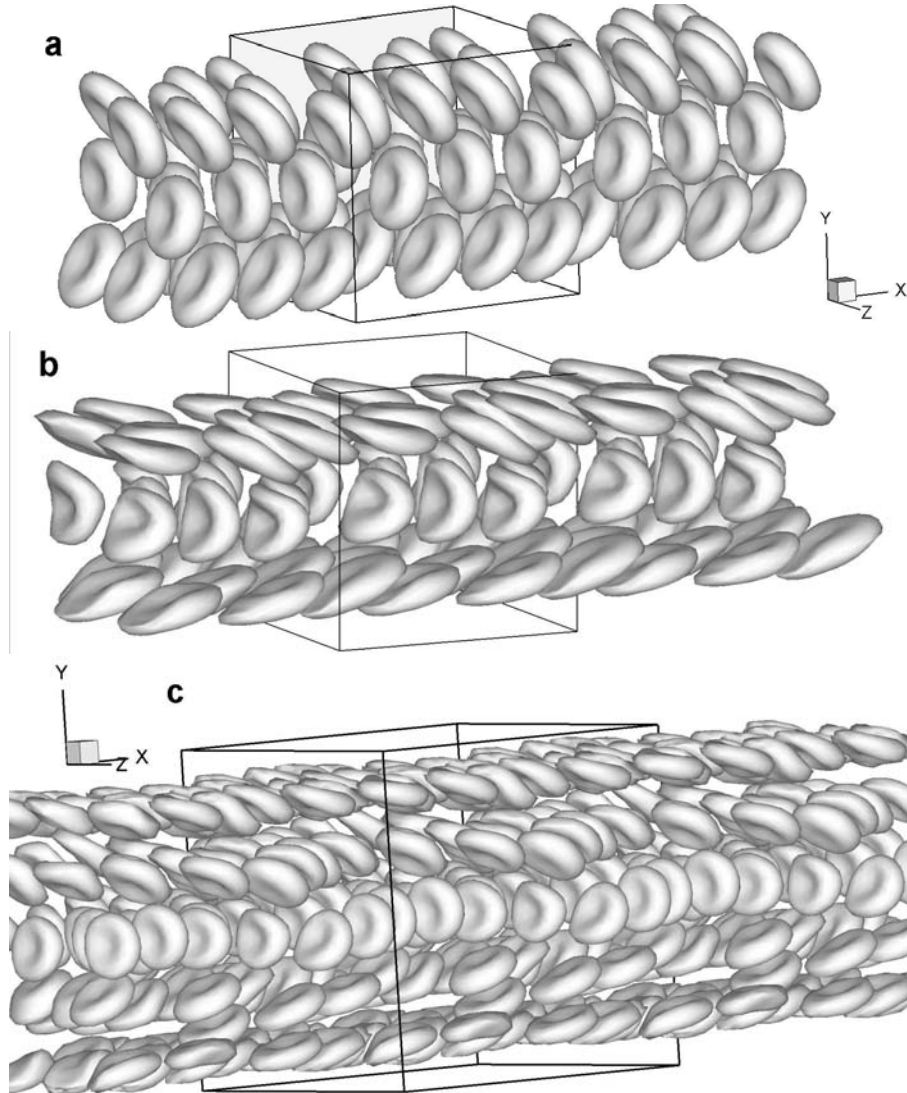


Figure 6.6: Instantaneous snapshots for suspension of biconcave cells. (a) Initial distribution and cell shape for $H/d = 3.1$. (b) and (c) show distribution and cell shape for $H/d = 3.1$ and 4.9, respectively, after the flow has reached a stationary state.

Cell trajectory and velocity traces

Position and velocity of individual cell are tracked in time in the simulations. These data allow us to visualize three-dimensional cell trajectory and velocity over time. Results on cell trajectories and instantaneous velocities are shown in figure 6.7. Here we consider lateral position (y) and lateral velocity (v) of cell centroids with respect to time. As evident, cells exhibit fluctuations in position and velocity due to interactions with neighboring cells. Though not shown here, fluctuations are also present in cross-stream location (z), and in axial and cross-stream velocities (u , and w) as the cells are dispersed in x and z directions as well. Figures 6.7a and b show results for a lower hematocrit of $H_t = 5\%$ for $Ca = 0.6$ and 0.005 , respectively. Center-ward migration of the cells in the near-wall regions is evident for higher Ca but not for lower Ca . The rate of migration in the suspension is less due to interaction from neighboring cells. Further, unlike in a dilute suspension, migration is not continuous. Motion at a higher hematocrit (18%) is shown in figures 6.7c and d for $Ca = 0.6$ and 0.005 , respectively. At this higher H_t , center-ward migration is nearly inhibited. However, fluctuations in lateral position have increased due to increasing cell-cell interaction. Also evident in figure 6.7d is formation of three layers of cells for lower Ca as the suspension reaches a stationary state implying a stack-like motion of the suspension. Such layered distribution is not prominent at higher Ca . Fluctuation in cell velocity is another indication of cell-cell interaction in the suspension. Velocity fluctuation increases with increasing hematocrit and decreasing Ca .

Root-mean-square (rms) of the fluctuations in the lateral position (y') and axial velocity (u') can be used as a measure of hydrodynamic dispersion. Once the suspension reaches a stationary state, these quantities are calculated in dimensionless form as (Bagchi 2007)

$$y' = \frac{\left[\int_0^t (y(t) - \bar{y})^2 dt / T \right]^{1/2}}{d}, \quad (6.2.4)$$

and

$$u' = \frac{\left[\int_0^t (u(t) - \bar{u})^2 dt / T \right]^{1/2}}{\bar{u}}, \quad (6.2.5)$$

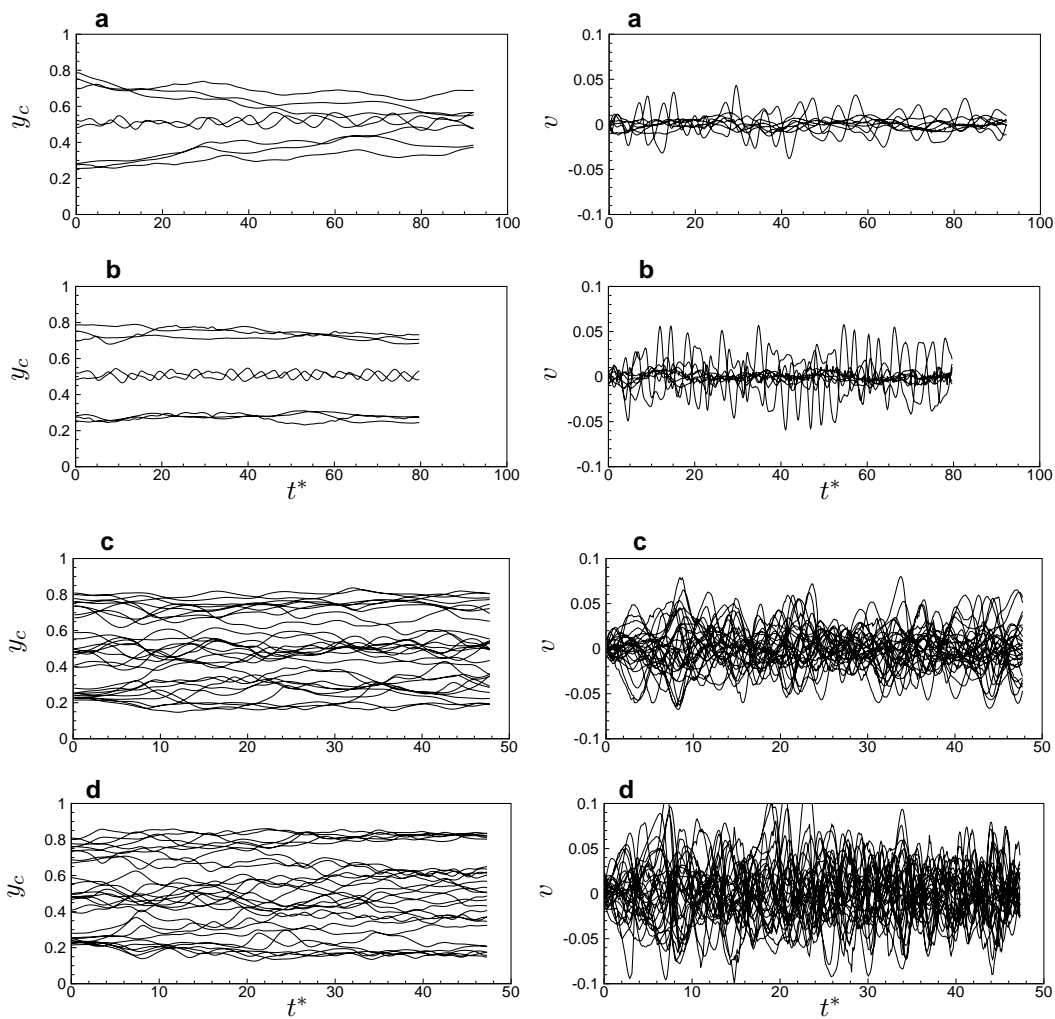


Figure 6.7: Sample cell trajectory (left panel) and velocity traces (right panel) for $H/d = 4.5$. (a) $Ca = 0.6$, $H_t = 0.05$; (b) $Ca = 0.005$, $H_t = 0.05$; (c) $Ca = 0.6$, $H_t = 0.18$; (d) $Ca = 0.005$, $H_t = 0.18$.

where \bar{y} and \bar{u} are the mean lateral position and axial velocity of a cell, and T is the time window over which data is collected. Figure 6.8a shows the variation of y' over the vessel cross-section for three different values of H_t (26, 18, and 5%) for $H/d = 6.3$ and $Ca = 0.05$. Here symbols represent individual cells, and lines are the quadratic fit through the data. In general, lateral position of a cell fluctuates over 1–25% of its diameter. We note that y' is higher near the center and reduces towards the wall. This is due to an increased local hematocrit (discussed later in figure 6.10) near the vessel center that resulted from the lateral migration of the cells. The best-fit curves become more parabolic at lower hematocrit, but it flattens at higher hematocrit. This is because at higher hematocrit, cells are nearly uniformly distributed over the cross-section, whereas at lower hematocrit, they migrate to the center, as shown earlier in figure 6.7.

Also shown in figure 6.8a is the range of rms fluctuation measured in vivo by Bishop *et al.* (2002) for red blood cells flowing in venules of 40–80 micron diameter in rat spino-trapezius muscle. On average, the in vivo data predicts higher fluctuation than those in the simulations.

The effect of cell deformability is shown in figure 6.8b which shows increasing rms fluctuation with decreasing Ca . This is because binary interaction results in higher lateral displacement of nearly rigid cells than that of deformable cells. The effect of H/d is shown in figure 6.8c which shows that y' profile becomes more flattened with increasing H/d . We also present a comparison of y' and z' in figure 6.8d. Variation of z' over the cross-section is nearly uniform unlike the parabolic variation of y' . The peak z' is also less than that of y' implying that hydrodynamic dispersion in the velocity gradient direction is higher than that in the direction of vorticity in agreement with earlier works on binary collision of liquid drops (Loewenberg & Hinch 1997).

The rms velocity fluctuation u' is shown in figure 6.9. u' decreases from the wall toward the center as the mean cell velocity \bar{u} increases. Dependence of u' on H_t is considered in figure 6.9a. u' increases with increasing H_t as \bar{u} decreases (shown later in figure 6.16). Velocity fluctuations in the simulations vary from 1–10% of the mean velocity. In contrast,

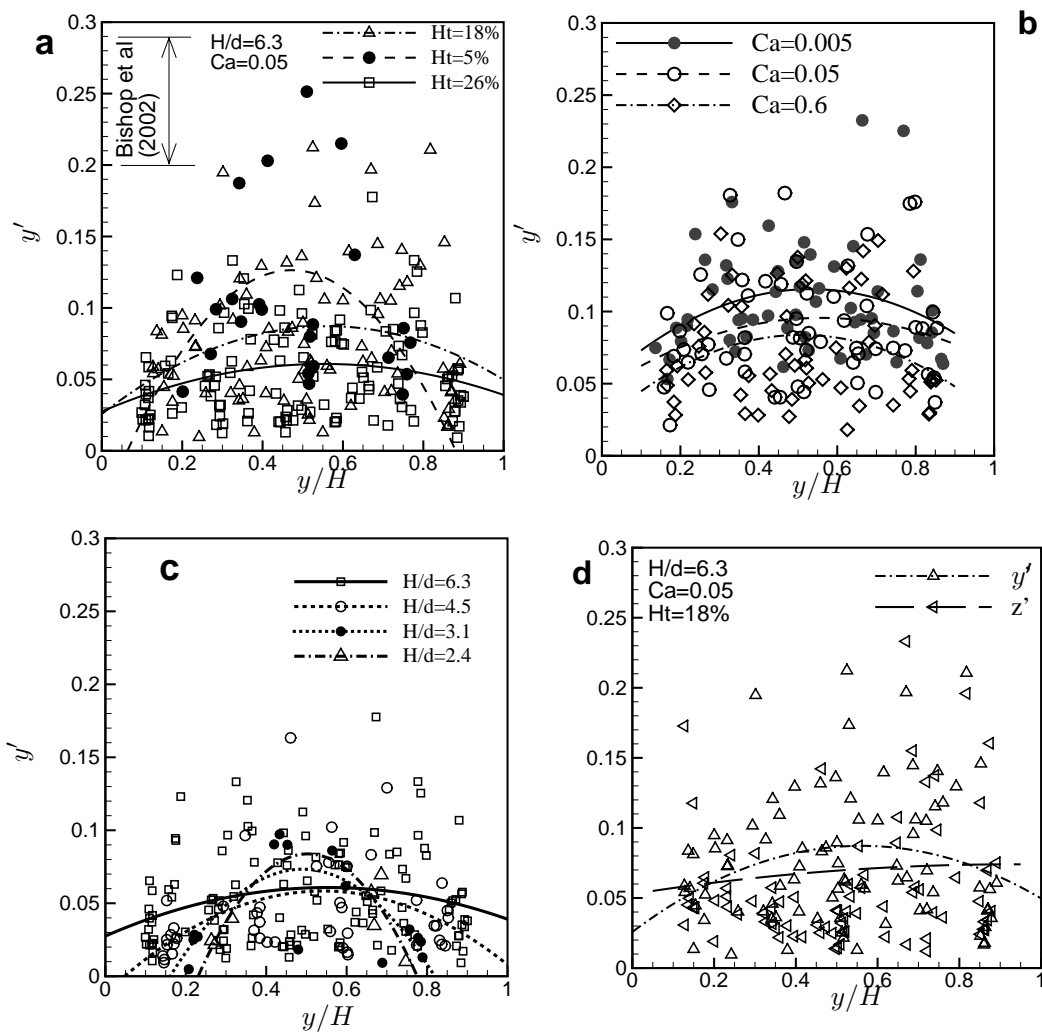


Figure 6.8: RMS fluctuation y' over channel cross-section. Effect of (a) hematocrit, (b) Ca , and (c) H/d . Fluctuations in two cross-stream directions are compared in (d).

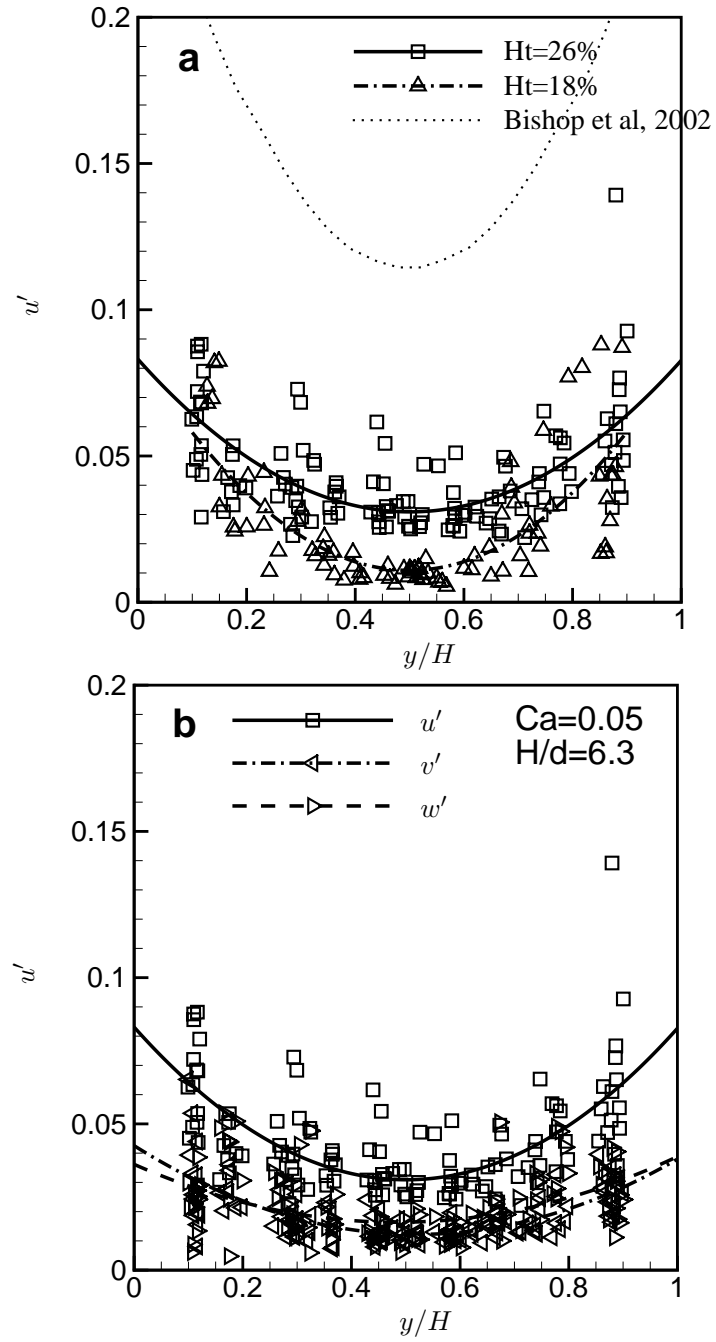


Figure 6.9: RMS velocity fluctuation over channel cross-section. (a) Effect of hematocrit is shown for $H/d = 6.3$ and $Ca = 0.05$. Also shown is the in vivo data of Bishop *et al.* (2002) (dotted line). (b) RMS of three velocity components.

the in vivo data of Bishop *et al.* (2002) which is also shown in the figure give higher velocity fluctuations as it did for rms position. Possible reasons for the difference are discussed later. Figure 6.9b compared the rms velocity fluctuations in three directions. Fluctuations in v and w components are similar in magnitude but less than that of u .

Cell-free layer

The simulations allow us a direct estimation of the cell-free layer thickness. This is obtained by from the cross-sectional variation of “local” hematocrit $H_c(y)$. Once the cell suspension has reached a statistically stationary state, the capsule distribution at frequent intervals are analyzed to obtain $H_c(y, t)$ at several time instances which are then averaged to obtain $H_c(y)$. The indicator function $I(x, y, z, t)$, as described in section 2.1.2 can be used to calculate $H_c(y, t)$. Noting that I changes from zero to one across the capsule membrane, we have

$$H_c(y, t) = \frac{\int_x \int_z I(x, y, z, t) dx dz}{\int_x \int_z dx dz} \quad (6.2.6)$$

Figure 6.10 shows the ratio $H_c(y)/H_t$ for spherical cell ($H/d = 6.3$) and biconcave cell ($H/d = 4.9$). The ratio goes to zero near the wall ($y/H \rightarrow 0$ in the figure) indicating particle depletion in the near-wall region. Away from the wall, $H_c(y)/H_t \approx 1$. The thickness of the cell-free layer, denoted by δ , can be precisely calculated from such plots, and is given in figure 6.11 in dimensionless form as $\delta/(H/2)$ as a function of H_t and H/d for different Ca and spherical and biconcave cells.

Figure 6.11a shows that $\delta/(H/2)$ decreases with increasing hematocrit and decreasing Ca . The reduction of δ with decreasing Ca is due to reduced center-ward migration of the cells. Figure 6.11b shows that $\delta/(H/2)$ decreases with increasing vessel size. Also presented in figure 6.11b is the in vivo data from Kim *et al.* (2007). Only qualitative comparison can be made, as the simulations represent flow in channels rather than cylindrical vessels. Further, Kim *et al.* (2007)’s data is for $H_d \approx 40\%$, while simulation results are for $H_d \approx 30\%$. Thus, the simulations predict lower $\delta/(H/2)$ in comparison to the in vivo data. This is possibly due to the limitation of the immersed boundary method implemented here which does not

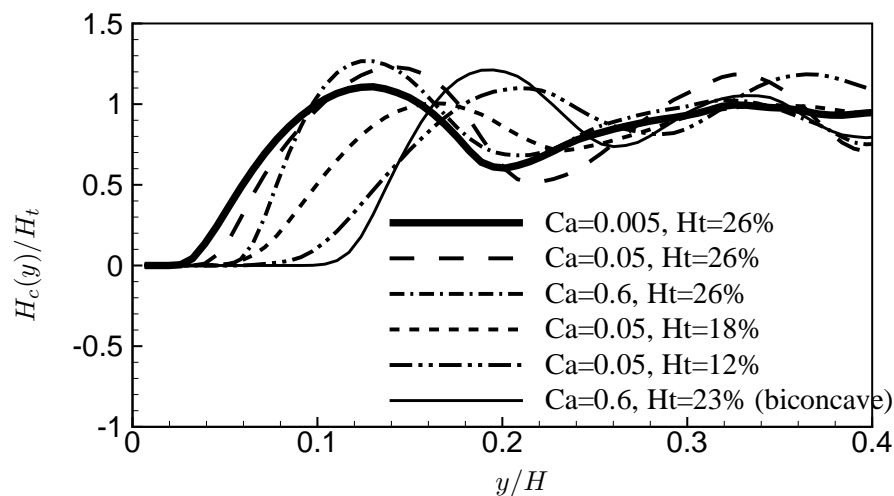


Figure 6.10: Cross-sectional variation of hematocrit. Results are shown for half channel width; $y/H = 0$ is the wall and $y/H = 0.5$ is the center.

allow the cells to physically contact each other yielding a higher intercellular spacing. The difference could also arise from limitation of the cell membrane model. Further the in vivo data may yield a reduced cell-free layer width due to nonuniform vessel geometry, branching and convergence, and influence of leukocytes.

Also note in figure 6.10 that $H_c(y)$ approaches its value at the core smoothly, rather than a sudden step change assumed in two-phase models for blood flow in small vessels (to be discussed later). The slope of $H_c(y)$ across the interface of the cell-free layer and the core region decreases with decreasing Ca and decreasing H_t . This is because highly elongated cells at higher Ca favor a more closed-pack distribution and hence a higher slope of $H_c(y)$. In contrast, lower hematocrit results in more cell-cell separation distance, and hence reduced slope of $H_c(y)$. As will be shown later, these results have consequences in the modeling of mean blood flow in microvessels.

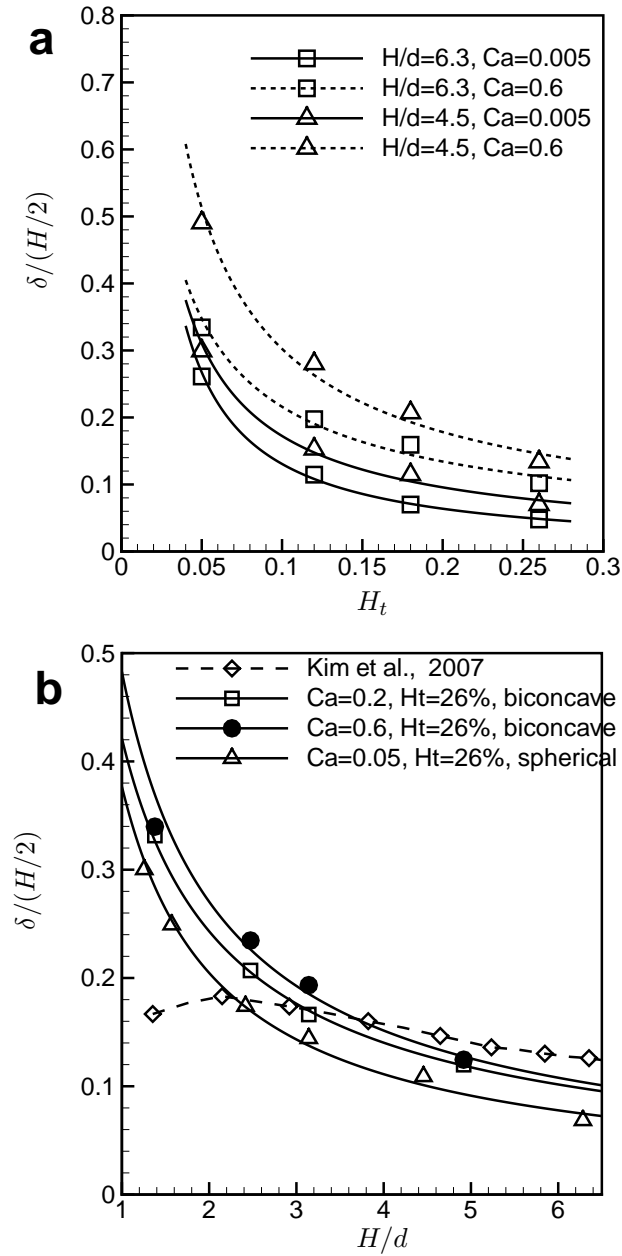


Figure 6.11: Dimensionless cell-free layer width $\delta/(H/2)$ as a function of (a) H_t for two values of Ca and H/d for spherical cells, and (b) as a function of H/d for biconcave and spherical cells. Also shown in (b) is the in vivo data of Kim *et al.* (2007).

Plug-flow profile

Mean (averaged in time, and in x and z directions) velocity profile of the cell suspension over the channel cross-section is shown in figure 6.12. Also shown is the parabolic profile of Poiseuille flow for the same pressure gradient. Results for spherical capsules are shown in figures 6.12a–c, and for biconcave cells in figure 6.12d. The effect of vessel size is considered in figure 6.12a at fixed $Ca = 0.05$ and $H_t = 26\%$. Experimental measurements of blood velocity shows the well-known plug-flow profile which is characterized by a parabolic profile near the wall and nearly constant velocity near the vessel center. Simulation results show a prominent plug-flow profile for the smallest vessel considered here ($H/d = 1.25$) for which single-file motion occurs. Constant velocity occurs in nearly 60% of the vessel cross-section. As H/d increases, the velocity profiles depart from plug-flow toward a blunt parabola. Qualitative comparison of this trend can be made with the in vivo measurements of Bishop *et al.* (2002) who obtained an empirical relation $u/U_{max} = 1 - (r/R)^k$ with k in the range 2.1 to 2.2 for blood flow in 45–75 μm venules. A clear plug-flow profile occurs when $k = 3$, and a parabolic profile occurs when $k = 2$. The present numerical results also predict values of k in the same range as that of Bishop *et al.* (2002). The bluntness of the profile increases with increasing hematocrit and decreasing vessel size. The mean velocity decreases with increasing H/d due to increasing number of cells, and hence more interfacial contacts, causing increased energy dissipation. For the same reason, the mean velocity decreases with increasing hematocrit, as well, as shown in figure 6.12b. Also shown in figure 6.12b is the mean velocity of several cells which is a Lagrangian quantity. In experiments, most often the velocity of the cells are measured and assumed to be equal to the Eulerian fluid velocity. The data shown in figure 6.12b shows that the difference between the cell velocity and the Eulerian fluid velocity is indeed insignificant.

Figure 6.12c shows that the mean velocity decreases also with decreasing Ca . This is probably due to additional energy loss due to increased fluctuation in cell velocity, and increased tank-treading and tumbling frequencies. Results for biconcave cells are shown in figure 6.12d for different H/d . As in case of spherical cells, the mean velocity of biconcave cell

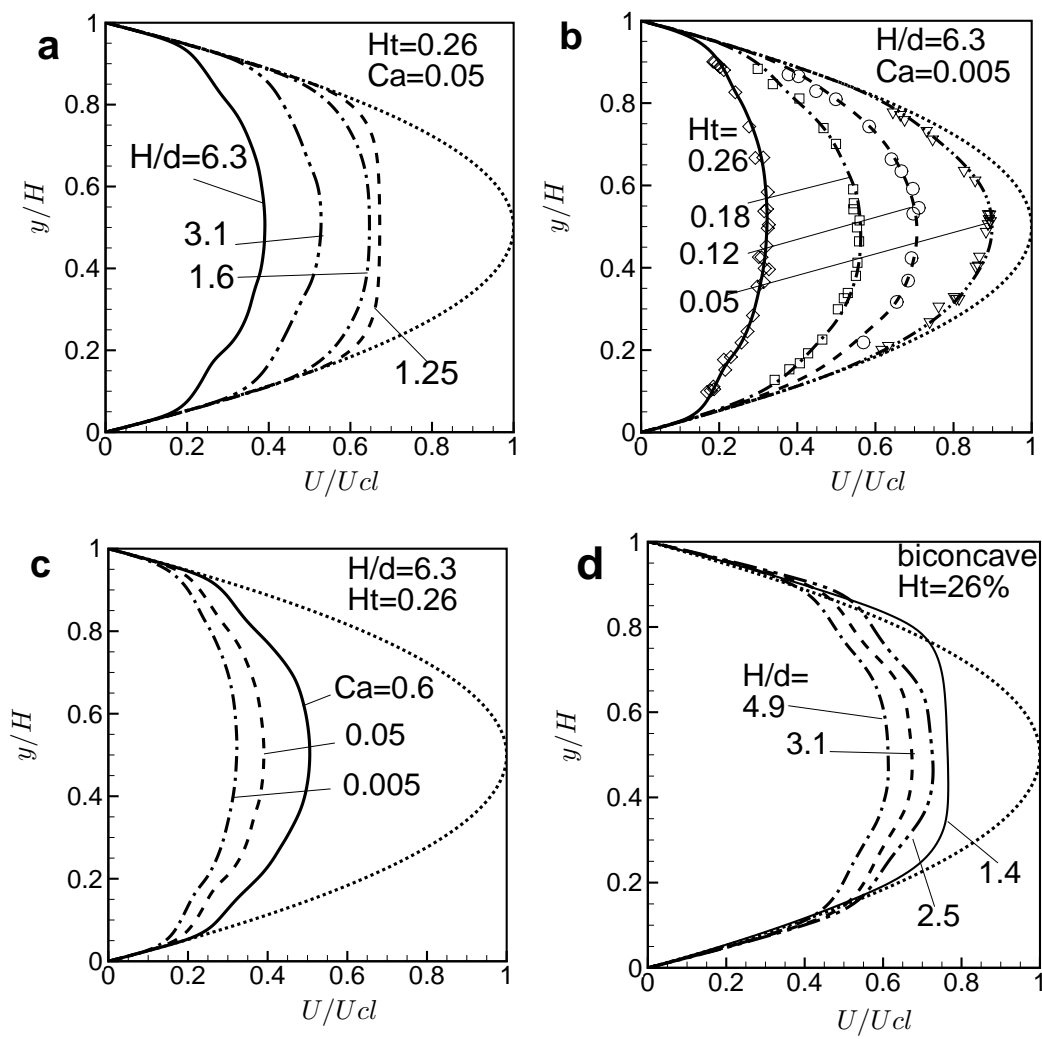


Figure 6.12: Mean velocity profile. Dotted line is the parabolic flow. In (b) symbols are the Lagrangian cell velocity.

suspension decreases with increasing H/d . Interestingly, for similar parameters, a biconcave cell suspension gives higher velocity than a spherical cell suspension. This is because of the near-horizontal orientation of the biconcave cells located near the wall, as shown in figure 6.6, which causes a larger cell-free layer.

Fahraeus-Lindqvist and Fahraeus Effects

Eq 6.2.2 can be integrated over time to obtain average values of the relative apparent viscosity μ_{rel} which depends on hematocrit, vessel size and cell deformability. The Fahraeus-Lindqvist effect refers to the decrease in μ_{rel} as the vessel size decreases. μ_{rel} computed from the present simulations are shown in figure 6.13a as a function of the size ratio H/d for three values of Ca and at $H_t = 26\%$. Results for spherical and biconcave capsules are shown. As evident in the figure, the Fahraeus-Lindqvist effect is qualitatively predicted by our simulations. Results also suggest that μ_{rel} increases with decreasing Ca . This is due to decreasing cell-free layer, as discussed in figure 6.11, as well as increased velocity fluctuations, as discussed in figure 6.12, resulting in higher dissipation with decreasing Ca . The figure also shows that for the range of Ca considered, μ_{rel} for the biconcave cells is less than that for the spherical cells. This is due to the larger extent of the cell-free layer arising due to the tilting of the biconcave cells as discussed in figures 6.6 and 6.12. Results from our simulations are compared with the in vitro data given in Pries *et al.* (1990, and 1992) who compiled a comprehensive database on in vitro measurements of blood viscosity by a number of investigators. Using the database, Pries *et al.* (1992) obtained an empirical relation for μ_{rel} as a function of hematocrit and vessel size. Relative viscosity obtained from their expression for $H_t = 26\%$ and as a function of d/H are also plotted in figure 6.13a. Simulation results for biconcave cells agree well with the empirical relation of Pries *et al.* (1992). It should be mentioned that the comparison in figure 6.13a should be taken as qualitative only as the simulations considered here represent blood flow in a microchannel whereas the empirical relation is based on blood flow in glass tubes.

Another important physiological phenomenon observed for blood flow in small vessels

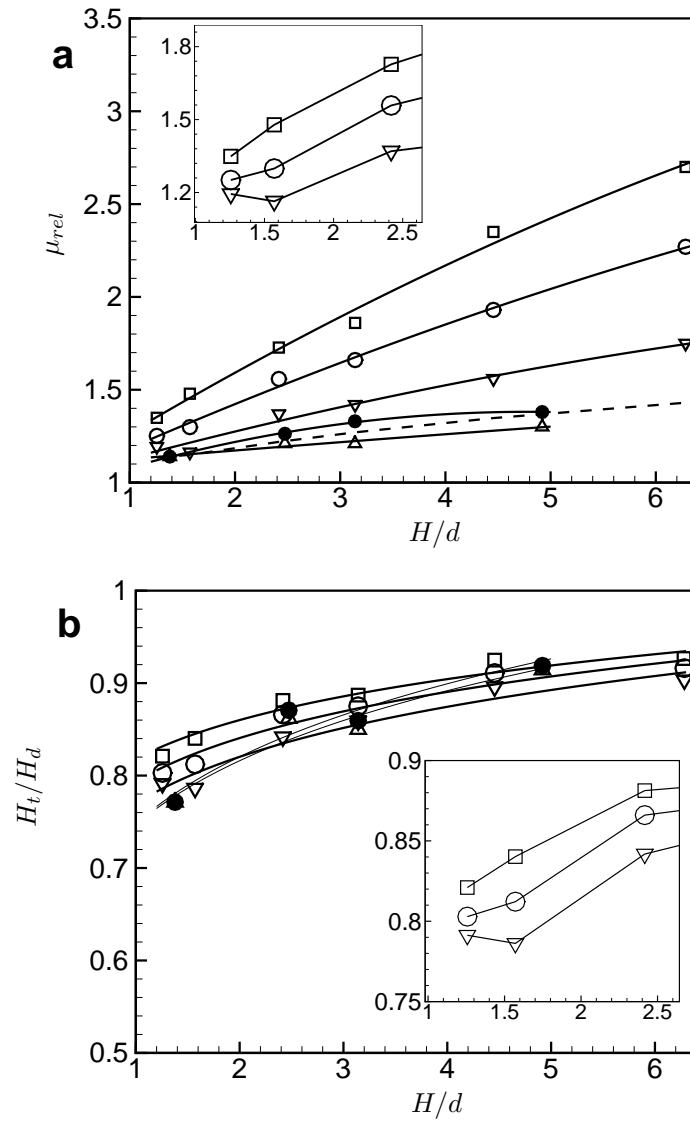


Figure 6.13: Fahraeus-Lindqvist and Fahraeus effects. Variation of (a) relative apparent viscosity μ_{rel} and (b) hematocrit ratio H_t/H_d as a function of vessel size for different Ca at $H_t = 26\%$. Results for spherical cells are shown for $Ca = 0.005$ —□—, $Ca = 0.05$ —○—, and $Ca = 0.6$ —▽—. Results for biconcave capsules are shown for $Ca = 0.05$ —●— and $Ca = 0.2$ —△—. In (a), dash line is the correlation of Pries *et al.* (1992) based on in vivo data. The insets in (a) and (b) show the results for lower range of H/d .

is the Fahraeus effect which refers to the decrease in the ratio of the vessel to discharge hematocrit H_t/H_d with decreasing vessel size. Simulation results for time-averaged H_t/H_d are shown in figure 6.13b as a function of H/d for three values of Ca and at $H_t = 26\%$ for spherical and biconcave capsules. Note that in the simulations H_t is specified, and the ratio H_t/H_d is extracted *posteriori* from the simulations as $H_t/H_d = \bar{U}/\bar{V}_c$ which is the ratio of the mean (time- and space-averaged) suspension velocity to the mean (time and ensemble-averaged) cell velocity. As evident in the figure, our simulations qualitatively predicted the Fahraeus effect. The figure also shows that H_t/H_d increases with decreasing Ca . There are two competing mechanisms that affect the dependence of H_t/H_d on Ca . First, the extent of the cell-free layer decreases with decreasing Ca so that \bar{U} approaches \bar{V}_c . Second, \bar{U} (hence, \bar{V}_c) decreases with increasing Ca .

Experiments using erythrocyte suspension in capillary glass tubes showed that decreasing the tube diameter below 8–10 μm results in a *reverse* Fahraeus and Fahraeus-Lindqvist effects, that is, the relative viscosity and hematocrit ratio increase with decreasing tube diameter. This is due to the transition from multifile to single-file type motion in which the cells flow in a tightly-fit manner and the friction between the cell and the wall causes the increased viscosity. The minimum relative viscosity and hematocrit ratio are obtained for tube diameter of 8–10 μm . Although simulating tightly-fitted cells is not of interest here, the present results on single-file motion suggest interesting feature of the reverse Fahraeus and Fahraeus-Lindqvist effects. In figure 6.13 the simulation results for lower range of H/d are shown in the insets. A reversing trend of μ_{rel} and H_t/H_d for $Ca = 0.6$ is evident in the figure. When curves for three capillary numbers are compared, results suggest that the vessel size at which μ_{rel} and H_t/H_d become minimum decreases with decreasing Ca . This is again due to wider cell-free layer at higher Ca .

6.2.4 Comparison of DNS results with two-phase model

Flow of blood in microvessels is often described by a two-phase model in which the vessel is divided into a cell-free region of thickness δ and a core region of $H - 2\delta$ as shown in figure

6.15a. Since the mean flow is steady and unidirectional, one can write

$$\frac{d\tau_{xy}}{dy} = \frac{dP}{dx} \quad (6.2.7)$$

where

$$\tau_{xy} = \mu(y)\dot{\gamma}(y) \quad (6.2.8)$$

is the shear stress, and $\dot{\gamma} = du/dy$ is the “local” shear rate. The above equations accounts for viscosity variation over the cross-section of the vessel. In the two-phase model, one writes $\mu(y)$ as

$$\mu(y) = \mu_f + (\mu_c - \mu_f) \mathcal{H}(y - \delta) \quad \text{for } 0 \leq y \leq H/2 \quad (6.2.9a)$$

$$= \mu_c + (\mu_f - \mu_c) \mathcal{H}(y - H + \delta) \quad \text{for } H/2 \leq y \leq H \quad (6.2.9b)$$

where μ_f and μ_c are the viscosity of the cell-free and core regions, respectively, and \mathcal{H} is the Heaviside function. In the two-phase model, μ_f and μ_c are assumed to be constants. Using appropriate boundary conditions, that is, no-slip at the wall, symmetry at the centerline, and continuity of velocity and shear stress at the interface at $y = \delta$, the solution is obtained as

$$u_f(y) = -\frac{dP}{dx} \frac{H^2}{2\mu_f} \left(\frac{y}{H} - \frac{y^2}{H^2} \right) \quad \text{for } 0 \leq y \leq \delta \quad (6.2.10a)$$

$$u_c(y) = -\frac{dP}{dx} \frac{H^2}{2\mu_f} \left[\frac{\mu_f}{\mu_c} \left(\frac{y}{H} - \frac{y^2}{H^2} \right) + \left(1 - \frac{\mu_f}{\mu_c} \right) \left(\frac{\delta}{H} - \frac{\delta^2}{H^2} \right) \right] \quad (6.2.10b)$$

for $\delta \leq y \leq H/2$.

where $u_f(y)$ and $u_c(y)$ are the velocity of the cell-free and core regions, respectively. The profile is written only for $0 \leq y \leq H/2$ as it is symmetric about $y = H/2$. There are three unknown parameters: δ , μ_f and μ_c , the values of which are often taken *ad hoc* to match the experimental values of relative apparent viscosity. While recent high-resolution experimental measurements have yielded values of δ , experimental data on μ_f and μ_c are scarce. In reality, the interface between the core and the cell-free layers cannot be well

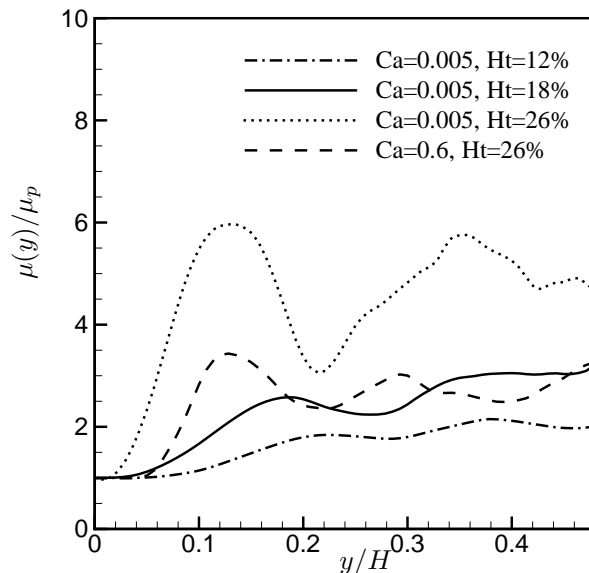


Figure 6.14: Cross-section variation of viscosity obtained from the simulations for some sample cases for $H/d = 6.3$. Results are shown for half channel width; $y/H = 0$ is the wall and $y/H = 0.5$ is the center.

defined as the cells are continuously dispersed due to hydrodynamic interaction. Thus the variation of viscosity across the vessel is expected to be smooth, rather than a step jump as in eq 6.2.9. Based on micro-PIV measurements of blood velocity, Long *et al.* (2004) and Damiano *et al.* (2004) showed that the “local” viscosity $\mu(y)$ varies smoothly across the channel, and it approaches μ_f near the wall, and μ_c near the center of the vessel.

The cross-section variation (or, “local” variation) of viscosity can be extracted from the present computational results following the approach used by Long *et al.* (2004) and Damiano *et al.* (2004) (also, Bagchi 2007). Since dP/dx is a constant, eq 6.2.7 can be integrated to give

$$\tau_{xy} = -\frac{dP}{dx} (y - H/2) \quad (6.2.11)$$

where we used the condition that $\tau_{xy} = 0$ at $y = H/2$. Invoking the constitutive relation

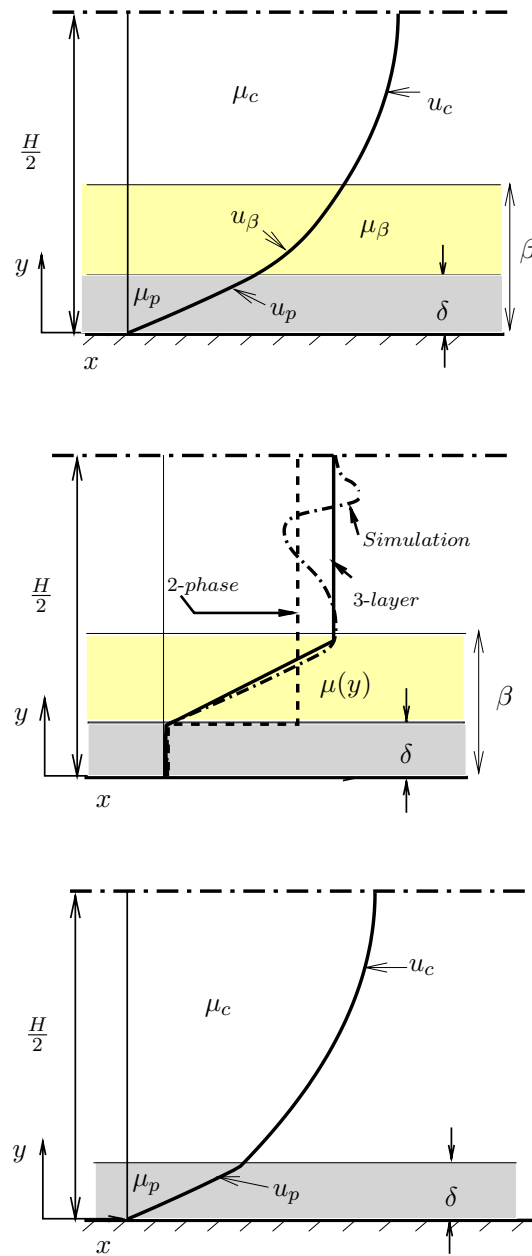


Figure 6.15: Schematic of two-phase (a) versus three-layer (b) models. In (c), cross-section variation of viscosity is shown. Only the lower half of the channel is shown.

given by eq 6.2.8 above, we get

$$\mu(y) = -\frac{dP}{dx} \frac{y - H/2}{\dot{\gamma}(y)} \quad (6.2.12)$$

A similar equation can be written for the Poiseuille flow of pure plasma. Then for a constant pressure drop,

$$\frac{\mu(y)}{\mu_p} = \frac{\dot{\gamma}_p(y)}{\dot{\gamma}(y)} \quad (6.2.13)$$

where $\dot{\gamma}_p(y)$ is the shear rate across the channel for the Poiseuille flow.

Simulations results for $\mu(y)/\mu_p$ are shown in figure 6.14. As expected $\mu(y)/\mu_p$ approaches unity near the wall, and it is higher than unity in the core region of the vessel. In the core region, it is often nonmonotonic with respect to y . The local maximum/minimum of $\mu(y)/\mu_p$ corresponds to the local maximum/minimum of the cell concentration shown earlier in figure implying high viscous dissipation near regions of interfacial contacts. Most importantly, over the interface of the core and cell-free layers, $\mu(y)/\mu_p$ varies smoothly, rather than the step-like manner assumed in the two-phase model. This smooth variation obtained from our simulation is in qualitative agreement with the micro-PIV measurement of Long *et al.* (2004) and Damiano *et al.* (2004). The slope of $\mu(y)/\mu_p$ across the interface of the cell-free and core regions increases with increasing H_t , and shows relatively less dependence with respect to Ca or H/d .

The simulations results of $\mu(y)/\mu_p$ and δ given in figures 6.14 and 6.11 respectively can be used to precisely calculate μ_f and μ_c as

$$\mu_f = \frac{1}{\delta} \int_0^\delta \mu(y) dy \quad \text{and} \quad \mu_c = \frac{1}{H/2 - \delta} \int_\delta^{H/2} \mu(y) dy \quad (6.2.14)$$

Their values are listed in Table 6.2. Interestingly, the cell-free layer viscosity μ_f is slightly higher than the plasma viscosity μ_p . This is likely due to occasional intrusion of the cells from the core region in to the cell-free layer due to the hydrodynamic interaction from the neighboring cells. Difference between μ_f and μ_p increases with increasing hematocrit and decreasing Ca . The core viscosity μ_c also increases with increasing hematocrit and

Table 6.2: Viscosity of the core (μ_c) and cell-free layer (μ_f), and the thickness $\beta - \delta$ of the transition layer obtained from the simulations

H/d	Ca	H_t	μ_f/μ_p	μ_c/μ_p for 2-phase model	μ_c/μ_p for 3-layer model	$\beta/(H/2)$	$(\beta - \delta)/(H/2)$
6.3	0.005	26	1.05	5.11	5.52	0.21	0.16
	0.05	26	1.05	4.02	4.25	0.20	0.13
	0.6	26	1.02	2.93	3.06	0.22	0.12
	0.005	18	1.02	2.45	2.68	0.37	0.30
	0.05	18	1.02	2.23	2.46	0.31	0.22
	0.6	18	1.00	2.01	2.06	0.35	0.19
	0.05	12	1.00	1.75	1.91	0.41	0.27
4.5	0.005	26	1.09	4.98	5.03	0.20	0.13
	0.05	26	1.04	3.82	3.90	0.22	0.12

decreasing Ca due to increased interfacial dissipation. In general, $\mu_c/\mu_f > 1$, and it increases with increasing hematocrit and decreasing Ca .

Using the values of μ_c and μ_f given in Table 6.2, the velocity profile from the two-phase model (eq 6.2.10) can be obtained. It of interest to compare the resulting velocity profile predicted by the two-phase model with that obtained directly from the simulations. This comparison is shown in figure 6.16. We see that the two-phase model underpredicts the mean velocity. This implies that the two-phase model would underpredict the flow rate, and hence overpredict the relative apparent viscosity. The difference between the results from the simulations and the two-phase model could be as high as 40% depending on y -location, and it increases with decreasing Ca . It must be emphasized that despite the difference between the two results, the two-phase model has been shown to agree with in vitro blood velocity. As mentioned before, this agreement, however depends on the choice of the empirical constants δ , μ_f and μ_c .

The difference between the velocity profiles predicted by the two-phase model and the simulation is due to the step-like variation of $\mu(y)$ assumed in the two-phase model. As shown in figure 6.15c the model overestimates the viscosity in the region immediately outside the cell-free layer compared to that obtained in the DNS. This overestimation of $\mu(y)$ results

in an underprediction of the fluid velocity.

6.2.5 A three-layer model of blood flow in microvessels

The above discussion suggests that a model that takes in to consideration the y -dependence of viscosity in the vicinity of $y = \delta$ would give more accurate prediction of the DNS result. Thus, we now present a three-layer model of blood flow in microvessel. This is illustrated in figure 6.15b. In this model the vessel is divided in three layers: a cell-free layer of thickness δ of constant viscosity μ_f , a transition layer of thickness $\beta - \delta$ wherein viscosity varies *linearly* with y , and a core region of half-width $H/2 - \beta$ of constant viscosity μ_c . Thus,

$$\text{cell free layer : } \mu(y) = \mu_f \quad \text{for } 0 \leq y \leq \delta, \quad (6.2.15)$$

$$\text{transition layer : } \mu(y) = \mu_f + \frac{\mu_c - \mu_f}{\beta - \delta} (y - \delta) \quad \text{for } \delta \leq y \leq \beta, \quad (6.2.16)$$

$$\text{and, core : } \mu(y) = \mu_c \quad \text{for } \beta \leq y \leq H/2. \quad (6.2.17)$$

Note that in this model μ_c must be calculated as

$$\mu_c = \frac{\int_0^H \mu(y) dy - \mu_f (\beta + \delta)}{H - (\beta + \delta)} \quad (6.2.18)$$

where $\mu(y)$ is obtained from the DNS results as given in figure 6.15c. The linear variation of viscosity in the intermediate region as assumed here can be improved further. However, as will be shown later, even such a linear variation can predict the DNS result with a high accuracy. We now solve for the velocity profiles in the three layers in a similar manner described above using the non-slip boundary condition at the wall, symmetry condition at the centerline, and continuity of velocity and shear stress across the interfaces at $y = \delta$ and

β . A close-form solution can be obtained as

$$u_f = -\frac{dP}{dx} \frac{1}{2\mu_f} (yH - y^2) \quad (6.2.19a)$$

$$u_\beta = -\frac{dP}{dx} \left(\frac{\beta - \delta}{\mu_c - \mu_f} \right) \left[-y + \left(\frac{\beta\mu_f - \delta\mu_c}{\mu_c - \mu_f} + \frac{H}{2} \right) \ln \frac{\mu_c}{\mu_f} + \left(\frac{\mu_c}{\mu_f} - 1 \right) \frac{H\delta - \delta^2}{2(\beta - \delta)} + \delta \right] \quad (6.2.19b)$$

$$u_c = -\frac{dP}{dx} \frac{1}{2\mu_c} \left[yH - y^2 - \frac{2(\beta - \delta)^2}{1 - \mu_f/\mu_c} \left(1 + \frac{\beta\mu_f - \delta\mu_c + (\mu_c - \mu_f)H/2}{\beta - \delta} \ln \frac{\mu_f}{\mu_c} \right) + (H\delta - \delta^2) \frac{\mu_c}{\mu_f} + \beta^2 - H\beta \right] \quad (6.2.19c)$$

where u_f , u_β and u_c are the velocity in the cell-free layer, intermediate layer, and in the core, respectively. Again, the values of δ , β , μ_f , and μ_c are obtained from the DNS as described earlier. β is taken as the lowest value of y where $H_t(y)$ has a local maximum. The values of β , thickness of the transition layer $\beta - \delta$, and μ_c for the three-layer model are given in Table 6.2. Note that β does not show any strong dependence on Ca or H , but it increases with decreasing H_t . The thickness of the transition layer $\beta - \delta$, however, depends on hematocrit and Ca . It decreases with increasing Ca . This is because elongated cell shape at higher Ca allows more close-packed arrangement in the vicinity of $y = \delta$. It also decreases with increasing H_t due to reduced cell-cell separation distance. Most importantly, the transition layer thickness is comparable and often greater than the cell-free layer thickness δ by several factors. Thus, it is expected to play a major role in determining blood velocity profile. Also note that μ_c values for the three-layer model (eq 6.2.18) are higher than those for the two-phase model (eq 6.2.14) due to the introduction of the transition layer.

Prediction based on the three-layer model given by eq 6.2.19 are compared in figure 6.16 against the DNS data. Excellent agreement between the proposed three-layer model and the DNS result is evident.

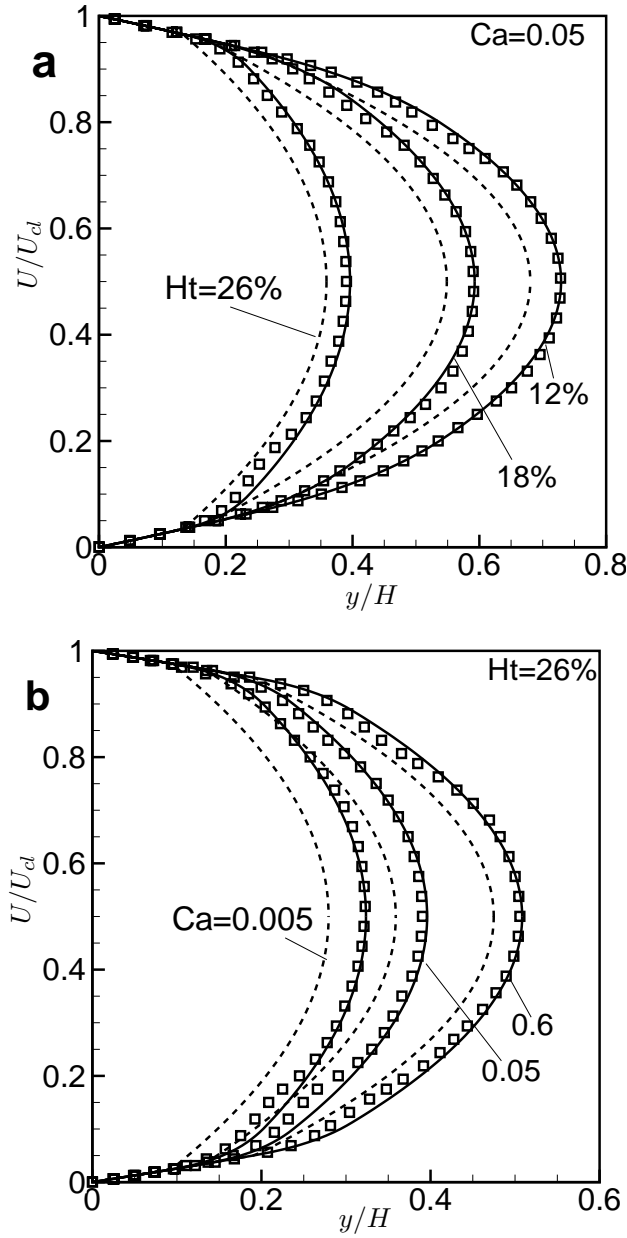


Figure 6.16: Comparison of mean velocity obtained from simulations (symbols), and predicted by two-phase model (eq 6.2.10, dash lines) and three-layer model (eq 6.2.19, solid lines). Results are shown for $H/d = 6.3$. In (a) H_t is varied while Ca is held fixed. In (b) Ca is varied and H_t is held fixed.

6.3 Conclusion

Three-dimensional computational simulation of a large number of deformable cells flowing in microchannels is presented. The focus is on hydrodynamics of multiple deformable cells flowing in microvessels, typical of mammalian microcirculation and microfluidic devices. The simulations generated a database with a wealth of information on the dynamics of flowing cell suspension which can be further post-processed to gain deeper insight in the general problem of suspension of deformable particles, and of erythrocytes, in particular. For example, the simulations results can be used to obtain collision frequency of cells as a function of cell deformability, volume fraction, and size ratio, which is of importance in modeling cell-cell aggregation. The coefficient of hydrodynamic dispersion of cells, and that of tracer particles can also be obtained, which are of importance in solute and drug transport in microvessels. In this chapter, we present results on radial migration of cells, and their tumbling motion as observed for erythrocytes, analyze the trajectory and velocity of individual cells in the suspension as functions of cell deformability, hematocrit, and channel width. The Fahraeus and Fahraeus-Lindqvist effects are also predicted by our simulations. The simulations allow us to directly estimate the width of the cell-free layer, and also the cross-section variation of effective viscosity. We then use these results to show that the two-phase models underpredict the mean velocity of blood obtained in the simulations. We develop a three-layer model, and show that this gives an accurate prediction of the simulation results.

Chapter 7

Conclusions of Thesis and Directions for Future Work

7.1 Summary and conclusions

We study dynamics of capsules as models for deformable blood cells. The focus is on development of a three-dimensional computational modeling that can resolve the motion and deformation of individual capsule, as well as a large number of hydrodynamically interacting capsules.

The main results of this thesis can be summarized as follows:

1. **Numerical development:** Three-dimensional direct numerical simulation is developed to consider large deformation of capsules in shear flow. An immersed boundary/front-tracking method is used for the fluid/structure interaction problem. The flow solver is based on a mixed finite-difference/Fourier transform method. Capsules are modeled as liquid drops surrounded by elastic membranes. Thus, unlike in a liquid drop, the interface of a capsule is governed by more complex constitutive laws that describe the mesoscopic behavior of lipid bilayers. In this study, we have used neo-Hookean model for the membrane, but the methodology can readily incorporate more complex models such as those given by Evans & Skalak (1980) and Skalak *et al.* (1973). The flow solver can also accommodate variable viscosity, and hence bi- or poly-disperse cell suspension. Extensive validation of the methodology is performed against experimental results using artificial capsules, and boundary integral simulation.

Using the simulation tool, we address a sequence of problems on capsule dynamics.

2. **Motion of a capsule in wall-bounded parabolic flow:** First, we consider the

motion of a deformable capsule in a channel flow in absence of inertia. As per the theory of viscous fluids (Stokes flow), a deformable particle in an wall-bounded shear flow drifts laterally away from the wall while translating axially with the flow. Such lateral migration results due to interfacial nonlinearity that leads to the generation of a hydrodynamic lift force normal to the flow direction. Lateral migration of liquid drops has been studied for nearly half-a-century. Similar study for liquid capsules in the limit of large deformation is absent, and is a topic in the present study. Motion of a capsule in wall-bounded parabolic flow is simulated over an extended period of time to consider both transient and steady-state motion. Lateral migration of the capsule towards the centerline of the channel is observed. Results are presented over a range of capillary number, viscosity ratio, capsule-to-channel size ratio, and lateral location. After an initial transient phase during which the capsule deforms very quickly, the flow of the capsule is observed to be a quasi-steady process irrespective of capillary number (Ca), capsule-to-channel size ratio (a/H), and viscosity ratio (λ). Migration velocity and capsule deformation are observed to increase with increasing Ca and a/H , but decrease with increasing λ , and increasing distance from the wall. Numerical results on the capsule migration are compared with the analytical results for liquid drops (Chan & Leal 1979), and capsules with Hookean membrane (Helmy & Barthes-Biesel 1980) which are valid in the limit of small deformation. Unlike the prediction for liquid drops (Chan & Leal 1979), capsules are observed to migrate toward the centerline for $0.2 \leq \lambda \leq 5$ range considered here. The migration velocity is observed to depend linearly on $(a/H)^3$, in agreement with the small-deformation theory, but non-linearly on Ca and the distance from the wall, in violation of the theory. Using the present numerical results and the analytical results of Shapira & Haber (1988), we present a correlation that can reasonably predict migration velocity of a capsule for moderate values of a/H and Ca .

3. Motion of a capsule-pair in channel flow: The effect of neighboring capsule on

lateral migration is studied by considering a pair capsules in a wall-bounded pressure-driven flow in absence of inertia. We observe completely different dynamics depending on the locations of the capsules in the channel. When the capsules are located in an equispaced array, all of them have the same migration velocity that is significantly lower than that of an isolated capsule. In a non-equispaced array, the capsules engage in a leap-frog motion, and the migration velocity can become periodically negative. If the capsules are released at different lateral location with respect to the wall, the so-called shear-induced diffusion process sets in. In the process, one capsule rolls over the other while both of them migrate away from the wall. We conclude that the shear-induced diffusion dominates over the deformation-induced migration process.

We also studied the tumbling motion of an ellipsoidal capsule, as simplified geometric model for a red blood cell. We further extend our study to consider the motion of an ellipsoidal capsule-pair. The leap-frog motion, and the shear-induced diffusion process observed for the spherical capsules are also observed for the ellipsoidal capsules. This study shows that the area of binary interaction of spherical and non-spherical deformable particles is rich with new and interesting physics, and further motivates for careful experimental studies to verify the numerical observations made here.

4. **Effect of inertia in capsule interaction:** Three-dimensional numerical simulations are performed to study the hydrodynamic interaction between two capsules suspended in simple shear flow in presence of inertia. In the limit of zero inertia, it has been known from past research that the hydrodynamic interaction between two deformable particles (drops/capsules) suspended in shear flow results in an irreversible shift in the trajectories of the particles as one particle rolls over the other. Here we found that when inertia is small but finite, the capsules do undergo an irreversible displacement, but the lateral separation between them first decreases before they roll over each other, unlike in $Re \ll 1$. For moderate to high inertia, the capsules reverse their directions of motion before coming close to each other. The reversal of motion occurs progressively earlier in time with increasing inertia. The long-time behavior of the capsule-capsule

interaction at finite inertia showed that the capsules engage in spiraling motions. Based on our simulations, four different regimes of capsule-capsule interaction at finite inertia are identified: (i) a self-diffusive type interaction, (ii) an outwardly spiraling motion, (iii) a fixed-orbit spiraling motion, and (iv) an inwardly spiraling motion in which the capsules settle with zero relative velocity. The reversal of motion, and the spiraling trajectories at finite inertia have no analogy in the limit of zero inertia. Such motions are explained by analyzing the flow field around a deformed capsule which shows reverse flow regions and off-surface stagnation points, similar to those previously reported in case of rigid spheres and cylinders under torque-free condition.

5. Motion of multiple deformable capsules: We perform 3D simulations of multiple deformable capsules flowing in microchannels. Both spherical and biconcave capsules, with 0(100) capsules at a maximum volume fraction of 26% are considered. The objective was to study some physiologically relevant quantities, such as the cell-free layer, apparent viscosity, and the Fahraeus and Fahraeus-Lindqvist effects. The channel width ranges from about 10–45 μm , which allows us to consider both single and multi-file motion. We present results on tumbling motion, and radial drift of biconcave capsules, as observed for erythrocytes. We analyze the trajectory and velocity fluctuations of individual capsules in the suspension, and the plug-flow velocity profile as functions of cell deformability, hematocrit, and channel width. Comparison with *in vitro* (Pries *et al.* 1992) and *in vivo* (Bishop *et al.* 2002; Kim *et al.* 2007) data is presented throughout. The Fahraeus and Fahraeus-Lindqvist effects predicted by our simulations are also presented. The simulations allow us to directly obtain the width of the cell-free layer. We then use these results to show that the two-phase (or, core-annular) model for blood flow in microvessels underpredicts the blood velocity in comparison to that obtained in the simulations. Based on a *posteriori* analysis of the simulations data, we develop a three-layer model for blood flow in microvessel. This model is shown to give an accurate prediction of the simulation results.

7.2 Future directions

Some problems of future interest that can be addressed by the present computational methodology are mentioned below:

- Modeling issues and capsule dynamics:** The present methodology can be readily extended to consider more complex constitutive laws for the membrane material. The dynamics of the capsule for different constitutive laws is an interesting area for future consideration. Further, the effect of internal-to-external viscosity ratio is not fully explored here. As mentioned before, a very rich inclination dynamics occurs when the viscosity ratio changes and the capsule makes transition from tank-treading, to wobbling, and to tumbling. Effect of viscosity ratio is relatively less studied as it poses further computational challenge due to more stringent diffusion stability limit. Dynamics of non-spherical capsules is also another topic that is less studied and can be addressed by the present methodology.
- Binary collision of dissimilar particles:** In the present thesis we addressed binary interaction of identical capsules which is relevant for monodisperse suspension. In many practical situations, however, bi- and poly-disperse suspensions are encountered. A very interesting problem that can be addressed using the present methodology is the shear-induced diffusion process for a pair of non-identical capsules, with and without inertia.
- Multi-particle interaction:** Finally, the ‘grand challenge’ problem in the present area of interest is the dynamics of suspension of deformable particles, as in case of blood flow in microcirculation. In Chapter 6, we have only briefly addressed this problem. With the current advances in computing resources, one can consider even larger ensemble comprising of more than a thousand capsules. Such a large system would enable us to compute more reliable statistics of the rheology of the suspension, and hence possibly a better low-dimensional model than the one described in Chapter 6, that would incorporate more physics. Extended simulations would also allow us

to compute dispersion coefficient that is of paramount importance in such modeling. Further, the simulations results can be used to obtain collision frequency of cells as a function of cell deformability, volume fraction, and size ratio, which is of importance in modeling cell-cell aggregation. The coefficient of hydrodynamic dispersion of tracer particles in a cell suspension is another problem of interest that is relevant for solute and drug transport in microvessels, and can be addressed by the present methodology.

Bibliography

- [1] Acrivos, A., Batchelor, G.K., Hinch, E.J., Koch, D.L., & Mauri, R., 1992. Longitudinal shear-induced diffusion of spheres in a dilute suspension. *Journal of Fluid Mechanics* 240, 651–657.
- [2] Ashgriz, N., & Poo, J.Y., 1990. Coalescence and separation in binary collisions of liquid drops. *Journal of Fluid Mechanics* 221, 183–204.
- [3] Bagchi, P., 2007. Mesoscale simulation of blood flow in small vessels. *Biophysical Journal* 92, 1858–1877.
- [4] Barthès-Biesel, D., 1980. Motion of a spherical microcapsule freely suspended in a linear shear flow. *Journal of Fluid Mechanics* 100, 831–853.
- [5] Barthès-Biesel, D., & Chim, V., 1981. Constitutive equation of a dilute suspension of spherical microcapsules. *International Journal of Multiphase Flow* 7, 473–493.
- [6] Barthès-Biesel, D., & Rallison, J.M., 1981. The time-dependent deformation of a capsule freely suspended in a linear shear flow. *Journal of Fluid Mechanics* 113, 251 - 267.
- [7] Barthès-Biesel, D., & Sgaier, H., 1985. Role of membrane viscosity in the orientation and deformation of a spherical capsule suspended in shear flow. *Journal of Fluid Mechanics* 160, 119–135.
- [8] Barthès-Biesel, D., Diaz, A., & Dhenin, E., 2002. Effect of constitutive laws for two-dimensional membranes on flow-induced capsule deformation. *Journal of Fluid Mechanics* 460, 211–222.

- [9] Barthès-Biesel, D., Diaz, A., & Dhenin, E., 2002. Effect of constitutive laws for two-dimensional membranes on flow-induced capsule deformation. *Journal of Fluid Mechanics* 460, 211–222.
- [10] Batchelor, G.K., & Green, J.T., 1972. The hydrodynamic interaction of two small freely-moving spheres in a linear flow field. *Journal of Fluid Mechanics* 56, 375–400.
- [11] Bishop, J. J., Popel, A.S., Intaglietta, M., & Johnson, P.C., 2002. Effect of aggregation and shear rate on the dispersion of red blood cells flowing in venules. *Am. J. Physiol.* 283:H1985H1996.
- [12] Borhan, A., & Gupta, N.R., 2003. Capsule motion and deformation in tube and channel flow. In *Modeling and Simulation of Capsules and Biological Cells*, edited by C. Pozrikidis. Chapman & Hall/CRC, Boca Raton, Florida.
- [13] Brady, J.F., & Bossis, G., 1985. The rheology of concentrated suspensions of spheres in simple shear flow by numerical simulation. *Journal of Fluid Mechanics* 155, 105–129.
- [14] Brady, J.F., & Morris, J.F., 1997. Microstructure of strongly sheared suspensions and its impact on rheology and diffusion. *Journal of Fluid Mechanics* 348, 103–139.
- [15] Breyiannis, G., & Pozrikidis, C., 2000. Simple shear flow of suspensions of elastic capsules. *Theoretical and Computational Fluid Dynamics* 13, 327–347.
- [16] Breedveld, V., van den Ende, D., Tripathi, A., & Acrivos, A., 1998. The measurement of the shear-induced particle and fluid tracer diffusivities in concentrated suspensions by a novel method. *Journal of Fluid Mechanics* 375, 297–318.
- [17] Breedveld, V., van den Ende, D., Bosscher, M., Jongschaap, R.J.J., & Mellema, J., 2001. Measuring shear-induced self-diffusion in a counterrotating geometry. *Physical Review E* 63, 1(021403).
- [18] Brenn, G., & Kolobaric, V., 2006. Satellite droplet formation by unstable binary drop collisions. *Physics of Fluids* 18, 087101.

- [19] Bunner, B., & Tryggvason, G., 2002. Dynamics of Homogeneous Bubbly Flows. Part 1. Rise Velocity and Microstructure of the Bubbles. *Journal of Fluid Mechanics* 466, 17–52.
- [20] Bunner, B., & Tryggvason, G., 2002. Dynamics of Homogeneous Bubbly Flows. Part 2. Fluctuations of the bubbles and the liquid. *Journal of Fluid Mechanics* 466, 53–84.
- [21] Chan, P. C.-H., & Leal, L. G., 1979. The motion of a deformable drop in a second-order fluid. *Journal of Fluid Mechanics* 92, 131–170.
- [22] Chang, K.S., & Olbricht, W.L., 1993. Experimental studies of the deformation of a synthetic capsule in extensional flow. *Journal of Fluid Mechanics* 250, 587–608.
- [23] Chang, C., & Powell, R.L., 1994. Self-diffusion of bimodal suspensions of hydrodynamically interacting spherical particles in shearing flow. *Journal of Fluid Mechanics* 281, 51–80.
- [24] Charles, R., & Pozrikidis, C., 1998. Effect of the dispersed phase viscosity on the simple shear flow of suspensions of liquid drops. *Journal of Fluid Mechanics* 365, 205–233.
- [25] Charrier, J. M., Shrivastava, S., & Wu, R., 1989. Free and constrained inflation of elastic membranes in relation to thermoforming-non-axisymmetric problems. *Journal of Strain Analysis* 24, No. 2, 55–74.
- [26] Cokelet, G.R., & Goldsmith, H.L., 1991. Decreased hydrodynamic resistance in the two-phase flow of blood through small vertical tubes at low flow rates. *Circ. Res.* 68, 1–17.
- [27] Coulliette, C., & Pozrikidis, C., 1998. Motion of an array of drops through a cylindrical tube. *Journal of Fluid Mechanics* 358, 1–28.
- [28] Cox, R.G., & Hsu, S.K., 1977. The lateral migration of solid particles in a laminar flow near a plane. *Int. Journal of Multiphase Flow* 3, 201–222

- [29] daCunha, F.R., & Hinch, E.J., 1996. Shear-induced dispersion in a dilute suspension of rough spheres. *Journal of Fluid Mechanics* 309, 211–223.
- [30] Damiano, E.R., 1998. Blood flow in microvessels lined with a poroelastic wall layer. *In* Poromechanics. J.F. Thimus, Y. Abousleiman, A.H.D. Chang, O. Coussy, and E. Detournay, editors. A.A. Balkema, Rotterdam, The Netherlands.
- [31] Damiano, E.R., Long, D.S., & Smith, M.L., 2004. Estimation of viscosity profiles using velocimetry data from parallel flows of linearly viscous fluids: application to microvascular hemodynamics. *Journal of Fluid Mechanics* 512, 1–19.
- [32] Darabaner, C.L., & Mason, S.G., 1967. Particle motion in sheared suspension. XXII. Interactions of rigid spheres (Experimental). *Rheology Acta* 6, 273.
- [33] Diaz, A., Pelekasis, N., & Barthès-Biesel, D., 2000. Transient response of a capsule subjected to varying flow conditions: Effect of internal fluid viscosity and membrane elasticity. *Physics of Fluids* 12, 948–958.
- [34] Diaz, A., Barthès-Biesel, D., & Pelekasis, N., 2001. Effect of membrane viscosity on the dynamic response of an axisymmetric capsule. *Physics of Fluids* 13, 3835–3839.
- [35] Ding, E.J., & Aidun, C.K., 2006. Cluster size distribution and scaling for spherical particles and red blood cells in pressure-driven flows at small Reynolds number. *Phys Rev Letters* 96(20):204502.
- [36] Drazer, G., Koplik, J., Khusid, B., & Acrivos, A., 2002. Deterministic and stochastic behavior of non-Brownian spheres in sheared suspensions. *Journal of Fluid Mechanics* 460, 307–335.
- [37] Eckstein, E.C., Bailey, D.G., & Shapiro, A.H., 1977. Self-diffusion of particles in shear flow of a suspension. *Journal of Fluid Mechanics* 79, 191–208.
- [38] Eggleton, C. D., & Popel, A. S., 1998. Large deformation of red blood cell ghosts in a simple shear flow. *Physics of Fluids* 10, No. 8, 1834–1845.

- [39] Evans, E. A., & Skalak, R., 1980. *Mechanics and Thermodynamics of Biomembranes*. (CRC, Boca Raton, FL.)
- [40] Feng, J., Hu, H.H., & Joseph, D.D., 1994. Direct simulation of initial value problems for the motion of solid bodies in a Newtonian fluid. Part 2. Couette and Poiseuille flows, *Journal of Fluid Mechanics* 277, 271 - 301.
- [41] Foss, D.R., & Brady, J.F., 1999. Self-diffusion in sheared suspensions by dynamic simulation. *Journal of Fluid Mechanics* 401, 243–274.
- [42] Freund, J.B., 2007. Leukocyte margination in a model microvessel. *Physics of Fluids* 19 (2), 023301.
- [43] Goldsmith, H.L., 1971. Red cell motions and wall interactions in tube flow. *Federation Proceedings* 30, 1578–1590.
- [44] Goldsmith, H.L., & Mason, S.G., 1962. The flow of suspensions through tubes. I. Single spheres, rods, and disks. *J. Colloid Sci.* 17, 448–476.
- [45] Goldsmith, H.L., G.R. Cokelet., & P. Gaehtgens., 1989. Robin Fahraeus: evolution of his concepts in cardiovascular physiology, *Am. J. Physiol.* 257, H1005.
- [46] Guido, S., & Simeone, M., 1998. Binary collisions of drops in simple shear flow by computer-assisted video optical microscopy. *Journal of Fluid Mechanics*, 357, 1–20.
- [47] Gutcho, M.H., 1979. *Microcapsules and other Capsules*, Noyes Data Corporation, Park Ridge, New Jersey.
- [48] Happel, J., & Brenner, H., 1983. *Low Reynolds Number Hydrodynamics*, Kluwer.
- [49] Helmy, A., & Barthès-Biesel, D., 1982. Migration of a spherical capsule freely suspended in an unbounded parabolic flow. *J. de Mecanique theorique et appliquee* 1, 859–880.
- [50] Hiller, W., & Kowalewski, T. A., 1987. An experimental study of the lateral migration of a droplet in a creeping flow. *Experiments in Fluids* 5, 43–48.

- [51] Ho, B. P., & Leal, L. G., 1974. Inertial migration of rigid spheres in two-dimensional unidirectional flows. *Journal of Fluid Mechanics* 65, 365–400.
- [52] Hsu, R., & Secomb, T.W., 1989. Motion of nonaxisymmetric red blood cells in cylindrical capillaries. *J. Biomech. Engg.* 111, 147–151.
- [53] Jeffery, G.B., 1922. The motion of ellipsoidal particles immersed in a viscous fluid. *Proc. R. Soc. London, Ser A* 102, 161–170.
- [54] Johnson, R. A., & Borhan, A., 2003. Pressure-driven motion of surfactant-laden drops through cylindrical capillaries: effect of surfactant solubility. *J. Colloid Interface Sci.* 261, 529–541.
- [55] Karnis, A., Goldsmith, H.L., & Mason, S.G., 1963. Axial migration of particles in Poiseuille flow. *Nature* 200, 159–160.
- [56] Keller, S.R., & Skalak, R., 1982. Motion of a tank-treading ellipsoidal particle in a shear flow. *Journal of Fluid Mechanics* 120, 27–47.
- [57] Kim, S., Kong, R.L., Popel, A.S., Intaglietta, M., & Johnson, P.C., 2007. Temporal and spatial variations of cell-free layer width in arterioles. *Am. J. Physiol. Heart Circ. Physiol.* 293:H1526–H1535.
- [58] Kwak, S., & Pozrikidis, C., 2001. Effect of membrane bending stiffness on the axisymmetric deformation of capsules in uniaxial extensional flow. *Physics of Fluids* 13, 1234–1244.
- [59] Kossack, C.A., & Acrivos, A., 1974. Steady simple shear flow past a circular cylinder at moderate Reynolds numbers: a numerical solution. *Journal of Fluid Mechanics* 66, 353–376.
- [60] Kromkamp, J., Van den Ende, D.T.M., Kandhai, D., Van der Sman, R.G.M., & Boom, R.M., 2005. Shear-induced self-diffusion and microstructure in non-Brownian suspensions at non-zero Reynolds numbers. *Journal of Fluid Mechanics* 529, 253–278.

- [61] Lac, E., Barthès-Biesel, D., Pelekasis, N.A., & Tsamopoulos, J., 2004. Spherical capsules in three-dimensional unbounded Stokes flows: effect of the membrane constitutive law and onset of buckling. *Journal of Fluid Mechanics* 516, 303-334.
- [62] Lac, E., & Barthès-Biesel, D., 2005. Deformation of a capsule in simple shear flow: Effect of membrane prestress. *Physics of Fluids* 17, 072105.
- [63] Lac, E., Morel, A., & Barthès-Biesel, D., 2007. Hydrodynamic interaction between two identical capsules in simple shear flow. *Journal of Fluid Mechanics* 573, 149 - 169.
- [64] Leighton, D.T., & Acrivos, A., 1987. Measurement of shear-induced self-diffusion in a concentrated suspension of spheres. *Journal of Fluid Mechanics* 177, 109-131.
- [65] Leyrat-Maurin, A., & Barthès-Biesel, D., 1994. Motion of a deformable capsule through a hyperbolic constriction. *Journal of Fluid Mechanics* 279, 135-163.
- [66] Li, X.Z., Barthès-Biesel, D., & Helmy, A., 1988. Large deformations and burst of a capsule freely suspended in an elongational flow. *Journal of Fluid Mechanics* 187, 179-196.
- [67] Li, X., & Pozrikidis, C., 2000. Wall-bounded and channel flow of suspensions of liquid drops. *Int. J. Multiphase Flow* 26, 1247-1279.
- [68] Li, X., & Sarkar, K., 2008. Front tracking simulation of deformation and buckling instability of a liquid capsule enclosed by an elastic membrane. *Journal of Comp. Physics*. 227, 4998-5018.
- [69] Loewenberg, M., & Hinch, E. J., 1997. Collision of two deformable drops in shear flow. *Journal of Fluid Mechanics* 338, 299-315.
- [70] Long D.S., Smith M.L., Pries, A.R., Ley K., & Damiano, E.R., 2004. Microviscometry reveals reduced blood viscosity and altered shear rate and shear stress profiles in microvessels after hemodilution. *Proc Natl Acad Sci. U S A*. 101(27):10060-5.

- [71] Marchioro, M., & Acrivos, A., 2001. Shear-induced particle diffusivities from numerical simulations. *Journal of Fluid Mechanics* 443, 101–128.
- [72] Mikulencak, D.R., & Morris, J.F., 2004. Stationary shear flow around fixed and free bodies at finite Reynolds number. *Journal of Fluid Mechanics* 520, 215–242.
- [73] Mohamed-Kassim, Z., & Longmire, E.K., 2004. Drop coalescence through a liquid/liquid interface. *Physics of Fluids* 16, 2170–2183.
- [74] Mortazavi, S., & Tryggvason, G., 2000. A numerical study of the motion of drops in Poiseuille flow. Part 1. Lateral migration of one drop. *Journal of Fluid Mechanics* 411, 325–350.
- [75] Nobari, M. R. H., & Tryggvason, G., 1996. Numerical simulations of three dimensional drop collisions. *AIAA Journal* 34, 750–755.
- [76] Nott, P. R., & Brady, J. F., 1994. Pressure-driven Flow of Suspensions: Simulation and Theory. *Journal of Fluid Mechanics* 275, 157–99.
- [77] Pan, Y., & Suga, K., 2005. Numerical simulation of binary liquid droplet collision. *Physics of Fluids* 17, 082105.
- [78] Pappu, V., & Bagchi, P., 2007. Hydrodynamic Interaction Between Erythrocytes and Leukocytes Affects Rheology of Blood in Microvessels. *Biorheology* 44 (3):191-215, 17851167.
- [79] Pappu, V., Doddi, S., & Bagchi, P., 2008. Cell Deformation and Rolling Velocity Affect Flow Resistance due to Adherent Leukocytes: A 3D Computational Study. *To appear in Journal of Theoretical Biology*.
- [80] Peskin, C.S., 1977. Numerical analysis of blood flow in the heart. *J. Comput. Physics* 25, 220-233.
- [81] Pigeonneau, F., & Feuillebois, F., 2002. Collision of drops with inertia effects in strongly sheared linear flow fields. *Journal of Fluid Mechanics* 455, 359–386.

- [82] Pivkin, I.V., Richardson, P.D., & Karniadakis, G., 2006. Blood flow velocity effects and role of activation delay time on growth and form of platelet thrombi. *Proc Natl Acad Sci. U S A.* 103(46):17164-9.
- [83] Poe, G.G., & Acrivos, A., 1975. Closed-streamline flows past rotating single cylinders and spheres: inertia effects. *Journal of Fluid Mechanics* 72, 605–623.
- [84] Popel, A.S., & Johnson, P.C., 2005. Microcirculation and hemorheology. *Annu. Rev. Fluid. Mech.* 37, 43–69.
- [85] Pozrikidis, C., 1993. On the transient motion of ordered suspensions of liquid drops. *J. Fluid Mech.* 246, 301–320.
- [86] Pozrikidis, C., 1995. Finite deformation of liquid capsules enclosed by elastic membranes in simple shear flow. *Journal of Fluid Mechanics* 297, 123–152.
- [87] Pozrikidis, C., 2001. Effect of membrane bending stiffness on the deformation of capsules in simple shear flow. *Journal of Fluid Mechanics* 440, 269–291.
- [88] Pozrikidis, C., 2003. *Modeling and Simulation of Capsules and Biological Cells* Chapman & Hall/CRC, Boca Raton, Florida.
- [89] Pries, A. R., Neuhaus, D., & Gaehtgens, P., 1992. Blood viscosity in tube flow: dependence on diameter. *Am. J. Physiol.* 263:H1770H1778.
- [90] Qian, J., & Law, C. K., 1997. Regimes of coalescence and separation in droplet collision. *Journal of Fluid Mechanics* 331, 59–80.
- [91] Queguiner, C., & Barthès-Biesel, D., 1997. Axisymmetric motion of capsules through cylindrical channels. *Journal of Fluid Mechanics* 348, 349–376.
- [92] Ramanujan, S., & Pozrikidis, C., 1998. Deformation of liquid capsules enclosed by elastic membranes in simple shear flow: large deformations and the effect of fluid viscosities. *Journal of Fluid Mechanics* 361, 117–143.

- [93] Rehage, H., Husmann, M., & Walter, A., 2002. From two-dimensional model networks to microcapsules. *Rheol. Acta* 41, 292–306.
- [94] Roisman, I.V., 2004. Dynamics of inertia dominated binary drop collisions. *Physics of Fluids* 16, 3438–3444.
- [95] Risso, F., Colle-Paillot, F., & Zagzoule, M., 2006. Experimental investigation of a bioartificial capsule flowing in a narrow tube. *Journal of Fluid Mechanics* 547, 149–174.
- [96] Secomb, T.W., Skalak, R., Ozkaya, N., & Gross, J.F., 1986. Flow of axisymmetric red blood cells in narrow capillaries. *Journal of Fluid Mechanics* 163, 405–423.
- [97] Secomb, T.W., 2003. Mechanics of red blood cells and blood flow in microcirculation. In *Modeling and simulation of capsules and biological cells.*, edited by C. Pozrikidis. Chapman & Hall/CRC.
- [98] Secomb, T.W., Styp-Rekowska, B., & Pries, A.R., 2007. Two-dimensional simulation of red blood cell deformation and lateral migration in microvessels. *Ann. Biomed. Eng.* 35(5), 755–765.
- [99] Segre, G., & Silberberg, A., 1962. Behavior of macroscopic rigid spheres in Poiseuille flow. Part 2. Experimental results and interpretation. *Journal of Fluid Mechanics* 14, 136–157.
- [100] Sierou, A., & Brady, J.F., 2004. Shear-induced self-diffusion in non-colloidal suspensions. *Journal of Fluid Mechanics* 506, 285–314.
- [101] Skalak, R., Tozeren, A., Zarda, P.R., & Chien, S., 1973. Strain energy function of red blood cell membranes. *Biophys. J.* 13, 245–264.
- [102] Stickel, J., & Powell, R., 2005. Fluid mechanics and rheology of dense suspensions. *Annual Review of Fluid Mechanics* 37, 129–149.

- [103] Skotheim, J.M., & Secomb, T.W., 2007. Red blood cells and other nonspherical capsules in shear flow: oscillatory dynamics and the tank-treading-to-tumbling transition. *Phys Rev Lett.* 98(7), 078301.
- [104] Skalak, R., Ozkaya, N. & Skalak, T.C., 1989. *Annual Review of Fluid Mechanics* 21, 167–204.
- [105] Sun, C., & Munn, L.L., 2005. Particulate nature of blood determines macroscopic rheology: a 2D Lattice-Boltzmann analysis. *Biophysical J.* 88, 1635–1645.
- [106] Tryggvason, G., Bunner, B., Esmaeeli, A. Juric., Al-Rawahi, N., Tauber, W., Han, J., Nas, S., & Jan, Y.-J., 2001. A Front Tracking Method for the Computations of Multiphase Flow. *J. Comp. Phys.* 169, 708–759.
- [107] Unverdi, S.O., & Tryggvason, G., 1992. A Front-tracking method for viscous, incompressible multi-fluid flows. *Journal of Computational Physics* 100, 25–37.
- [108] Vasseur, P., & Cox, R. G., 1976. The lateral migration of a spherical particle in two-dimensional shear flows. *Journal of Fluid Mechanics* 78, 385–413.
- [109] Wang, H.W., Zinchenko, A., & Davis, R.H., 1994. The collision rate of small drops in linear flow fields. *Journal of Fluid Mechanics* 265, 161–188.
- [110] Wang, Y., Mauri, R., & Acrivos, A., 1996. The transverse shear-induced liquid and particle tracer diffusivities of a dilute suspension of spheres undergoing a simple shear flow. *Journal of Fluid Mechanics* 327, 255–272.
- [111] Yurkovetsky, Y., 1998. I. Statistical mechanics of bubbly liquids. II. Behavior of sheared suspensions of non-Brownian particles. PhD thesis, California Institute of Technology.
- [112] Zhang, J., Johnson, P. C., & Popel, A.S., 2007. An immersed boundary lattice Boltzmann approach to simulate deformable liquid capsules and its application to microscopic blood flows. *Phys Biol.* 4(4), 285–295.

- [113] Zhao, H., Freund, J.B., & Moser, R.D., 2008. A fixed-mesh method for incompressible flow-structure systems with finite solid deformations *Journal of Computational Physics* 227(6), 3114–3140.
- [114] Zhou, H., & Pozrikidis, C., 1993. The flow of ordered and random suspension of two-dimensional drops in a channel. *Journal of Fluid Mechanics* 255, 103–127.
- [115] Zhou, H., & Pozrikidis, C., 1994. Pressure-driven flow of suspensions of liquid drops. *Physics of Fluids* 6, 80–94.

Vita

Sai Doddi

- 2008** Ph. D. in Mechanical and Aerospace Engineering, Rutgers University
- 2004** M.S. in Mechanical Engineering, University of Kentucky, Lexington
- 2001** B.Tech. in Mechanical Engineering, Indian Institute of Technology, Madras
-
- 2004-2007** Teaching assistant, Department of Mechanical and Aerospace Engineering,
Rutgers University